VIBRATION ANALYSIS AND IDENTIFICATION OF FAULTS IN A SPUR GEARED ROTOR SYSTEM INTEGRATED WITH ACTIVE MAGNETIC BEARINGS

A Thesis Submitted in Partial Fulfilment of the Requirements for the Degree of

DOCTOR OF PHILOSOPHY

by

GARGI MAJUMDER

DEPARTMENT OF MECHANICAL ENGINEERING

INDIAN INSTITUTE OF TECHNOLOGY GUWAHATI

GUWAHATI 781039, INDIA

MAY 2022

VIBRATION ANALYSIS AND IDENTIFICATION OF FAULTS IN A SPUR GEARED ROTOR SYSTEM INTEGRATED WITH ACTIVE MAGNETIC BEARINGS

A Thesis Submitted in Partial Fulfilment of the Requirements for the Degree of

DOCTOR OF PHILOSOPHY

by

GARGI MAJUMDER

DEPARTMENT OF MECHANICAL ENGINEERING

INDIAN INSTITUTE OF TECHNOLOGY GUWAHATI

GUWAHATI 781039, INDIA

MAY 2022

Department of Mechanical Engineering
Indian Institute of Technology Guwahati
Guwahati-781039, INDIA

CERTIFICATE

It is certified that the work contained in the thesis titled, **Vibration Analysis and Identification of Faults in a Spur Geared Rotor System Integrated with Active Magnetic Bearings**, submitted by **Ms. Gargi Majumder** (Roll. no. 156103014) to the Indian Institute of Technology Guwahati for the award of the degree of Doctor of Philosophy has been carried out under my supervision in the Department of Mechanical Engineering, Indian Institute of Technology Guwahati. This work has not been submitted elsewhere for the award of any other degree or diploma.

May 2022

Dr. Rajiv Tiwari
Professor
Department of Mechanical Engineering
Indian Institute of Technology Guwahati
Guwahati – 781039, INDIA

For my mother Smt. Banani Majumder and

father Sri Shibupada Majumder

Acknowledgment

"Dream is not the thing you see in sleep but is that thing that doesn't let you sleep"

Foremost, I would like to express my sincere gratitude and thanks to my advisor, Prof. Rajiv Tiwari for the continuous support, motivation and patience to continue my Ph.D. research work. His guidance and support has helped me pass smoothly through the ups and downs of my Ph.D. life specially, at the time when my former Ph.D. supervisor Dr. Annem Narayana Reddy unexpectedly left us for his heavenly abode. I will always remember Dr. Reddy as an epitome of knowledge, compassionate, young, dynamic, and an enthusiastic professor, researcher, and mentor. His taught values and ethics have and will always benefit me to shape my future. I will be always grateful to Prof. Tiwari for extending a helping hand and mental support at the extreme time of my need. I believe that without his guidance this research work wouldn't have been successfully completed within the stipulated time. His articulate work plans made the most complicated objectives look simple and easy. I place on record the time and efforts Prof. Tiwari put in to mold me into a better person, and a focused researcher in particular. It will be an extreme honour to collaborate with him in the near future and work on more interesting problems.

Besides my advisor, I want to thank Dr. Dhrubajyoti Bordoloi, who was instrumental in helping me smoothly conduct the various lab experiments. I would like to thank my doctoral committee comprising of Prof. Sashindra Kumar Kakoty, Prof. Praveen Kumar, and Prof. Sachin Singh Gautam, for their insightful comments, encouragement and questions which incented me to widen my research from various perspectives. I would also like to thank all the anonymous reviewers for taking time off to go through my research and giving me thought-provoking ideas to better the understanding of the problem under consideration.

I am deeply indebted to the Department of Mechanical Engineering, IIT Guwahati for providing me with necessary infrastructure and funds to carry out this research. The financial

support assisted me to successfully built the test rig and conduct the experiments, and an opportunity to attend the prestigious international conference, where I could showcase my research to the veterans in the fields of Gear dynamics, Vibrations and Condition monitoring from all over the world.

I would like to thank all my friends who have actively supported me through this journey. I would like to specially mention the contribution of my lab mates: Dr. Shruti Rapur, Dr. Nilakshi Sharma, Gyan Ranjan, Dr. Dipendra Kumar, Atul Kumar Gautam, Pantho Pradip Das, Dr. Prabhat Kumar, Rajeswara Rao, and a few others, with whom I had interesting discussions, sleepless nights before deadlines, and lots of fun in the last six years. Apart from my lab mates, my other friends, Dr. Firdausa Ahmed, Dr. Saswati Ray have always remained as a constant source of encouragement.

My parents stood as my pillars of support in the hardest of times. They made sure that I had the necessary emotional stability and supported me every day all through my journey. They believed in me and never let me lose my focus towards work. I am ever grateful for their enormous love and patience.

“Little drops of water make the mighty ocean,” I would like to thank the Almighty God for making me a channel to contribute to the might of this enormous ocean of knowledge.

May 2022

Gargi Majumder

IIT Guwahati

Abstract

Gearbox is widely used in industrial, transportation and military applications. The gearbox vibrations and noise caused by variation of contact forces often causes failure in the components of gearbox, which are then transmitted to the surrounding structures. The sources of error between the mating gears while in the operation are the gear mesh deformation, transmission error, and runout; resulting in dynamic forces, excessive vibration, and noise. To avoid any undesirable effect on the gear-pair and other supporting structures, it is essential to investigate these forced vibrations in time and frequency domain. The concept of active control of gearbox vibrations with piezoelectric actuators at mounting points of the gearbox is analysed earlier in several studies, then with certain limitations. The aim of this work is to investigate the feasibility of active vibration control with Active Magnetic Bearings (AMBs), being applied for supressing the transverse vibrations in a geared rotor system against transmission error excitations at the gear mesh. The AMBs are capable of suppressing the vibration of the system (transients as well as steady-state) by controlled electromagnetic forces considering the rotor vibrational displacement with a closed loop feedback system. A concept of active vibration control by Active Magnetic Bearings (AMBs) on the shaft of a spur gearbox has been introduced having conventional bearings as well. The AMB suppresses the response of the system by generating controlled electromagnetic forces based on the gear shaft vibration measurement. The AMB force is applied in two mutual perpendicular directions without any physical contact as opposed to mechanical forces in conventional bearings. Hence, an approach to monitor and control the transverse vibration of mating gears is presented with the help of AMBs. To understand the system dynamics and prediction of vibration responses, numerical models have been developed to carry out gear rotordynamic analysis of transverse vibration, transverse vibration with gyroscopic effect and coupled torsional-lateral vibration with geared rotor faults, like the mesh deformation, gear run-out, mass unbalance and asymmetric transmission error. The dynamic transmission error has been modeled as the sum of mean and varying components of error in two orthogonal transverse directions. With a feedback PID controller, the vibration amplitude is observed to get suppressed. The frequency domain analysis is done using a full spectrum, which shows that multiple harmonics of gear mesh frequency is minimized simultaneously.

Due to high service load, harsh operating conditions, faults may develop in gears. If the gear faults are not detected early, the health may continue to degrade, causing heavy economic loss or even catastrophe. Early fault detection and diagnosis is much needed for properly scheduled shutdowns to prevent any catastrophic failure and higher cost reduction. While focusing upon the dynamics based gearbox fault modeling, detection and diagnosis, identification algorithm has been developed to estimate the geared rotor fault parameters. Considering full spectrum analysis of the geared rotor system, from rotor vibration and AMB current information, estimation of system parameters, i.e. the equivalent mesh stiffness, mesh damping, gear runouts, the mean and varying transmission error magnitude and phase angles, and the current and displacement constants of AMBs has been performed. Gaussian noise in responses and modeling errors in mathematical models have been added to test the robustness of the proposed algorithm to comply with the experimental settings.

Based on the proposed model, an experiment test rig has been set up in the laboratory and the effectiveness of the proposed model is compared with and without the application of AMBs. The approach is based on an active control of the shaft transverse vibration with an electromagnetic actuator. The control forces are applied to the rotor shafts supported on conventional rolling element bearings by an eight-pole radial AMB, as an auxiliary component and a closed-loop linear output feedback control is employed for stable, reliable, and robust operation. A linear PD controller working on differential mode is used to generate the appropriate control signals and the experimental results are presented. Simulation and experimental results showed that there is considerable amount of reduction in the geared rotor vibration levels and correspondingly in overall measured gear noise levels.

Table of Contents

List of Figures

List of Tables

Abbreviations and nomenclature

Nomenclature

A_a Area of flux in air gap between rotor and pole of actuator, mm^2

c_m Average mesh damping, Ns/m

c_p, c_g Viscous damping coefficients of the input and output shafts, respectively, Ns/m

c_1 Constant for a particular bearing

e_p, e_g Pinion and gear eccentricity, m

e_m Amplitude of mean transmission error, m

$e_{fi}(t)$ Amplitude of fluctuating dynamic transmission error under loaded condition, m

f_M Magnetic force, N

i_{cx}, i_{cy} Control currents in the *x* and *y* directions, respectively, A

i_m Total coil current, A

i_o Bias current, A

I_{p_1}, I_{p_2} Polar mass moments of inertia of input and output gear respectively, kg-m^2

I_{d_1}, I_{d_2} Diametral moments of inertia of the pinion and gear, respectively, kg-m^2

I_M, I_L Polar mass moments of inertia of motor and load respectively, kg-m^2

k_p, k_g Input and output shafts lateral stiffness, N/m

k_{tp}, k_{tg} Shaft torsional stiffness, Nm/rad

$k_{px\varphi_y}, k_{gx\varphi_y}$ Input and output shafts cross-coupled stiffness due to tilting of gear, N/rad

$k_{p\varphi_x\varphi_x}, k_{g\varphi_x\varphi_x}$ Input and output shaft transverse rotational stiffness due to tilting of gear, Nm/rad

k_m Average mesh stiffness, N/m

K_p Proportional gain, A/m

K_I Integral gain, A/m-s

K_D Derivative gain, A-s/m

k_s Displacement stiffness factor of electromagnetic actuator, N/m

k_i Current stiffness factor of electromagnetic actuator, N/A

m_1, m_2 Mass of pinion and gear, respectively, kg

N Number of windings in AMB

s_o Air gap between the electromagnetic actuator pole and rotor, mm

t Time, s

x_1, y_1 Transverse displacement of pinion in the *x* and *y* directions, respectively, m

x_2, y_2 Transverse displacement of gear in the *x* and *y* directions, respectively, m

x_p, y_p Transverse displacement of eccentric pinion in the *x* and *y* directions, respectively, m

x_g, y_g Transverse displacement of eccentric gear in the *x* and *y* directions, respectively, m

θ_p, θ_g Torsional displacement of pinion and gear about the z-direction, respectively, rad

θ_M, θ_L Torsional displacement of motor and load about the z-direction, respectively, rad

T_p, T_g Constant torque at pinion and gear, respectively, Nm.

α Half of the angle between two actuator poles, rad

δ_x, δ_y Component of gear-mesh deformation at pitch point in the *x* and *y* directions, respectively, m.

ω_e Gear mesh frequency, rad/s

ω_p, ω_g Pinion and gear angular velocities, respectively, rad/s

μ_o Magnetic permeability of free space, W/Am

$\varphi_{y_1}, \varphi_{x_1}$ Transverse rotational displacement of pinion due to tilting in *z-x* and *y-z* plane, respectively, rad

$\varphi_{y_2}, \varphi_{x_2}$ Transverse rotational displacement of gear due to tilting in *z-x* and *y-z* plane, respectively, rad

ϕ_m Phase of mean transmission error, rad

ϕ_{fi} Phase of varying dynamic transmission error under loaded condition, rad

ϕ_p, ϕ_g Phase of pinion and gear runouts, respectively, rad

Matrices and vectors

$\mathbf{A}_1, \mathbf{A}_2, \mathbf{A}$ Regression matrices

$\mathbf{b}$ Vector of known quantities

$\mathbf{C}$ Damping matrix of geared rotor

$\mathbf{f}_{amb}$ AMB controlling force vector

$\mathbf{f}_{mesh}$ Mesh dynamic force vector

$\mathbf{f}_{r\_out}$ Force vector due to gear runout

$\mathbf{f}_{unb}$ Unbalance force vector

$\mathbf{f}_{tor}$ force vector due to torque

$\mathbf{K}$ Stiffness matrix of geared rotor

$\mathbf{M}$ Mass matrix of geared rotor

$\mathbf{G}$ Gyroscopic matrix of geared rotor

$\mathbf{q}_i$ Vector co-ordinate of geared rotor

Abbreviations

AMBs Active magnetic bearings

DOFs Degrees of freedom

DTE Dynamic transmission error

EOM Equation of motion

PID Proportional-Integral-Derivative

STE Static transmission error

GTE Geometric transmission error

KTE Kinematic transmission error

TE Transmission error

NLTE no load transmission error

TPMs Tooth profile modifications.

CHAPTER 1 Introduction and Literature Review

This chapter proposes a state of the art on the gear vibration problem and their consequences. A review of literature has been done to show the different types of existing gear dynamic models with different types of excitations generated at the mesh due to various gear fault parameters, gear mesh stiffness evaluation, transmission error and fault diagnosis techniques, and method validation. The concepts of active vibration control are introduced as key parameter for this research study. The smart condition monitoring techniques practised these days in rotating machineries are discussed. In the end, summary and objectives of this PhD work is highlighted.

1.1 Introduction

Ever since the invention of machines, many rotating components are coupled through gearing mechanisms. Gears are mechanical components used for transmitting motion and torque from one shaft to another and are one of the most essential elements of rotating machineries. Gears play a crucial role in our daily lives right from the applications in industrial machineries, power transmission systems, electric vehicles, marine, aerospace, home appliances and so on. However, sometimes unwanted vibration and noise are inevitable during gear operations. These not only deteriorates the working environment, but also reduces the durability and reliability of the machine.

Usually, the vibration excitations occur due to the resultant varying amplitude of contact forces between the gears. In involute gears the force variation is due to the combination of small variations of the tooth from a true involute profile or varying elastic deflection of the teeth, which disrupts the smoothness of the drive. The variation in the direction of contact forces is due to the friction effect although the effect is small and are usually neglected for normal gears. The relative displacement variation between the gears acts via the system dynamics to give a force variation resulting in vibration. Under normal driving conditions, a typical geared rotor system is subjected to large dynamic loads and the noise radiated from the gear transmission is directly related to the vibration level of the geared system (Smith, 1999).

Gearboxes are subjected to transmit power and produce high rotational speed changes or change the direction of motion. Gearbox noise emission can be either structure born or airborne. The majority of gear noise experienced in gear transmissions are classified into two

distinct categories: rattle and whine. Generally, gear whine is the main concern for acoustic comfort. Gear whine gives rise to a tonal noise, which is annoying to the human ears and vibration disturbances causing damage to the gearboxes (Smith, 1999). Gear whine occurs when vibrations driven by small fluctuations in rotation caused by the tooth profile or manufacturing error are transmitted via the bearings that support the gear shaft to the housing, resulting in vibration on the surface of the housing. These fluctuations in rotation are due to errors in the rotational angle of the gear teeth as they get meshed, that is known as transmission error. The noise characteristics varies with number of teeth and shaft rotational speed. A whine noise is a high frequency noise and is mainly caused by small errors in the gear tooth profile and tooth stiffness.

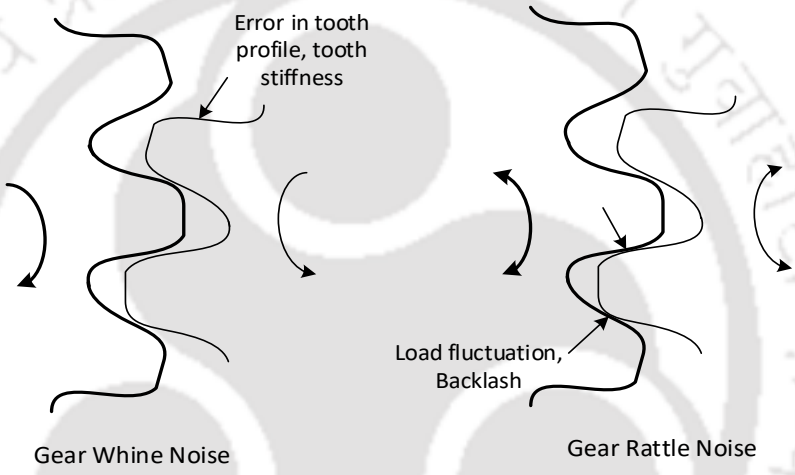

Figure. 1.1 Types of gear noise

Gear rattle in contrast is a low frequency noise (impulsive noise). the impact noise of contacting gear tooth flank and is mainly caused by the fluctuating input load to the gear or clearances between the teeth flanks (backlashes).

Other than the gear rattle, the impacts that occur in the gear contact are mainly due to the occurrence of corner contacts. Corner contact between gear teeth mainly occurs when the teeth just make contact or interfere with the root of the teeth. The corner contact promotes deviation from the intended line of contact and can usually be avoided by good design. In most applications, corner contact is avoided by applying the necessary relief to the teeth.

Interference is commonly avoided either by increasing the pressure angle, or providing protuberance by applying long addendum and short dedendum on the pinion and gear respectively (Townsend, 1991). In high-speed gearing, the excessive supply of lubricant is another cause of gear noise. When the lubricant oil cannot escape fast through the backlash gap

between gear teeth as the gears rotates while meshed, the oil is forced to expel axially from the roots of the teeth, causing time varying forces. This is more common in spur gears as they have variable backlash coefficients depending on applications, but not so common in helical gears as the helix angle helps guide the lubricant oil out smoothly (Smith, 2003). These types of lubrication issues in most of the gears are resolved by increasing the backlash and also designing gear teeth with sufficient whole depth to provide sufficient clearance between tip and root of the respective mating teeth. Sometimes gear noise also occurs due to air entrapment or air pocketing, when air is rapidly squeezed through the gear teeth as gears mesh. In high speed gearing applications, like the aircraft transmissions, air velocities can approach the speed of sound and thus produces intense sounds at gear mesh frequencies.

Transmission error is considered as the main reason for the generation of gear noise. (Munro, 1990) briefly stated that TE is the deviation in position of the driven gear (for any given position of the driving gear), relative to the position that the driven gear would occupy if both the gears are geometrically perfect and undeformed. A correctly spaced, rigid, perfectly involute gears would have no vibration generated while meshing. In practice, this does not happen and transmission error occurs for a variety of reasons i.e., usually due to manufacturing/ geometry errors, such as the gear tooth profile, mesh stiffness variation and shaft deflections etc. (Smith, 1999).

1.2 State of the Art

The study on gear transmission in rotor system spans multiple domains although the following section provides a literature review for the most relevant of them vital for this study.

1.2.1 Gear Dynamic Models

Over the last few decades, many attempts have been made by numerous authors to set up mathematical and numerical models aimed at simulating the dynamic behaviour of gears. To prevent gear vibrations and noise, it is essential to understand the dynamic behaviour of the system consisting of the gears, shafts, bearings and supporting structures. Although, gear transmissions are quite complicated and is difficult to model. According to Özgüven and Houser (1988) the literature suggests that many different models have been developed following the physical laws, i.e. simple dynamic factor models, models with tooth compliance, models for gear dynamics, models for geared rotordynamics, models for torsional vibrations and so on. For simple geared systems generally lumped parameter dynamic models with

springs, masses and viscous damping are used keeping low computational burden. For more complex models, i.e., which includes the gearbox casing and supports, finite element modelling is often used. Lumped parameter model and finite element model are the two commonly used techniques to model gear systems. The first the dynamic models were used to determine dynamic loads on gear teeth, and they were developed in the 1920s, the first mass–spring models were introduced in the 1950s.

1.2.1.1 Lumped Parameter Models

Özgüven and Houser (1988b) developed a lumped parameter model for the dynamic analysis of a spur gear pair to calculate the dynamic mesh and tooth forces, dynamic factors based on stresses, and dynamic transmission error from measured responses and calculated the static transmission errors under different loading conditions. Kahraman and Singh (1990) used a two-degree-of-freedom lumped parameter model of a spur gear pair with backlash, to investigate the non-linear frequency response characteristics, for both internal and external excitations. The transmission error due to variation in the mesh stiffness was used as the internal excitation and the low frequency torque variations were used as external excitation. Two solution methods, digital simulation technique and the method of harmonic balance, were used to develop the steady state solutions for the internal sinusoidal excitation. Analytical predictions were shown to match satisfactorily with experimental data available in the literature. A parameter study was done to show that the mean load governs the conditions for no impacts, single sided impacts and double-sided impacts.

Eritenel and Parker (2012) developed a three-dimensional lumped-parameter model for a pair of helical gears considering the nonlinearity of the gear mesh due to partial contact loss of gear teeth. The lumped-parameter model accounts the net force and moment arising from an arbitrary load distribution including partial contact loss equivalent to a four-parameter model defined by a translational stiffness and a twist stiffness. The twist stiffness generates a moment, which is solely due to the spread of contact across the tooth face. The movement of the translational stiffness across the tooth face generates an additional moment. The four parameters in the model are the output quantities to track and interpret the gear mechanics and the mesh forces and moments that develop under the static or dynamic conditions. The twist stiffness fluctuates periodically with gear rotation generating fluctuating moments (shuttling)

that can potentially excite vibrations. Tooth surface modifications smoothens the translational stiffness profile and decreases the twist stiffness.

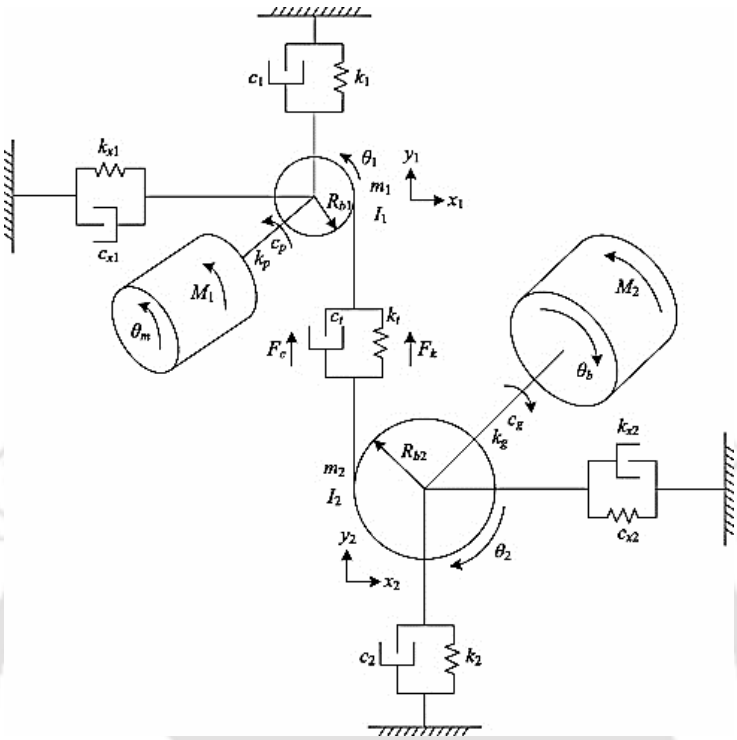

Figure. 1.2 Modelling of gearbox system with six degrees of freedom (Walter, 2001)

The gear system in Fig. 1.2 is driven by electric motor moment M_1 and loaded with external moment M_2; gear inertia I_1, I_2 gear masses m_1, m_2; gearing stiffness k_t and damping c_t, gearing stiffness force F_k and damping force F_c, shaft stiffness and damping (k_p, k_g, c_p, c_g), stiffness and damping parameters of upper and lower supports (k_1, k_2, c_1, c_2), stiffness and damping parameters of left and right supports (k_{x1}, k_{x2}, c_{x1}, c_{x2})

Velex et al. (2016) used a modular three-dimensional model of multi-mesh gears to theoretically analyze the relation between dynamic mesh excitations and transmission errors. It is demonstrated that dynamic mesh forces are mostly controlled by the local transmission errors associated with each individual mesh. A design criterion is proposed, which can be used to define the optimum tooth shape modifications minimizing the dynamic tooth loading. The results from two examples of application on idler and planetary systems proved that the proposed theory can be applied to a variety of gear geometries. Also, they discussed the limits

of using transmission errors while modelling a single pinion-gear pair in the context of multi-mesh gears.

1.2.1.2 Finite Element Models

The analytical methods using finite element method include more complete models of the system components and geometry. Initially, the models were analysed consisting of only the teeth in mesh, but it is now becoming common to include the remaining teeth, gear body, shaft system, and bearings. In the research work carried out by Andrews (1991) the finite element method was used for predicting the fillet stress distribution experienced by loaded spur gears. Finite element modelling is quite flexible to model any shaped gear and gear fault. But it is sensitive to contact tolerances, mesh density and the type of element selected, Lin and Liou (1998). As the mesh density increases, the numerical accuracy is improved, while the computational cost goes up, (Dudley, 1984).

To save the computation cost, Parker et al. (2000) proposed a combined element/contact mechanics model to investigate the non-linear dynamic response of a spur gear pair. Later, this model was extended to investigate the dynamic response of a planetary gear system. This finite element/contact mechanics approach did not require a highly refined mesh at the contacting tooth surfaces. In addition, the time-varying mesh stiffness and mesh contact forces were evaluated internally at each time step.

Guangjian et al. (2017) presented theoretical formulas of no-load transmission error (NLTE) and time-varying backlash, which can be used for double eccentric gear system, whose contact ratio is random. The finite element model was developed to calculate the dynamic transmission error (DTE), and was predicted in consideration of gear eccentricities and varying load. Under three different cases (no backlash, constant backlash and time-varying backlash), the influence of backlash on DTE was investigated with the gear pairs suffering from sinusoidal varying loads.

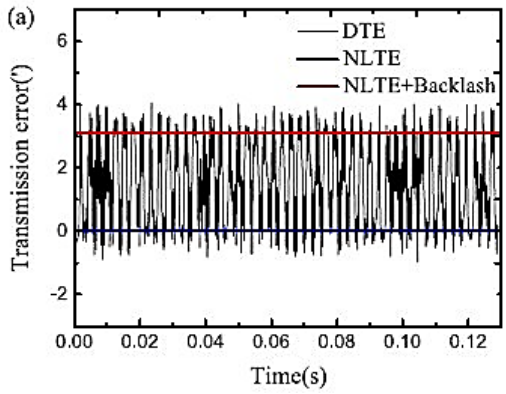

Figure 1.3 TE curves of the gear pair with constant backlash (Guangjian et al., 2017)

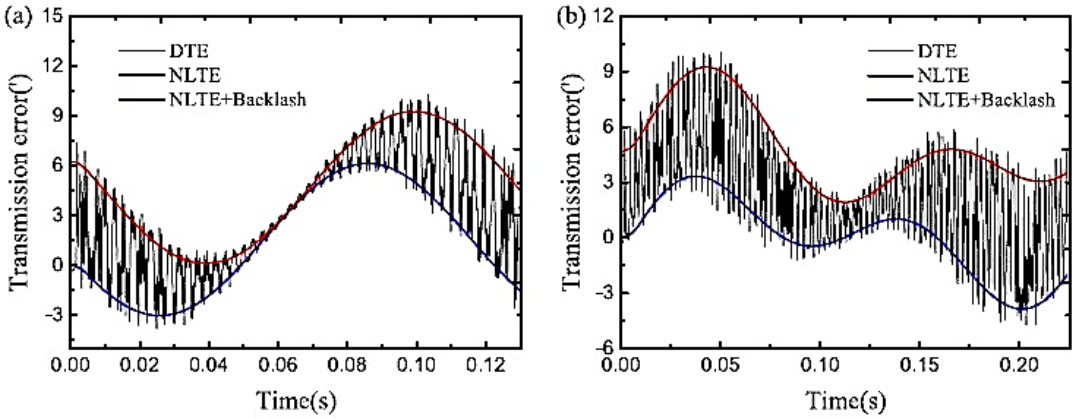

Figure 1.4 TE curves of the gear pair with time-varying backlash (a) single gear eccentricity, (b) double gear eccentricities (Guangjian et al., 2017)

It was found that the DTE curve jumps as the load direction changes, and the discontinuity value are equal to the backlash size at that time. Also, if the frequency of load change is high (here, mesh frequency), the DTE curve distributes in a certain region, whose lower outline are approximately consistent with the NLTE curve and the upper outline are approximately consistent with the curve of NLTE plus backlash.

In a study by Li and Kahraman (2010) a numerical non-Newtonian contact model of an involute spur gear tooth was developed with respect to various contact parameters, such as the surface velocities, normal load and radii of curvature. Maliha et al. (2004) presented a nonlinear dynamic model for a gear-shaft-disc-bearing system with a spur gear pair coupled with linear finite element models of shafts carrying them, and discrete models of bearings and discs. The nonlinear elasticity term resulting from backlash was expressed by a describing function, and

the multi-harmonic responses of nonlinear multi-degree-of-freedom systems was obtained. The excitations considered in the model were external static torque and internal excitation caused by mesh stiffness variation, gear errors and gear tooth profile modifications. The model suggested the solution method combining the shaft-bearing-disc model that can have any configuration without a limitation to the total degree of freedom, with the accuracy of a nonlinear gear mesh interface model that allows to predict jumps and double solutions in frequency response. With the developed model it was possible to calculate dynamic gear loads, dynamic bearing forces, dynamic transmission error and bearing displacements altogether.

Literature published on the effect of varying contact conditions in gear tooth interactions through finite element method, on the perceived transmission error from gear pair models is quite sparse. Lin et al. (2007) proposed a finite element method for 3D dynamic contact/impact problems of gears. This method is based on the derivation of the effective flexibility matrix equation, which is very efficient in computation for gear drives as only very small contact region is involved in tooth meshing at any time instant.

The models on gear dynamics are ample and comprises of several kind of varying complexity depending on the objectives of the study. It can be seen that lumped parameter model and finite element model are the two commonly used techniques to model gear systems. Since FEM modelling is usually for detailed stress-strain analysis of gear teeth deformation or for complex models, i.e., which includes flexible bearings, gearbox casing etc. and this study is focused on dynamic vibration control and identification of fault parameters. Herein, the method of lumped parameter dynamic models considering shaft flexibility with springs, masses and viscous damping has been used for mathematical model of geared rotordynamics.

1.2.2 Evaluation of Gear Parameters

There are several gear parameters which needs to be addressed while performing the dynamics-based modelling, fault detection and diagnosis of geared rotor systems. Here, the state of art and challenges for evaluation of mesh stiffness and transmission error have been reviewed and discussed in the next section.

1.2.2.1 Mesh Stiffness Models

The mesh stiffness model forms the basis of a gear dynamic model. In early research, the mesh stiffness of gear teeth was considered to be constant. The mathematical formulation ranges from a single-degree-of freedom (SDOF) system to finite element three-dimensional ones. Almost all gear dynamic models consider that transmission error (TE) and variations in mesh stiffness are the primary sources of excitation. As the gears rotates, the number of teeth pairs in contact through the mesh cycle and their points of contact or the contact ratio changes and therefore the mesh stiffness varies with the rotation. The mesh stiffness varies due to geometrical imperfections of the teeth, acceleration/deceleration of gears due to impact and changing contact ratios of the gears. This is one of the main reasons TE of gear pairs in not a single value, but rather a continuous variable through gear rotations, and should be measured at different relative positions of the gear with its mesh cycle. Generally, four methods are applied to evaluate time-varying gear mesh stiffness for gear fault diagnosis: square waveform method, potential energy method, finite element method, and experimental method (Liang et al. 2018).

Gear mesh stiffness is a periodic function for a healthy gear pair running at constant speed. Some researchers have used a square waveform to approximate gear mesh stiffness (Liang et al., 2018) as shown in Fig. 1.5. The period of a square waveform is called mesh period, which equals to the time duration for one revolution divided by the number of teeth. The square waveform can reflect the change of tooth contact number but ignores the change of tooth contact position. As we know, a square waveform can be approximated using Fourier Series. A few researchers used the first several terms of Fourier Series to represent the time-varying mesh stiffness. When a fault occurs on a gear, gear mesh stiffness reduces due to increase in vibrations caused by gear damage.

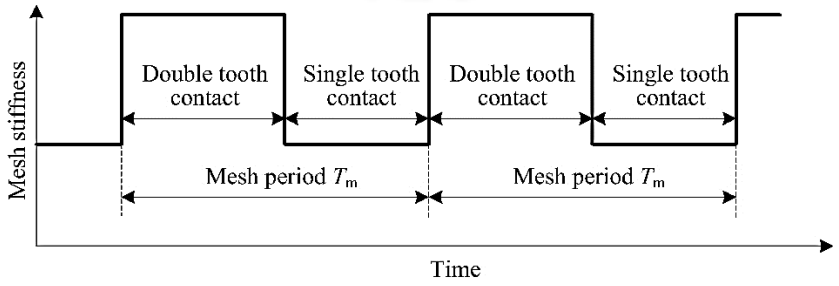

Figure 1.5 Square waveform to approximate gear mesh stiffness (Liang et al., 2018)

Liang et al. (2014) used the potential energy method to analytically evaluate the mesh stiffness of a planetary gear set. A modified cantilever beam model was used to represent the external gear tooth. The time-varying mesh stiffness represented as a function of the angular displacement of the gear, considering the Hertzian contact stiffness, bending stiffness, shear stiffness and axial compressive stiffness. A crack propagation model was developed and the reduction in mesh stiffness was quantified when crack occurs in the sun gear, the planet gear (sun gear side) or the planet gear (ring gear side).

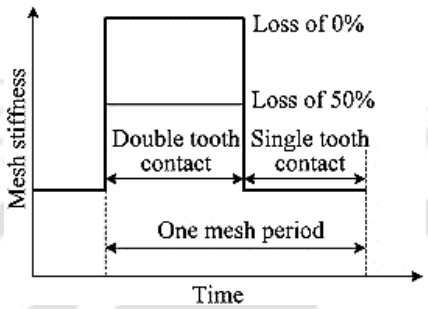

Figure 1.6 Amplitude loss of 50% due to a crack in the sun gear (Liang et al., 2016)

Later Liang et al. (2016) extended this study to evaluate the time varying mesh stiffness of a pair of external spur gears with the growth of gear tooth fault, i.e. the pitting. The mesh stiffness amplitude changes and consequently the dynamic properties of the gear system changes. The different severity of pitting levels were mimicked with the number of pits. The tooth pitting influences the gear mesh stiffness and the relationship between pitting severity and mesh stiffness was shown.

Rincon et al. (2013) described an advanced model for the analysis of contact forces and deformations in spur gear transmissions. The deformation at each gear contact point was formulated as a combination of global and local term. The former was obtained by means of a finite element model and the latter was described by an analytical approach derived from Hertzian contact theory leading to nonlinear equations. A numerical example was presented where the quasi-static behaviour of a single stage spur gear transmission was discussed, to obtain the loaded transmission error under several load levels as well as the load ratio or the meshing stiffness.

Iwatsubo and Kawai (1984) studied the lateral and torsional vibrations of geared rotors, mainly considering the effect of the periodic variation of the mesh stiffness. The combined mesh stiffness of the two gears in mesh varies with the meshing position as the teeth rotate within

the mesh cycle. In particular, the mesh stiffness decreases and increases dramatically as the meshing teeth changes from the double pair of teeth in contact, to the single pair of teeth in contact. (see Fig. 1.4). The combined mesh stiffness is defined as the ratio between the torsional load and the angular rotation of the gear body. The mesh stiffness associated with elastic tooth bending varies as the number of teeth in contact changes. The parametric excitation from the time-varying mesh stiffness causes instability and severe vibration under certain operating conditions.

Experiments conducted by Harris (1991) and Mark (1978) demonstrated that large amplitude of vibration are induced by the parametric instability, where the gear meshing frequency is equal twice the natural frequency. Furthermore, mesh stiffness variation directly affects the tooth deflections and the transmission error. Kamaya (2005) suitably summarized that mesh stiffness along with the transmission error are the primary causes of gear noise and vibration.

Frolov and Kosarev (2003) highlighted the importance of mesh stiffness under variable load as one of the primary causes of gear vibrations, along with pitch error and profile error. They concluded that the factors causing gear vibration can generally be eliminated by profile modifications, adjustment of contact ratio and high-precision manufacture of gears.

The existing literature on gear mesh models depicts, gear mesh stiffness fluctuation excites vibration and several approaches have been proposed to quantify mesh stiffness and its fluctuations. Mesh stiffness models are developed to evaluate time varying gear mesh stiffness for various gear fault diagnosis. Thereafter, for profile shifted gears addendum modifications and tooth profile modifications (TPMs) are done to reduce transmission error and also to identify the gear is in healthy or damaged condition.

1.2.2.2 Transmission Error Models

As it known the transmission error is the difference in torsional vibration of two matting gears, scaled so as to represent linear motion along the line of action. The concept of transmission error is illustrated in Fig. 1.7. $TE = \left(\theta_{gear} - \frac{R_{pinion}}{R_{gear}} \theta_{pinion} \right)$.

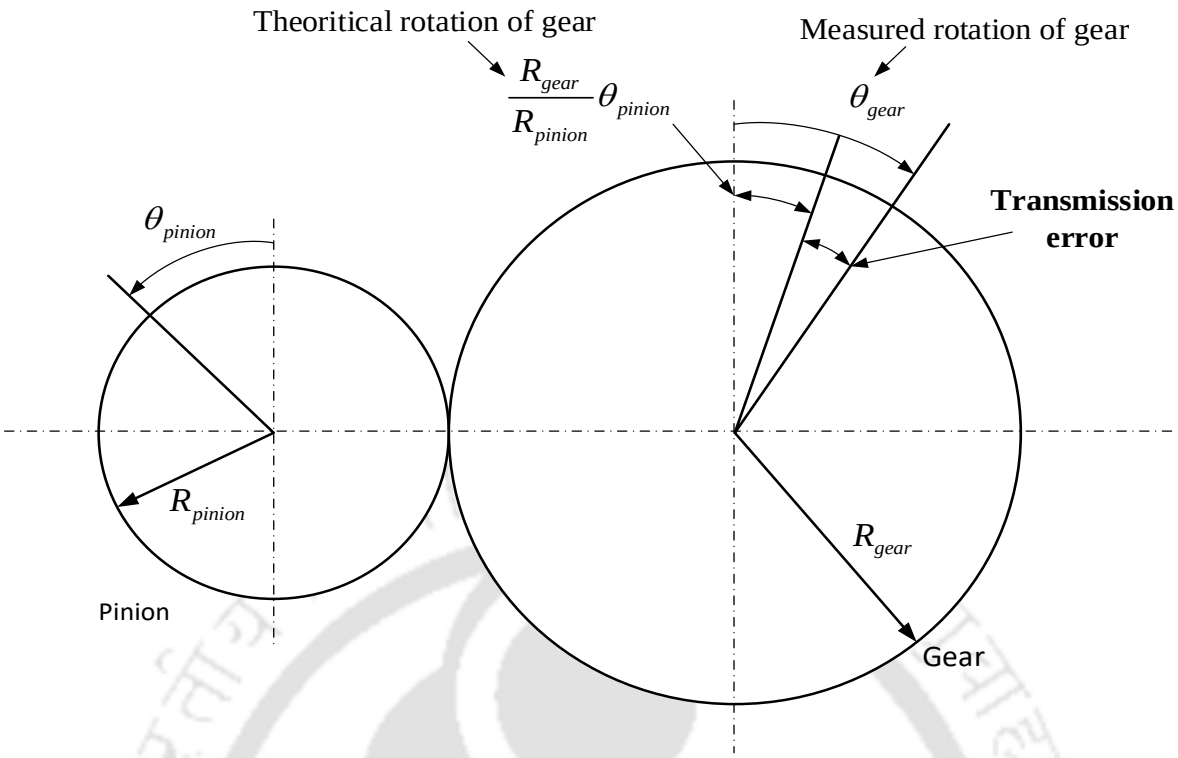

Figure 1.7 Definition of transmission error

Numerous works have been published on modelling of TE. One of the method for the minimization of transmission error variations [27–29] for low noise gears relies on tooth modifications. Numerous studies have pointed out the correlation between transmission error and gear whine and several of the key research publications by [28, 30, 31, 32, 33] has given a very good overview and introduction into the area of transmission error in gears. The mean mesh load has been used by several researchers in aid of formulating an expression for the transmission error, including Gregory et al. (1963), who showed that even a gear with perfect involute geometry will have a periodic transmission error due to the variation in the mesh stiffness as the gears rotate through the mesh. They also summarized that the transmission error can be decomposed into a steady component and a varying component. The steady component of transmission error has an effect on the tooth meshing frequency and its harmonics, while the varying component affects the remaining portion of the frequency spectrum. The vibratory analysis conducted by Mark (1978) provided a good insight into the decomposition of the transmission error into the components that make up the noise. He uses the decomposition of the transmission error to derive an expression for TE and hence predicted the Fourier coefficients of the transmission error.

The work by Munro and Houser (2003) provided a fundamental insight into the components of transmission error, which includes an analytical method for predicting the transmission error. Although the measurements are made in terms of angular movements, the errors generated are rarely given as angles as it is much more informative when converted to linear displacement. Even though the transmission error is known to be time dependent and relative to the respective position of the gear teeth in contact, it is almost always reported as a single peak-to-peak value as given by Houser et al. (1999). Other researchers have looked into the Fourier analysis of transmission error and identified the problem in the gear system by the frequency content in the data. If there is a profile error on one of the teeth, it will show up on the frequency spectrum at the tooth frequency and its harmonics, as the rest of the frequency response from tooth to tooth will be consistent.

In practise, TE can be measured by different types of instruments and some commonly used methods are: rotary encoders, putting strain gauge on the drive shaft, torsional vibration transducers, magnetic signal methods, tachometers, tangential accelerometers. There are several sources of TE which is briefly described in the next section.

1.2.3 Sources of Transmission Error

According to Smith (1983), the TE results from three main sources: (a) Gear geometrical errors, (b) Elastic deformation of the gears and associated components and (c) Errors in mounting. Fig. 1.8 illustrates the relationship between TE and its sources.

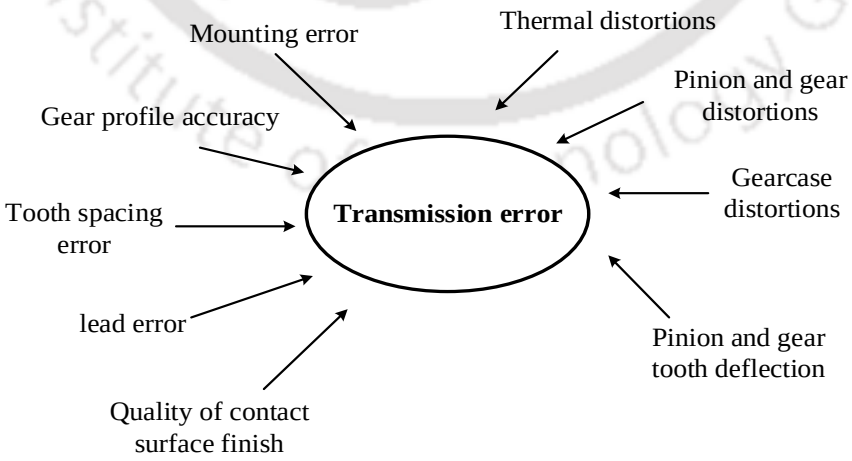

Figure 1.8 Sources of transmission error (Hiroaki and Nader, 2012)

It was noted that TE may happen due to deviations in geometry of the combined tooth profiles from the ideal involute, elastic deformation of the teeth being load dependent, inertial as well as stiffness effects, and thus is speed and load dependent. Hence, the main sources of transmission error originate from geometry, deflection and dynamics of the gears. The geometry errors are mainly from manufacturing and practical assembly of gears within systems that yield profile, lead, run-out and tooth spacing errors. The misalignment of gears and shafts during assembly is also another important contributor to the generation of transmission error stated by Athavale et al. (2001).

Deflections and deformations associated with the gear teeth, shaft and housing also contribute in a way to the generation of transmission error. Another factor that has an effect is the mesh stiffness, which varies as the gears rotate through the mesh, generating a time varying deflection of the gear teeth in contact. If the pinion and the gear have ideal involute profiles running with no loading torque, they should theoretically run with zero transmission error. However, when these same gears transmit torque, the combined torsional mesh stiffness of each gear changes throughout the mesh cycle as the teeth deflect, causing variations in angular rotation of the gear body. Even though the transmission error is relatively small, these slight variations can create noise at a frequency, which when coincides with a resonance of the shafts or the gearbox housing, causing the noise to be enhanced. Considering the transmission error as a major source of noise, the actual noise does not come directly from the angular speed variations. The torsional accelerations cause vibratory bearing reactions that excite the gearbox casing, which then propagates the noise through the pulsation of the casing walls.

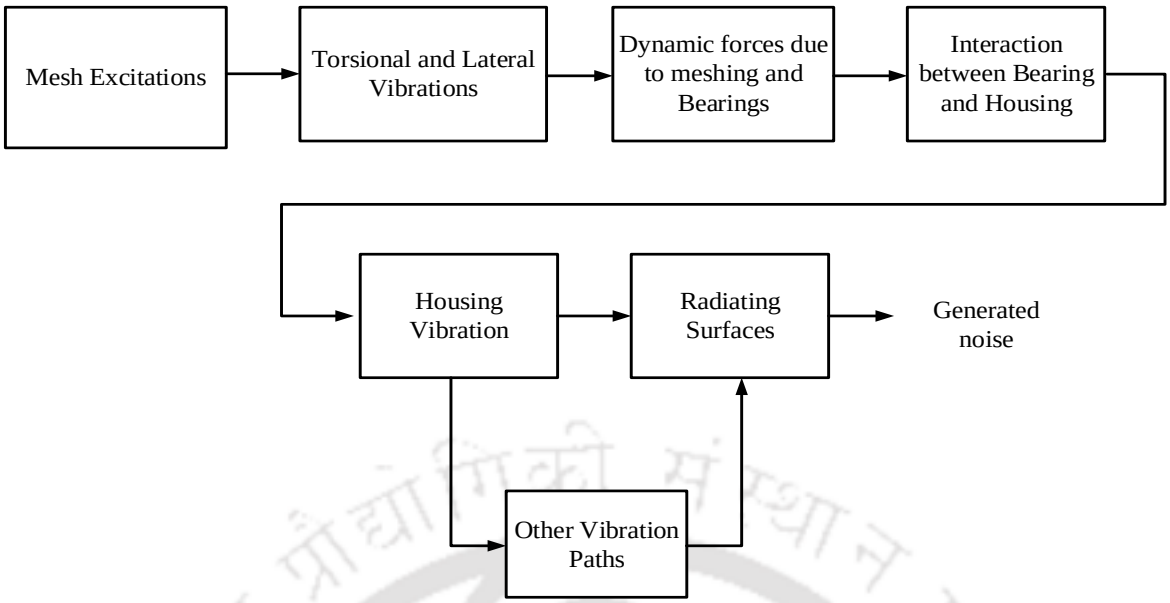

Figure 1.9 Gear noise transmission path (Townsend, 1991)

1.2.4 Types of Transmission Error

There are a few types of transmission errors that are frequently referred to in the literature and they vary in small measures from one another. These are:

1.2.4.1 Geometry Transmission Error

This is quite simple to understand, as the gear tooth geometry directly influences the angular position of the output gear for a given position of the input gear, so that any change in the tooth contact point would give rise to transmission error. This change being due to the manufacture of the gears is called manufacturing/geometry transmission error (GTE). This is the only kind of transmission error that is a measure of a single gear error. Generally, the transmission error relates to the meshing of two gears, and hence can be said to be the sum of the respective transmission errors of the individual gears, Mark (1978). The manufacturing transmission error (MTE) is measured under no load or lightly loaded conditions and can be used to test the accuracy of gears on a production line, as used on single flank machines. An example is shown in Fig. 1.10 to show the discrepancy in gear geometry due to manufacturing errors.

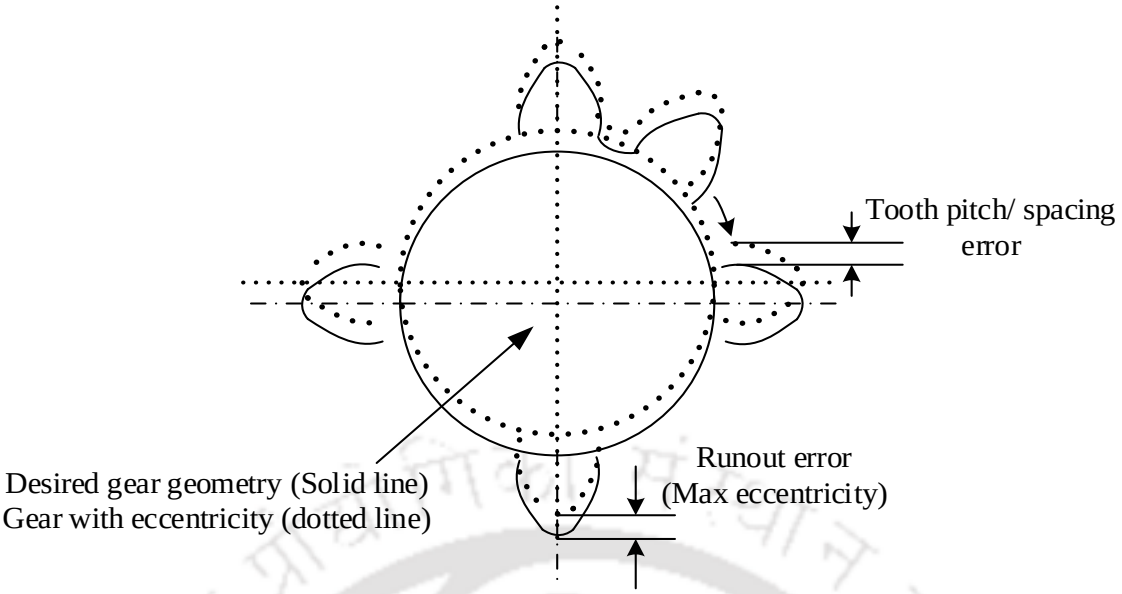

Figure 1.10 (a) Eccentricity in a gear caused by manufacturing errors, (b) Resulting errors in gear geometry (Hiroaki and Nader, 2012)

1.2.4.2 Static Transmission Error

When two gears mesh under the presence of low load conditions, the gear teeth deform elastically along with the gearbox casing, bearing, and the shafts. Hence, it is supposed that the transmission error calculated at operating load is the static transmission error (STE), and also takes into consideration stiffness of all the components in the system. The static transmission error is measured at low speeds to avoid the dynamic effects of the system. The teeth of the gear pair experience deformation due to loading in the form of bending and contact between them, subsequently influencing the mesh stiffness. There have been several approaches to approximate the variable mesh stiffness in the static case. Blankenship and Singh (1992) suggested that the stiffness might also depend on the mesh load, and Mark (1978) has defined the stiffness in terms of an area integral over the contact zone, while taking into account the local surface irregularities.

1.2.4.3 Kinematic Transmission Error

The kinematic transmission error (KTE) is a derivation of the GTE**,** which takes into consideration of the asperities present on the tooth surfaces. Asperities are local unevenness of the surface, roughness and ruggedness that cannot be seen with the naked eye. When two surfaces with such asperities come into contact these asperities deform until the contact area increases and can support the load. Blankenship and Singh (1992) investigated this type of

subtle elastic deformations on the gear teeth surfaces that take place under low load. They suggested that under low load, the contact deformations of the teeth are averages of the local deformation of the asperities present on the working surfaces. As the asperities are not an intentional design feature, they can be attributed to a manufacturing error. Practically, there is very small difference between the GTE and KTE as the GTE is simply a special case of KTE under no load.

1.2.4.4 Dynamic Transmission Error

The concept of dynamic transmission error considers that the gear system has components with masses and variable stiffness. By taking into consideration of the masses of the gears, and their rotations, the inertial forces of the system cause dynamic mesh forces. The dynamic factor is a ratio of the dynamic load to the static load as a result of tooth geometry errors and are used for gear life calculations. According to Kayama (2005) while the dynamic factor does not accurately represent the dynamics of the tooth mesh, it shows that the dynamic loading in the mesh is a result of the static transmission error. This static transmission error is the source of excitation for the dynamic transmission error. The dynamic transmission error is speed dependent and can be mathematically represented by multiplying static transmission error by a transfer function.

In this section, literature elaborating the definition of transmission error, the causes of TE and types of transmission error is presented that forms the basis of understanding and modeling the gear dynamic transmission error in this work. In the next section, the vibration-based monitoring techniques is elaborated for diagnosis of faults in rotors which is later extended to gears.

1.2.5 Identification of Fault Parameters in Rotors

Vibration monitoring is one of the most popular condition monitoring techniques practiced in rotating machineries. The vibration-based analysis is classified into three main categories, i.e. the model and signal based, model properties based, and machine learning based. Different authors have used different methods to estimate the system level parameters. In the present work, the model-based fault identification approach has been taken into account. Model based methods carry out the analytical procedures for modeling the state of the system.

Understanding of the system dynamics gets better as it helps insight into the physics of the problem so the model can be used for more complex issues.

Tiwari (2005) presented a model based identification algorithm for simultaneous estimation of the residual unbalance along with bearing dynamic parameters for multi-degree-of-freedom rotor-bearing systems. The identification algorithm was found to be highly ill-conditioned for the conventional measurement techniques. The measurement of responses, while rotating the rotor alternatively in clockwise or counter clockwise direction leads to a well-conditioned identification algorithm. However, this was useful for educational and research experimental set-ups.

Tiwari and Chakravarthy (2009) described two separate identification algorithms, for the simultaneous estimation of the residual unbalance and bearing dynamic parameters in a rigid rotor-bearing system, both by numerical simulations and experimental measurements. The first method used the impulse response measurements of the journal from bearing housings in the horizontal and vertical directions, for two independent impulses on the rotor in these directions. Time-domain signals of the impulse forces and displacement responses were transformed to the frequency domain for the estimation of the residual unbalance and bearing dynamic parameters. The second method employed the unbalance responses from three different unbalance configurations. Unbalance response measurements were taken for both the clockwise and counter-clockwise rotations of the rotor. Then experimental measurement responses were used to identify the residual unbalance and bearing dynamic parameters by both the methods. To check the suitability of the identified parameters, they were substituted in a numerical model of the test rig to generate the simulated responses. The identified unbalance masses were found to get matched quite well with the residual masses taken in the dynamically balanced rotor-bearing test rig.

Lees et al. (2004) did the identification of unbalance (both amplitude and phase) from machine rundown vibration data and suggested that the unbalance can be estimated with the split frequency range instead of dividing the whole frequency range into number of frequency bands by judicious choice of weighing function.

According to Hiroaki and Nader (2012), the fault detection and diagnostic techniques based on vibration signal analysis are the ideal non-destructive machine health monitoring method, that can be applied in a minimally intrusive manner; i.e., by attaching an accelerometer on a gearbox casing. However, the dynamic interaction amongst the machine elements of a gearbox is often complex and the vibration signals measured from the gearbox is not easy to interpret. The diagnostic information that directly related to an emerging fault in a gear or a bearing is typically buried in the dominating signal components that are driven by the mechanisms of the transmission system themselves. For example, gear meshing signals. In the next section some of the gear fault prediction and diagnosis techniques is presented.

1.2.5.1 Diagnosis of Gear Faults

As we know faults may develop in gears due to high service load, harsh operating conditions or inevitable fatigue. If the gear faults are not detected early, the health will continue to degrade, perhaps causing heavy economic loss or even catastrophe. Hence, early fault detection and diagnosis is needed for proper scheduled shutdowns to prevent catastrophic failure and consequently a safer operation and higher cost reduction. Many studies have been conducted to understand the gear fault generation mechanism and develop an effective fault detection and diagnosis method. While DTE is considered to be the most common factor for gear noise, it is of course the most difficult to obtain, either by analysis or measurement. However, it has been recognised that TE can be measured by phase demodulation of the signals of shaft encoders rigidly attached to each of the gears in mesh, i.e., the GTE at low speed and low load, the STE at low speed and higher load, and the DTE at higher speed and higher load. Since the dynamic transmission error is excited by the static transmission error, it is fruitful to reduce noise by addressing the static transmission error. The alternating component of the static transmission error is reduced by specifying tooth modifications that compensate the stiffness variation. By plotting transmission error curves for multiple loads on the same graph, one can easily see how load affects the transmission error. This plot is called a Harris Map (Fig. 1.11). Munro and Houser (2003) showed how the gear geometry can be used to synthesize no load transmission error curves.

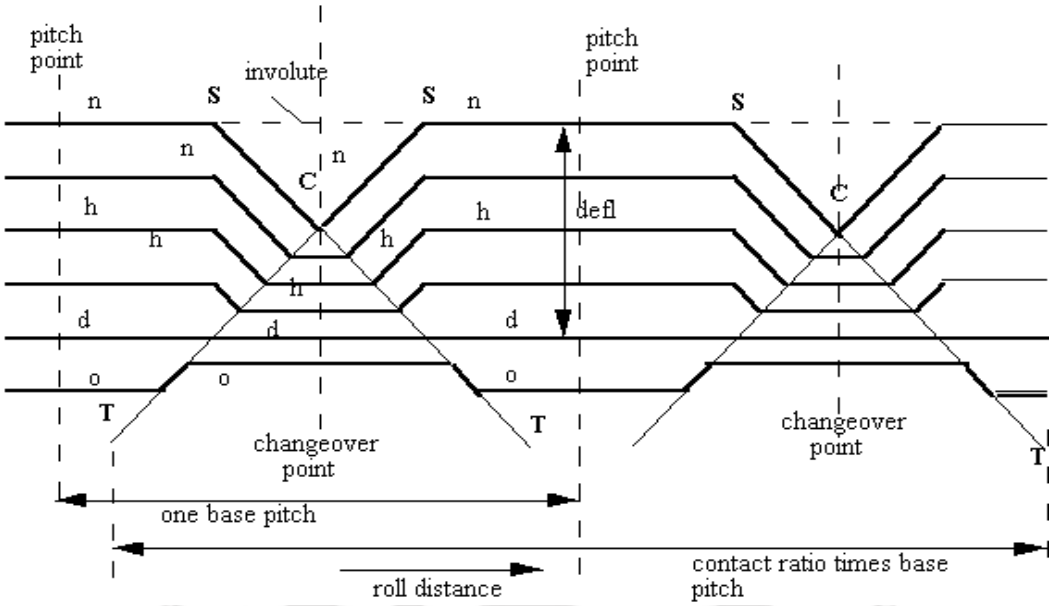

Figure 1.11 Harris map of TE of a pair of gears showing effect of varying load on teeth deflection. (Munro and Houser, 2003)

Fig. 1.11 depicts that at no-load, the shapes of the two gears meshing give the top curve labelled "*n*" which shows the variations (in the *y*-axis) of movement from the idealised horizontal dashed line which corresponds to perfect, rigid involutes meshing and with no transmission error. The tip relief sections from S to C on one pair of teeth and C to S on the next pair give a dip in the transmitted motion. The third curve, "*h*", is for half design load and shows how the elastic deflections combine with the original profiles. At the design load, curve "*d*", the elastic deflections have exactly cancelled the profile corrections and the TE is a straight line so no vibration would be generated. The sixth curve, labelled "o" is for 25% overload and gives a raised section where double tooth contact is occurring. This work by Munro and Houser (2003) enabled gear designers to apply tip relief in a rational manner when designing gears.

Houser et al. (1994) showed that sound power measurements (sum of harmonics and sidebands) can be correlated well with predicted transmission error in the parallel axis arrangement. They compared spur, helical and double helical (herringbone) gears. They tested conventional and high contact ratios and other tooth modifications. The transmission error was determined by analysis using LDP (Load Distribution Program). They also stated that the transmission error is less sensitive to the load at higher contact ratios. Loutridis (2006) proposed an energy-based feature for the gear fault prediction and diagnosis. The instantaneous energy density was shown to obtain high values when defected teeth were engaged. Three methods were compared, i.e.

the Wigner–Ville distribution was contrasted to the wavelet transform and the empirical mode decomposition scheme. It was shown that all three methods were capable of a reliable prediction. An empirical law, which relates the energy content to the crack magnitude was established.

Feng et al. (2012) summarized the spectral characteristics of planetary gear vibration signals for the fault diagnosis of planetary gearboxes. By considering both the amplitude modulation and frequency modulation effects due to gear damage and periodically time variant working condition, as well as the effect of vibration transfer path, signal models of gear damage for fault diagnosis of planetary gearboxes were given. Meanwhile, theoretical derivations using explicit equations for calculating the characteristic frequency of local and distributed gear fault were deduced and validated using both experimental and industrial signals. Using the derived theoretical basis, they were able to detect and locate the manually created local gear damage of different levels and naturally developed gear damage in a planetary gearbox.

Torsional vibration signals are theoretically free from the amplitude modulation effect caused by time variant vibration transfer paths due to the rotation of planet carrier and sun gear, and therefore their spectral structure are simpler than transverse vibration signals. Thus, it is potentially easy and effective to diagnose planetary gearbox faults via torsional vibration signal analysis. Feng et al. (2013) gave explicit equations to model torsional vibration signals, considering both distributed gear faults (like the manufacturing or assembly errors) and local gear faults (like the pitting, crack or breakage of one tooth), and derive the characteristics of both the traditional Fourier spectrum and the proposed demodulated spectra of amplitude envelope and instantaneous frequency.

These derivations are not only effective to diagnose single gear fault of planetary gearboxes, but can also be generalized to detect and locate multiple gear faults. In this thesis, we will carry out dynamic based modeling and analysis of gear vibration problem and fault identification in a spur gear set.

1.2.6 Active Gear Vibration and Noise Control

In many cases, undesired vibrations are eliminated via a passive control, i.e. by using vibration isolators, dampers etc. and is widely accepted in industries due to their ease of installation and

efficiency at higher frequency. However, they have certain limitations, like poor restoring capacity, residual vibration and so on, that is carried on to the support structure. Also, passive devices are quite inefficient in low to mid-range frequencies due to space constraints and are unable to provide the required amount of damping to reduce vibration to acceptable levels. In recent years, a great amount of work has been done on the application of active control. The main advantage of active control over passive control is the ease with which active control can adjust to varying loading conditions. Other advantages of active vibration control include the low weight, compact size, and versatile operating conditions.

1.2.6.1 Struts

The interior noise of modern helicopters is usually dominated by high frequency tonal noise components generated mainly by the gear meshing. The frequency range for the gear meshing tones generally lays between 500 Hz and 4 kHz [48]. Due to the high sound pressure level and the high frequency, the gear meshing tones are very annoying to crewmembers and passengers. Comprehensive analysis has shown that the transfer path for structure-borne noise is dominant. Thus, the gear meshing noise is mainly caused by the vibrations of the gearbox, which are transmitted to the cabin structure via the gearbox struts. Significantly improvements of the comfort in helicopter cabins can be achieved with active vibration isolation by active gearbox struts. Gembler et al. (1998) attached the inertial actuators to the gearbox strut system outside of the gearbox of helicopter. The vibration measurement, transfer functions and interior noise showed that structure-borne noise path characterised by the gear meshing frequency is a dominant factor. An adaptive feedforward system was optimised and experimental trials were conducted to show the reduction in the interior cabin noise with the active strut system.

Sutton et al. (1997) had set up a helicopter gearbox support strut in the laboratory under realistic loading conditions to investigate the active control of longitudinal and lateral vibration transmission to a connected receiving structure. They used three magnetostrictive actuators clamped to a support strut in the gearbox to minimise the kinetic energy of vibration transmitted through the strut by controlling the vibration at the interface between the gearbox and the host structure. The tests confirmed that the active control of vibration transmission through a helicopter strut is practical at frequencies up to at least 1250 Hz. Although these studies were observed to be quite successful, the external actuation concepts can treat only the specific

structure-borne path and as the control force is located quite far from the gear pair excitation source, they have essentially no impact on the air-borne path.

1.2.6.2 Piezoelectric Actuators

Few researchers have introduced the concept of active vibration control of gear systems through piezoelectric actuators. Montague et al. (1994) were among the first few researchers to perform the active vibration control of gear transmission systems using piezoelectric actuators, experimentally. A force was applied on the gearbox drive shaft using piezoelectric actuators attached to the shafts supporting the gear pair and the high frequency gear mesh vibration component were controlled with an analog feedforward controller. Their experiments reported 70% vibration reduction at the fundamental gear mesh frequency.

Wang et al. (2018) developed a built-in piezoelectric actuator to generate the control forces, which can be transmitted to the shaft through additional support bearings. They proposed an adaptive fuzzy based proportion-integration-differentiation (PID) control algorithm to reduce the transverse vibrations of the shaft. A line diagram has been shown in Fig. 1.12.

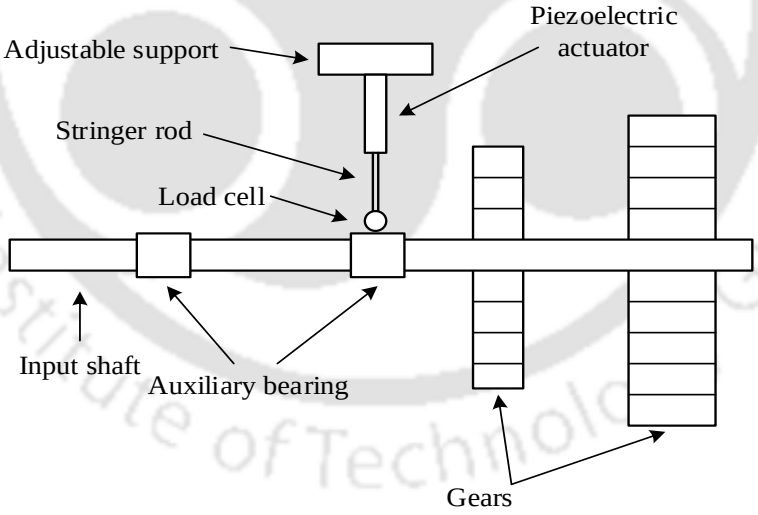

Figure 1.12 Active shaft transverse vibration control model through piezoelectric actuator

Similarly, Barrett et al. (1995) with a feedback control mechanism used three piezoelectric actuators applied at each of the two bearings of the rotor to suppress vibration at the interface of machine and its host structure.

A non-linear controller for an active vibration control of a single-stage spur gearbox was proposed by Dogruer et al. (2017), which can modulate the input torque acting on the driving gear that minimizes the dynamic transmission error and compensates the periodic changes in mesh stiffness. The gearbox was analysed by a finite element software to calculate the mesh stiffness curve. The change in mesh stiffness, which is nonlinear, was predicted and cancelled by a feed-forward loop and the remaining linear dynamics was controlled by pole placement techniques. Under these premises, it was claimed that any acceleration and velocity profile of the input shaft can be tracked accurately. Thereby, dynamic transmission error can be kept to a minimum possible value and a spur gearbox can be designed, which does not emit much noise and vibration.

Rebbechi et al. (1999) made an improvement to the earlier study by developing an adaptive feedforward controller suppressing the response of the fundamental gear mesh frequency along with its first two harmonics. Their study utilized a pair of magnetostrictive actuators mounted at one of the support bearing, actively isolating the vibrations occurring between the shaft and the housing. They attained an attenuation of 20–28 dB in the vibration level at the fundamental mesh frequency, while reductions of less than 10 dB were obtained at the second and third mesh harmonics.

In a similar way, Guan et al. (2003) simulated a direct hybrid adaptive controller that can adapt both the feedback and feed-forward gains, and only requires to know the fundamental gear mesh frequency to tackle gear pair torsional and translational vibrations, simultaneously, by using several inertial actuators on both gear bodies. Guan et al. (2004) also compared the performance of four actuation concepts aimed at suppressing the gearbox housing mesh frequency vibration due to transmission error (TE) excitation from the gear pair system.

The studies showed that the concept of active internal shaft transverse vibration control is the most suitable approach for this application, which is the basis of the present study.

1.2.7 Smart Condition Monitoring of Rotors with AMB

This section presents an introduction to Active Magnetic Bearings (AMBs) and its basic principles that will pave a way for understanding of the subsequent literature review. The demand for the use of active magnetic bearings (AMBs) in condition monitoring of rotating machineries is increasingly growing for replacing the oil lubricated bearings as well as retaining the vibration level at minimum such that the undue stresses that causes catastrophic failures are minimum (Siva et al., 2018).

1.2.7.1 Active Magnetic Bearings

The function of AMBs is to suspend a spinning rotor with no contact, wear and lubrication, and controlling its dynamic behaviour. The control law of the feedback is responsible for the stability of the hovering state as well as the stiffness and the damping of such a suspension. Fig. 1.13 presents the main components and explains the function for suspending a rotor in radial direction. The stiffness and damping parameters of a flexible rotor support can be varied actively during operation; hence it is possible to traverse through several transverse critical speeds, which provides increased reliability of the system with a longer life. Despite ~~of~~ the many advantages, the application of magnetic bearings in the past has been limited by the large size of the magnetic bearings, the complexity of integrating magnetic bearings into the machine, the need of a large external control system, and the high cost, Tiwari (2017). Although recent advances in magnetic bearing technology, including miniaturization, simplicity and integration have overcome many of these limitations. The performance measurement of AMBs are the dynamics, load, size, temperature, precision, speed and power losses. One important aspect is the influence of the bearing control system.

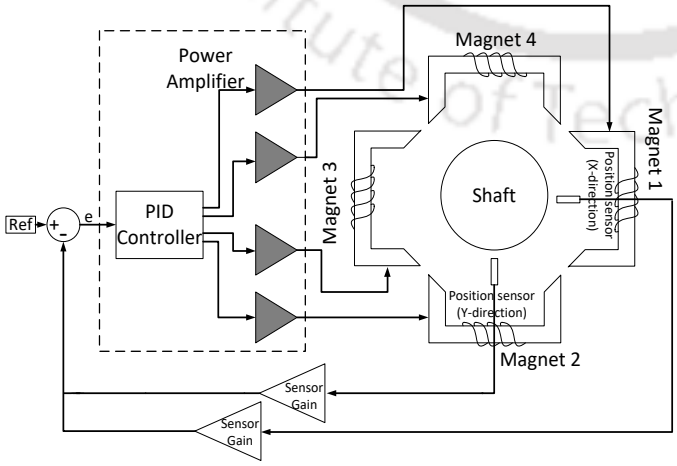

Figure 1.13 Schematic of two axis control

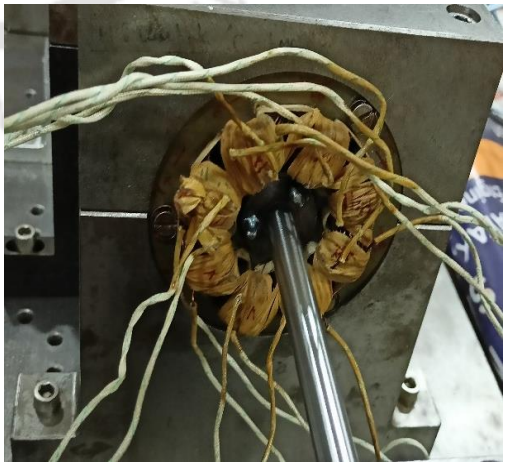

Figure 1.14 Magnetic bearing actuator (Advanced Dynamics Lab, IIT Guwahati

1.2.7.2 Application of Active Magnetic Bearings

The application of AMBs is very much demanding with emphasis on turbomachinery, blood pumps, centrifuges, machine drilling tools, energy storage flywheel, high-speed motors and generators. Schweitzer et al. (2009) have demonstrated the design and development of a variety of compact and simple structured AMBs and their control systems.

The focus does not prevail only to high-speed, high-power density, or the control of rotor dynamics but also on the prevention from contamination by lubrication and mechanical wear, low energy consumption, extreme environment and low maintenance costs.

Maslen (2000) presented the design and dynamic analysis of both the axial and radial magnetic bearings of rotors, and discussed the different elements along with control for the working of active magnetic bearing systems, such as the position sensors, controllers and power amplifiers. High-speed machining (HSM) offers substantial economic benefits as a result of increased metal cutting productivity. Critical to realizing this technology's promise are the intertwined challenges of spindle dynamic stiffness and cutting process stability. Active magnetic bearings enable greater spindle dynamic stiffness through higher attainable bearing surface speeds, and also provide a means for enhancing cutting process stability.

Knopse (2007) presented experimental results from two test rigs illustrating the potential of magnetic bearings for the active suppression of machining chatter. AMBs hold considerable promise for HSM applications and for that number of technical challenges need to be tackled, including actuator design, sensor noise, and high-performance feedback control. Experimental results demonstrated that model-based approaches to controller design can be highly effective for this problem. Two approaches have proven effective in this regard: speed-independent controllers where the delay element is treated as complex uncertainty and chatter suppression is achieved through gain-stabilization; and speed-specified controllers where the delay element is approximated by a high order, finite-dimensional system so as to capture its phase information.

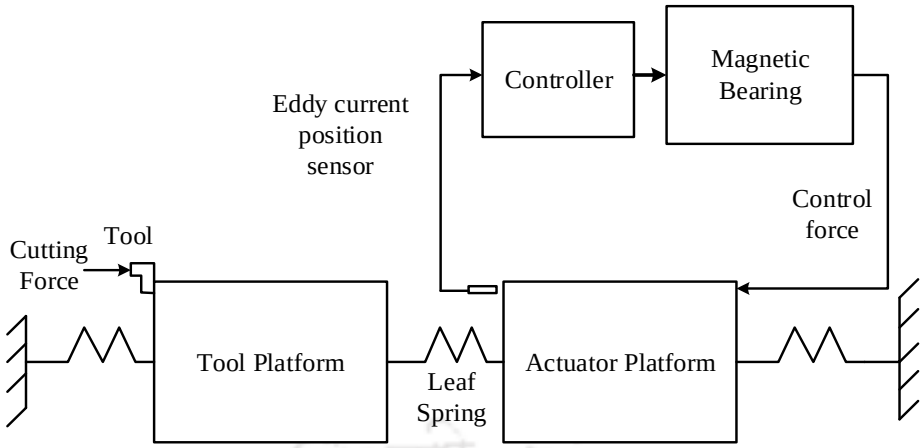

Figure 1.15 Schematic of chatter control experiment (Knopse, 2007).

Li et al. (2006) developed a systematic approach to model an accurate analytical model of the rotor and magnetic bearings, and compared it with the experimental data of a high-speed rotor magnetic bearing test rig. Closed loop tests were conducted to identify parameters in the system model. Zhong et al. (2014) utilized homo-polar type electro-magnetic (EM) actuators and employed proportional-derivative (PD) type controller for the position control by AMB. They used the multiple objective genetic algorithms (MOGAs) to optimize the control law and geometrical features of homo-polar magnetic bearings (HOMB) supporting a generic flexible, spinning shaft. The minimization objectives included the shaft dynamic response, actuator mass and total actuator power losses. Levitation of the spinning rotor and dynamic stability were taken as constraint conditions for the control law search along with nonlinearities, like the magnetic flux saturation, and current and voltage limits. Pareto fronts were applied to identify the best-compromised solution.

Imlach et al. (1991) developed closed-loop stiffness and load capacity (force) equations to design a radial magnetic bearing actuator and manufactured two sets of bearings to be installed in two canned motor pumps. They predicted the force and stiffness values from these equations and compared them to experimental measurements to determine their validity with measured current and displacement information from the magnetic bearing equipped machinery.

Kimman et al. (2010) presented the design and realization of a miniature milling spindle with AMBs. Permanent magnet biased, reluctance type actuators position the rotor in five degrees of freedom (DOF), leaving the rotation unconstrained. To reach higher rotational speeds, the

rotor diameter must be decreased to lower the centrifugal stresses in the rotor. The reduction of the spindle length will allow for the increase of the rotational speed while remaining below the flexible resonances of the rotor shaft. A rotordynamic model was developed to expedite the controller design, and enabled modelling of the spindle's performance under the influence of cutting forces. A PID controller model, with a negative stiffness compensation scheme, was implemented. A cross-feedback controller partly compensated the gyroscopic effect and the spindle could reach a maximum speed of 150 000 rpm.

Mushi et al. (2011) presented the framework of a model-based control design to ensure efficient, reliable, and safe operation of turbomachinery on AMBs. This paper gave a detailed description of the design, construction, and modelling process for a high performance AMB test rig, which resembles a small industrial super-critical centrifugal compressor. Two additional radial AMBs were used to allow the application of simulated destabilizing fluid or electromagnetic forces to the rotor since these forces are difficult to predict and can lead to rotordynamic instability. This test rig provided a realistic platform to evaluate stabilizing control algorithms for high performance turbomachinery. A complete model of rotor, AMB actuators and accompanying electronics, was constructed from individually verified component models. Model validation was confirmed through the successful design and implementation of a μ-synthesis controller.

Barbaraci et al. (2013) proposed a method of varying the journal ratio to resolve the size issue in implementing the AMBs on shafts rotating on conventional bearings. They stated that variation of journal ratio does not produce a variation of the pole's surface so the reaction load does not change. The results were analysed by numerical analysis by mathematical relationships involving the design parameters, magneto-static simulations and dynamic simulation on the shaft when tested by disturbance rejection and reference tracking input in order to analyze the differences on dynamic behaviour of the shaft on its suspended sections. Results show that the displacement pattern of the suspended sections remains unchanged, confirming that the reaction load, produced by pole expansion, remains the same varying the journal ratio.

Polajžer et al. (2006) discussed a closed-loop decentralized control for active magnetic bearings and presented a cascade connection of PI and PD position controllers. It showed the advantages

of applying the proposed PI/PD controls over the conventional PID controller and guaranteed satisfactory high damping and stiffness of the overall system.

In this section, an overview of AMB technology and its applications has been given. In the current topics of AMB research work, high speeds, control of elastic rotors, touch-down dynamics, magnetic levitation and smart rotating machinery are addressed.

1.2.7.3 Identification of Parameters in Rotor-AMB System

Several methods have been described in the literature for identification of parameters on different types of AMB systems in both the time and frequency domains.

In general, identification algorithms are obtained from the current and displacement coefficients of a linearized AMB model. In recent years, it has been shown that predictor-based subspace identification algorithms (PBSID) give consistent estimates of the parameters even in the presence of feedback. A linear model of an experimental AMB system has been obtained using a $PBSID_{opt}$ by Balini et al. (2010). However, the control synthesis based on the system with flexible modes resulted in unstable controllers and could not be implemented in practise. Instead, it was shown that a controller could be synthesised based on a reduced order model, which were designed to be robust against the neglected flexible behaviour of the shaft. The disadvantage of this kind of method, which is solely based on experimental data, is the limited prediction capabilities of the resulting controller. For instance, such a model is generally unable to predict what happens if a physical parameters changes, such as the rotational speed. In that case, a new model must be identified for example, for a new speed, and these models must be linked together. For the same reason, a perturbed plant representation using a parametric uncertainty cannot directly be obtained, whereas it could be if the model was established with parameters with physical meanings.

Another method by Gahler et al. (1997) identified the modal parameters, i.e. the natural frequencies and damping, using a predefined model structure. Here, the system matrices are represented using a two-stage optimisation. Li et al. (2006) presented a comprehensive modelling and identification method with individual mathematical modelling and identification of the subcomponents, followed by an overall identification of a closed loop transfer function. The global system comprises the dynamics of a flexible rotor, a flexible substructure base, two

radial AMBs and electronic components. The goal was to obtain a model for synthesising robust controllers.

Vázquez et al. (2001) presented the identification of a long flexible rotor with three magnetic bearing journals, experimentally. The rotor was hung horizontally with piano wire and frequency response functions were measured between the magnetic bearing journals and the sensor locations. Transfer functions were calculated from these frequency response functions and used in the reconciliation method to modify a nominal model of the rotor. The frequency response functions are then compared with the responses of a rotor model and a reconciliation process was used to reduce the discrepancies between the model and the measured data, and equivalent dynamic stiffness was calculated for the piano wire and the fit of the magnetic bearing journals. The reconciliation process reduced the error between the model response and the measured response by several orders of magnitude, demonstrating the effectiveness of the method. The identified dynamics of the wire and the fit of the magnetic bearing journals show the expected behaviour only at low frequency.

Ranjan and Tiwari (2020) developed an identification algorithm to execute high-speed balancing of a flexible rotor system supported on conventional bearings. The system was integrated with Active Magnetic Bearings (AMBs) as a suppression actuator as well as an excitation actuator. The AMB suppresses, the vibration of the system and identifies the orientation and magnitude of the residual unbalances present in the system through virtual trial unbalances. An Advanced Influence Coefficient Method (AICM) was developed that utilizes the influence coefficients obtained at high speed and unbalances identified at the low speed to effectively estimate the balance masses required for the high-speed flexible rotor balancing. The influence coefficients are required to be obtained just once, whereas the balance masses can be estimated periodically by identifying the unbalances at low speeds. After balancing, the system can easily cross through its critical speeds with less vibration. The AMB also controls abrupt change in vibration amplitude due to any uncertain faults, while operating at high speeds. Additionally, the virtual trial unbalances as a magnetic force generated through AMB reduces the mechanical effort involved in placing the trial masses for the unbalance compensation. This method allows on-site condition monitoring of the system periodically to reduce the impairment of high-speed machinery.

The literature suggests that AMBs has been chosen as an efficient component in vibration control and condition monitoring of flexible rotor-bearing systems. The proposed work involves the novel use of AMB technology not for geared rotor support but rather as an actuator for reduction of vibration and noise emanating from the system. The current study deals with application of AMBs for vibration suppression and identification of faults in geared rotor systems.

1.3 Shortcomings of the Existing Literature

The above literature survey portrays that there exists a lot of different techniques to model the gear system dynamics. When considering the internal responses of the gearbox, forces generated by the mating gears between the gear teeth continually results in subsequent vibration and noise. The vibrations are transmitted from the gears to the shaft and through the bearings to the gear case. Sometimes, it becomes quite expensive to take out this damaged gearbox and replace it especially in offshore wind turbines, complex and large rotating machinery. As noted above, a number of factors needs be considered in order to reduce the transmission error in gears. The unmodified gear with less profile error provides better performance with regard to transmission error fluctuation when the load torque is low whereas the gear with a modified profile is better above a certain level of load torque. This shows how fluctuations in transmission error can be minimized by modifying the tooth profile to suit the load applied to the gear. So, usually tooth profile modification is suggested at the gear design stage or manufacturing stage to control the DTE (most important factor for gear noise) however this consumes time and is quite cumbersome. Evidently, gears are prone to failures and not much literature can be found on the identification of dynamic transmission error with experimental validation. For example, loaded transmission errors can be predicted by using software such as the LDP (Load Distribution Program) from Ohio State University's Gear Dynamics and Gear Noise Research Laboratory (1994). Most transmission error analysis tools compute static transmission error. Additionally, TE is modelled in a single direction, which does not give the complete information, like its orientation and phase.

Addition of vibration isolators/struts is among the most common practices to reduce the vibration transmitted to the support structure. However, even with a well-designed isolator, there is always some residual vibration that is transmitted to the support structure. So, the concept of active vibration control of geared rotor systems with piezoelectric actuators was

introduced by few researchers. Unfortunately, there are also few limitations with piezoelectric actuator technology, i.e., the structural vibrations intensify at frequencies close to the resonant frequency, so the positioning speed of piezo-based systems is limited by the lowest structural vibrational frequency, causing significant positioning errors. The major drawback of this actuation concept is that the slip rings configured to transfer electrical power to the rotating actuators are complex. Other practical limitations are the actuator's limited strength in tension, hysteresis in the movement and acceleration increasing exponentially with frequency, and the power dissipation stemming from the mass of the actuators increases significantly at higher frequencies. Furthermore, there are electrical limitations in piezoelectric actuators [79].

1.4 Aim of the Present Work

This thesis work presents a novel concept of integrating active magnetic bearings into the geared rotor system. The aim of the present study is to reduce the gear mesh vibrations by applying actively controlled electromagnetic forces with AMBs placed on the geared shafts and then identification of different types of geared rotor faults from the vibration responses of the proposed rotor system. For that it is essential to have an accurate model representation of the complete rotordynamic test facility and the model should describe the dynamic behaviour of the rotor, mechanism of gear meshing, the flexible links with the motor, load, and the characteristics of the electronics involved with magnetic bearing. There are various parameters in geared rotors which are directly not measurable like the gear mesh damping, mesh stiffness, gear runout, dynamic transmission error etc. In an attempt to estimate those parameters, an identification algorithm has been developed. The desired goal is achieved by undertaking the following objectives:

1. Develop the mathematical formulation for a single stage spur geared rotor system based on lumped parameter gear dynamic models devising various faults and integrated with Active Magnetic Bearings.

2. Conduct gear dynamic analysis of the proposed geared rotor-AMB system by taking the following cases:

(a) Rotor with gears at mid span of the shaft and integrated with AMB generating the vibrational displacement only in transverse direction.

(b) Rotor with gears placed slightly away from mid span of the shaft, integrated with AMB and creating the vibrational displacement in transverse direction along with gyroscopic effect.
(c) Rotor with gears placed slightly away from mid span of the shaft and integrated with AMB causing the coupled torsional-lateral vibrations along with gyroscopic effect.

3. Develop an identification algorithm from developed models using regression method for identification of various geared rotor faults, like the gear runout error, unbalance, variable transmission error with corresponding phases, AMB parameters like displacement stiffness and current stiffness factors, thereafter solve the inverse problem with least-squares technique. Random noise and modelling error is added to the simulated data to accurately model the system performance and test the algorithm.

4. Design and fabricate the proposed geared-rotor AMB laboratory test rig for the experimental validation and investigation of active internal shaft vibration control caused by rotor unbalance, gear runout, transmission error, which usually resides within the gearbox with an aim of minimizing the effects of transmission error to have quieter gear operation.

5. Utilize the full spectrum responses obtained experimentally from the developed rotor AMB test rig as an input to the developed identification algorithm for prediction of the different rotor faults that were considered in the mathematical model.

1.5 Outline of the thesis work

The thesis is divided into seven chapters. The introduction and literature review are presented in Chapter 1. The mathematical modelling, numerical simulation for transverse vibration analysis of the geared rotor AMB system in time and frequency domain has been carried out in Chapter 2. Later, an identification algorithm based on mathematical model has been developed and geared rotor faults, transmission error and AMB parameters are predicted by undertaking the full spectrum of vibration responses. Chapter 3 discusses the mathematical modelling considering offset gears and numerical simulation of the proposed system is carried out for the transverse vibration analysis with gyroscopic effect. The identification algorithm is developed accordingly and faults, AMB parameters are identified. Similarly, in Chapter 4 the work is extended to numerical investigation of the coupled torsional-lateral vibration analysis with gyroscopic effect. Based on the mathematical model the identification algorithm is developed and parameters are estimated. The detailed description of the various components

for design and fabrication of the laboratory test rig is given in Chapter 5. Furthermore, the numerical results of the proposed model are compared with that of the responses obtained from the experimental test rig. The practical design guidelines of the active control system of a magnetic bearing in terms of sensors, actuators, power amplifiers and real-time controller implementation is presented and its effectiveness in suppressing the gear induced housing vibrations and noise are explicitly described. The identification of various rotor-AMB parameters are experimentally obtained from the rotor test rig vibration responses and the developed algorithm is validated. In the end, the conclusions, limitations, and future scope of the current work is presented in Chapter 6.

CHAPTER 2 TRANSVERSE VIBRATION ANALYSIS OF GEARED ROTOR-AMB SYSTEM

2.1 Introduction

The dynamic analysis of a rotor with a single stage spur gear has been carried out using lumped parameter model subjected to different types of geared rotor faults. AMB is applied to the geared rotor dynamics as an auxiliary active support to see the effectiveness of the active vibration control against the dynamic transmission error (DTE). The study of torsional vibration of geared rotors is important, not only in high-speed applications and high-power transmission. Torsional vibrations may occur due to torques related to gear mesh frequencies. However, torsional vibrations in rotating machines may result not only from direct torsional excitations, but also from common lateral mode excitations, as the torsional-lateral mode coupling mechanism is related to the eccentricity of the bending and twisting centre along the rotor. The torsional vibration travels across the driveline and becomes coupled to the lateral vibrations at gear meshes, giving rise to undesired dynamic forces through the bearings and support locations. With this assumption, at first transverse vibration analysis has been carried out. A feedback PID controller has been used as a control scheme in AMB. DTE is modelled as an asymmetric transmission error expressed in Fourier series consisting of both odd and even harmonics in the full spectrum. An identification algorithm based on mathematical model through least-square regression technique has been built and the prediction of geared rotor faults, transmission error and AMB parameters are done using the vibration and current responses obtained by undertaking the full spectrum of time domain signals.

2.2 Geared Rotor System Configuration

The most easily visualized common gears are the spur gear that transmits motion between two parallel shafts. As shown in Fig. 2.1, a single pair of spur gear is considered at the middle of two elastic shafts supported on two rolling element bearings (REBs) i.e., single row deep groove ball bearings at shaft ends. The deformation of the tooth is neglected except at the pitch point of the driving and driven gears. The damping is added as an equivalent translational viscous mesh damping, connected in parallel by a linear spring model with equivalent mesh stiffness added along the contact pressure line, i.e., tangent to the base circle of the driving and

driven gears. The coupling between transverse and torsional vibration is ignored and only transverse vibration is considered.

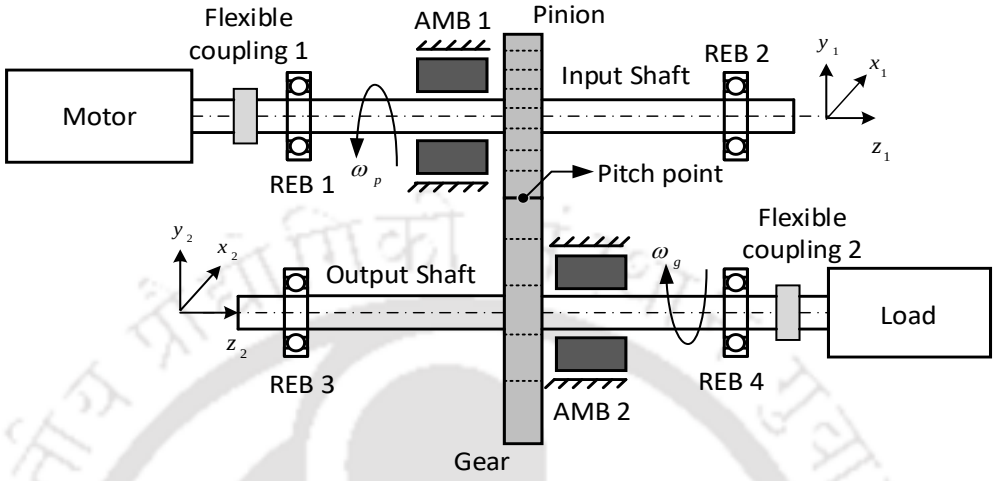

Figure 2.1 Proposed geared rotor-AMB system

Herein, *z*-axis is taken along the shaft centreline, and translational displacements of the pinion and the gear is defined along the *x* and *y* axes with appropriate subscripts. As a result of assembling error, the gear eccentricity is added to the model, which contributes to the effect of runout and unbalance onto the gear transmission system described in Fig. 2.2.

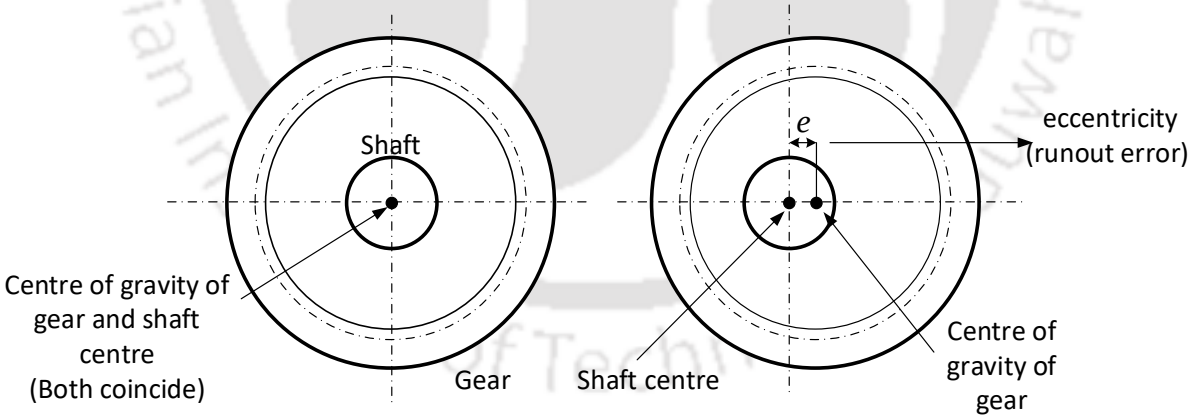

Figure 2.2 Runout error in a gear caused by assembly error

The rolling element bearing is considered as rigid, and shafts are of uniform cross-section and flexible that allows transverse displacement only. The motor drives the input (driver or pinion) gear and the load provides the brake torque to the driven (output) gear. AMBs are placed near the input and output gears to control the vibratory motion. The couplings are flexible and the angular twist due to motor and load is neglected while undertaking transverse vibration

analysis. The AMB serves to perform as the condition monitoring device to characterise the faults as well as attenuate the vibration of the rotor system.

2.2.1 Mathematical Model of Meshing of Gear-Pair

A mathematical formulation of spur gear system is developed with four degrees-of-freedom lumped parameter model to carry out the transverse vibration analysis due to the gear mesh. The model is defined by flexible shafts with lateral stiffness k_p and k_g, and damping c_p and c_g; which can be considered as equivalent stiffness and damping due to shaft as well as support bearings. On considering rigid bearings, the bearing stiffness and damping is ignored. It is assumed that the centres of pinion and gear wheel is displaced from the respective shaft centres by an eccentricity e_p and e_g, respectively, causing runout, and ϕ_p, ϕ_g are the phase of pinion and gear wheel runouts, respectively. Runout gives unbalance and also displacement to mating gears. The base circle radii of pinion and gear are represented by r_p and r_g. The model has four translational displacements in the vertical and horizontal directions of the pinion and the gear due to meshing forces along the line of action. The displacements of the gear-shaft centres during the meshing of gears in the *x* and *y* directions are given by x_1, y_1, x_2, y_2 and the lateral displacements of the runout pinion (driver) and gear (driven) wheel centres are given by x_p, y_p, x_g, y_g, respectively, as shown in Fig. 2.3. ω_p and ω_g are the angular velocities of pinion and gear, respectively. Combining all geometrical parameters defined above, we can write the displacement equation as

$$\begin{aligned} x_p &= x_1 + e_p \cos\left(\omega_p t + \phi_p\right); \quad y_p = y_1 + e_p \sin\left(\omega_p t + \phi_p\right) \\ x_g &= x_2 + e_g \cos\left(-\omega_g t + \phi_g\right); \quad y_g = y_2 + e_g \sin\left(-\omega_g t + \phi_g\right) \end{aligned} \tag{2.1}$$

The average meshing stiffness at the pitch point along the pressure line is given by k_m and gear mesh damping by c_m as shown in Fig. 2.3. The tooth frictional effect on the shear stress, bending stress and transmission error in gear meshing is neglected.

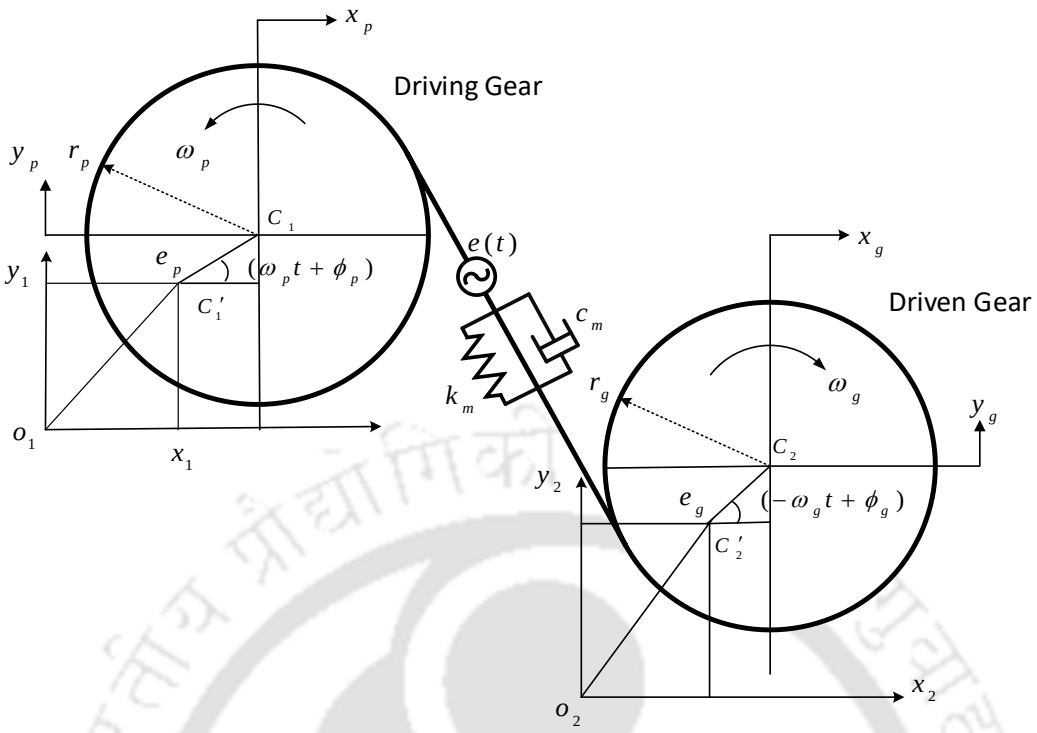

Figure 2.3 Co-ordinate system of a gear pair at the pressure line

An external displacement or error excitation $e(t)$ is applied at the gear mesh interface along the line of action to model the transmission error. (Rao and Tiwari, 2020), detected the asymmetric transmission error in geared rotor system for transverse vibration analysis with full spectrum. Unlike the consideration of transmission error along the line of action in a single direction, this study assumes the DTE in two orthogonal directions to study the forward and backward harmonics of geared rotor. Hence, $e_x(t)$ and $e_y(t)$ indicate the horizontal and vertical components of the static transmission error (STE), respectively, under the loaded condition. The STE with n as the number of harmonics is modelled as the sum of static and varying components of the transmission error. The components of the STE, in the *x* and *y* directions, are expressed as

$$e_x(t) = e_{mx} + \sum_{i=-n}^{n} e_{fxi}(t) \quad \text{and} \quad e_y(t) = e_{my} + \sum_{i=-n}^{n} e_{fyi}(t) \tag{2.2}$$

where in subscripts *m* and *f* refer to the mean and fluctuating components, respectively. Maximum harmonics to be considered is represented by *n* with the negative refer to the

backward whirl and the positive to the forward whirl. The gear mesh frequency is denoted by ω_e and is dependent on the number of pinion/gear teeth and rotational speed of pinion/gear respectively. It is found that multiple harmonics of exist in a geared rotor system due to transmission error, not only in forward whirl direction but also in backward whirl direction. The STE, in the *x* and *y* directions can further be written in terms of its magnitudes and phases in expanded form as

$$\begin{aligned} e_x(t) &= e_m \cos\phi_m + \sum_{i=-n}^{n} e_{fi} \cos\left(i\omega_e t + \phi_{fi}\right) \\ e_y(t) &= e_m \sin\phi_m + \sum_{i=-n}^{n} e_{fi} \sin\left(i\omega_e t + \phi_{fi}\right) \end{aligned} \tag{2.3}$$

The component of gear mesh deformation at the pitch point of the mating gears in the *x* and *y* directions are denoted by δ_x and δ_y, respectively. Then, from Fig. 2.3 displacement increment along the pressure line due to the shaft deformation, gear runouts and transmission error in the *x* and *y* directions, respectively, can be expressed as the dynamic transmission error (DTE)

$$\begin{aligned} \delta_x &= x_p - x_g - e_x(t) = x_1 - x_2 + e_p \cos\left(\omega_p t + \phi_p\right) - e_g \cos\left(-\omega_g t + \phi_g\right) - e_x(t) \\ \delta_y &= y_p - y_g - e_y(t) = y_1 - y_2 + e_p \sin\left(\omega_p t + \phi_p\right) - e_g \sin\left(-\omega_g t + \phi_g\right) - e_y(t) \end{aligned} \tag{2.4}$$

2.2.2 Characteristics of Active Magnetic Bearings

The design of magnetic bearings has to consider two key elements, the magnetic bearing actuator and its control system. In this section, from the literature available in [84-85] the design characteristics of a radial active magnetic bearing has been briefly described. Fig. 2.4 shows the cross section, where the eight-pole AMB actuator has the stator and core made of ferromagnetic material with 'μ_0' as the magnetic permeability of free space and 'α' as half the angle between two poles about the mean position of rotor. The area between the stator poles is 'A_a' the cross-sectional area of flux in the air that is equal to the area of iron core and slots are having 'N' number of coil windings. The stator yoke completes the magnetic paths of the eight stator poles. The width of the stator yoke is designed to be wide enough to avoid magnetic saturation and produce high mechanical stiffness in order to avoid vibration caused by radial magnetic forces. The eight poles create four-pair of electromagnets and 's_o' represents the air

gap between the electromagnetic actuator pole and rotor at operating point. 'i_o' is the bias current to the coils. The design of the actuator depends upon the maximum load capacity, air gap between rotor and stator, number of poles, power consumption and so on.

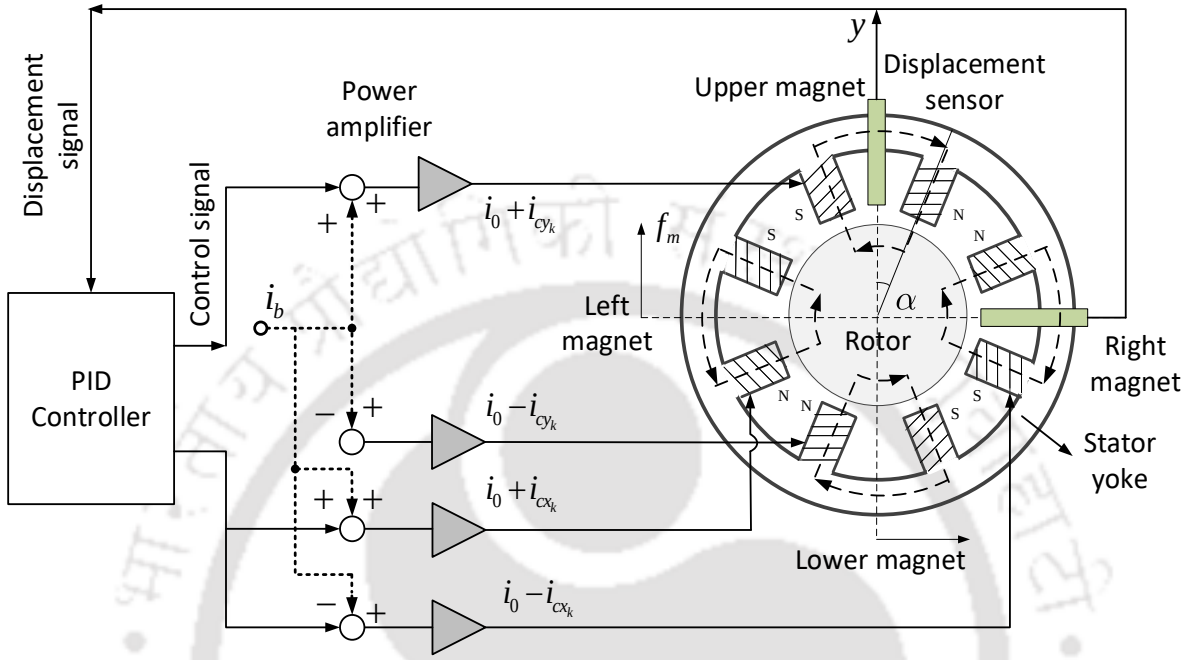

Figure 2.4 Feedback control system of AMB actuator

For a precise motion control of the rotor, closed-loop control system [86-87] is employed as the strength of the electromagnetic forces can be controlled proficiently even if the load on the rotor is varied. When the rotor gets shifted from its equilibrium position, it is controlled by a linear proportional-integral-derivative (PID) controller with differential driving mode. In Fig. 2.4 f_m is the difference of magnetic forces exerted by both the magnets on the rotor acting radially. Both the magnetic forces are obtained by inserting currents i_{cx_k+} and i_{cx_k-} to corresponding air gaps $s_o + x_k$ and $s_o - x_k$ in *x* direction as given in eqn. (2.5), where subscript *k* = 1, 2 representing the input and output shafts, respectively. Thus, the resultant magnetic force in x-direction is

$$f_m = c_1 \left\{ \left(\frac{i_0 + i_{cx_k}}{s_0 + x_k} \right)^2 - \left(\frac{i_0 - i_{cx_k}}{s_0 - x_k} \right)^2 \right\} \cos\alpha \qquad \text{with} \quad c_1 = 0.25 \mu_0 N^2 A_a \tag{2.5}$$

Here, c_1 is a constant calculated for a particular bearing configuration.

Which can be combined as $f_m = c_1 \left\{ \dfrac{ i_0 + i_{cx_k}{}^2 \; s_0 - x_k{}^2 - i_0 - i_{cx_k}{}^2 \; s_0 + x_k{}^2 }{ s_0 + x_k{}^2 \; s_0 - x_k{}^2 } \right\} \cos\alpha$ (2.6)

After simplification, we get $f_m = c_1 \left\{ \dfrac{ -4 s_0 x_k i_0^2 - 4 s_0 x_k i_{cx_k}^2 + 4 i_0 i_{cx_k} s_0^2 + 4 i_0 i_{cx_k} x_k^2 }{ s_0 + x_k{}^2 \; s_0 - x_k{}^2 } \right\} \cos\alpha$ (2.7)

Neglecting higher order terms of x_k, since $x_k << s_0$, we get

$$f_m = c_1 \left\{ \frac{ -4 s_0 x_k \;\; i_0^2 + i_{cx_k}^2 \;\; + 4 i_0 i_{cx_k} s_0^2 }{ s_0^4 } \right\} \cos\alpha \tag{2.8}$$

Which simplifies to $f_m = c_1 \left\{ \dfrac{ -4 s_0 x_k \;\; i_0^2 + i_{cx_k}^2 \;\; + 4 i_0 i_{cx_k} s_0^2 }{ s_0^4 } \right\} \cos\alpha$ (2.9)

After rearrangement of terms, we get $f_m = -\left(\dfrac{4 c_1 i_0^2 \cos\alpha}{s_0^3} \right) x_k + \left(\dfrac{4 c_1 i_0 \cos\alpha}{s_0^2} \right) i_{cx_k}$ (2.10)

Thus the total instantaneous magnetic force f_m as a function of displacement and current at the operating point in linearized equation is given by $f_m = -k_s x_k + k_I i_{cx_k}$ (2.11)

The rotor position is detected by the displacement sensors and sent as an input to a digital controller. The dynamic force suppression characteristics are examined by fine tuning the PID controller gains, which stabilizes the rotor vibrations. The output current from the PID controller is amplified by the power amplifiers, which is then sent to the actuator coils.

2.2.3 Working Principle of Control of Active Magnetic Bearings

The working layout of magnetic bearing control system is shown in Fig. 2.5. In this work two radial magnetic bearings have been used to support and position the input and output shafts in the radial direction. When the rotor position gets shifted from its equilibrium position, it is controlled by a closed-loop feedback system. The electromagnets generate radial forces in differential mode in the *x* and *y* directions. With 'i_m' as the total coil current, the general magnetic force 'f_M' acting on the rotor in an AMB (Tiwari, 2017) is given by

$$f_m = c_1 \left(\frac{i_m}{s_o} \right)^2 \cos\alpha \tag{2.12}$$

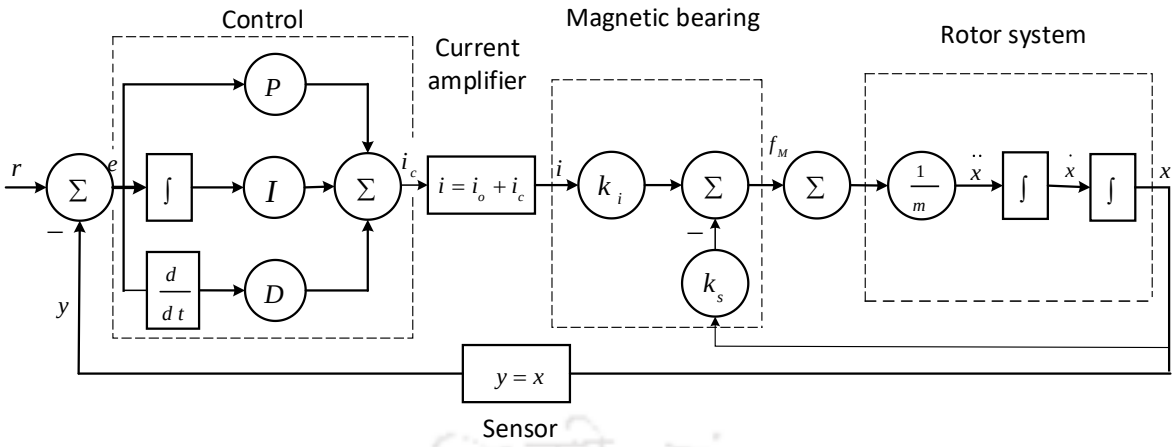

Figure 2.5 Linearized rotor-AMB model with PID control loop

The local displacements are detected from the shaft position sensors and the signals are sent as an input to a digital controller. The controller processes these signals, and calculates how to re-distribute the currents in the electromagnets to restore the shaft to its centred position. Power amplifiers in the controller then amplifies the currents to be sent to the electromagnets. The dynamic force suppression characteristics are examined with an adjustment of PID controller gains given by K_P, K_D and K_I, which is tuned digitally to stabilize the geared rotor displacement. The current output from the PID controller is then sent to the actuator coils accordingly. The expression of the control current i_{cx_k} and i_{cy_k} from the PID controller for two perpendicular transverse directions, i.e. the x and y directions, with subscript k = 1, 2 representing the input and output shaft [62], respectively, are expressed as,

$$\begin{aligned} i_{cx_k}(t) &= K_P x_k(t) + K_I \int x_k(t)dt + K_D \frac{dx_k(t)}{dt} \\ i_{cy_k}(t) &= K_P y_k(t) + K_I \int y_k(t)dt + K_D \frac{dy_k(t)}{dt} \end{aligned} \tag{2.13}$$

According to the dynamics of AMB, assuming linear characteristics of the magnetic forces, the total instantaneous radial magnetic force f_m can be expressed in terms of a function of rotor lateral displacements x_k and y_k (deviation of rotor from mean position) and coil current i_{cx_k} and i_{cy_k} (control current). Thus, the balancing magnetic bearing force in x and y directions can be written, respectively, as

$$f_m = \begin{Bmatrix} -k_s x_k + k_I i_{cx_k} \\ -k_s y_k + k_I i_{cy_k} \end{Bmatrix} \tag{2.14}$$

$$\text{with, } k_s = \frac{4c_1 i_0^2 \cos\alpha}{s_0^3}; \quad k_I = \frac{4c_1 i_0 \cos\alpha}{s_0^2} \tag{2.15}$$

2.2.4 Equations of Motion of Geared Rotor System with AMB

The energy equation, i.e. the kinetic energy '*T*', the potential energy '*U*', the dissipation function '*D*' and the force vector '*P*' considering transmission errors, and gear runouts (runouts gives mass unbalances on shafts, and elastic and damping forces at the pitch point) of geared rotor AMB system can be written as

$$T = \frac{1}{2}\left\{m_1\left(\dot{x}_p^2 + \dot{y}_p^2\right) + m_2\left(\dot{x}_g^2 + \dot{y}_g^2\right)\right\} \tag{2.16}$$

$$U = \frac{1}{2}\left\{k_p\left(x_p^2 + y_p^2\right) + k_g\left(x_g^2 + y_g^2\right) + k_m\left(\delta_x^2 + \delta_y^2\right)\right\} \tag{2.17}$$

$$D = \frac{1}{2}\left\{c_p\left(\dot{x}_p^2 + \dot{y}_p^2\right) + c_g\left(\dot{x}_g^2 + \dot{y}_g^2\right) + c_m\left(\dot{\delta}_x^2 + \dot{\delta}_x^2\right)\right\} \tag{2.18}$$

To derive the equation of motion of the given mechanical system, on using the extended Lagrange's formulation, we know that

$$\frac{d}{dt}\left(\frac{\partial L}{\partial \dot{q}_i}\right) - \frac{\partial L}{\partial q_i} + \frac{\partial D}{\partial \dot{q}_i} = P_i \ (i = 1, 2, \ldots) \tag{2.19}$$

With $L = T - U$

By substituting *L* in eqn. (2.19), the equations of motion for the system is derived by using Lagrange's dynamics, which is given by the expression

$$\frac{d}{dt}\left(\frac{\partial T}{\partial \dot{q}_i}\right) - \frac{d}{dt}\left(\frac{\partial U}{\partial \dot{q}_i}\right) - \frac{\partial T}{\partial q_i} + \frac{\partial U}{\partial q_i} + \frac{\partial D}{\partial \dot{q}_i} = P_i \ (i = 1, 2, \ldots) \tag{2.20}$$

Noting eqn. (2.20) and energy equations given by (2.16), (2.17) and (2.18), subsequently the equations of motion of the rotor corresponding to each DOF with forces due to the mass

unbalance, gear runout errors, mesh dynamic force with corresponding transmission errors and AMB controlling force is obtained directly by rearranging the mass, stiffness and damping matrices, and can be put into matrix form as

$$\mathbf{M}\ddot{\mathbf{q}} + \mathbf{C}\dot{\mathbf{q}} + \mathbf{K}\mathbf{q} = \mathbf{f}_{\text{unb}} + \mathbf{f}_{\text{r\_out}} + \mathbf{f}_{\text{mesh}} + \mathbf{f}_{\text{amb}} \tag{2.21}$$

with

$$\mathbf{M} = \begin{bmatrix} m_1 & 0 & 0 & 0 \\ 0 & m_1 & 0 & 0 \\ 0 & 0 & m_2 & 0 \\ 0 & 0 & 0 & m_2 \end{bmatrix}; \quad \mathbf{C} = \begin{bmatrix} c_p + c_m & 0 & -c_m & 0 \\ 0 & c_p + c_m & 0 & -c_m \\ -c_m & 0 & c_g + c_m & 0 \\ 0 & -c_m & 0 & c_g + c_m \end{bmatrix}; \quad \mathbf{q} = \begin{bmatrix} x_1 \\ y_1 \\ x_2 \\ y_2 \end{bmatrix};$$

$$\mathbf{K} = \begin{bmatrix} k_p + k_m & 0 & -k_m & 0 \\ 0 & k_p + k_m & 0 & -k_m \\ -k_m & 0 & k_g + k_m & 0 \\ 0 & -k_m & 0 & k_g + k_m \end{bmatrix}; \quad \mathbf{f}_{\text{unb}} = \begin{bmatrix} \left(m_1 e_p \omega_p^2\right)\cos\left(\omega_p t + \phi_p\right) \\ \left(m_1 e_p \omega_p^2\right)\sin\left(\omega_p t + \phi_p\right) \\ \left(m_2 e_g \omega_g^2\right)\cos\left(-\omega_g t + \phi_g\right) \\ \left(m_2 e_g \omega_g^2\right)\sin\left(-\omega_g t + \phi_g\right) \end{bmatrix};$$

$$\mathbf{f}_{\text{r\_out}} = \begin{bmatrix} c_p e_p \omega_p \sin\left(\omega_p t + \phi_p\right) \\ -c_p e_p \omega_p \cos\left(\omega_p t + \phi_p\right) \\ -c_g e_g \omega_g \sin\left(-\omega_g t + \phi_g\right) \\ c_g e_g \omega_g \cos\left(-\omega_g t + \phi_g\right) \end{bmatrix} + \begin{bmatrix} -k_p e_p \cos\left(\omega_p t + \phi_p\right) \\ -k_p e_p \sin\left(\omega_p t + \phi_p\right) \\ -k_g e_g \cos\left(-\omega_g t + \phi_g\right) \\ -k_g e_g \sin\left(-\omega_g t + \phi_g\right) \end{bmatrix}; \quad \mathbf{f}_{\text{amb}} = \begin{bmatrix} -k_s x_1 + k_I i_{cx_1} \\ -k_s y_1 + k_I i_{cy_1} \\ -k_s x_2 + k_I i_{cx_2} \\ -k_s y_2 + k_I i_{cy_2} \end{bmatrix};$$

$$\mathbf{f}_{\text{mesh}} = c_m \begin{bmatrix} e_p \omega_p \sin\left(\omega_p t + \phi_p\right) + e_g \omega_g \sin\left(-\omega_g t + \phi_g\right) + \dot{e}_x(t) \\ -e_p \omega_p \cos\left(\omega_p t + \phi_p\right) - e_g \omega_g \cos\left(-\omega_g t + \phi_g\right) + \dot{e}_y(t) \\ -e_p \omega_p \sin\left(\omega_p t + \phi_p\right) - e_g \omega_g \sin\left(-\omega_g t + \phi_g\right) - \dot{e}_x(t) \\ e_p \omega_p \cos\left(\omega_p t + \phi_p\right) + e_g \omega_g \cos\left(-\omega_g t + \phi_g\right) - \dot{e}_y(t) \end{bmatrix} +$$

$$k_m \begin{bmatrix} -e_p \cos\left(\omega_p t + \phi_p\right) + e_g \cos\left(-\omega_g t + \phi_g\right) + e_x(t) \\ -e_p \sin\left(\omega_p t + \phi_p\right) + e_g \sin\left(-\omega_g t + \phi_g\right) + e_y(t) \\ e_p \cos\left(\omega_p t + \phi_p\right) - e_g \cos\left(-\omega_g t + \phi_g\right) - e_x(t) \\ e_p \sin\left(\omega_p t + \phi_p\right) - e_g \sin\left(-\omega_g t + \phi_g\right) - e_y(t) \end{bmatrix} \tag{2.22}$$

The right side of the eqn. (2.21) shows the forces due to mass unbalance, gear run out error, mesh dynamic force with corresponding transmission error and AMB controlling force. Further the identification algorithm is developed from the above systems equation of motion.

2.3 Development of Identification Algorithm

In this section, the development of an algorithm for the model-based parameter identification of geared-rotor-AMB system using the full spectrum of complex vibration signal from the shafts has been done. The identification algorithm is obtained from developed EOMs in the form of regression equations and the system parameters are estimated by using least-square fitting technique from the full spectrum data of rotor vibration and AMB current.

2.3.1 Representation of equations of motion in complex form

The vibration response based on EOMs from eqn. (2.22) can be generated in both time and frequency domain. For easy of computation, translational displacements (x_1, y_1) and (x_2, y_2) of geared rotors are combined as complex vectors r_1 and r_2, respectively, with $\mathrm{j} = \sqrt{-1}$ as

$$r_1 = x_1 + \mathrm{j}\, y_1 \qquad \text{and} \qquad r_2 = x_2 + \mathrm{j}\, y_2 \tag{2.23}$$

Likewise, the varying transmission error defined in eqn. (2.3) along the line of action between two mating gears with n number of harmonics in complex form can be written as

$$E = e_x(t) + \mathrm{j}e_y(t) = e_m e^{\mathrm{j}\phi_m} + \sum_{i=-n}^{n} e_{fi} e^{\mathrm{j}\left(i\omega_e t + \phi_{fi}\right)} \tag{2.24}$$

Differentiating equation (2.24) with respect to time, it can be expressed as

$$\dot{E} = \dot{e}_x(t) + \mathrm{j}\dot{e}_y(t) = \mathrm{j}\sum_{i=-n}^{n} i\omega_e e_{fi} e^{\mathrm{j}\left(i\omega_e t + \phi_{fi}\right)} \tag{2.25}$$

Similarly, the AMB control currents (i_{cx_1}, i_{cy_1}) and (i_{cx_2}, i_{cy_2}) can be combined as complex vectors i_{c_1} and i_{c_2}, respectively, as follows

$$i_{c1} = i_{cx_1} + \mathrm{j}\, i_{cy_1} \text{ and } i_{c2} = i_{cx_2} + \mathrm{j}\, i_{cy_2} \tag{2.26}$$

Taking into account eqns. (2.21) through (2.26), time domain EOMs from (2.21) and (2.22) transformed into the following complex form as

For input shaft:

$$\begin{aligned} &m_1\ddot{r}_1 + \left(c_p + c_m\right)\dot{r}_1 - c_m\dot{r}_2 + \left(k_p + k_m - k_s\right)r_1 - k_m r_2 = \left(m_1 e_p \omega_p^2 - k_p e_p - k_m e_p\right)e^{\mathrm{j}(\omega_p t + \phi_p)} \\ &-\mathrm{j}\left(c_p + c_m\right)e_p\omega_p e^{\mathrm{j}(\omega_p t+\phi_p)} + k_m e_g e^{\mathrm{j}(-\omega_g t+\phi_g)} - \mathrm{j}c_m e_g \omega_g e^{\mathrm{j}(-\omega_g t+\phi_g)} + k_m E + c_m\dot{E} - k_I i_1 \end{aligned} \tag{2.27}$$

For output shaft:

$$\begin{aligned} &m_2\ddot{r}_2 + \left(c_g + c_m\right)\dot{r}_2 - c_m\dot{r}_1 + \left(k_g + k_m - k_s\right)r_2 - k_m r_1 = \left(m_2 e_g \omega_g^2 - k_g e_g - k_m e_g\right)e^{\mathrm{j}(-\omega_g t + \phi_g)} \\ &+\mathrm{j}\left(c_g + c_m\right)e_g\omega_g e^{\mathrm{j}(-\omega_g t+\phi_g)} + k_m e_p e^{\mathrm{j}(\omega_p t+\phi_p)} + \mathrm{j}c_m e_p \omega_p e^{\mathrm{j}(\omega_p t+\phi_p)} - k_m E - c_m\dot{E} - k_I i_2 \end{aligned} \tag{2.28}$$

From eqns. (2.27) and (2.28), it can be observed that the input and output shafts are rotating in opposite direction. The full spectrum due to mass unbalance is expected to have larger 1X peak and smaller -1X peak. Hence, runout force vectors (including unbalance, elastic and damping forces) in input geared shaft, which is rotating in anticlockwise direction is in the form $F_1(\omega_p)e^{\mathrm{j}\omega_p t}$ accordingly the runout force vectors in output geared shaft rotating in clockwise direction is in the form $F_2(\omega_g)e^{-\mathrm{j}\omega_g t}$. The excitation forces due to gear meshing are multi-harmonic in nature and are of the form $F_3(\omega_e)e^{\mathrm{j}i\omega_e t}$ for $i = -n,...,-1,0,1,2...n$ harmonics. Herein, gear meshing forces are common to both shaft but opposite in direction hence a forward excitation in pinion will give a backward excitation in gear and vice-versa and since the systems EOM are linear, thereby applying principle of superposition, the assumed basic solution for eqns. (2.27) and (2.28) with three forcing frequencies are combined and added. Hence, considering the different excitation frequencies, i.e. $\omega_L = \omega_p, \omega_g$ and ω_e, the complex displacements $r_1(t), r_2(t)$ and the complex current $i_1(t), i_2(t)$ containing each harmonics from the full spectrum can be represented in summation form as

$$r_1(t) = R_{-npe}e^{-nj\omega_e t} + \cdots + R_{-1pe}e^{-j\omega_e t} + R_{-1pg}e^{-j\omega_g t} + R_{0p}e^{0j\omega_p t} + R_{1pp}e^{j\omega_p t} + R_{1pe}e^{j\omega_e t} + \cdots + R_{npe}e^{nj\omega_e t} \tag{2.29}$$

$$r_2(t) = R_{-nge}e^{-nj\omega_e t} + \cdots + R_{-1ge}e^{-j\omega_e t} + R_{-1gg}e^{-j\omega_g t} + R_{0g}e^{0j\omega_g t} + R_{1gp}e^{j\omega_p t} + R_{1ge}e^{j\omega_e t} + \cdots + R_{nge}e^{nj\omega_e t} \tag{2.30}$$

where, $R_{1pp}, R_{-1pg}, \sum_{i=-n}^{i=n} R_{ipe}$ and $R_{1gp}, R_{-1gg}, \sum_{i=-n}^{i=n} R_{ige}$ represent complex frequency domain displacement response due to the individual effect of $\omega_p, \omega_g, \omega_e$ on both input and output shafts, and R_{0p}, R_{0g} represents the static deflection in complex form for the pinion and gear shafts, respectively. Similarly, current harmonics should have the same frequency components as that of displacement harmonics. So, at any instant of time the output current signals from a PID controller can be expressed as

$$i_1(t) = I_{-npe}e^{-nj\omega_e t} + \cdots + I_{-1pe}e^{-j\omega_e t} + I_{-1pg}e^{-j\omega_g t} + I_{0p}e^{0j\omega_p t} + I_{1pp}e^{j\omega_p t} + I_{1pe}e^{j\omega_e t} + \cdots + I_{npe}e^{nj\omega_e t} \tag{2.31}$$

$$i_2(t) = I_{-nge}e^{-nj\omega_e t} + \cdots + I_{-1ge}e^{-j\omega_e t} + I_{-1gg}e^{-j\omega_g t} + I_{g0}e^{0j\omega_g t} + I_{1gp}e^{j\omega_p t} + I_{1ge}e^{j\omega_e t} + \cdots + I_{nge}e^{nj\omega_e t} \tag{2.32}$$

where, $I_{1pp}, I_{-1pg}, \sum_{i=-n}^{i=n} I_{ipe}$ and $I_{1gp}, I_{-1gg}, \sum_{i=-n}^{i=n} I_{ige}$ represent the complex frequency domain current responses under the effect of ω_p, ω_g and ω_e on the on both input and output shafts, and I_{0p} and I_{0g} represent the control current responses in complex form for the static deflection in the pinion and gear shafts, respectively.

From eqns. (2.29) to (2.32), upon differentiating the assumed solution $R_{ipL}(t)$ and $R_{igL}(t)$, with subscript L belonging to p, g and e depending upon the excitation frequencies ω_p, ω_g and ω_e, respectively, taken at a time yields

$$\dot{R}_{ipL}(t)=\mathrm{j}i\omega_L R_{ipL}(\omega_L)e^{\mathrm{j}i\omega_L t},\quad \ddot{R}_{ipL}(t)=-i^2\omega_L^2 R_{ipL}(\omega_L)e^{\mathrm{j}i\omega_L t}$$

$$\dot{R}_{igL}(t)=\mathrm{j}i\omega_L R_{igL}(\omega_L)e^{\mathrm{j}i\omega_L t},\quad \ddot{R}_{igL}(t)=-i^2\omega_L^2 R_{igL}(\omega_L)e^{\mathrm{j}i\omega_L t} \tag{2.33}$$

Noting eqns. (2.29) through (2.33) and substituting in eqns. (2.27) and (2.28), the time domain equations can further be converted into multi-harmonic frequency domain equations as follows

(a) Input shaft equation:

$$\begin{aligned}
&m_1\left\{-i^2\omega_L^2 R_{ipL}(\omega_L)e^{\mathrm{j}i\omega_L t}\right\}+\left(c_p+c_m\right)\left\{\mathrm{j}i\omega_L R_{ipL}(\omega_L)e^{\mathrm{j}i\omega_L t}\right\}-c_m\left\{\mathrm{j}i\omega_L R_{igL}(\omega_L)e^{\mathrm{j}i\omega_L t}\right\}+\\
&\left(k_p+k_m-k_s\right)\left\{R_{ipL}(\omega_L)e^{\mathrm{j}i\omega_L t}\right\}-k_m\left\{R_{igL}(\omega_L)e^{\mathrm{j}i\omega_L t}\right\}=\begin{Bmatrix}\left(m_1e_p\omega_p^2-k_pe_p-k_me_p\right)\\-\mathrm{j}\left(c_p+c_m\right)e_p\omega_p\end{Bmatrix}e^{\mathrm{j}(\omega_p t+\phi_p)}\\
&+\left(k_me_g-\mathrm{j}c_me_g\omega_g\right)e^{\mathrm{j}(-\omega_g t+\phi_g)}+k_m\left\{e_me^{\mathrm{j}\phi_m}+\sum_{i=-n}^{n}\left(e_{fi}e^{\mathrm{j}i(\omega_e t+\phi_{fi})}\right)\right\}+c_m\left\{\mathrm{j}\sum_{i=-n}^{n}\left(i\omega_e e_{fi}e^{\mathrm{j}i(\omega_e t+\phi_{fi})}\right)\right\}-k_Ii_1
\end{aligned} \tag{2.34}$$

(b) Output shaft equation:

$$\begin{aligned}
&m_2\left\{-i^2\omega_L^2 R_{igL}(\omega_L)e^{\mathrm{j}i\omega_L t}\right\}+\left(c_g+c_m\right)\left\{\mathrm{j}i\omega_L R_{igL}(\omega_L)e^{\mathrm{j}i\omega_L t}\right\}-c_m\left\{\mathrm{j}i\omega_L R_{ipL}(\omega_L)e^{\mathrm{j}i\omega_L t}\right\}+\\
&\left(k_g+k_m-k_s\right)\left\{R_{igL}(\omega_L)e^{\mathrm{j}i\omega_L t}\right\}-k_m\left\{R_{ipL}(\omega_L)e^{\mathrm{j}i\omega_L t}\right\}=\begin{Bmatrix}\left(m_2e_g\omega_g^2-k_ge_g-k_me_g\right)\\+\mathrm{j}\left(c_g+c_m\right)e_g\omega_g\end{Bmatrix}e^{\mathrm{j}(-\omega_g t+\phi_g)}\\
&+\left(k_me_p+\mathrm{j}c_me_p\omega_p\right)e^{\mathrm{j}(\omega_p t+\phi_p)}-k_m\left\{e_me^{\mathrm{j}\phi_m}+\sum_{i=-n}^{n}\left(e_{fi}e^{\mathrm{j}i(\omega_e t+\phi_{fi})}\right)\right\}-c_m\left\{\mathrm{j}\sum_{i=-n}^{n}\left(i\omega_e e_{fi}e^{\mathrm{j}i(\omega_e t+\phi_{fi})}\right)\right\}-k_Ii_2
\end{aligned} \tag{2.35}$$

The frequency domain EOM are further expanded and arranged suitably to obtain the regression equations. After expanding and separating the equations based on different forcing frequency components, the so obtained complex regression equations are as follows:

(a) Considering equation (2.34) for input shaft:

Case I. On extracting terms for $i=0$, equation representing the static deflection of the input shaft

$$\left(k_p+k_m-k_s\right)\left(R_{0p}e^{0\mathrm{j}\omega_p t}\right)-k_m\left(R_{0g}e^{0\mathrm{j}\omega_p t}\right)=-k_I\left(I_{0p}e^{0\mathrm{j}\omega_p t}\right) \tag{2.36}$$

Case II. When $i=1$, excitation frequency $\omega_L=\omega_p$ represents the forward whirl of the input shaft since pinion is rotating in the anticlockwise direction.

$$\begin{aligned}&m_1\left(-\omega_p^2R_{1pp}e^{\mathrm{j}\omega_p t}\right)+\left(c_p+c_m\right)\left(\mathrm{j}\omega_pR_{1pp}e^{\mathrm{j}\omega_p t}\right)-c_m\left(\mathrm{j}\omega_pR_{1gp}e^{\mathrm{j}\omega_p t}\right)-k_m\left(R_{1gp}e^{\mathrm{j}\omega_p t}\right)\\&+\left(k_p+k_m-k_s\right)\left(R_{1pp}e^{\mathrm{j}\omega_p t}\right)=\left(m_1e_p\omega_p^2-k_pe_p-k_me_p\right)e^{\mathrm{j}(\omega_p t+\phi_p)}-\mathrm{j}\left(c_p+c_m\right)e_p\omega_pe^{\mathrm{j}(\omega_p t+\phi_p)}-k_I\left(I_{1pp}e^{\mathrm{j}(\omega_p t)}\right)\end{aligned} \tag{2.37}$$

Case III. When $i=-1$, excitation frequency $\omega_L=\omega_g$ represents backward whirl in input shaft

$$\begin{aligned}&m_1\left(-\omega_g^2R_{-1pg}e^{-\mathrm{j}\omega_g t}\right)+\left(c_p+c_m\right)\left(-\mathrm{j}\omega_gR_{-1pg}e^{-\mathrm{j}\omega_g t}\right)-c_m\left(-\mathrm{j}\omega_gR_{-1gg}e^{-\mathrm{j}\omega_g t}\right)-k_m\left(R_{-1gg}e^{-\mathrm{j}\omega_g t}\right)\\&+\left(k_p+k_m-k_s\right)\left(R_{-1pg}e^{-\mathrm{j}\omega_g t}\right)=\left(k_me_g-\mathrm{j}c_me_g\omega_g\right)e^{\mathrm{j}(-\omega_g t+\phi_g)}-k_I\left(I_{-1pg}e^{\mathrm{j}(-\omega_g t)}\right)\end{aligned} \tag{2.38}$$

Case IV. When $i=-n,\ldots,-1,0,1,\ldots,n$, excitation frequency $\omega_L=\omega_e$, i.e. represents both forward and backward whirls in the input shaft can be taken up to n^{th} harmonics of the gear mesh frequency in this work.

$$\begin{aligned}&m_1\left(-i^2\omega_e^2R_{ipe}e^{\mathrm{j}i\omega_e t}\right)+\left(c_p+c_m\right)\left(\mathrm{j}i\omega_eR_{ipe}e^{\mathrm{j}i\omega_e t}\right)-c_m\left(\mathrm{j}i\omega_eR_{ige}e^{\mathrm{j}i\omega_e t}\right)+\left(k_p+k_m-k_s\right)\left(R_{ipe}e^{\mathrm{j}i\omega_e t}\right)\\&-k_m\left(R_{ige}e^{\mathrm{j}i\omega_e t}\right)=k_m\left[e_me^{\mathrm{j}\phi_m}+\sum_{i=-n}^{n}\left(e_{fi}e^{\mathrm{j}i(\omega_e t+\phi_{fi})}\right)\right]+c_m\left\{\mathrm{j}\sum_{i=-n}^{n}\left(i\omega_ee_{fi}e^{\mathrm{j}i(\omega_e t+\phi_{fi})}\right)\right\}-k_I\left(I_{ipe}e^{\mathrm{j}i\omega_e t}\right)\end{aligned} \tag{2.39}$$

(b) Considering equation (2.35) for output shaft:

Case I. Similarly, extracting the terms for $i=0$ represents the static deflection of the output shaft

$$\left(k_g + k_m - k_s\right)\left(R_{0g}e^{0\,\mathrm{j}\omega_g t}\right) - k_m\left(R_{0p}e^{0\,\mathrm{j}\omega_g t}\right) = -k_I\left(I_{0g}e^{0\,\mathrm{j}\omega_g t}\right) \tag{2.40}$$

Case II. For $i=1$, excitation frequency $\omega_L = \omega_p$, represents the backward whirl of the output shaft since the gear has clockwise rotation direction.

$$\begin{aligned} &m_2\left(-\omega_p^2 R_{1gp}e^{\mathrm{j}\omega_p t}\right) + \left(c_g + c_m\right)\left(\mathrm{j}\omega_p R_{1gp}e^{\mathrm{j}\omega_p t}\right) - c_m\left(\mathrm{j}\omega_p R_{1pp}e^{\mathrm{j}\omega_p t}\right) - k_m\left(R_{1pp}e^{\mathrm{j}\omega_p t}\right) \\ &\left(k_g + k_m - k_s\right)\left(R_{1gp}e^{\mathrm{j}\omega_p t}\right) = \left(k_m e_p + \mathrm{j}c_m e_p \omega_p\right)e^{\mathrm{j}(\omega_p t + \phi_p)} - k_I\left(I_{1gp}e^{\mathrm{j}\omega_p t}\right) \end{aligned} \tag{2.41}$$

Case III. When $i=-1$, excitation frequency $\omega_L = \omega_g$, represents the forward whirl of the output shaft

$$\begin{aligned} &m_2\left(-\omega_g^2 R_{-1gg}e^{-\mathrm{j}\omega_g t}\right) + \left(c_g + c_m\right)\left(-\mathrm{j}\omega_g R_{-1gg}e^{-\mathrm{j}\omega_g t}\right) - c_m\left(-\mathrm{j}\omega_g R_{-1pg}e^{-\mathrm{j}\omega_g t}\right) - k_m\left(R_{-1pg}e^{-\mathrm{j}\omega_g t}\right) \\ &+\left(k_g + k_m - k_s\right)\left(R_{-1gg}e^{-\mathrm{j}\omega_g t}\right) = \left\{\left(m_2 e_g \omega_g^2 - k_g e_g - k_m e_g\right) + \mathrm{j}\left(c_g + c_m\right)e_g\omega_g\right\}e^{\mathrm{j}(-\omega_g t + \phi_g)} - k_I\left(I_{-1gg}e^{-\mathrm{j}\omega_g t}\right) \end{aligned} \tag{2.42}$$

Case IV. When, $i=-n,\ldots,-1,0,1,\ldots,n$, excitation frequency $\omega_L = \omega_e$ represents both forward and backward whirls of the output shaft can be taken up to n^{th} harmonics of gear mesh frequency in this work.

$$\begin{aligned} &m_2\left(-i^2\omega_e^2 R_{ige}e^{\mathrm{j}i\omega_e t}\right) + \left(c_g + c_m\right)\left(\mathrm{j}i\omega_e R_{ige}e^{\mathrm{j}i\omega_e t}\right) - c_m\left(\mathrm{j}i\omega_e R_{ipe}e^{\mathrm{j}i\omega_e t}\right) + \left(k_g + k_m - k_s\right)\left(R_{ige}e^{\mathrm{j}i\omega_e t}\right) \\ &-k_m\left(R_{ipe}e^{\mathrm{j}i\omega_e t}\right) = -k_m\left[e_m e^{\mathrm{j}\phi_m} + \sum_{i=-n}^{n}\left(e_{fi}e^{\mathrm{j}i(\omega_e t + \phi_{fi})}\right)\right] - c_m\left\{\mathrm{j}\sum_{i=-n}^{n}\left(i\omega_e e_{fi}e^{\mathrm{j}i(\omega_e t + \phi_{fi})}\right)\right\} - k_I\left(I_{ige}e^{\mathrm{j}i\omega_e t}\right) \end{aligned} \tag{2.43}$$

2.3.2 Formulation of Identification Matrix

For the identification of parameters of the geared-rotor-AMB system, the complex regression equations are so arranged that the known and unknowns are separated and kept on either side of equality. Both left and right sides of the equations contain multi-harmonic components ranging in $i=-n,\ldots,-1,0,1,\ldots,n$. The complex responses $\boldsymbol{R}_{ipL}, \boldsymbol{R}_{igL}$ and complex AMB currents $\boldsymbol{I}_{ipL}, \boldsymbol{I}_{igL}$ for i^{th} harmonic can be written in the form

$$R_{ipL} = R_{ipL,Re} + \mathrm{j}R_{ipL,Im}, \quad R_{igL} = R_{igL,Re} + \mathrm{j}R_{igL,Im}$$

and $$I_{ipL} = I_{ipL,Re} + \mathrm{j} I_{ipL,Im},\ \ I_{igL} = I_{igL,Re} + \mathrm{j} I_{igL,Im} \tag{2.44}$$

Equations (2.36) through (2.43) are converted into real regression equations considering the eqn. (2.44), by segregating the real and imaginary parts (refer **Appendix A1**). Thereafter, the equations are rearranged suitably according to the forward whirl and backward whirl frequency components that leads to 52 numbers of equation on considering $n=5$, and expressed in a standard matrix form as

$$\mathbf{Ax = b} \tag{2.45}$$

here, $\mathbf{x}$ denotes the unknown column vector, $\mathbf{b}$ the known matrix and $\mathbf{A}$ the regressor, are provided in **Appendix B1**. There are 38 unknown parameters in eqn. (2.46), which are to be estimated from the real regression equations (refer **Appendix A1**)

$$\{\mathbf{x}\}_{38\times 1} = \begin{bmatrix} k_m & c_m & k_m e_p \cos\phi_p & k_m e_p \sin\phi_p & k_m e_g \cos\phi_g & k_m e_g \sin\phi_g & c_m e_p \cos\phi_p & c_m e_p \sin\phi_p \\ c_m e_g \cos\phi_g & c_m e_g \sin\phi_g & e_p \cos\phi_p & e_p \sin\phi_p & e_g \cos\phi_g & e_g \sin\phi_g & k_s & k_I & k_m e_m \cos\phi_m \\ k_m e_m \sin\phi_m & k_m e_{f1} \cos\phi_{f1} & k_m e_{f2} \cos\phi_{f2} & k_m e_{f3} \cos\phi_{f3} & k_m e_{f4} \cos\phi_{f4} & k_m e_{f5} \cos\phi_{f5} & & \\ k_m e_{f1} \sin\phi_{f1} & k_m e_{f2} \sin\phi_{f2} & k_m e_{f3} \sin\phi_{f3} & k_m e_{f4} \cos\phi_{f4} & k_m e_{f5} \cos\phi_{f5} & c_m e_{f1} \cos\phi_{f1} & & \\ c_m e_{f2} \cos\phi_{f2} & c_m e_{f3} \cos\phi_{f3} & c_m e_{f4} \cos\phi_{f4} & c_m e_{f5} \cos\phi_{f5} & c_m e_{f1} \sin\phi_{f1} & c_m e_{f2} \sin\phi_{f2} & & \\ c_m e_{f3} \sin\phi_{f3} & c_m e_{f4} \sin\phi_{f4} & c_m e_{f5} \sin\phi_{f5} & & & & & \end{bmatrix}^T \tag{2.46}$$

It should be noted that some of system unknown parameters are in multiplicative form i.e., in multiples of two or more unknown parameters. The parameters so obtained from eqn. (2.46) are further combined to determine the desired independent 20 identifiable system parameters, i.e. the gear mesh stiffness, gear mesh damping, eccentricity in input, output gear with respective unbalance phase, AMB displacement stiffness factor, AMB current stiffness factor, magnitude and phase of mean transmission error, magnitude and phase of variable transmission error corresponding to their respective harmonics (considering $n=5$) and is given in eqn. (2.47), as

$$\begin{bmatrix} k_m & c_m & e_p & \phi_p & e_g & \phi_g & k_s & k_I & e_m & \phi_m & e_{f1} & e_{f2} & e_{f3} & e_{f4} & e_{f5} & \phi_{f1} & \phi_{f2} & \phi_{f3} & \phi_{f4} & \phi_{f5} \end{bmatrix}^T \tag{2.47}$$

The identifiable parameters are solved by using least-square regression method and is given by expression

$$\mathbf{x} = \left(\mathbf{A}^{\mathrm{T}}\mathbf{A}\right)^{-1}\mathbf{A}^{\mathrm{T}}\mathbf{b} \tag{2.48}$$

The condition of the matrix is improved if the identification is done with combined spin speeds taking cumulative data over N range of speeds with subscript L belonging to p, g and e depending upon the excitation frequencies ω_p, ω_g and ω_e, respectively, taken one at a time and is given by the expression

$$\begin{Bmatrix} \mathbf{A}(\omega_{1_L}) \\ \mathbf{A}(\omega_{2_L}) \\ \vdots \\ \mathbf{A}(\omega_{N_L}) \end{Bmatrix} \mathbf{x} = \begin{Bmatrix} \mathbf{b}(\omega_{1_L}) \\ \mathbf{b}(\omega_{2_L}) \\ \vdots \\ \mathbf{b}(\omega_{N_L}) \end{Bmatrix} \tag{2.49}$$

The identification algorithm developed in this section is numerically simulated and the results obtained on the estimation of parameters given by 20 identifiable system parameters (eqn. 2.47) is presented in the next section.

2.4 Numerical Analysis of Geared Rotor AMB System

This section creates, analyses and implements the algorithm for solving numerically the identification problem. Initially the system's time domain response from EOM given by eqn. (2.21) is obtained by using Simulink block in MATLAB™ environment as shown in Fig. 2.6. The 'clock' time, and the pinion and gear spin speeds are the input to run the geared-rotor-AMB Simulink model. The sub blocks, i.e. 'transmission error', 'mesh dynamic force', 'unbalance force' and 'gear runout' are the excitation forces, which give the displacement responses from the geared-rotor-AMB system. The displacement reference signal is set to zero at the nominal position. The vibration signals are directed to the PID controller, where it is processed and the output current signals are sent to the actuator, which generates the electromagnetic force of the same frequency as that of the excitation frequency.

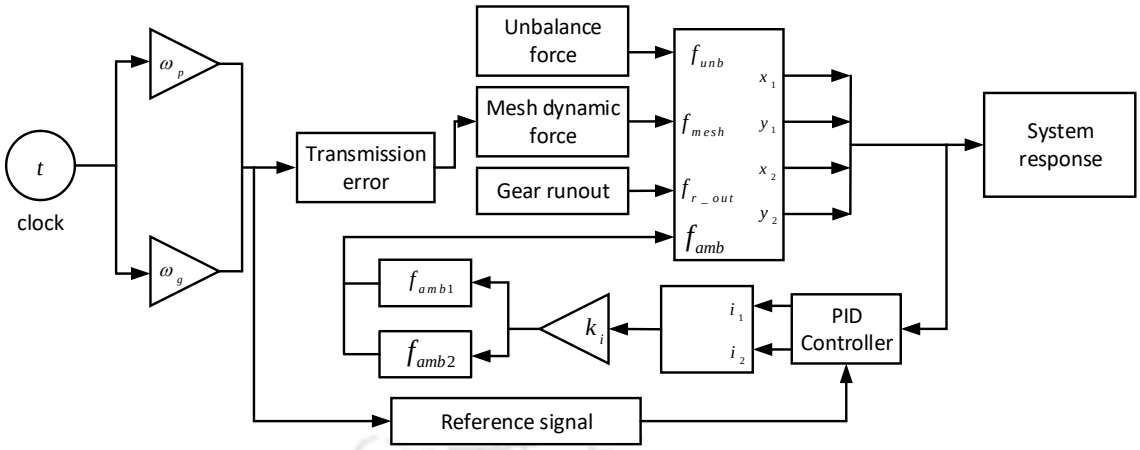

Figure 2.6 Simulink block of the proposed geared rotor AMB model

The parameters taken for the design of AMB actuator is shown in Table 2.1. The dimensions of the actuator are based on design criteria, like the maximum load capacity, air gap and number of poles. The assumed physical geared rotor parameters used in simulation have been summarized in Table 2.2

Table 2.1

Assumed parameters for AMB actuator

Parameters	Values	Units
i_0	2-4	A
s_0	0.4-0.8	mm
μ_o	$4\pi\times10^{-7}$	W/Am
α	22.5	deg.
N	100	-
A_a	300	mm^2
k_s	217573	N/m
k_I	43.5	N/A

Table 2.2

Gear physical parameters assumed for numerical simulation

Parameters	Assumed values
Diameter of input and output shaft	0.012 m
Span of input and output shaft	0.6 m
Module	2
Gear ratio	2
Pressure angle (FDI)	20 deg.
Number of teeth (pinion)	28
Number of teeth (gear)	56
Shaft density	7860 kg/m^3
Damping ratio	0.01
Young's modulus	2.068×10^{11} Pa
m_1, m_2	2.88 kg, 3.38 kg
ω_p, ω_g	30:2:38 Hz, 15:1:19 Hz
e_p, e_g	0.0003 m, 0.0004 m
c_p, c_g	49.63 N-s/m, 69.5 N-s/m
c_m	250 N-s/m
k_m	45.0257×10^6 N/m
k_p, k_g	4.25×10^5 N/m, 6.62×10^5 N/m
ω_e	750:50:950 Hz
ϕ_p, ϕ_g	1.078 rad, 1.598 rad.
e_m	31 nm
ϕ_m	0.5236 rad.
e_{fi}	30 nm, 25 nm, 35 nm, 11 nm, 12 nm
ϕ_{fi}	0.9471 rad, 0.5640 rad, 0.3283 rad, 0.3654 rad, 0.3954 rad.

Since two AMBs are mounted near the input and output gears so the PID controllers working on differential driving mode has been used. The control parameter has to be chosen suitably to make the geared rotor-AMB system stable, which is stated in next subsection. The PID controller gains are tuned suitably followed by the Nyquist stability criteria, which is listed in Table 2.3 to provide the necessary control current to the AMB actuators, such that the vibration levels of the system are minimised.

Table 2.3

Tuning of PID controller gains

	Gains	Values	Units
AMB 1	K_p	7000	A/m
	K_D	9	As/m
	K_I	4000	A/m-s
AMB 2	K_p	6000	A/m
	K_D	8	As/m
	K_I	4000	A/m-s

2.4.1 Stability Analysis using Nyquist Criterion

The Nyquist stability criterion can be used to determine the stability of linear time-invariant dynamical systems from its open-loop frequency response and open-loop poles (Tiwari, 2017). The closed-loop geared rotor-AMB system with the sensor in the feedback loop is shown in Fig. 2.7, where x gives the displacement of rotor from the centre position, which is an output of the closed loop system. The control system containing transfer function, $G_{CBA}(s)$, for geared-rotor-AMB system and the transfer function, $G_{sn}(s)$, for sensor gain are connected in parallel.

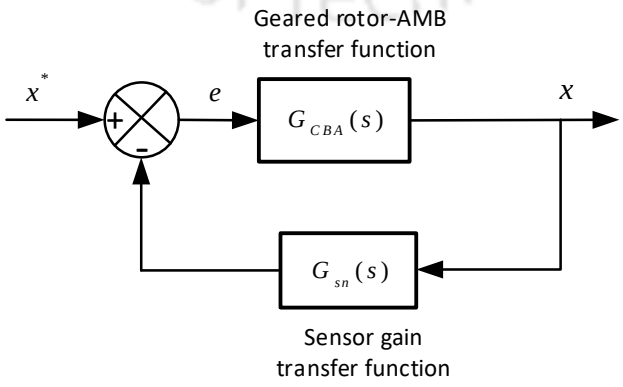

Figure 2.7 Closed loop feedback system of geared rotor with AMB

The characteristic equation of the system considering input and output rotational motion is obtained by equating the denominator of the transfer function from equation (C1.5) given in **Appendix C** to zero, as

$$m_1 s^3 + \left(c_p + c_m + K_D k_I k_A k_{sn}\right)s^2 + \left(k_p + k_m + k_s + K_p k_I k_A k_{sn}\right)s + K_I k_I k_A k_{sn} = 0 \tag{2.50}$$

and

$$m_2 s^3 + \left(c_g + c_m + K_D k_I k_A k_{sn}\right)s^2 + \left(k_g + k_m + k_s + K_p k_I k_A k_{sn}\right)s + K_I k_I k_A k_{sn} = 0 \tag{2.51}$$

The stability criterion can be expressed as

$$Z = N + P \tag{2.52}$$

where Z is the number of zeros of $1 + G_{CBA}(s)G_{sn}(s)$ in the right half s-plane, N is the number of clockwise encirclements of the $(-1 + \mathrm{j}\,0)$ point and P is the number of poles of $G_{CBA}(s)G_{sn}(s)$ in the right half s-plane.

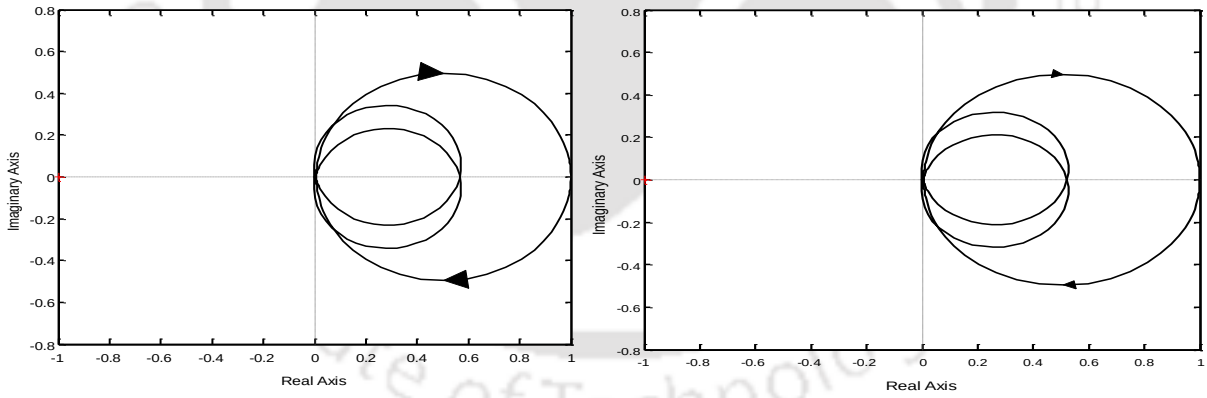

(a) (b)

Figure 2.8 Nyquist plot of (a) Input shaft (b) Output shaft

As per the Nyquist plot shown in Fig.2.8 (a) and (b), there is no loop which encircles the critical point $(-1 + \mathrm{j}0)$, hence $N = 0$. By using the assumed system parameters listed in Table 2.1-2.3, it was found that all the roots of characteristic equation as per eqn. (2.44) and (2.45) have negative real parts so, $P = 0$ (i.e., open loop stable system). Therefore, from the Nyquist stability criteria, $Z = 0$, i.e., no roots on right-hand side of s-plane. This ensures that the

proposed geared rotor system is stable with the chosen PID controller parameters during operation.

2.4.2 Time Domain Response

The time domain response from the EOMs (2.21) and (2.22) are solved by fourth-order Runge-Kutta method. The simulation is run for a duration of 7 sec. and the solution is obtained taking a time step of 0.00006 s. To obtain the steady state response and avoid the effect of transient response, the generated signals are considered from 6-7 s. The transverse vibration of geared rotor is controlled predominantly by radial forces generated by the AMB actuator; hence the rotor lateral displacement is suppressed effectively. This can be observed from the time domain responses. Orbit plots are obtained from time domain responses and a comparison is made to illustrate the rotor whirling behaviour in both geared shafts considering the transverse vibration with and without the application of AMB, and is shown in Fig. 2.9. The response clearly indicates the combined rotor transverse displacement characteristics in perpendicular directions and the kind of controlled motion with the help of AMB.

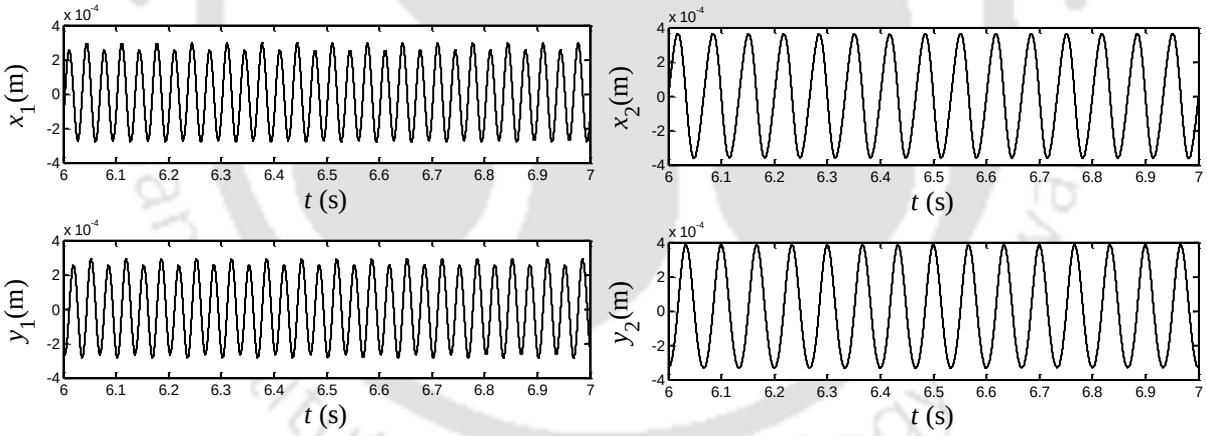

(a) (b)

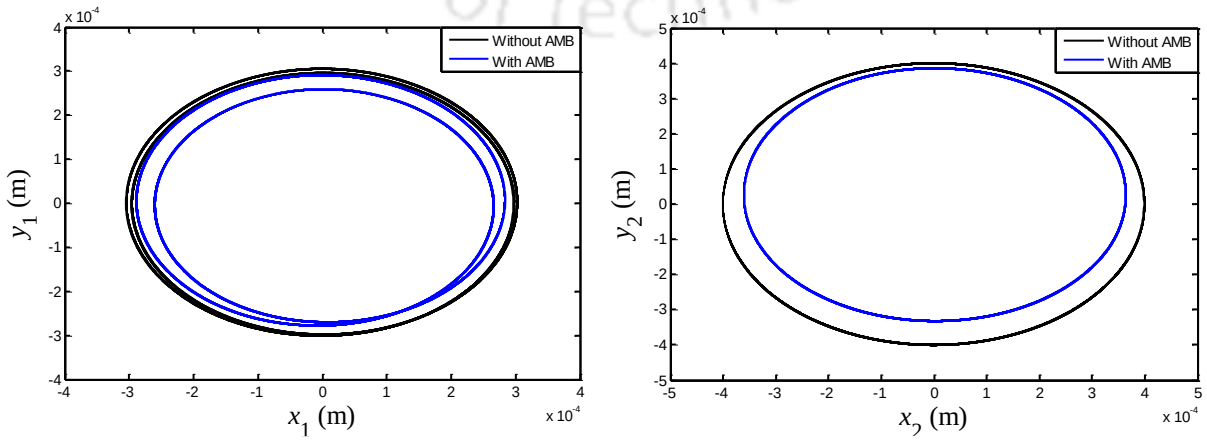

(c) (d)

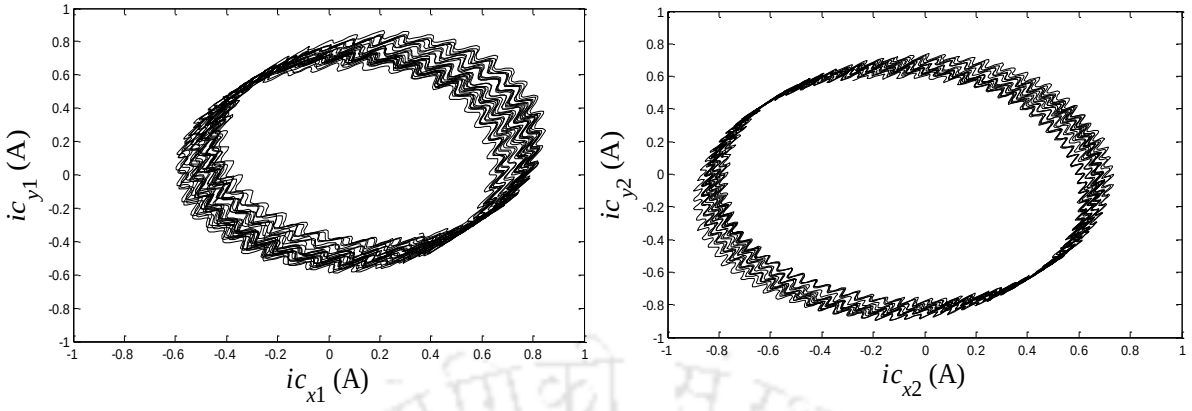

(e) (f)

Figure 2.9 Time domain response at $\omega_p = 30\text{Hz}$, $\omega_g = 15\text{Hz}$, $\omega_e = 750\text{Hz}$ in the x and y directions (a) displacement of input geared shaft (b) displacement of output geared shaft (c) orbit plot of AMB controlled transverse vibration from input geared shaft (blue coloured) (d) orbit plot of AMB controlled transverse vibration from output geared shaft (blue coloured) (e) Orbit plot for AMB control current from input geared shaft (f) Orbit plot for AMB control current from output geared shaft.

2.4.3 Full Spectrum Response

Time domain solutions are further utilized to carry out the full spectrum analysis. The full spectrum is more complete in displaying the information contained in the frequency spectrum. The full spectrum plot is obtained by first coupling the orthogonal vibration displacement signals into a complex signal and then performing a Fourier transform. The complex data on Fourier transform gives information of both the forward and backward whirl frequencies. In this paper, the input geared shaft has an anticlockwise rotation and the output geared shaft has clockwise rotation. The full spectrum shows multiple harmonics of excitation frequencies, which is solely due to the gear meshing error causing the DTE. These can be observed from the displacement and current peaks of full spectrum plot as given in Fig. 2.10 and Fig. 2.11, respectively. The geared rotor has both forward and backward whirl frequency components due to asymmetric transmission error, where the harmonics of forward whirl excites the rotor in the same sense of rotation whereas the backward whirl harmonics excites the rotor in the reverse sense of rotation, simultaneously, with respect to the rotational direction of input shaft.

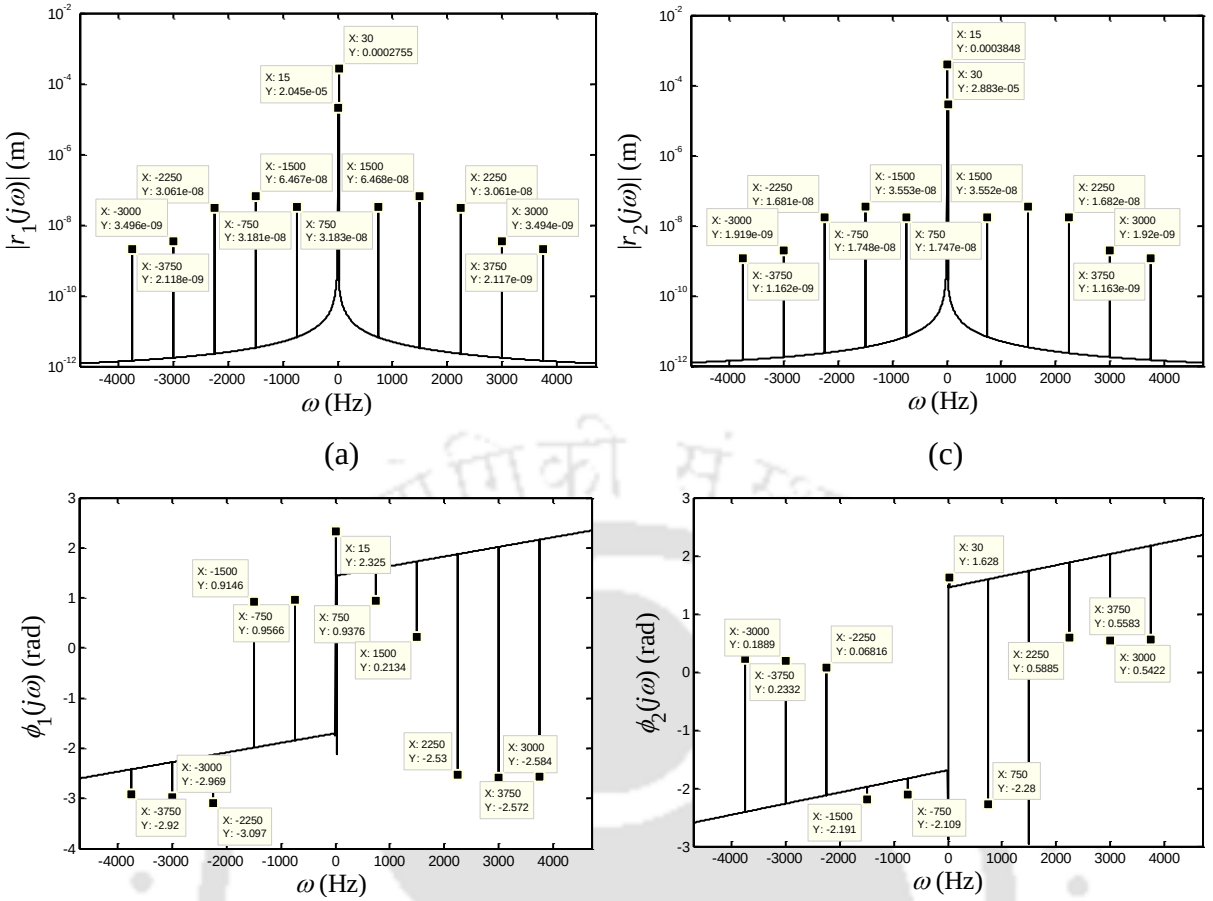

Figure 2.10 Full spectrum response generated at $\omega_p = 30\text{Hz}$, $\omega_g = 15\text{Hz}$, $\omega_e = 750\text{Hz}$ (a) Amplitude of complex translational displacement for input geared shaft (b) Phase of complex translational displacement for input geared shaft (c) Amplitude of complex translational displacement for output geared shaft (d) Phase of complex translational displacement for output geared shaft.

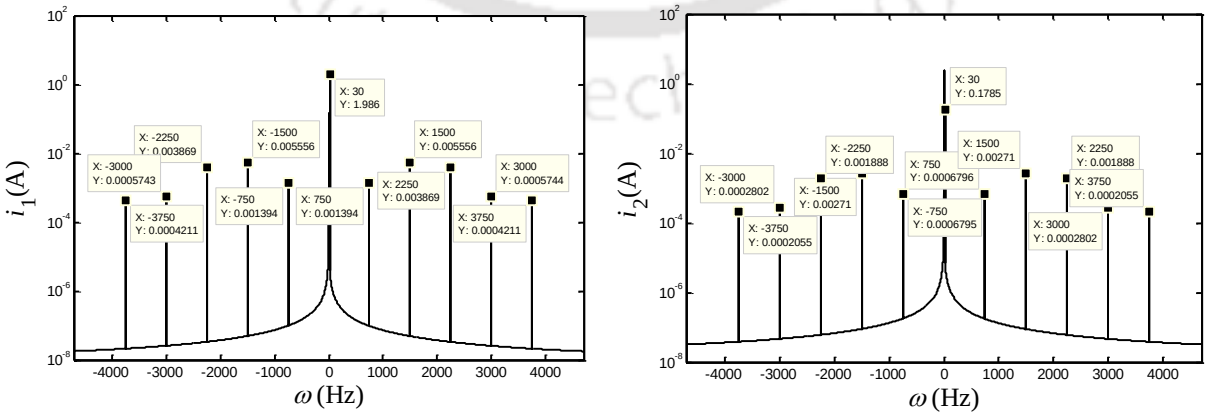

Figure 2.11. Full spectrum plot for AMB control current at $\omega_p = 30\text{Hz}$, $\omega_g = 15\text{Hz}$, $\omega_e = 750\text{Hz}$ (a) Amplitude of complex current for input geared shaft (b) Amplitude of complex current for output geared shaft

2.4.4 Estimation of Parameters with Addition of Noise and Modelling Error

The multi-harmonic magnitude and phase information from the full spectrum are used in the identification problem. The numerical responses generated from the full spectrum are fed into the identification algorithm (refer eqn. B1.1 to B1.3 given in **Appendix B1**). The rotor-AMB physical parameters are considered to be known listed in Tables 2.1, 2.2, 2.3. Initially, the 38 unknown parameter values in the multiplicative form, i.e., eqn. (2.46), are obtained from the identification algorithm. Thereafter, the estimation of 20 required independent parameters, i.e. equation (2.47), is performed by correlating the terms as

$$\text{Amplitude}= e_L = \sqrt{\text{Re}^2 + \text{Im}^2} = \sqrt{(e_L \cos\phi_L)^2 + (e_L \sin\phi_L)^2}\,; \tag{2.53}$$

$$\text{Phase}= \phi_L = \tan^{-1}\left(\frac{\text{Im}}{\text{Re}}\right) = \tan^{-1}\left(\frac{e_L \sin\phi_L}{e_L \cos\phi_L}\right) \tag{2.54}$$

where, subscript L depicts p, g, m, fi for determining the amplitude and phase information of the eccentricity, and the mean and fluctuating transmission error components present in the system.

Since external noises are always present in the real system responses while measuring the vibration signals. To obtain real measurement conditions and to ascertain robustness of the identification algorithm against instrument and measurement errors, random noise of 1%, 2% and 5% has been added to the generated response. Here, the Gaussian white noise is added to time domain signals during the numerical simulation. It is defined as a statistical noise that has its probability density function equal to that of the normal distribution. It is a random signal with a flat power spectral density, uncorrelated and normally distributed with a mean zero and unit variance. The noising response signal could be obtained as

$$r_{noise}(t) = r(t) + \left\{ r(t) \frac{(R_{and} - 0.5) N_p}{100} \right\} \tag{2.55}$$

Here, $r(t)$ is the vibrational displacement as in Eqn. (2.55), R_{and} is a random scalar value with mean 0 and standard deviation 1 and N_p is the noise %. Noisy response for AMB current is obtained similarly.

Also, it is inevitable that real system properties, like the mass, stiffness and damping may differ from the assumed values of the parameters, taken for the numerical analysis. So, in a similar way bias errors are added to check the sensitiveness of the algorithm. This is done by introducing the bias error in the density, length and Young's modulus of the system. The parameters so obtained from the developed algorithm after adding different noise level and modelling error is shown in Table 2.4 and Table 2.5, respectively. To get a better accuracy of the estimation a suitable range of multiple speeds, i.e., $\omega_p = 30 - 38$ Hz in step of 2 Hz, $\omega_g = 15 - 19$Hz in step of 1 Hz, and $\omega_e = 750 - 950$ Hz in step of 50 Hz are taken for the simulation.

Table 2.4

Identification of parameters with addition of noise at multiple spin speed

Parameters	**Assumed values**	**Estimated values with different percentage of noise**			
		0%	1%	2%	5%
c_m	250 Nsm^{-1}	265	270	227	282
k_m	45.2×10^6 Nm^{-1}	45.3×10^6	45.6×10^6	45.11×10^6	51.1×10^6
e_p	3×10^{-4} m	293.4×10^{-6}	298.6×10^{-6}	282.1×10^{-6}	273.9×10^{-6}
e_g	4×10^{-4} m	399.3×10^{-6}	397.4×10^{-6}	442.11×10^{-6}	413.91×10^{-6}
ϕ_p	1.078 rad	1.103	1.112	1.0971	1.082
ϕ_g	1.598 rad	1.607	1.623	1.606	1.602
k_s	217573 Nm^{-1}	242705	238629	200343	226793
k_I	43.5NA^{-1}	42.9	44.12	51	59
e_m	31 nm	30.9	31	32	35

ϕ_m	0.5236 rad	0.526	0.531	0.512	0.581
e_{f1}	30 nm	4.0	3.9	4.1	4.8
e_{f2}	25 nm	2.5	2.95	2.8	2.4
e_{f3}	35 nm	3.5	3.8	3.0	3.6
e_{f4}	11 nm	1.1	1.2	1.5	1.8
e_{f5}	12 nm	1.3	1.6	1.5	1.3
ϕ_{f1}	0.9471 rad	0.941	0.926	0.945	0.974
ϕ_{f2}	0.564 rad	0.564	0.583	0.636	0.789
ϕ_{f3}	0.3283 rad	0.329	0.333	0.383	0.423
ϕ_{f4}	0.3654 rad	0.365	0.377	0.354	0.531
ϕ_{f5}	0.3954 rad	0.395	0.356	0.426	0.309

Table 2.5

Identification of Parameters with addition of modelling error

Parameters	**Assumed values**	**Estimated values with different percentage of noise**			
		0%	1%	2%	5%
c_m	250 Nsm^{-1}	265	276	235	262
k_m	45.2×10^6 Nm^{-1}	45.3×10^6	45.5×10^6	44.6×10^6	47.1×10^6
e_p	3×10^{-4} m	293.4×10^{-6}	297.3×10^{-6}	292.5×10^{-6}	283.3×10^{-6}
e_g	4×10^{-4} m	399.3×10^{-6}	389.4×10^{-6}	420.11×10^{-6}	403.91×10^{-6}
ϕ_p	1.078 rad	1.103	1.056	1.107	1.092
ϕ_g	1.598 rad	1.607	1.577	1.602	1.709
k_s	217573 Nm^{-1}	242705	218629	230343	254838
k_I	43.5NA^{-1}	42.9	45.12	49.1	52.3

e_m	31 nm	30.9	32.1	30.8	35
ϕ_m	0.5236 rad	0.526	0.535	0.527	0.519
e_{f1}	30 nm	4.0	4.1	3.6	4.5
e_{f2}	25 nm	2.5	2.6	2.5	2.8
e_{f3}	35 nm	3.5	3.7	3.1	3.8
e_{f4}	11 nm	1.1	1.5	1.3	1.2
e_{f5}	12 nm	1.3	1.5	1.1	1.3
ϕ_{f1}	0.9471 rad	0.941	0.962	0.973	0.921
ϕ_{f2}	0.564 rad	0.564	0.535	0.536	0.689
ϕ_{f3}	0.3283 rad	0.329	0.312	0.353	0.377
ϕ_{f4}	0.3654 rad	0.365	0.386	0.384	0.431
ϕ_{f5}	0.3954 rad	0.395	0.369	0.326	0.409

It can be observed that all the estimated parameters are quite close to their assumed values at 0% noise level and modelling error. The range of spin speeds required for the identification algorithm should be chosen so as to have a well-conditioned matrix. Having used the cumulative data over a range of speeds can result in desirable effect on closeness of the estimated parameters. In this paper three spin speeds are taken at a time for the identification algorithm. With an increase in levels of noise in the vibration and current signals, the maximum deviation of estimated values increases by approximately 57% and with an addition of different amount of modelling error in system properties the estimated values get an approximate maximum deviation of 42% in the chosen speed range. At moderate speed, i.e. $\omega_p = 30-34$ Hz in step of 2 Hz, $\omega_g = 15-17$Hz in step of 1 Hz, and $\omega_e = 750-850$ Hz in step of 50 Hz, the equivalent mesh stiffness, the amplitude and phase of the mean transmission error, mesh damping, gear eccentricity with corresponding runout phase, suffers the least deviation whereas the value of pinion eccentricity and corresponding runout phase, amplitude and phase of varying transmission error has a moderate deviation. Of all the parameters, AMB displacement stiffness and current stiffness have comparatively higher deviation from the

assumed values. While the deviation of pinion eccentricity, runout phase and AMB parameters declines with an increase in rotor speed, i.e. $\omega_p = 34 - 38$ Hz in step of 2 Hz, $\omega_g = 17 - 19$Hz in step of 1 Hz, and $\omega_e = 850 - 950$ Hz in step of 50 Hz, however, the other gear parameter values, like the equivalent mesh stiffness, amplitude and phase of varying transmission error get affected. So, it is recommended to choose a suitable range of speeds for better approximation of various estimated parameters. Table 2.4 and Table 2.5 shows the closest approximate estimation obtained with different speed ranges. With an addition of 0%, 1%, 2% and 5% levels of noise in the response and current data and 0%, 1%, 2%, and 5% addition of modelling error in the system properties, a comparison is shown by representation of the trend of error percentage in estimated values from the assumed values in Fig. 2.12.

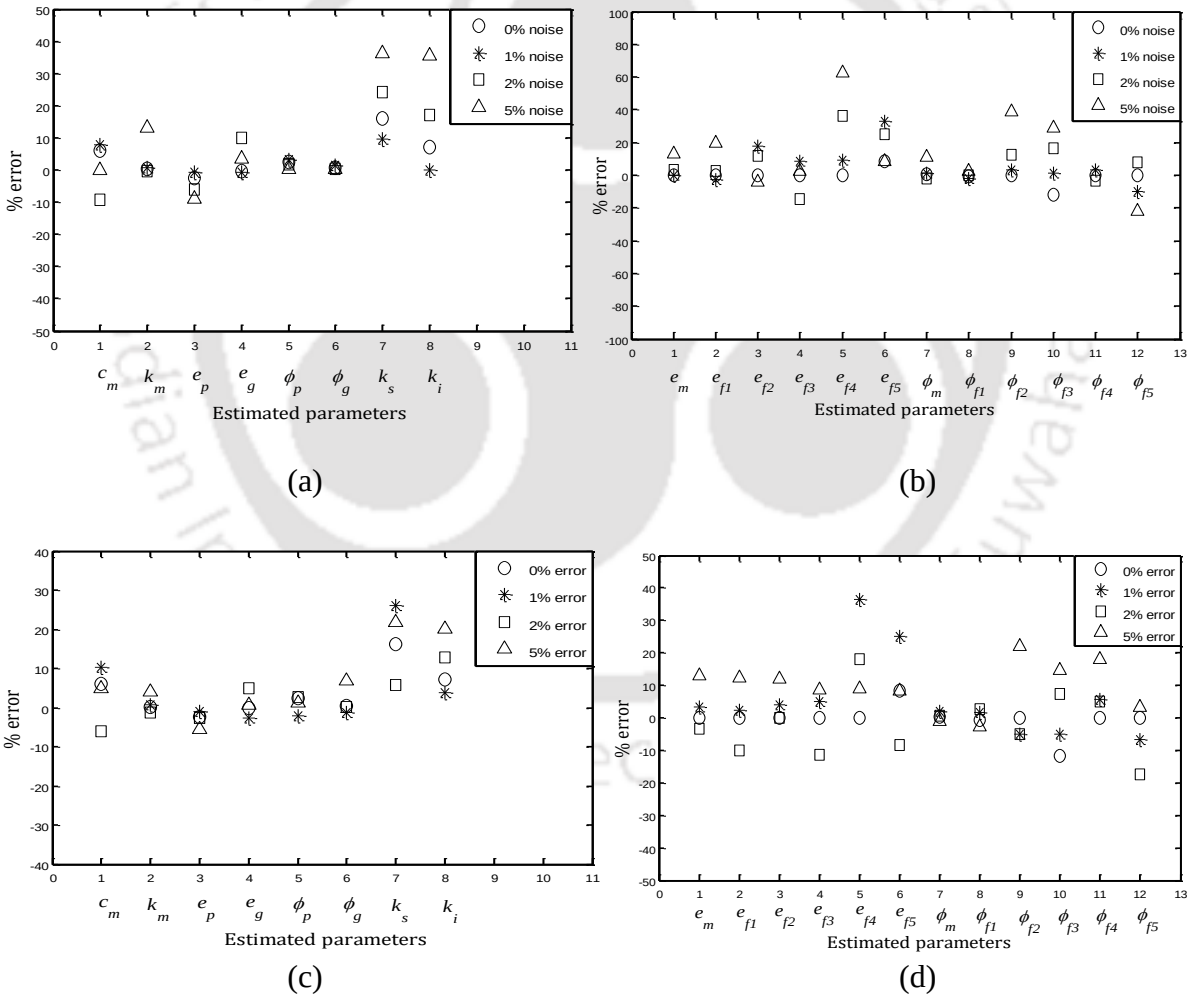

Figure 2.12. Error percentage in estimated rotor-AMB physical parameters and dynamic transmission error with respective phase angle taking (a)-(b) various levels of noise at multiple spin speed (c)-(d) various percentage of modelling error at multiple spin speed.

2.5 Conclusions

The transverse vibration analysis of a geared rotor system with gear run-out and asymmetric dynamic transmission error was done with help of lumped parameter model. The present case, a time varying mesh stiffness is considered in the form of transmission error for a single pair of teeth engagement. However, this model can be used to determine the DTE due to variable gear mesh stiffness for different combinations of teeth pairs. With the introduction of new novel concept of active vibration control by active magnetic bearings, the transverse vibrations in a spur gearbox was controlled quite effectively. The DTE is modeled as a periodic function in the form of asymmetric transmission error so full spectrum was chosen for spectrum analysis and determines multiple harmonics of gear meshing error. Generally, the transmission error is determined by knowing the output torque and input torque of the system, however, it is difficult to quantify the amount and position of the dynamic transmission error. A novel identification algorithm has been developed using regression equations from the mathematical model to quantify the system fault parameters, i.e. the gear mesh stiffness, gear mesh damping, runout of input gear and phase, runout of output gear and phase, AMB displacement stiffness constant, AMB current stiffness constant, mean transmission error and phase, variable transmission error corresponding to different harmonics and respective phase angles. This identification was done using responses from full spectrum since it gives information about both the positive and negative frequencies present in the spectrum. When the negative frequency is greater than their positive counterpart, the precession happens to be in the reverse direction. This can provide vital information in diagnosing a problem in real rotor systems. The estimated parameters were also tested with different random noise and modelling errors to check the robustness of the developed algorithm, which showed quite promising results.

Here, the analysis was limited having the rotor system with gears placed at mid-span of the shaft. In the next chapter the rotor analysis with gears placed away from the mid-span of the shaft will be discussed leading to gyroscopic effects. The identification algorithm will be developed and its sensitivity will be tested through numerical simulation.

CHAPTER 3 GYROSCOPIC EFFECT ON TRANSVERSE VIBRATION ANALYSIS OF GEARED ROTOR AMB SYSTEM

3.1 Introduction

The present chapter explores a rotor bearing system with an axially offset spur gear. The rotor configuration necessitates analysis with gyroscopic effects in 8-DOF model, which introduces additional complexity in the form of skew-symmetry in the gyroscopic matrix. To overcome this, dynamic condensation (Singh and Tiwari, 2015) has been applied to eliminate rotational DOFs from EOMs before developing the identification algorithm. The algorithm has been developed in frequency domain with the harmonics of vibration displacement and AMB current as described in Chapter 2 which is based on inverse problem approach and the parameters are obtained using the least-square estimation method. Numerical testing of the developed algorithm is performed with noise in responses and bias error in system parameters.

3.2 Proposed Geared-Rotor AMB Model with Offset Gears

This chapter also deals with spur involute gears that transmits motion between two parallel shafts since this type of drive dominates in the field of power transmission. Here, the geared rotor is assumed to have lateral movement, i.e., having displacements perpendicular to the gear axis due to bending of shafts with additional gyroscopic effect. A rotor system is shown in Fig. 3.1, where an axially offset spur gear pair is mounted on two elastic shafts supported by two mechanical bearings at ends. It should be observed that the whirling of shaft takes place due to runout of eccentric geared rotor. It would whirl at a frequency equal to the spin speed of the rotor (synchronous whirl) or at any other excitation frequency (forward or backward whirl) due to a variety of other faulty conditions. The deformation of the tooth is neglected except at the pitch point of the driving and driven gears. Considering rigid bearings, the bearing stiffness and damping is neglected and the model is assumed to have flexible shafts. The coupling between transverse and torsional vibration is ignored and only transverse vibration with gyroscopic effect is considered. As mentioned in Chapter 2, herein, *z*-axis is taken along the shaft centreline, and translational displacements of pinion and gear is defined along the *x* and *y* axes with appropriate subscripts**.**

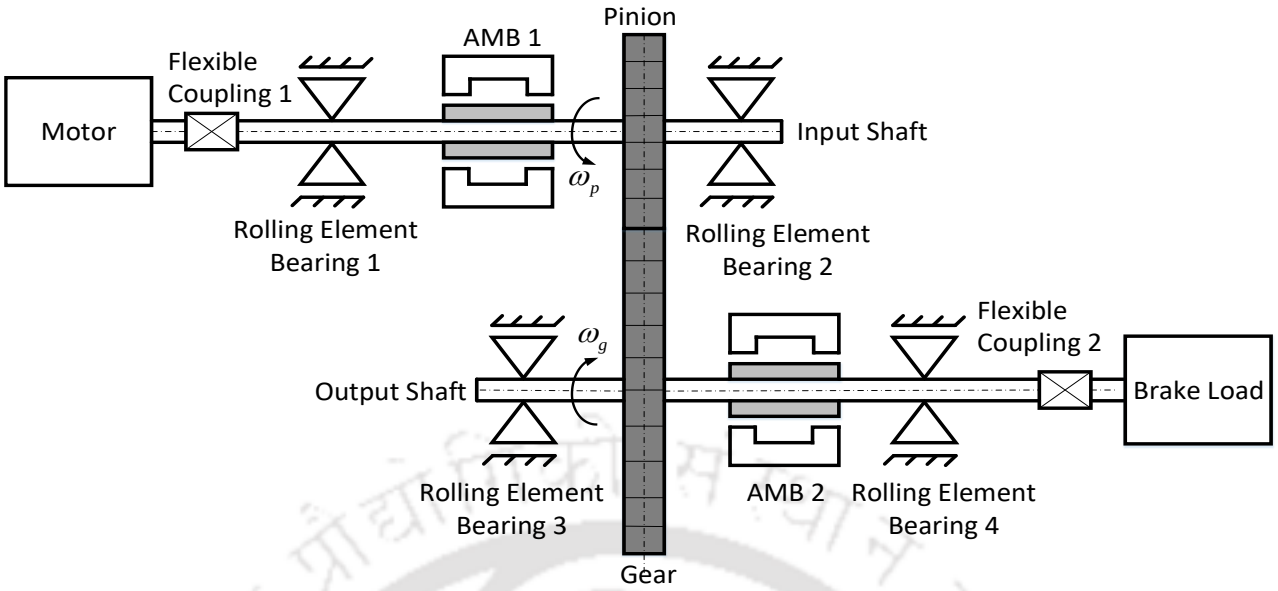

Figure 3.1 Proposed geared rotor-AMB system

As a result of assembling error, the gear eccentricity is added to the model, which contributes to the effect of runout and unbalance onto the gear transmission system. The motor drives the input gear and the load provides the brake torque to the driven gear. AMBs are placed near the input and output gears to control the vibratory motion. The AMB serves to perform as the condition monitoring device to characterise the faults as well as attenuate the vibration of the rotor system.

3.3 Mathematical Model of Offset Gear-pair

Considering an offset spur geared rotor spinning at a very high speed with I_{p_1} and I_{p_2} as input and output gear polar mass moments of inertia respectively then it has an angular momentum. Due to flexibility of the shafts, the rotor has precession (slow or fast) about its transverse (diametral) axes with I_{d_1} and I_{d_2} as diametral mass moments of inertia. As a result, it develops a change in angular momentum due to change in its direction. This leads to an inertia moment called the gyroscopic moment, which basically develops due to the Coriolis acceleration component. The geared rotor is assumed such that it is spinning and whirling about the *z*-axis in an inertial frame *x*-*y*-*z*, fixed in space with an angular velocity of precession equal to spinning velocity at an inclination/tilting angle φ_x in *y*-*z* plane and φ_y in *x*-*z* plane. As a result, there are four angular displacements due to tilting of the gears on shafts given by φ_{y_1} and φ_{x_1} in input gear and

φ_{y_2} and φ_{x_2} in output gear. It could be seen from Fig. 3.2 that the gyroscopic effect leads to coupling of motions in the *y*–*z* and *z*–*x* planes. Hence, for both the shafts *x* and *y* represent two orthogonal transverse displacements of the center of the gear disc/wheel and φ_y and φ_x represents the tilting (transverse rotational displacement) of the gear disc/wheel about the *x*- and *y*- axes. For the input shaft k_{pxx} and k_{pyy} are the lateral stiffness coefficients, $k_{px\varphi_y}, k_{p\varphi_y x}, k_{py\varphi_x}$ and $k_{p\varphi_x y}$ are cross-coupled stiffness coefficients, $k_{p\varphi_x\varphi_x}$ and $k_{p\varphi_y\varphi_y}$ are the transverse angular/rotational components of stiffness coefficients due to tilting of the pinion wheel. Similarly, for the output shaft k_{gxx} and k_{gyy} are the lateral stiffness coefficients, $k_{gx\varphi_y}, k_{g\varphi_y x}, k_{gy\varphi_x}$ and $k_{g\varphi_x y}$ are the cross-coupled stiffness coefficients and, $k_{g\varphi_x\varphi_x}$ and $k_{g\varphi_y\varphi_y}$ are the transverse angular/rotational components of stiffness coefficients due to tilting of the gear wheel.

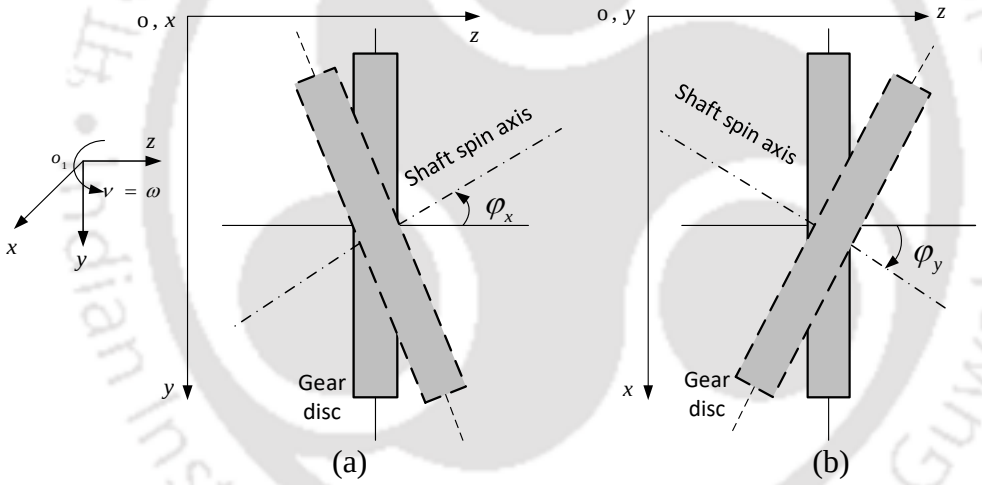

Figure 3.2 Coordinate axes and positive conventions for rotational displacements (a) tilting of shaft axis *y*-*z* plane (b) tilting of shaft axis *z*-*x* plane

This gyroscopic moment on the gears, depends upon the spin speed, the precession velocity, and polar mass moment of inertia of the geared rotor. In a similar way, while considering the damping for the input shaft, c_{pxx}, c_{pyy} $c_{px\varphi_y}, c_{p\varphi_y x}, c_{py\varphi_x}, c_{p\varphi_x y}$ $c_{p\varphi_x\varphi_x}$ and $c_{p\varphi_y\varphi_y}$ are the viscous damping coefficients and for the output shaft, c_{gxx}, c_{gyy} $c_{gx\varphi_y}, c_{g\varphi_y x}, c_{gy\varphi_x}, c_{g\varphi_x y}$ $c_{g\varphi_x\varphi_x}$ and $c_{g\varphi_y\varphi_y}$ are the viscous damping coefficients. The meshing of gear pair is shown in Fig. 2.2 in Chapter 2, accordingly the model has four translational displacements of the gear-shaft centres in the *x*

and y directions during the meshing of gears given by x_1, y_1, x_2 and y_2 and the lateral displacements of the runout pinion and gear wheel centres given by x_p, y_p, x_g and y_g, respectively. The tooth frictional effect on the shear stress, bending stress and transmission error in gear meshing is ignored. Maximum harmonics to be considered is represented by n with negative terms referring to backward whirls and positive terms to forward whirls. Due to meshing of two mating spur gear teeth, there is a combined effect of one pair of teeth meshing under loaded conditions. The modelling of the control forces acting upon the rotor by AMB actuator is given in earlier Chapter 2 in Section 2.2.3

3.4 Dynamic Equation of the Geared-shaft-AMB System with Gyroscopic Effect

An eight degrees-of-freedom lumped parameter model of spur gear rotor system has been developed with gyroscopic effect to carry out the transverse vibration analysis considering transmission errors, and gear runouts (runouts gives mass unbalances on shafts, and the elastic and damping forces at the pitch point) with AMB and equations of motions are derived. For that in inertial frame of reference, the energy equation of the geared-rotor with gyroscopic effect, i.e. the kinetic energy 'T' is expressed by

$$\begin{aligned} T = &\frac{1}{2}\left\{m_1\left(\dot{x}_p^2 + \dot{y}_p^2\right) + I_{d_1}(\dot{\varphi}_{x_1}^2 + \dot{\varphi}_{y_1}^2) + I_{p_1}\omega_p(\dot{\varphi}_{x_1}\varphi_{y_1} - \varphi_{x_1}\dot{\varphi}_{y_1}) + I_{p_1}\omega_p^2\right\} \\ &+\frac{1}{2}\left\{m_2\left(\dot{x}_g^2 + \dot{y}_g^2\right) + I_{d_2}(\dot{\varphi}_{x_2}^2 + \dot{\varphi}_{y_2}^2) + I_{p_2}\omega_g(\dot{\varphi}_{x_2}\varphi_{y_2} - \varphi_{x_2}\dot{\varphi}_{y_2}) + I_{p_2}\omega_g^2\right\} \end{aligned} \tag{3.1}$$

The gyroscopic term could also be written as (because for the conservation of angular momentum, we have $\frac{d}{dt}\left(\varphi_x\varphi_y\right) = 0$ or, $\left(\dot{\varphi}_x\varphi_y\right) = \left(-\varphi_x\dot{\varphi}_y\right)$), which implies

$$\begin{aligned} T = &\frac{1}{2}\left\{m_1\left(\dot{x}_p^2 + \dot{y}_p^2\right) + I_{d_1}(\dot{\varphi}_{x_1}^2 + \dot{\varphi}_{y_1}^2) + I_{p_1}\omega_p(2\dot{\varphi}_{x_1}\varphi_{y_1}) + I_{p_1}\omega_p^2\right\} \\ &+\frac{1}{2}\left\{m_2\left(\dot{x}_g^2 + \dot{y}_g^2\right) + I_{d_2}(\dot{\varphi}_{x_2}^2 + \dot{\varphi}_{y_2}^2) + I_{p_2}\omega_g(2\dot{\varphi}_{x_2}\varphi_{y_2}) + I_{p_2}\omega_g^2\right\} \end{aligned} \tag{3.2}$$

or,

$$T = \frac{1}{2}\left\{m_1\left(\dot{x}_p^2 + \dot{y}_p^2\right) + I_{d_1}(\dot{\varphi}_{x_1}^2 + \dot{\varphi}_{y_1}^2) - I_{p_1}\omega_p(\varphi_{x_1}\dot{\varphi}_{y_1}) + I_{p_1}\omega_p^2\right\}$$
$$+ \frac{1}{2}\left\{m_2\left(\dot{x}_g^2 + \dot{y}_g^2\right) + I_{d_2}(\dot{\varphi}_{x_2}^2 + \dot{\varphi}_{y_2}^2) - I_{p_2}\omega_g(\varphi_{x_2}\dot{\varphi}_{y_2}) + I_{p_2}\omega_g^2\right\} \quad (3.3)$$

The term for the potential energy '*U*' is given as

$$U = \frac{1}{2}\left\{k_{pxx}x_p^2 + k_{pyy}y_p^2 + k_{px\varphi_y}x_p\varphi_{y_1} + k_{p\varphi_y x}\varphi_{y_1}x_p + k_{py\varphi_x}y_p\varphi_{x_1} + k_{p\varphi_x y}\varphi_{x_1}y_p + k_{p\varphi_x\varphi_x}\varphi_{x_1}^2 + k_{p\varphi_y\varphi_y}\varphi_{y_1}^2\right\}$$
$$+ \frac{1}{2}\left\{k_{gxx}x_g^{\ 2} + k_{gyy}y_g^{\ 2} + k_{gx\varphi_y}x_g\varphi_{y_2} + k_{g\varphi_y x}\varphi_{y_2}x_g + k_{gy\varphi_x}y_g\varphi_{x_2} + k_{g\varphi_x y}\varphi_{x_2}y_g + k_{g\varphi_x\varphi_x}\varphi_{x_2}^2 + k_{g\varphi_y\varphi_y}\varphi_{y_2}^2\right\} \quad (3.4)$$
$$+ \frac{1}{2}\left\{k_m\left(\delta_x^{\ 2} + \delta_y^{\ 2}\right)\right\}$$

It is assumed that for input shaft

$$k_{pxx} = k_{pyy} = k_p\ ;\ k_{p\varphi_x\varphi_x} = k_{p\varphi_y\varphi_y}\ ;\ k_{px\varphi_y} = k_{py\varphi_x}\ ;\ k_{p\varphi_y x} = k_{p\varphi_x y} \quad (3.5)$$

Similarly, for the output shaft

$$k_{gxx} = k_{gyy} = k_g\ ;\ k_{g\varphi_x\varphi_x} = k_{g\varphi_y\varphi_y}\ ;\ k_{gx\varphi_y} = k_{gy\varphi_x}\ ;\ k_{g\varphi_y x} = k_{g\varphi_x y} \quad (3.6)$$

Also, when in the linear range, with homogeneous and isotropic material for both shafts

$$k_{px\varphi_y} = k_{p\varphi_y x}\ ;\ k_{py\varphi_x} = k_{p\varphi_x y} \text{ and } k_{gx\varphi_y} = k_{g\varphi_y x}\ ;\ k_{gy\varphi_x} = k_{g\varphi_x y} \quad (3.7)$$

Hence, on taking the assumptions taken in eqn. (3.5) through (3.7), and substituting in eqn. (3.2), it becomes

$$U = \frac{1}{2}\left\{k_p(x_p^2 + y_p^2) + k_{px\varphi_y}(x_p\varphi_{y_1} + y_p\varphi_{x_1}) + k_{p\varphi_y x}(\varphi_{y_1}x_p + \varphi_{x_1}y_p) + k_{p\varphi_x\varphi_x}(\varphi_{x_1}^2 + \varphi_{y_1}^2)\right\}$$
$$+ \frac{1}{2}\left\{k_g(x_g^2 + y_g^2) + k_{gx\varphi_y}(x_g\varphi_{y_2} + y_g\varphi_{x_2}) + k_{g\varphi_y x}(\varphi_{y_2}x_g + \varphi_{x_2}y_g) + k_{g\varphi_x\varphi_x}(\varphi_{x_2}^2 + \varphi_{y_2}^2)\right\} \quad (3.8)$$
$$+ \frac{1}{2}\left\{k_m\left(\delta_x^{\ 2} + \delta_y^{\ 2}\right)\right\}$$

Likewise, the dissipative function '*D*' due to the viscous damping can be written as

$$D = \frac{1}{2}\left\{c_{pxx}\dot{x}_p^2 + c_{pyy}\dot{y}_p^2 + c_{px\varphi_y}\dot{x}_p\dot{\varphi}_{y_1} + c_{p\varphi_y x}\dot{\varphi}_{y_1}\dot{x}_p + c_{py\varphi_x}\dot{y}_p\dot{\varphi}_{x_1} + c_{p\varphi_x y}\dot{\varphi}_{x_1}\dot{y}_p + c_{p\varphi_x\varphi_x}\dot{\varphi}_{x_1}\dot{\varphi}_{x_1} + c_{p\varphi_y\varphi_y}\dot{\varphi}_{y_1}\dot{\varphi}_{y_1}\right\}$$
$$+\frac{1}{2}\left\{c_{gxx}\dot{x}_g^2 + c_{gyy}\dot{y}_g^2 + c_{gx\varphi_y}\dot{x}_g\dot{\varphi}_{y_2} + c_{g\varphi_y x}\dot{\varphi}_{y_2}\dot{x}_g + c_{gy\varphi_x}\dot{y}_g\dot{\varphi}_{x_2} + c_{g\varphi_x y}\dot{\varphi}_{x_2}\dot{y}_g + c_{g\varphi_x\varphi_x}\dot{\varphi}_{x_2}\dot{\varphi}_{x_2} + c_{g\varphi_y\varphi_y}\dot{\varphi}_{y_2}\dot{\varphi}_{y_2}\right\} \quad (3.9)$$
$$+\frac{1}{2}\left\{c_m\left(\dot{\delta}_x^{\,2} + \dot{\delta}_y^{\,2}\right)\right\}$$

It is assumed that for input shaft

$$c_{pxx} = c_{pyy} = c_p\,;\, c_{p\varphi_x\varphi_x} = c_{p\varphi_y\varphi_y}\,;\; c_{px\varphi_y} = c_{py\varphi_x}\,;\; c_{p\varphi_y x} = c_{p\varphi_x y} \quad (3.10)$$

Similarly, for the output shaft

$$c_{gxx} = c_{gyy} = c_g\,;\; c_{g\varphi_x\varphi_x} = c_{g\varphi_y\varphi_y}\,;\; c_{gx\varphi_y} = c_{gy\varphi_x}\,;\; c_{g\varphi_y x} = c_{g\varphi_x y} \quad (3.11)$$

Also, neglecting the coupled and rotational components of damping terms and taking linear range, in homogeneous and isotropic material, we get

$$c_{px\varphi_y} = c_{p\varphi_y x} = 0;\; c_{gx\varphi_y} = c_{g\varphi_y x} = 0\;;\; c_{p\varphi_x\varphi_x} = c_{g\varphi_x\varphi_x} = 0 \quad (3.12)$$

Hence, on taking the assumptions taken in eqn. (3.10) through (3.12), and substituting in eqn. (3.9), it becomes

$$D = \frac{1}{2}c_p\left(\dot{x}_p^2 + \dot{y}_p^2\right) + \frac{1}{2}c_g\left(\dot{x}_g^2 + \dot{y}_g^2\right) + \frac{1}{2}c_m\left(\dot{\delta}_x^2 + \dot{\delta}_y^2\right) \quad (3.13)$$

To derive the equations of motion of the given geared rotor system, on using the extended Lagrange's formulation, we know that

$$\frac{d}{dt}\left(\frac{\partial L}{\partial \dot{q}_i}\right) - \frac{\partial L}{\partial q_i} + \frac{\partial D}{\partial \dot{q}_i} = P_i \quad (i = 1, 2, ...) \qquad \text{With} \quad L = T - U \quad (3.14)$$

where **q** is the column vector of generalised coordinates.

$$\mathbf{q} = \begin{Bmatrix} q_1 & q_2 & q_3 & q_4 & q_5 & q_6 & q_7 & q_8 \end{Bmatrix}^T = \begin{Bmatrix} x_1 & y_1 & \varphi_{y_1} & \varphi_{x_1} & x_2 & y_2 & \varphi_{y_2} & \varphi_{x_2} \end{Bmatrix}^T \tag{3.15}$$

So, according to extended Lagrange's equation from eqn. (3.14), in time domain, the general form of equations of motion of the geared rotor system, led to the following expression in the matrix form

$$\mathbf{M}\ddot{\mathbf{q}} + \left(\mathbf{C} - \omega_L \mathbf{G}\right)\dot{\mathbf{q}} + \mathbf{K}\mathbf{q} = \mathbf{f}_{\text{unb}} + \mathbf{f}_{\text{r\_out}} + \mathbf{f}_{\text{mesh}} - \mathbf{f}_{\text{amb}} \tag{3.16}$$

where, **M** is the mass matrix, **C** is the damping matrix, **K** is the stiffness matrix, the gyroscopic effect is characterised by a skew-symmetric matrix called **G** as gyroscopic matrix, $\mathbf{f}_{\text{unb}}(t)$ is the unbalance force vector, $\mathbf{f}_{\text{r\_out}}(t)$ is the force vector due to gear runout, $\mathbf{f}_{\text{amb}}(t)$ is the controlled magnetic force vector, $\mathbf{f}_{\text{mesh}}(t)$ is the dynamic mesh force vector acting on the system, and **q** is the generalised coordinate vector considering excitation at the pitch point of the gear mesh, while the details of the matrices are given below.

$$\mathbf{M} = \begin{bmatrix} m_1 & 0 & 0 & 0 & 0 & 0 & 0 & 0 \\ 0 & m_1 & 0 & 0 & 0 & 0 & 0 & 0 \\ 0 & 0 & I_{d_1} & 0 & 0 & 0 & 0 & 0 \\ 0 & 0 & 0 & I_{d_1} & 0 & 0 & 0 & 0 \\ 0 & 0 & 0 & 0 & m_2 & 0 & 0 & 0 \\ 0 & 0 & 0 & 0 & 0 & m_2 & 0 & 0 \\ 0 & 0 & 0 & 0 & 0 & 0 & I_{d_2} & 0 \\ 0 & 0 & 0 & 0 & 0 & 0 & 0 & I_{d_2} \end{bmatrix}; \qquad \mathbf{q} = \begin{bmatrix} x_1 \\ y_1 \\ \varphi_{y_1} \\ \varphi_{x_1} \\ x_2 \\ y_2 \\ \varphi_{y_2} \\ \varphi_{x_2} \end{bmatrix};$$

$$\mathbf{K} = \begin{bmatrix} (k_p + k_m) & 0 & k_{px\varphi_y} & 0 & -k_m & 0 & 0 & 0 \\ 0 & (k_p + k_m) & 0 & k_{px\varphi_y} & 0 & -k_m & 0 & 0 \\ k_{px\varphi_y} & 0 & k_{p\varphi_x\varphi_x} & 0 & 0 & 0 & 0 & 0 \\ 0 & k_{px\varphi_y} & 0 & k_{p\varphi_x\varphi_x} & 0 & 0 & 0 & 0 \\ -k_m & 0 & 0 & 0 & (k_g + k_m) & 0 & k_{gx\varphi_y} & 0 \\ 0 & -k_m & 0 & 0 & 0 & (k_g + k_m) & 0 & k_{gx\varphi_y} \\ 0 & 0 & 0 & 0 & k_{gx\varphi_y} & 0 & k_{g\varphi_x\varphi_x} & 0 \\ 0 & 0 & 0 & 0 & 0 & k_{gx\varphi_y} & 0 & k_{g\varphi_x\varphi_x} \end{bmatrix};$$

$$\mathbf{(C - \omega_L G)} = \begin{bmatrix} c_p + c_m & 0 & 0 & 0 & -c_m & 0 & 0 & 0 \\ 0 & c_p + c_m & 0 & 0 & 0 & -c_m & 0 & 0 \\ 0 & 0 & 0 & -\omega_p I_{p_1} & 0 & 0 & 0 & 0 \\ 0 & 0 & \omega_p I_{p_1} & 0 & 0 & 0 & 0 & 0 \\ -c_m & 0 & 0 & 0 & c_g + c_m & 0 & 0 & 0 \\ 0 & -c_m & 0 & 0 & 0 & c_g + c_m & 0 & 0 \\ 0 & 0 & 0 & 0 & 0 & 0 & 0 & -\omega_g I_{p_2} \\ 0 & 0 & 0 & 0 & 0 & 0 & \omega_g I_{p_2} & 0 \end{bmatrix}$$

The force vector equation in simplified form is written as

$$\mathbf{f}_{\text{amb}} = \begin{bmatrix} -k_s & 0 & 0 & 0 & 0 & 0 & 0 & 0 \\ 0 & -k_s & 0 & 0 & 0 & 0 & 0 & 0 \\ 0 & 0 & 0 & 0 & 0 & 0 & 0 & 0 \\ 0 & 0 & 0 & 0 & 0 & 0 & 0 & 0 \\ 0 & 0 & 0 & 0 & -k_s & 0 & 0 & 0 \\ 0 & 0 & 0 & 0 & 0 & -k_s & 0 & 0 \\ 0 & 0 & 0 & 0 & 0 & 0 & 0 & 0 \\ 0 & 0 & 0 & 0 & 0 & 0 & 0 & 0 \end{bmatrix} \begin{bmatrix} x_1 \\ y_1 \\ \varphi_{y_1} \\ \varphi_{x_1} \\ x_2 \\ y_2 \\ \varphi_{y_2} \\ \varphi_{x_2} \end{bmatrix} + \begin{bmatrix} k_I & 0 & 0 & 0 & 0 & 0 & 0 & 0 \\ 0 & k_I & 0 & 0 & 0 & 0 & 0 & 0 \\ 0 & 0 & 0 & 0 & 0 & 0 & 0 & 0 \\ 0 & 0 & 0 & 0 & 0 & 0 & 0 & 0 \\ 0 & 0 & 0 & 0 & k_I & 0 & 0 & 0 \\ 0 & 0 & 0 & 0 & 0 & k_I & 0 & 0 \\ 0 & 0 & 0 & 0 & 0 & 0 & 0 & 0 \\ 0 & 0 & 0 & 0 & 0 & 0 & 0 & 0 \end{bmatrix} \begin{Bmatrix} i_{cx_1} \\ i_{cy_1} \\ 0 \\ 0 \\ i_{cx_2} \\ i_{cy_2} \\ 0 \\ 0 \end{Bmatrix}$$

$$\mathbf{f}_{\text{unb}} = \begin{bmatrix} \left(m_1 e_p \omega_p^2\right)\cos\left(\omega_p t + \phi_p\right) \\ \left(m_1 e_p \omega_p^2\right)\sin\left(\omega_p t + \phi_p\right) \\ 0 \\ 0 \\ \left(m_2 e_g \omega_g^2\right)\cos\left(-\omega_g t + \phi_g\right) \\ \left(m_2 e_g \omega_g^2\right)\sin\left(-\omega_g t + \phi_g\right) \\ 0 \\ 0 \end{bmatrix};$$

$$\mathbf{f}_{\text{r\_out}} = \begin{bmatrix} -k_p e_p \cos\left(\omega_p t + \phi_p\right) \\ -k_p e_p \sin\left(\omega_p t + \phi_p\right) \\ -k_{p x \varphi_y} e_p \cos\left(\omega_p t + \phi_p\right) \\ -k_{p x \varphi_y} e_p \sin\left(\omega_p t + \phi_p\right) \\ -k_g e_g \cos\left(-\omega_g t + \phi_g\right) \\ -k_g e_g \sin\left(-\omega_g t + \phi_g\right) \\ -k_{g x \varphi_y} e_g \cos\left(-\omega_g t + \phi_g\right) \\ -k_{g x \varphi_y} e_g \sin\left(-\omega_g t + \phi_g\right) \end{bmatrix} + \begin{bmatrix} c_p e_p \omega_p \sin\left(\omega_p t + \phi_p\right) \\ -c_p e_p \omega_p \cos\left(\omega_p t + \phi_p\right) \\ 0 \\ 0 \\ -c_g e_g \omega_g \sin\left(-\omega_g t + \phi_g\right) \\ c_g e_g \omega_g \cos\left(-\omega_g t + \phi_g\right) \\ 0 \\ 0 \end{bmatrix}$$

$$\mathbf{f}_{\text{mesh}} = k_m \begin{bmatrix} -e_p \cos(\omega_p t + \phi_p) + e_g \cos(-\omega_g t + \phi_g) + e_x(t) \\ -e_p \sin(\omega_p t + \phi_p) + e_g \sin(-\omega_g t + \phi_g) + e_y(t) \\ 0 \\ 0 \\ e_p \cos(\omega_p t + \phi_p) - e_g \cos(-\omega_g t + \phi_g) - e_x(t) \\ e_p \sin(\omega_p t + \phi_p) - e_g \sin(-\omega_g t + \phi_g) - e_y(t) \\ 0 \\ 0 \end{bmatrix} + c_m \begin{bmatrix} e_p \omega_p \sin(\omega_p t + \phi_p) + e_g \omega_g \sin(-\omega_g t + \phi_g) + \dot{e}_x(t) \\ -e_p \omega_p \cos(\omega_p t + \phi_p) - e_g \omega_g \cos(-\omega_g t + \phi_g) + \dot{e}_y(t) \\ 0 \\ 0 \\ -e_p \omega_p \sin(\omega_p t + \phi_p) - e_g \omega_g \sin(-\omega_g t + \phi_g) - \dot{e}_x(t) \\ e_p \omega_p \cos(\omega_p t + \phi_p) + e_g \omega_g \cos(-\omega_g t + \phi_g) - \dot{e}_y(t) \\ 0 \\ 0 \end{bmatrix} \tag{3.17}$$

The geared rotor-AMB systems equation of motion for transverse vibration analysis with gyroscopic effect has been derived in this section. Further the identification algorithm will be developed in the next section.

3.5 Development of Identification Algorithm

A model-based method is presented in this section that can be used for the development of an identification algorithm for the parameter estimation of geared-rotor-AMB system by captivating the full spectrum responses of the rotor vibration and the AMB current. The algorithm is obtained after converting the time domain EOMs into regression equations, and system parameters are obtained by applying linear least-square fitting technique.

3.5.1 Conversion of Equations of Motion into Complex Form

The complex form of above EOMs, i.e. equation (3.16), with $\mathrm{j}=\sqrt{-1}$ are obtained by converting the rotor vibrational displacements into complex variables form defined by r_1 and r_2 representing complex transverse displacements, and complex angular displacements by φ_1 and φ_2 due to titling of gear disc and the AMB complex control currents by i_1 and i_2 defined for the input and output shaft, respectively, are given as

$$r_1 = x_1 + \mathrm{j}\,y_1;\quad r_2 = x_2 + \mathrm{j}\,y_2;\quad \varphi_1 = \varphi_{y_1} + \mathrm{j}\varphi_{x_1};\quad \varphi_2 = \varphi_{y_2} + \mathrm{j}\varphi_{x_2};\; i_1 = i_{c_{x1}} + \mathrm{j}i_{c_{y1}};\; i_2 = i_{c_{x2}} + \mathrm{j}i_{c_{y2}} \tag{3.18}$$

While combining above equations into the complex form, the gyroscopic terms are also combined as

$$\left(-I_{p_1}\omega_p\dot{\varphi}_{x_1}\right) + \mathrm{j}\left(I_{p_1}\omega_p\dot{\varphi}_{y_1}\right) = \mathrm{j}\,I_{p_1}\omega_p\dot{\varphi}_1 \text{ and } \left(-I_{p_2}\omega_g\dot{\varphi}_{x_2}\right) + \mathrm{j}\left(I_{p_2}\omega_g\dot{\varphi}_{y_2}\right) = \mathrm{j}\,I_{p_2}\omega_g\dot{\varphi}_2 \tag{3.19}$$

Thus, the EOMs of geared rotor in the complex form taking gyroscopic effects in the inertial co-ordinate frame is as follows

$$\bar{\mathbf{M}}\ddot{\mathrm{v}} + \left(\bar{\mathbf{C}} - \mathrm{j}\omega_L\bar{\mathbf{G}}\right)\dot{\mathrm{v}} + \bar{\mathbf{K}}\mathrm{v} = \bar{\mathbf{f}}_{\mathrm{unb}} + \bar{\mathbf{f}}_{\mathrm{r\_out}} + \bar{\mathbf{f}}_{\mathrm{mesh}} - \bar{\mathbf{f}}_{\mathrm{amb}} \tag{3.20}$$

where the evaluated geared rotor AMB system matrices are defined below.

$$\bar{\mathbf{M}}=\begin{bmatrix} m_1 & 0 & 0 & 0 \\ 0 & I_{d_1} & 0 & 0 \\ 0 & 0 & m_2 & 0 \\ 0 & 0 & 0 & I_{d_2} \end{bmatrix};\bar{\mathbf{C}}=\begin{bmatrix} c_p+c_m & 0 & -c_m & 0 \\ 0 & 0 & 0 & 0 \\ -c_m & 0 & c_g+c_m & 0 \\ 0 & 0 & 0 & 0 \end{bmatrix};\bar{\mathbf{G}}=\begin{bmatrix} 0 & 0 & 0 & 0 \\ 0 & -I_{p_1} & 0 & 0 \\ 0 & 0 & 0 & 0 \\ 0 & 0 & 0 & -I_{p_2} \end{bmatrix};$$

$$\bar{\mathbf{K}}=\begin{bmatrix} k_p+k_m & k_{px\varphi_y} & -k_m & 0 \\ k_{px\varphi_y} & k_{p\varphi_x\varphi_x} & 0 & -k_m \\ -k_m & 0 & k_g+k_m & k_{gx\varphi_y} \\ 0 & -k_m & k_{gx\varphi_y} & k_{g\varphi_x\varphi_x} \end{bmatrix};\mathrm{v}=\begin{Bmatrix} r_1 \\ \varphi_1 \\ r_2 \\ \varphi_2 \end{Bmatrix};\bar{\mathbf{f}}_{\mathrm{unb}}=\begin{Bmatrix} m_1e_p\omega_p^2e^{\mathrm{j}(\omega_pt+\phi_p)} \\ 0 \\ m_2e_g\omega_g^2e^{\mathrm{j}(-\omega_gt+\phi_g)} \\ 0 \end{Bmatrix};$$

$$\bar{\mathbf{f}}_{\mathrm{r\_out}}=\begin{Bmatrix} -k_pe_pe^{\mathrm{j}(\omega_pt+\phi_p)} \\ -k_{px\varphi_y}e_pe^{\mathrm{j}(\omega_pt+\phi_p)} \\ -k_ge_ge^{\mathrm{j}(-\omega_gt+\phi_g)} \\ -k_{gx\varphi_y}e_ge^{\mathrm{j}(-\omega_gt+\phi_g)} \end{Bmatrix}+\begin{Bmatrix} -\mathrm{j}c_pe_p\omega_pe^{\mathrm{j}(\omega_pt+\phi_p)} \\ 0 \\ \mathrm{j}c_ge_g\omega_ge^{\mathrm{j}(-\omega_gt+\phi_g)} \\ 0 \end{Bmatrix};\quad \bar{\mathbf{f}}_{\mathrm{amb}}=-k_s\begin{Bmatrix} r_1 \\ 0 \\ r_2 \\ 0 \end{Bmatrix}+k_i\begin{Bmatrix} i_1 \\ 0 \\ i_2 \\ 0 \end{Bmatrix};$$

$$\bar{\mathbf{f}}_{\mathrm{mesh}}=k_m\begin{Bmatrix} -e_pe^{\mathrm{j}(\omega_pt+\phi_p)}+e_ge^{\mathrm{j}(-\omega_gt+\phi_g)}+\left(e_me^{\mathrm{j}\phi_m}+\sum_{i=-n}^{n}e_{fi}e^{\mathrm{j}i(\omega_et+\phi_{fi})}\right) \\ 0 \\ e_pe^{\mathrm{j}(\omega_pt+\phi_p)}-e_ge^{\mathrm{j}(-\omega_gt+\phi_g)}-\left(e_me^{\mathrm{j}\phi_m}+\sum_{i=-n}^{n}e_{fi}e^{\mathrm{j}i(\omega_et+\phi_{fi})}\right) \\ 0 \end{Bmatrix}$$

$$+c_m\begin{Bmatrix} -\mathrm{j}e_p\omega_pe^{\mathrm{j}(\omega_pt+\phi_p)}-\mathrm{j}e_g\omega_ge^{\mathrm{j}(-\omega_gt+\phi_g)}+\left(\mathrm{j}\omega_e\sum_{i=-n}^{n}ie_{fi}e^{\mathrm{j}i(\omega_et+\phi_{fi})}\right) \\ 0 \\ \mathrm{j}e_p\omega_pe^{\mathrm{j}(\omega_pt+\phi_p)}+\mathrm{j}e_g\omega_ge^{\mathrm{j}(-\omega_gt+\phi_g)}-\left(\mathrm{j}\omega_e\sum_{i=-n}^{n}ie_{fi}e^{\mathrm{j}i(\omega_et+\phi_{fi})}\right) \\ 0 \end{Bmatrix} \tag{3.21}$$

3.5.2 Dynamic Condensation Method

Dynamic condensation methods have been employed in many structural health monitoring processes. Meanwhile it is hard to take the experimental measurement of the tilting of gear disc so this method is applied to eliminate the rotational DOFs for the convenience of parameter estimation from the identification algorithm. In the dynamic condensation method, the original DOFs of the model are separated into the retained and truncated DOFs, classified as masters

and slaves, respectively. The truncated coordinates (slaves) correspond to points in the model, which are non-critical, such as the rotational DOFs and intermediate locations on the shaft. The structural matrices, i.e., the mass, stiffness, and damping matrices, and the state (displacement vector) and force vectors, are partitioned into sub-vectors and sub-matrices relating to master DOFs that are to be retained, and slave DOFs, which are to be eliminated. The frequency domain EOMs, eqn. (3.20), can be partitioned as follows, where subscript m and s represent the masters and slaves, respectively, and $\omega_L = \omega_p, \omega_g, \omega_e$, i.e., the three different excitation frequencies. The eight DOFs of the system further reduces to four DOFs as given below

$$\begin{Bmatrix} x_1 & y_1 & \varphi_{y_1} & \varphi_{x_1} & x_2 & y_2 & \varphi_{y_2} & \varphi_{x_2} \end{Bmatrix}^T = \begin{Bmatrix} \mathbf{Q}_{1m} & \mathbf{Q}_{1s} & \mathbf{Q}_{2m} & \mathbf{Q}_{2s} \end{Bmatrix}^T$$

$$\text{with, } \mathbf{Q}_{1m} = \begin{Bmatrix} x_1 & y_1 \end{Bmatrix},\ \mathbf{Q}_{1s} = \begin{Bmatrix} \varphi_{y1} & \varphi_{x1} \end{Bmatrix},\ \mathbf{Q}_{2m} = \begin{Bmatrix} x_2 & y_2 \end{Bmatrix},\ \mathbf{Q}_{2s} = \begin{Bmatrix} \varphi_{y2} & \varphi_{x2} \end{Bmatrix} \tag{3.22}$$

Further the final EOMs after separating the master and slave DOFs takes the form

$$\left[\left(-(i^2\omega_L^2)\tilde{\mathbf{M}}\right)+\mathrm{j}(i\omega_L)\left(\tilde{\mathbf{C}}-\mathrm{j}\omega_L\tilde{\mathbf{G}}\right)+\tilde{\mathbf{K}}\right]\tilde{\mathrm{v}}_i = \tilde{\mathbf{f}}_{\mathrm{unb}}+\tilde{\mathbf{f}}_{\mathrm{r\_out}}+\tilde{\mathbf{f}}_{\mathrm{mesh}}-\tilde{\mathbf{f}}_{\mathrm{amb}} \tag{3.23}$$

For which the matrices of EOMs i.e. Eqn. (3.23) are given as follows.

$$\left(\begin{array}{l} -(i\omega_L)^2\begin{bmatrix} \mathbf{M}_{1mm} & \mathbf{0} & \mathbf{0} & \mathbf{0} \\ \mathbf{0} & \mathbf{M}_{1ss} & \mathbf{0} & \mathbf{0} \\ \mathbf{0} & \mathbf{0} & \mathbf{M}_{2mm} & \mathbf{0} \\ \mathbf{0} & \mathbf{0} & \mathbf{0} & \mathbf{M}_{2ss} \end{bmatrix} + \mathrm{j}(i\omega_L)\left(\begin{bmatrix} \mathbf{C}_{1mm} & \mathbf{C}_{1ms} & -c_m\mathbf{I} & \mathbf{0} \\ \mathbf{C}_{1sm} & \mathbf{C}_{1ss} & \mathbf{0} & \mathbf{0} \\ -c_m\mathbf{I} & \mathbf{0} & \mathbf{C}_{2mm} & \mathbf{C}_{2ms} \\ \mathbf{0} & \mathbf{0} & \mathbf{C}_{2sm} & \mathbf{C}_{2ss} \end{bmatrix} - \mathrm{j}\omega_L\begin{bmatrix} \mathbf{0} & \mathbf{0} & \mathbf{0} & \mathbf{0} \\ \mathbf{0} & \mathbf{G}_{1ss} & \mathbf{0} & \mathbf{0} \\ \mathbf{0} & \mathbf{0} & \mathbf{0} & \mathbf{0} \\ \mathbf{0} & \mathbf{0} & \mathbf{0} & \mathbf{G}_{2ss} \end{bmatrix}\right) \\ \qquad + \begin{bmatrix} \mathbf{K}_{1mm} & \mathbf{K}_{1ms} & -k_m\mathbf{I} & \mathbf{0} \\ \mathbf{K}_{1sm} & \mathbf{K}_{1ss} & \mathbf{0} & \mathbf{0} \\ -k_m\mathbf{I} & \mathbf{0} & \mathbf{K}_{2mm} & \mathbf{K}_{2ms} \\ \mathbf{0} & \mathbf{0} & \mathbf{K}_{2sm} & \mathbf{K}_{2ss} \end{bmatrix} \end{array}\right)\begin{Bmatrix} \mathbf{Q}_{1m} \\ \mathbf{Q}_{1s} \\ \mathbf{Q}_{2m} \\ \mathbf{Q}_{2s} \end{Bmatrix} = \begin{Bmatrix} \mathbf{f}_{1m} \\ \mathbf{f}_{1s} \\ \mathbf{f}_{2m} \\ \mathbf{f}_{2s} \end{Bmatrix} \tag{3.24}$$

in which

$$\mathbf{M}_{1mm}=\begin{bmatrix} m_1 & 0 \\ 0 & m_1 \end{bmatrix};\ \mathbf{M}_{2mm}=\begin{bmatrix} m_2 & 0 \\ 0 & m_2 \end{bmatrix};\ \mathbf{M}_{1ss}=\begin{bmatrix} I_{d_1} & 0 \\ 0 & I_{d_1} \end{bmatrix};\ \mathbf{M}_{2ss}=\begin{bmatrix} I_{d_2} & 0 \\ 0 & I_{d_2} \end{bmatrix};$$

$$\mathbf{G}_{1ss}=\begin{bmatrix} 0 & I_{p_1} \\ -I_{p_1} & 0 \end{bmatrix};\ \mathbf{G}_{2ss}=\begin{bmatrix} 0 & I_{p_2} \\ -I_{p_2} & 0 \end{bmatrix};\ \mathbf{C}_{1mm}=\begin{bmatrix} c_p+c_m & 0 \\ 0 & c_p+c_m \end{bmatrix};$$

$$\mathbf{C}_{1ms}=\mathbf{C}_{1sm}=\begin{bmatrix} 0 & 0 \\ 0 & 0 \end{bmatrix};\ \mathbf{C}_{2mm}=\begin{bmatrix} c_g+c_m & 0 \\ 0 & c_g+c_m \end{bmatrix};\ \mathbf{C}_{2ms}=\mathbf{C}_{2sm}=\begin{bmatrix} 0 & 0 \\ 0 & 0 \end{bmatrix};$$

$$\mathbf{C}_{1ss}=\mathbf{C}_{2ss}=\begin{bmatrix} 0 & 0 \\ 0 & 0 \end{bmatrix};\quad \mathbf{K}_{1mm}=\begin{bmatrix} k_p+k_m & 0 \\ 0 & k_p+k_m \end{bmatrix};\ \mathbf{K}_{2mm}=\begin{bmatrix} k_g+k_m & 0 \\ 0 & k_g+k_m \end{bmatrix};$$

$$\mathbf{K}_{1ss}=\begin{bmatrix} k_{p\varphi_x\varphi_x} & 0 \\ 0 & k_{p\varphi_x\varphi_x} \end{bmatrix};\ \mathbf{K}_{2ss}=\begin{bmatrix} k_{g\varphi_x\varphi_x} & 0 \\ 0 & k_{g\varphi_x\varphi_x} \end{bmatrix};\ \mathbf{K}_{1ms}=\mathbf{K}_{1sm}=\begin{bmatrix} k_{px\varphi_y} & 0 \\ 0 & k_{px\varphi_y} \end{bmatrix};$$

$$\mathbf{K}_{2ms}=\mathbf{K}_{2sm}=\begin{bmatrix} k_{gx\varphi_y} & 0 \\ 0 & k_{gx\varphi_y} \end{bmatrix} \tag{3.25}$$

3.5.3 Development of Transformation Matrix

The general method for derivation of the transformation matrix, from the equation are given as follows: -

$$\begin{aligned} &\mathbf{K}_{1sm}\mathbf{Q}_{1m}+\mathbf{K}_{1ss}\mathbf{Q}_{1s}+i\omega_L^2\mathbf{G}_{1ss}\mathbf{Q}_{1s}-(i\omega_L)^2\mathbf{M}_{1ss}\mathbf{Q}_{1s}=\mathbf{0} \\ &\mathbf{K}_{2sm}\mathbf{Q}_{2m}+\mathbf{K}_{2ss}\mathbf{Q}_{2s}+i\omega_L^2\mathbf{G}_{2ss}\mathbf{Q}_{2s}-(i\omega_L)^2\mathbf{M}_{2ss}\mathbf{Q}_{2s}=\mathbf{0} \end{aligned} \tag{3.26}$$

and

$$\mathbf{Q}_{1m}=\mathbf{I}\mathbf{Q}_{1m},\ \mathbf{Q}_{2m}=\mathbf{I}\mathbf{Q}_{2m} \tag{3.27}$$

where **I** is the identity matrix and **0** is the null matrix. The transformation matrix is represented by '$\mathbf{T}^d$'. A general method for derivation of '$\mathbf{T}^d$' is available in literature, for instance – Friswell and Mottershead (1995). This transformation is used in the same way as the static transformation. This is a modified Guyan's method and represents the exact response of the structure at any frequency. There is no apparent choice of frequency for the exact response. It is suggested that the centre frequency in the range of interest can be selected or a geometric mean. In rotordynamic application, this freedom to choose the frequency of reduction is an advantage, since the reduction can be performed at the frequency of external forcing which in

turn is a multiple/factor of the shaft spin frequency. The transformation matrix '$\mathbf{T}^d$' is formed including the inertia terms and assumption of negligible damping.

After the dynamic condensation eliminating the four rotational coordinates φ_{y_1} and φ_{x_1} and φ_{y_2} and φ_{x_2} from eight generalised coordinates holds the following form

$$\begin{Bmatrix} \mathbf{Q}_{1m} \\ \mathbf{Q}_{1s} \\ \mathbf{Q}_{2m} \\ \mathbf{Q}_{2s} \end{Bmatrix} = \mathbf{T}^d \begin{Bmatrix} \mathbf{Q}_{1m} \\ \mathbf{Q}_{2m} \end{Bmatrix} \tag{3.28}$$

with,

$$\mathbf{T}^d = \begin{bmatrix} \mathbf{I} & \mathbf{0} \\ -\{\mathbf{K}_{1ss} + i\omega_L^2 \mathbf{G}_{1ss} - (i\omega_L)^2 \mathbf{M}_{1ss}\}^{-1} \mathbf{K}_{1sm} & \mathbf{0} \\ \mathbf{0} & \mathbf{I} \\ \mathbf{0} & -\{\mathbf{K}_{2ss} + i\omega_L^2 \mathbf{G}_{2ss} - (i\omega_L)^2 \mathbf{M}_{2ss}\}^{-1} \mathbf{K}_{2sm} \end{bmatrix} \tag{3.29}$$

Or, $\mathbf{T}^d = \begin{bmatrix} 1 & 0 & 0 & 0 \\ 0 & 1 & 0 & 0 \\ t^{d_1} & 0 & 0 & 0 \\ 0 & t^{d_1} & 0 & 0 \\ 0 & 0 & 1 & 0 \\ 0 & 0 & 0 & 1 \\ 0 & 0 & t^{d_2} & 0 \\ 0 & 0 & 0 & t^{d_2} \end{bmatrix}$

with, $t^{d_1} = \dfrac{-k_{px\varphi_y}}{-(i\omega_L)^2 I_{d_1} + i\omega_L^2 I_{p_1} + k_{p\varphi_x\varphi_x}}$; $t^{d_2} = \dfrac{-k_{gx\varphi_y}}{-(i\omega_L)^2 I_{d_2} + i\omega_L^2 I_{p_2} + k_{g\varphi_x\varphi_x}}$ (3.30)

On substituting the transformation matrix (eqn. 3.30) into EOMs (eqn. 3.13), we get reduced order matrices with slave DOFs eliminated. The placement of reduced sub-matrices and vectors yields the final obtained equations of motion expressed in terms of master DOFs as

$$\left\{-\left(i\omega_L\right)^2\mathbf{M}^d+\mathrm{j}\left(i\omega_L\right)\left(\mathbf{C}^d-\mathrm{j}\,\omega_L\mathbf{G}^d\right)+\mathbf{K}^d\right\}\mathbf{Q}_m=\mathbf{f}^d \tag{3.31}$$

where the dynamically condensed matrices are defined as follows:

$$\mathbf{M}^d=\left(\mathbf{T}^d\right)^T\begin{bmatrix}\mathbf{M}_{1mm} & \mathbf{0} & \mathbf{0} & \mathbf{0}\\ \mathbf{0} & \mathbf{M}_{1ss} & \mathbf{0} & \mathbf{0}\\ \mathbf{0} & \mathbf{0} & \mathbf{M}_{2mm} & \mathbf{0}\\ \mathbf{0} & \mathbf{0} & \mathbf{0} & \mathbf{M}_{2ss}\end{bmatrix};$$

$$\mathbf{T}^d=\begin{bmatrix}m_1+\left(t^{d_1}\right)^2 I_{d_1} & 0 & 0 & 0\\ 0 & m_1+\left(t^{d_1}\right)^2 I_{d_1} & 0 & 0\\ 0 & 0 & m_2+\left(t^{d_2}\right)^2 I_{d_2} & 0\\ 0 & 0 & 0 & m_2+\left(t^{d_2}\right)^2 I_{d_2}\end{bmatrix}$$

$$\mathbf{K}^d=\left(\mathbf{T}^d\right)^T\begin{bmatrix}\mathbf{K}_{1mm} & \mathbf{K}_{1ms} & -k_m\mathbf{I} & \mathbf{0}\\ \mathbf{K}_{1sm} & \mathbf{K}_{1ss} & \mathbf{0} & \mathbf{0}\\ -k_m\mathbf{I} & \mathbf{0} & \mathbf{K}_{2mm} & \mathbf{K}_{2ms}\\ \mathbf{0} & \mathbf{0} & \mathbf{K}_{2sm} & \mathbf{K}_{2ss}\end{bmatrix}\mathbf{T}^d=\begin{bmatrix}k_p^{'} & 0 & -k_m & 0\\ 0 & k_p^{'} & 0 & 0\\ -k_m & 0 & k_g^{'} & 0\\ 0 & 0 & 0 & k_g^{'}\end{bmatrix}$$

with, $k_p^{'}=\left(k_p+k_m\right)-2\left(t^{d_1}\right)k_{px\varphi_y}+\left(t^{d_1}\right)^2 k_{p\varphi_x\varphi_x}$; $k_g^{'}=\left(k_g+k_m\right)-2\left(t^{d_2}\right)k_{gx\varphi_y}+\left(t^{d_2}\right)^2 k_{g\varphi_x\varphi_x}$

$$\mathbf{C}^d=\left(\mathbf{T}^d\right)^T\begin{bmatrix}\mathbf{C}_{1mm} & \mathbf{C}_{1ms} & -c_m\mathbf{I} & \mathbf{0}\\ \mathbf{C}_{1sm} & \mathbf{C}_{1ss} & \mathbf{0} & \mathbf{0}\\ -c_m\mathbf{I} & \mathbf{0} & \mathbf{C}_{2mm} & \mathbf{C}_{2ms}\\ \mathbf{0} & \mathbf{0} & \mathbf{C}_{2sm} & \mathbf{C}_{2ss}\end{bmatrix}\mathbf{T}^d=\begin{bmatrix}c_p^{'} & 0 & -c_m & 0\\ 0 & c_p^{'} & 0 & 0\\ -c_m & 0 & c_g^{'} & 0\\ 0 & 0 & 0 & c_g^{'}\end{bmatrix}$$

with, $c_p^{'}=(c_p+c_m)$; $c_g^{'}=(c_g+c_m)$

$$\mathbf{G}^d = \left(\mathbf{T}^d\right)^T \omega_L \begin{bmatrix} \mathbf{0} & \mathbf{0} & \mathbf{0} & \mathbf{0} \\ \mathbf{0} & \mathbf{G}_{1ss} & \mathbf{0} & \mathbf{0} \\ \mathbf{0} & \mathbf{0} & \mathbf{0} & \mathbf{0} \\ \mathbf{0} & \mathbf{0} & \mathbf{0} & \mathbf{G}_{2ss} \end{bmatrix} \mathbf{T}^d = \begin{bmatrix} 0 & -\left(t^{d_1}\right)^2 I_{p_1}\omega_p & 0 & 0 \\ \left(t^{d_1}\right)^2 I_{p_1}\omega_p & 0 & 0 & 0 \\ 0 & 0 & 0 & -\left(t^{d_2}\right)^2 I_{p_2}\omega_g \\ 0 & 0 & \left(t^{d_2}\right)^2 I_{p_2}\omega_g & 0 \end{bmatrix}$$

$$\mathbf{f}^d = \left(\mathbf{T}^d\right)^T \mathbf{f} = \begin{bmatrix} e_p\left(k_{px\varphi_y} t_{d_1} - k_p\right) e^{\mathrm{j}\left(\omega_p t + \phi_p\right)} \\ e_p\left(k_{px\varphi_y} t_{d_1} - k_p\right) e^{\mathrm{j}\left(\omega_p t + \phi_p\right)} \\ e_g\left(k_{gx\varphi_y} t_{d_2} - k_g\right) e^{\mathrm{j}\left(-\omega_g t + \phi_g\right)} \\ e_g\left(k_{gx\varphi_y} t_{d_2} - k_g\right) e^{\mathrm{j}\left(-\omega_g t + \phi_g\right)} \end{bmatrix} \tag{3.32}$$

With all the variables in eqn. (3.31) now associated with master DOFs, this equation will be used further to develop regression equations for the identification of fault and AMB parameters.

3.5.4 Formulation of Identification Matrix

The identification algorithm is derived and written in the matrix form in this section. As mentioned in Chapter 2, the gears create vibrations at specific frequencies, related to number of teeth and the rotational speed of gears. Hence, the excitation forces due to gear meshing are the multi-harmonic in nature. Herein, gear meshing forces are common to both shafts but opposite in direction so a forward excitation in pinion will give backward excitation in gear and since the systems EOM are linear, thereby applying principle of superposition, the assumed solution for Equations (3.31) considering three different excitation frequencies, i.e. ω_p, ω_g and ω_e are combined. Now taking only the complex transverse vibrational displacements $r_1(t)$ and $r_2(t)$, the complex current $i_1(t)$ and $i_2(t)$, with dynamically condensed angular displacements $\varphi_1(t)$ and $\varphi_2(t)$ containing each harmonics from $i = -n,\ldots,-1,0,1,2\ldots n$ can be summed up as provided in Eqn. (2.29) and Eqn. (2.30) in Chapter 2, Section 2.3.1, as follows

$$r_1(t)=\sum_{i=-n}^{i=n} R_{ipL}=R_{-npe}e^{-n\mathrm{j}\omega_e t}+\cdots+R_{-1pe}e^{-\mathrm{j}\omega_e t}+R_{-1pg}e^{-\mathrm{j}\omega_g t}+R_{0p}e^{0\mathrm{j}\omega_p t}+R_{1pp}e^{\mathrm{j}\omega_p t}+R_{1pe}e^{\mathrm{j}\omega_e t}+\cdots+R_{npe}e^{n\mathrm{j}\omega_e t} \tag{3.33}$$

$$r_2(t)=\sum_{i=-n}^{i=n} R_{igL}=R_{-nge}e^{-n\mathrm{j}\omega_e t}+\cdots+R_{-1ge}e^{-\mathrm{j}\omega_e t}+R_{-1gg}e^{-\mathrm{j}\omega_g t}+R_{0g}e^{0\mathrm{j}\omega_g t}+R_{1gp}e^{\mathrm{j}\omega_p t}+R_{1ge}e^{\mathrm{j}\omega_e t}+\cdots+R_{nge}e^{n\mathrm{j}\omega_e t} \tag{3.34}$$

In the above equations, $\sum_{i=-n}^{i=n} R_{ipL}$ and $\sum_{i=-n}^{i=n} R_{igL}$ represent complex frequency domain displacement responses due to the effect of ω_L with subscript L belongs to p, g, e on the pinion and gear shafts, respectively, and R_{0p} and R_{0g} represent the static deflection in the complex form for the pinion and gear shafts, respectively.

Similarly, as the harmonics of current signals should have the same frequency components as that of the rotor displacement signals, so at any instant of time the output current signals from a PID controller can be expressed as given in Eqn. (2.31) and Eqn. (2.32) in Chapter 2, section 2.3.1, as

$$i_1(t)=\sum_{i=-n}^{i=n} I_{ipL}=I_{-npe}e^{-n\mathrm{j}\omega_e t}+\cdots+I_{-1pe}e^{-\mathrm{j}\omega_e t}+I_{-1pg}e^{-\mathrm{j}\omega_g t}+I_{0p}e^{0\mathrm{j}\omega_p t}+I_{1pp}e^{\mathrm{j}\omega_p t}+I_{1pe}e^{\mathrm{j}\omega_e t}+\cdots+I_{npe}e^{n\mathrm{j}\omega_e t} \tag{3.35}$$

$$i_2(t)=\sum_{i=-n}^{i=n} I_{igL}=I_{-nge}e^{-n\mathrm{j}\omega_e t}+\cdots+I_{-1ge}e^{-\mathrm{j}\omega_e t}+I_{-1gg}e^{-\mathrm{j}\omega_g t}+I_{g0}e^{0\mathrm{j}\omega_g t}+I_{1gp}e^{\mathrm{j}\omega_p t}+I_{1ge}e^{\mathrm{j}\omega_e t}+\cdots+I_{nge}e^{n\mathrm{j}\omega_e t} \tag{3.36}$$

In the above equations, $\sum_{i=-n}^{i=n} I_{ipL}$ and $\sum_{i=-n}^{i=n} I_{igL}$ represent the complex frequency domain current responses under the effect of ω_L with subscript L belongs to *p*, *g* and *e* on the pinion and gear shafts, respectively, and I_{0p}, I_{0g} represent the control current responses in complex form for the static deflection in the pinion and gear shafts, respectively. For the identification of parameters from the geared rotor system, the complex regression equations are so arranged that the known and unknowns are separated and kept on either side of equation. Both left and right

sides of the equations contain multi-harmonic components ranging in $i=-n,...,-1,0,1,...,n$. The complex responses R_{ipL}, R_{igL}, and complex AMB currents I_{ipL}, I_{igL} for i^{th} harmonic can be written in the following form

$$R_{ipL}=R_{ipL,Re}+\mathrm{j}R_{ipL,Im};\qquad R_{igL}=R_{igL,Re}+\mathrm{j}R_{igL,Im}$$

and

$$I_{ipL}=I_{ipL,Re}+\mathrm{j}I_{ipL,Im};\qquad I_{igL}=I_{igL,Re}+\mathrm{j}I_{igL,Im} \tag{3.37}$$

and upon differentiating the assumed solution $R_{ipL}(t)$ and $R_{igL}(t)$, with subscript L belonging to *p,g,e* depending upon the excitation frequencies, $\omega_p,\omega_g,\omega_e$ respectively, taken at a time yields

$$\dot{R}_{ipL}(t)=\mathrm{j}i\omega_L R_{ipL}(\omega_L)e^{\mathrm{j}i\omega_L t};\ \ddot{R}_{ipL}(t)=-i^2\omega_L^2 R_{ipL}(\omega_L)e^{\mathrm{j}i\omega_L t}$$

$$\dot{R}_{igL}(t)=\mathrm{j}i\omega_L R_{igL}(\omega_L)e^{\mathrm{j}i\omega_L t};\ \ddot{R}_{igL}(t)=-i^2\omega_L^2 R_{igL}(\omega_L)e^{\mathrm{j}i\omega_L t} \tag{3.38}$$

Taking into account the eqns. from (3.33) through (3.38), the dynamic condensed EOM (eqn. (3.31)) is changed into the complex form with multi-harmonic frequencies and can be written as

(a) For the input shaft:

$$\left[\begin{pmatrix}-(i\omega_L)^2\left\{m_1+\left(t^{d_1}\right)^2 I_{d_1}\right\}+\mathrm{j}i\omega_L\left\{(c_p+c_m)+\mathrm{j}I_{p_1}\omega_L\left(t^{d_1}\right)^2\right\}\\ +\left(k_p+k_m\right)-2\left(t^{d_1}\right)k_{pla}+\left(t^{d_1}\right)^2 k_{pa}\end{pmatrix}\left(R_{ipL}\right)-\left(\mathrm{j}i\omega_L c_m+k_m\right)\left(R_{igL}\right)\right]\left(e^{\mathrm{j}i\omega_L t}\right)$$
$$=\left\{\left(m_1 e_p\omega_p^2+k_{pla}t_{d_1}e_p-k_p e_p-k_m e_p\right)-\mathrm{j}\left(c_p+c_m\right)e_p\omega_p\right\}e^{\mathrm{j}(\omega_p t+\phi_p)}+\left(k_m e_g-\mathrm{j}c_m e_g\omega_g\right)e^{\mathrm{j}(-\omega_g t+\phi_g)}$$
$$+k_m\left[e_m e^{\mathrm{j}\phi_m}+\sum_{i=-n}^{n}\left\{\left(e_{fi}\right)e^{\mathrm{j}i(\omega_e t+\phi_{fi})}\right\}\right]+c_m\left\{\mathrm{j}\omega_e\sum_{i=-n}^{n}\left\{\left(ie_{fi}\right)e^{\mathrm{j}i(\omega_e t+\phi_{fi})}\right\}\right\}+k_s R_{ipL}e^{\mathrm{j}i\omega_L t}-k_I\sum_{i=-n}^{n}I_{ipL}e^{\mathrm{j}i\omega_L t}$$

(3.39)

(b) For the output shaft:

$$\left[\begin{pmatrix} -(i\omega_L)^2\left\{m_2+\left(t^{d_2}\right)^2 I_{d_2}\right\}+\mathrm{j}i\omega_L\left\{(c_g+c_m)+\mathrm{j}I_{p_2}\omega_L\left(t^{d_2}\right)^2\right\} \\ +\left(k_g+k_m\right)-2\left(t^{d_2}\right)k_{gla}+\left(t^{d_2}\right)^2 k_{ga} \end{pmatrix}\left(R_{igL}\right)-\left(\mathrm{j}i\omega_L c_m+k_m\right)\left(R_{ipL}\right)\right]\left(e^{\mathrm{j}i\omega_L t}\right)$$
$$=\left\{\left(m_2 e_g\omega_g^2+k_{gla}t_{d_2}e_g-k_g e_g-k_m e_g\right)+\mathrm{j}\left(c_g+c_m\right)e_g\omega_g\right\}e^{\mathrm{j}(-\omega_g t+\phi_g)}+\left(k_m e_p+\mathrm{j}c_m e_p\omega_p\right)e^{\mathrm{j}(\omega_p t+\phi_p)}$$
$$-k_m\left[e_m e^{\mathrm{j}\phi_m}+\sum_{i=-n}^{n}\left\{\left(e_{fi}\right)e^{\mathrm{j}i(\omega_e t+\phi_{fi})}\right\}\right]-c_m\left\{\mathrm{j}\omega_e\sum_{i=-n}^{n}\left\{\left(ie_{fi}\right)e^{\mathrm{j}i(\omega_e t+\phi_{fi})}\right\}\right\}+k_s R_{igL}e^{\mathrm{j}i\omega_L t}-k_I\sum_{i=-n}^{n}I_{igL}e^{\mathrm{j}i\omega_L t}$$

(3.40)

Thus, by following the same procedure as mentioned in Chapter 2. The real regression equations are obtained by segregating the real and imaginary parts (refer **Appendix A2**). Subsequently, there are 52 number of equations obtained considering $n=5$ and rearranged separating the rotor forward and backward whirl frequency components and expressed in the matrix form as

$$\mathbf{Ax = b} \tag{3.41}$$

Here, $\mathbf{x}$ denotes the unknown column vector, $\mathbf{b}$ the known matrix and $\mathbf{A}$ the regressor, as given in **Appendix B2**. There are 38 unknown parameters, which needs to be estimated from the real regression equations (refer **Appendix A2**)

The values so obtained from eqn. (2.46) as given in Chapter 2 are recombined suitably to determine the final looked-for 20 identifiable system parameters (i.e. the gear mesh stiffness, gear mesh damping, eccentricity of input, output gear with respective unbalance phase, AMB displacement stiffness factor, AMB current stiffness factor, amplitude and phase of mean transmission error, amplitude and phase of variable transmission error (considering $n=5$) harmonics), as

$$\left\lfloor k_m \;\; c_m \;\; e_p \;\; \phi_p \;\; e_g \;\; \phi_g \;\; k_s \;\; k_I \;\; e_m \;\; \phi_m \;\; e_{f1} \;\; e_{f2} \;\; e_{f3} \;\; e_{f4} \;\; e_{f5} \;\; \phi_{f1} \;\; \phi_{f2} \;\; \phi_{f3} \;\; \phi_{f4} \;\; \phi_{f5} \right\rfloor^T$$

(3.42)

The identifiable parameters are solved by using the least-square regression method, which is given by the expression

$$\mathbf{x} = \left(\mathbf{A}^{\mathrm{T}}\mathbf{A}\right)^{-1}\mathbf{A}^{\mathrm{T}}\mathbf{b} \tag{3.43}$$

The condition number of the identification matrix is improved with combined spin speeds taking cumulative data over wide range of speeds so depending upon the excitation frequencies $\omega_p, \omega_g, \omega_e$ taken one at a time equation (3.43) is given by the expression

$$\begin{Bmatrix} \mathbf{A}(\omega_{1_L}) \\ \mathbf{A}(\omega_{2_L}) \\ \vdots \\ \mathbf{A}(\omega_{N_L}) \end{Bmatrix} \mathbf{x} = \begin{Bmatrix} \mathbf{b}(\omega_{1_L}) \\ \mathbf{b}(\omega_{2_L}) \\ \vdots \\ \mathbf{b}(\omega_{N_L}) \end{Bmatrix} \tag{3.44}$$

where subscript *L* belongs to *p,g* and *e*. The analysis of simulated responses from the proposed rotor-AMB model with offset gears and identification of parameters from the developed algorithm is illustrated numerically in Section 3.6

3.6 Numerical Analysis of Geared Rotor-AMB System with gyroscopic effect

The numerical analysis of the mathematical model of geared rotor AMB system taking the gyroscopic effect into account is approached in this section. Later, the parameter estimation is done by solving the identification problem using the developed algorithm.

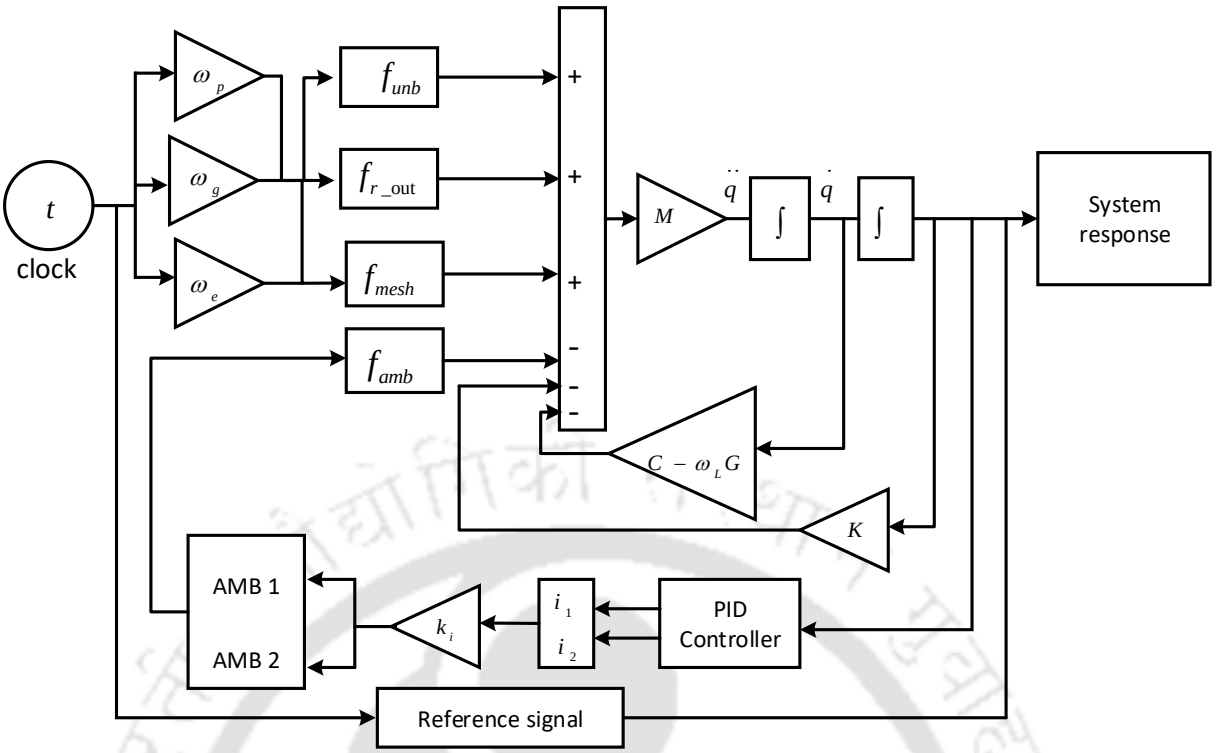

Figure 3.3 Simulink block of proposed rotor AMB model

Initially from the system's EOM stated in eqn. (3.16), time domain solution is found by using Simulink block in MATLAB^{TM} environment, which is shown in Fig. 3.3. To run the Simulink model, the input given is the 'clock' time. The external forces to the model are the mesh dynamic force, unbalance, runout error, and transmission error, which causes vibrational displacement in the geared-rotor. The model output signals are directed towards the PID controller, where the gains are adjusted to obtain the desired output current and the signals are sent to the actuator, which should be at the same frequency as that of the excitation frequency of the system. This creates an electromagnetic pull in order to bring back the rotor to the reference position, which is set to zero at the nominal position.

The dynamic response of the one-stage spur gear with the gyroscopic effect is obtained for the selected parameters given in Table 3.1.

Table 3.1

Gear physical parameters assumed for numerical simulation

Parameters	Assumed values

Diameter of input and output shafts	0.012 m
Length of input and output shafts	0.6 m
Gear-pair module	2
Gear ratio	2
Gear-pair pressure angle (FDI)	20 deg.
Number of teeth (pinion)	28
Number of teeth (gear)	56
Shaft material density	7860 kg/m^3
Young's modulus	2.068×10^{11} Pa
m_1, m_2	2.88 kg, 3.38 kg
ω_p, ω_g	50:2:60 Hz, 25:1:30 Hz
e_p, e_g	0.0003 m, 0.0004 m
c_p, c_g	49.63 N-s/m, 69.5 N-s/m
c_m	250 N-s/m
k_m	45.0257×10^7 N/m
k_p, k_g	4.25×10^5 N/m, 6.62×10^5 N/m
$k_{px\varphi_y}, k_{gx\varphi_y}$	4.5×10^3 N/rad, 5.5×10^3 N/rad
$k_{p\varphi_x\varphi_x}, k_{g\varphi_x\varphi_x}$	1.7×10^3 Nm/rad, 1.5×10^3 Nm/rad
ω_e	1250:50:1500 Hz
ϕ_p, ϕ_g	1.047 rad, 1.545 rad.
I_{p_1}, I_{p_2}	0.0048,0.0088 kg-m^2
I_{d_1}, I_{d_2}	0.0024,0.0044 kg-m^2
e_m	31 nm
ϕ_m	0.5236 rad.
e_{fi}	30 nm, 25 nm, 35 nm, 11 nm, 12 nm

ϕ_{fi}	0.9471 rad, 0.5640 rad, 0.3283 rad, 0.3654 rad, 0.3954 rad.

Here two AMBs, one each, are placed near the input and output gears to control the displacements due to gear meshing error and PID controllers, working on differential driving mode, has been used. The control parameters are chosen such that geared rotor-AMB system remains stable. The tuning of PID controller gains is done on trial basis and checked with Nyquist stability criteria (refer Chapter 2). Table 3.2 shows the adjustable controller gain values, which gives the desired control current to the actuator poles, such that the vibration levels of the system are minimised.

Table 3.2

Tuning of PID controller gains

	Gains	Values	Units
AMB 1	K_p	7000-9000	A/m
	K_D	9	As/m
	K_I	4000	A/m-s
AMB 2	K_p	6000-10000	A/m
	K_D	8	As/m
	K_I	4000	A/m-s

3.6.1 Campbell Diagram

The Campbell diagram gives the plot of the spin speed versus the whirl frequency. It can be observed that due to the gyroscopic effect on the geared rotor, the splitting of whirl frequencies takes place into the forward and backward whirling motions. The distinction between the rotor spin speed, the whirl natural frequency, and the critical speed is shown in the Campbell diagram (Fig. 3.4). For the estimation of geared rotor parameters from the identification algorithm, the range of spin speeds are chosen in such a way that it is away from the critical speeds by looking into the Campbell diagram, since it is often accompanied with transients during the measurement of responses.

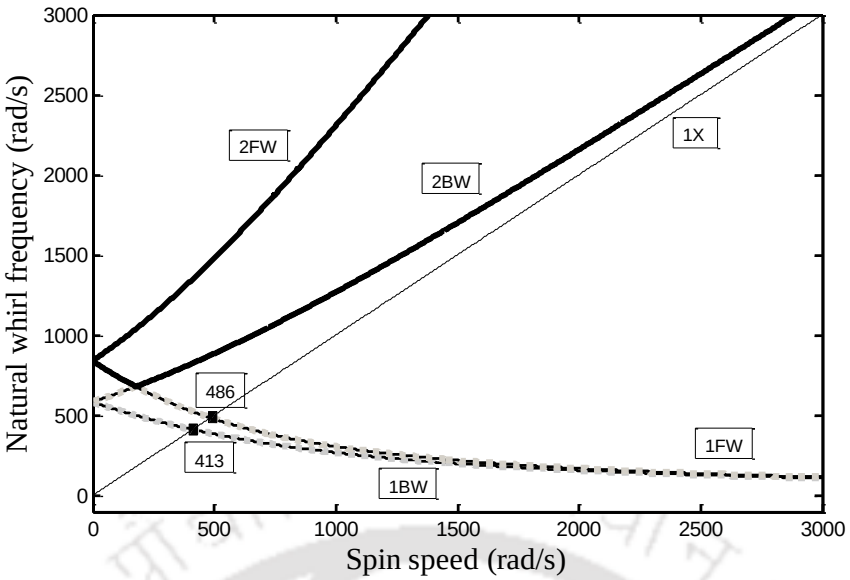

Figure 3.4 Campbell diagram of geared rotor

The natural frequencies are split into two flexural natural frequencies. The first critical speeds are at around 413 rad/s (65.7 Hz) in the (1BW) backward whirling and 486 rad/s (77.3 Hz) in the (1FW) forward whirling, respectively. This is due to curve veering phenomenon. When two eigen values are trying to coincide, the forward and backward whirl tends to intersect each other. Hence, speed range of ω_p =50-60 Hz in steps of 2 Hz and ω_g =25-30 Hz in steps of 1 Hz has been taken for the analysis.

3.6.2 Time Domain Response

The solution of equation (3.14) is obtained by using the fourth-order Runge-Kutta integration method. To obtain a steady state response, the transient part is removed and the response is taken from 6-7 s with a time step of 0.00006 s. The transverse vibration is controlled by a linear PID controller. From the time domain responses, it is observed that the rotor lateral displacement is suppressed effectively by the radial forces generated by actuator poles. The plot of $x(t)$ versus $y(t)$ gives the orbit plots, which illustrates the rotor whirling behaviour from the pinion and gear displacements with and without the application of AMB, shown in Fig. 3.5. The response visibly shows the combined rotor displacement characteristics in transverse plane and the motion attained after the application AMB.

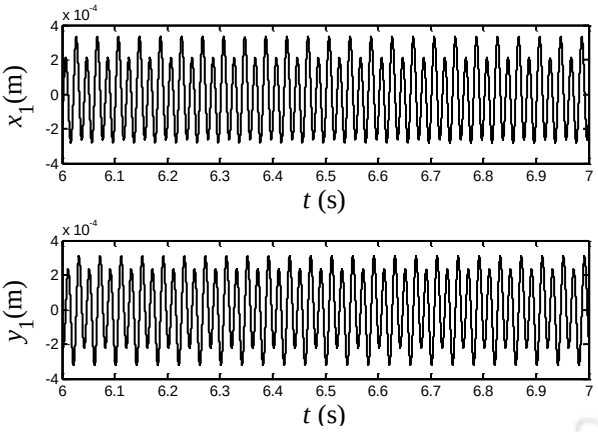

(a)

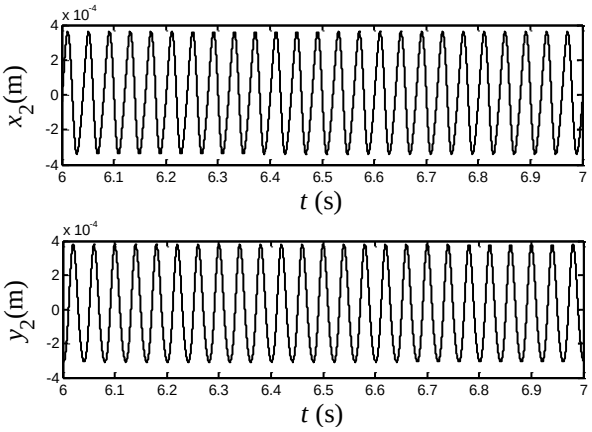

(b)

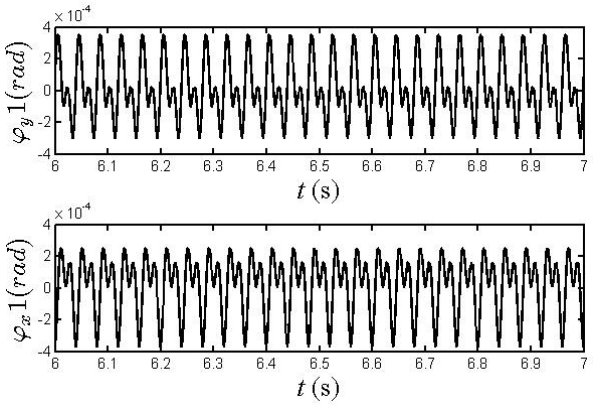

(c)

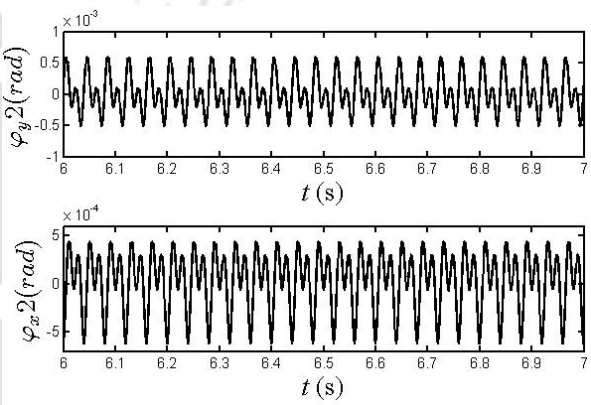

(d)

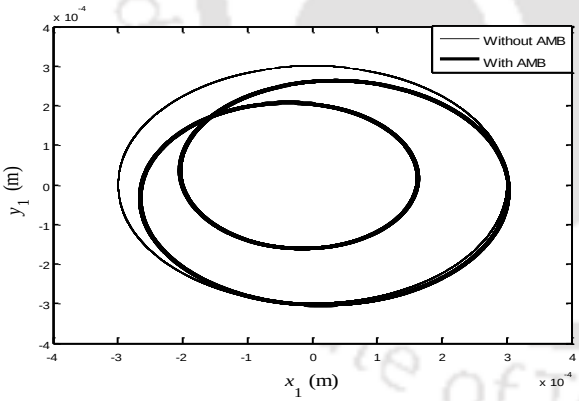

(e)

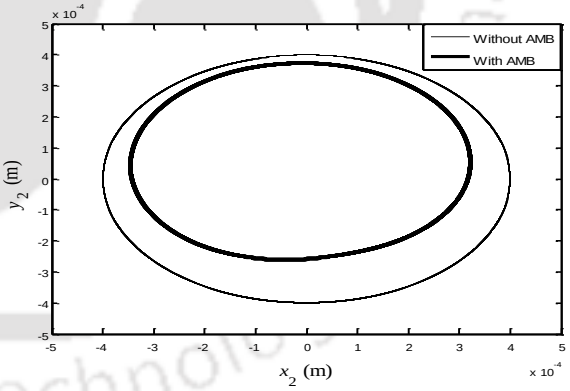

(f)

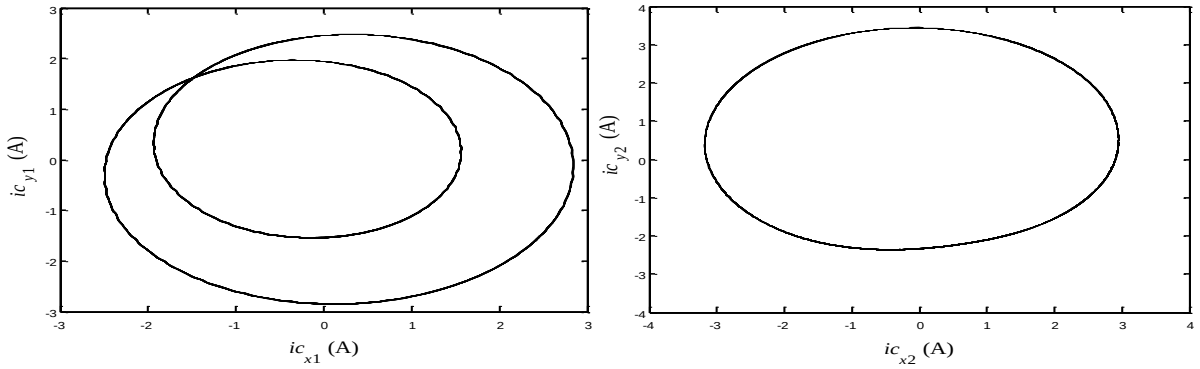

(g) (h)

Figure 3.5 Time domain response at ω_p =50 Hz, ω_g =25 Hz, ω_e =1250 Hz (a) displacement of input shaft (b) displacement of output shaft (c) angular displacement due to titling of pinion (d) angular displacement due to titling of gear (e) orbit plot of transverse vibration from input shaft (f) orbit plot of transverse vibration from output shaft (g) Orbit plot for AMB control current from input shaft (h) Orbit plot for AMB control current from output shaft.

3.6.3 Full Spectrum Analysis

To obtain the full spectrum the response data taken for a period of 1 second is considered, i.e. a complete one cycle. The amplitude and phase from the full spectrum display the characteristics of vibration level at each frequency. The relative amplitude between the forward and backward components indicates the orbit eccentricity and the direction of precession. Later, the signals from full spectrum analysis are used for estimation of fault parameters, where amplitude and phase spectrum of the fault is required from rotor. The full spectrum plot is obtained by coupling the orthogonal vibrational displacements into a complex form followed by the Fourier transform. Here, the pinion shaft has anticlockwise rotation whereas the gear shaft has clockwise rotation. The full spectrum displays multiple harmonics of excitation frequencies, which is solely due to the gear meshing error causing the DTE. The spectrum shows number of peaks at the mesh frequency (ω_e) of the gear pair and its harmonics ($n\omega_e$). These can be observed from the displacement and current spectrum shown in Figs. 3.6 and 3.7, respectively. The geared rotor has both the forward and backward whirl frequency components due to asymmetric DTE, where the harmonics of forward whirl excites the rotor in the same sense of rotation whereas the backward whirl excites the rotor in reverse sense of rotation, concurrently, with the rotation of pinion shaft. The amplitudes of full spectrum are shown on a logarithmic scale to emphasize the low amplitudes.

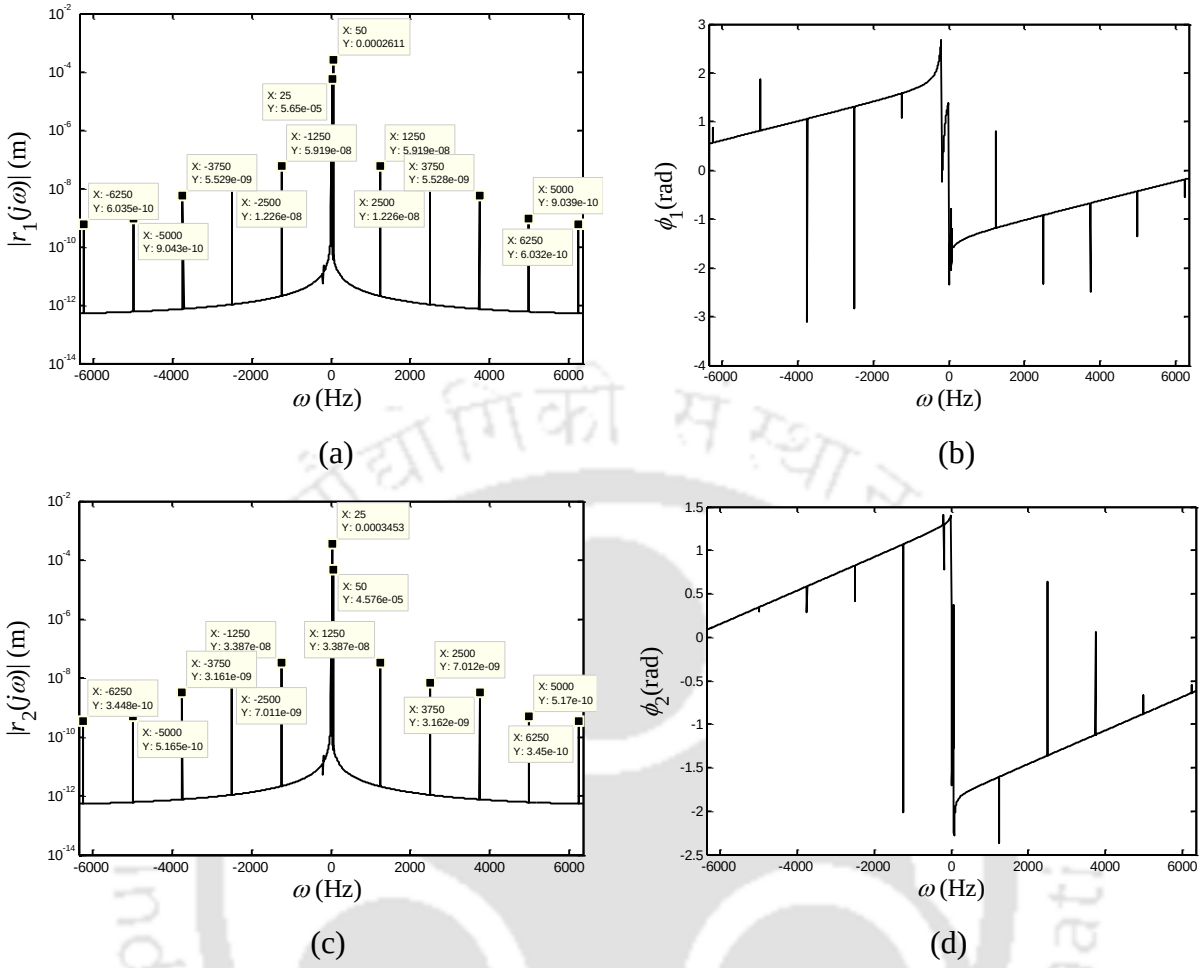

Figure 3.6 Full spectrum response generated at ω_p=50 Hz, ω_g=25 Hz, ω_e=1250 Hz (a) Amplitude of complex translational displacement for input shaft (b) Phase of complex translational displacement for input shaft (c) Amplitude of complex translational displacement for output shaft (d) Phase of complex translational displacement for output shaft.

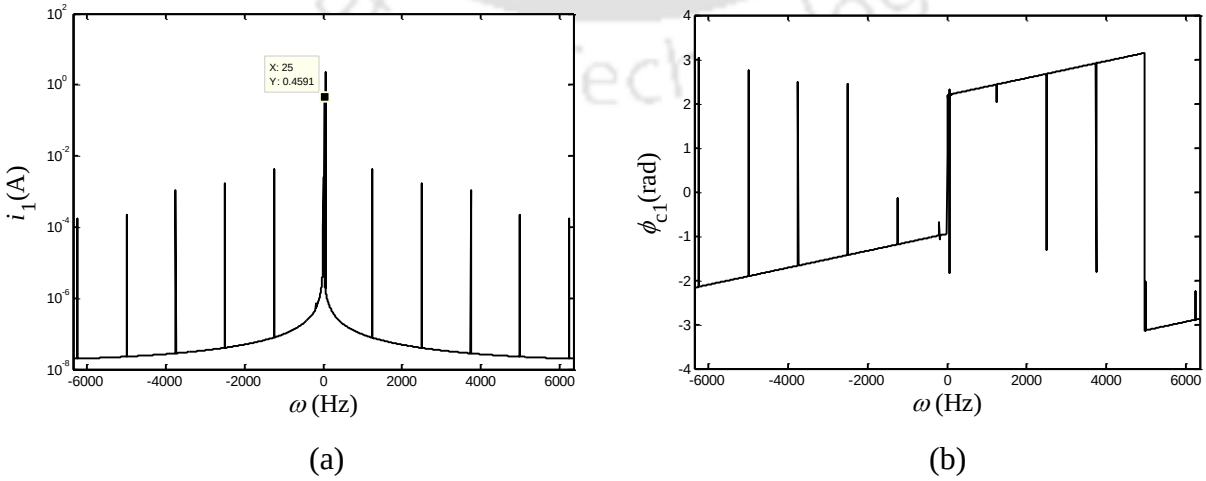

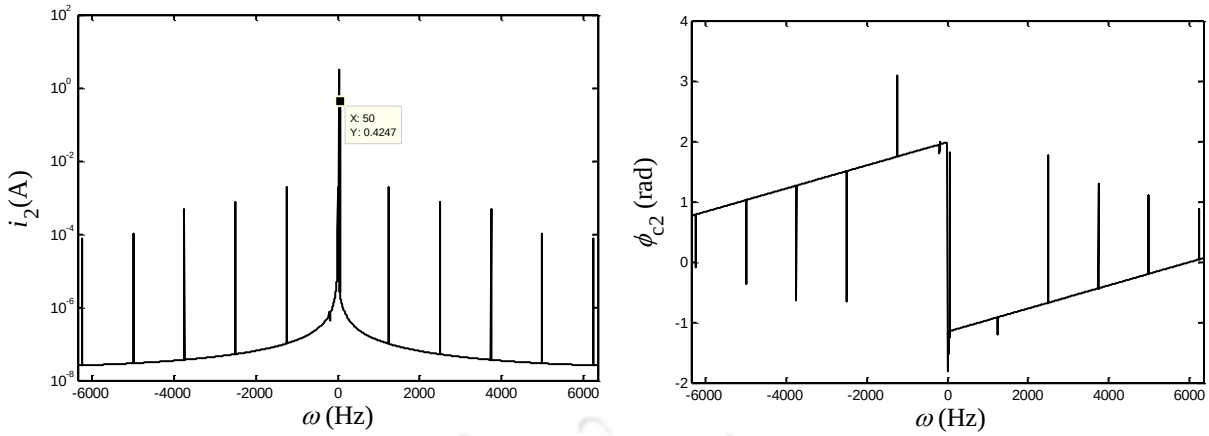

(c) (d)

Figure 3.7 Full spectrum plot for AMB control current at ω_p =50 Hz, ω_g =25 Hz, ω_e =1250 Hz (a) Amplitude of complex current for input shaft (b) Phase of complex current in input shaft (c) Amplitude of complex current for output shaft (d) Phase of complex current in output shaft

3.6.4 Estimation of Parameters with Addition of Noise and Modelling Error

The parameter estimation is done by using the multi-harmonic amplitude and phase information from the full spectrum in the identification problem. The identification algorithm obtained from the regression equation is given in **Appendix B2**. Here the assumed rotor-AMB physical parameters listed in Tables 3.1 to 3.2 are known values for the identification problem.

Due to external factors some noises are always present in the signals of real system while measuring the vibration levels, so random Gaussian noise is added to time domain solution obtained from the numerical simulation to check the robustness of the identification algorithm. Also, it is expected that the assumed physical parameters, taken for the numerical analysis, like the mass, stiffness and damping will differ from the actual system properties. Hence, the sensitiveness of the identification algorithm is checked with the addition of bias errors in the density, length and Young's modulus of the system. The parameters so obtained from the developed algorithm after addition of different noise levels and modelling error is shown in Tables 3.3 and 3.4, respectively. For the estimation, a suitable range of multiple speeds, i.e. $\omega_p = 50-60$ Hz in step of 2 Hz, $\omega_g = 25-30$ Hz in step of 1 Hz, and $\omega_e = 1250-1500$ Hz in step of 50 Hz is defined for the simulation.

Table 3.3

Identification of parameters with addition of noise at multiple spin speeds

Parameters	Assumed values	Estimated values with different percentage of noise			
		0%	1%	2%	5%
c_m	250 Nsm^{-1}	253	270	227	296
k_m	45.2×10^7 Nm^{-1}	45.3×10^7	45.5×10^7	48.11×10^7	51.1×10^7
e_p	3×10^{-4} m	299×10^{-6}	291×10^{-6}	314.1×10^{-6}	273.9×10^{-6}
e_g	4×10^{-4} m	400×10^{-6}	394.7×10^{-6}	441.1×10^{-6}	419.5×10^{-6}
ϕ_p	1.047 rad	1.047	1.012	1.109	1.241
ϕ_g	1.545 rad	1.545	1.593	1.614	1.659
k_s	217573 Nm^{-1}	219026	226491	251741	306484
k_I	$43.5NA^{-1}$	43.45	45.7	52	55
e_m	31 nm	31	31	33	40
ϕ_m	0.5236 rad	0.525	0.543	0.527	0.596
e_{f1}	30 nm	31	35	33	41
e_{f2}	25 nm	20	25	28	29
e_{f3}	35 nm	33	38	39	35
e_{f4}	11 nm	12	14	15	13
e_{f5}	12 nm	14	15	13	17
ϕ_{f1}	0.9471 rad	0.946	0.935	0.978	0.986
ϕ_{f2}	0.564 rad	0.564	0.573	0.536	0.689
ϕ_{f3}	0.3283 rad	0.329	0.345	0.393	0.413
ϕ_{f4}	0.3654 rad	0.365	0.367	0.375	0.431
ϕ_{f5}	0.3954 rad	0.395	0.386	0.326	0.429

Table 3.4

Identification of parameters with addition of modelling error

Parameters	Assumed values	Estimated values with different percentage of modelling error			
		0%	1%	2%	5%
c_m	250 Nsm^{-1}	253	260	272	289
k_m	45.2×10^7 Nm^{-1}	45.3×10^7	44.9×10^7	41.2×10^7	49.1×10^7
e_p	3×10^{-4} m	299×10^{-6}	298.3×10^{-6}	295.5×10^{-6}	273.3×10^{-6}
e_g	4×10^{-4} m	400×10^{-6}	396.4×10^{-6}	412×10^{-6}	422×10^{-6}
ϕ_p	1.047 rad	1.047	1.056	1.007	1.098
ϕ_g	1.545 rad	1.545	1.567	1.502	1.609
k_s	217573 Nm^{-1}	219026	284285	251363	297538
k_I	$43.5NA^{-1}$	43.45	47.2	49.6	58.3
e_m	31 nm	31	34	30	29
ϕ_m	0.5236 rad	0.525	0.545	0.537	0.591
e_{f1}	30 nm	31	32	26	23
e_{f2}	25 nm	20	26	25	28
e_{f3}	35 nm	33	37	31	38
e_{f4}	11 nm	12	15	13	12
e_{f5}	12 nm	14	15	11	13
ϕ_{f1}	0.9471 rad	0.946	0.952	0.983	0.941
ϕ_{f2}	0.564 rad	0.564	0.535	0.556	0.619
ϕ_{f3}	0.3283 rad	0.329	0.322	0.350	0.387
ϕ_{f4}	0.3654 rad	0.365	0.371	0.382	0.423

ϕ_{f5}	0.3954 rad	0.395	0.387	0.363	0.459

Table 3.5

Identification of parameters with addition of both noise and modelling error

Parameters	**Assumed values**	**Estimated values with different percentage of noise and modelling error**			
		0%	1%	2%	5%
c_m	250 Nsm^{-1}	253	267.27	167.7	126
k_m	45.2×10^7 Nm^{-1}	45.3×10^7	38.87×10^7	55×10^7	73.7×10^7
e_p	3×10^{-4} m	299×10^{-6}	334.2×10^{-6}	288×10^{-6}	366×10^{-6}
e_g	4×10^{-4} m	400×10^{-6}	414.7×10^{-6}	379×10^{-6}	459×10^{-6}
ϕ_p	1.047 rad	1.047	1.0508	1.0467	1.045
ϕ_g	1.545 rad	1.545	1.5405	1.5401	1.5401
k_s	217573 Nm^{-1}	219026	2.4×10^5	2.5×10^5	2.89×10^5
k_I	$43.5NA^{-1}$	43.45	69.5	52	71
e_m	31 nm	31	26	23	19
ϕ_m	0.5236 rad	0.525	0.525	0.516	0.605
e_{f1}	30 nm	31	20	19	24
e_{f2}	25 nm	20	17.61	13.79	13.6
e_{f3}	35 nm	33	21	26.73	25.3
e_{f4}	11 nm	12	13	15	17
e_{f5}	12 nm	14	16	13	18
ϕ_{f1}	0.9471 rad	0.946	0.996	1.0312	1.0708
ϕ_{f2}	0.564 rad	0.564	0.553	0.685	0.684

ϕ_{f3}	0.3283 rad	0.329	0.471	0.517	0.4183
ϕ_{f4}	0.3654 rad	0.365	0.3007	0.295	0.2932
ϕ_{f5}	0.3954 rad	0.395	0.364	0.30	0.435

The range of speeds taken for the identification problem should be suitably chosen so that the identification matrix is a well-conditioned matrix. Using the cumulative data over a range of speeds results in desirable approximation of the estimated parameters. In this paper, a range of five speeds has been taken for the identification. At 0 % noise and modelling error, the estimated values have good approximation with respect to the assumed values. With the addition of 5% noise in the vibration and current data, the maximum deviation of estimated values increases by approximately 45% and with an addition of different amount of modelling error in system properties, the estimated values get an approximate maximum deviation of 40% in the chosen speed range. It was observed that the approximate values of pinion and gear eccentricities with corresponding phase angles, AMB displacement stiffness and current stiffness can be determined quite effectively by taking less range of speeds. High-speed ranges are required for determining the values of rotor faults, which are multi-harmonic in nature. At speed range, i.e. $\omega_p = 50-58$ Hz in step of 2 Hz, $\omega_g = 25-29$ Hz in step of 1 Hz, and $\omega_e = 1250-1450$ Hz in step of 50 Hz, the amplitude and phase of the mean transmission error, mesh damping, phase of varying transmission error, suffers the least deviation. Of all the parameters, AMB displacement stiffness have comparatively higher deviation from the assumed values. It can be observed that with addition of both noise and modelling error, the mesh stiffness as well as the AMB current stiffness factor are the most varied values. Tables 4 through 6 show the closest approximate values obtained with different speed ranges. A graphical comparison is shown with addition of 0 %, 1 %, 2 % and 5 % noise in the response and current data, and 0 %, 1 %, 2 %, and 5 % addition of modelling error in the system properties, by trend of error percentage in estimated values from the expected values in Fig. 3.8.

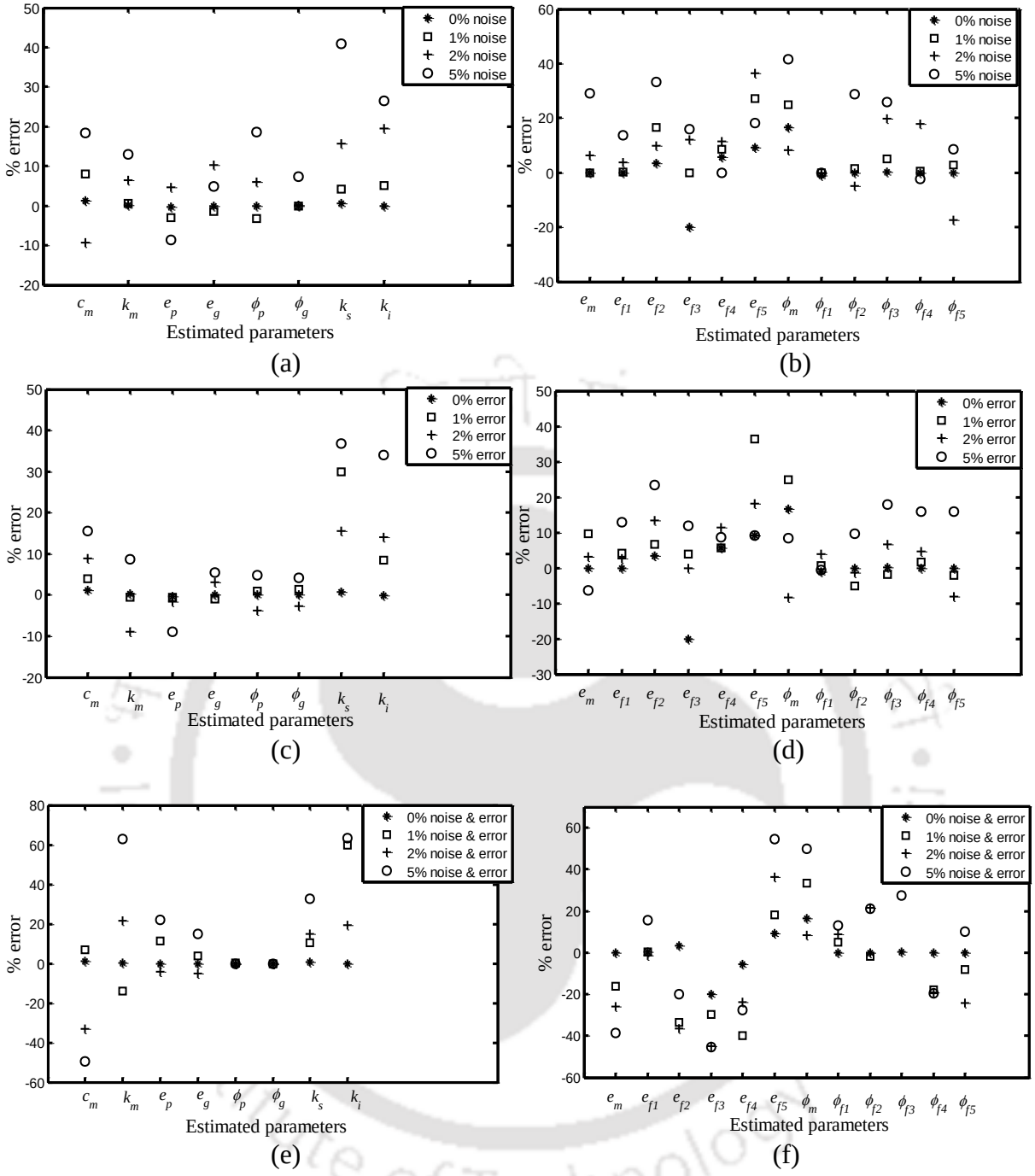

Figure. 3.8. Error percentage in estimated rotor-AMB physical parameters and dynamic transmission error with respective phase angle taking (a), (b) various levels of noise at multiple spin speed (c), (d) various percentage of modelling error at multiple spin speed (e), (f) various levels of noise and modelling error

3.7 Conclusions

A mathematical model has been developed for the transverse vibration analysis of a geared rotor system including the gyroscopic effect considering gear run-out and asymmetric dynamic transmission error. Here, the simplified model with case of transverse vibration as given in Chapter 2 is updated by adding the complexity due to the gyroscopic effect. If the gear disc is not placed in the middle, in addition to bending of shaft, the gear disc at higher spin speeds can exhibit wobbling effect. Input parameters were assumed in the numerical model. So, the effect is not much visible in simulated responses except the shift in natural frequency which is shown with help of Campbell diagram. Continuing with the mesh stiffness to be modeled in the form of dynamic transmission error for a single pair of teeth engagement, the DTE is modeled as a periodic function with multiple forward and backward harmonics in the form of asymmetric DTE**.** The dynamic transmission error is predicted under loaded condition as this excitation determines the vibration levels in a gear operation along with other rotor faults. In the present scenario, it is quite difficult to measure the rotational DOFs hence, dynamic condensation scheme has been applied to eliminate the rotational DOFs and an identification algorithm is developed from the mathematical model using regression equations to quantify the system and gear fault parameters, i.e. the gear mesh stiffness, gear mesh damping, amplitude and phase of pinion runout error, amplitude and phase of gear runout error, AMB displacement stiffness constant, AMB current stiffness constant, mean transmission error and phase, variable transmission error corresponding to different harmonics and respective phase angles. Like in Chapter 2, the identification was done using the vibration and current full spectrum responses since it gives information about both the positive and negative frequencies present in the spectrum. The estimated parameters were tested in a similar way with different percentage of random noise and modelling errors and sensitivity of the developed algorithm has been tested.

This work is further extended to conduct the coupled torsional-lateral vibration analysis with a desire to suppress the torsional vibration and development of fault identification algorithm to be continued in the next Chapter 4.

CHAPTER 4 COUPLED TORSIONL-LATERAL VIBRATION ANALYSIS OF GEARED ROTOR AMB SYSTEM WITH GYROSCOPIC EFFECT

4.1 Introduction

In the previous chapters, transverse vibrations in spur geared rotors integrated with Active Magnetic Bearings was studied and identification algorithm was developed to estimate the various geared rotor-AMB system fault parameters. In the present chapter, with similar assumptions of rotor components the analysis is extended to coupled vibrations along with gyroscopic effect where the torsional vibrations due to torques related to gear mesh frequencies are coupled with lateral vibrations.

4.2 Mathematical Model for Coupled Torsional-Lateral Vibration analysis

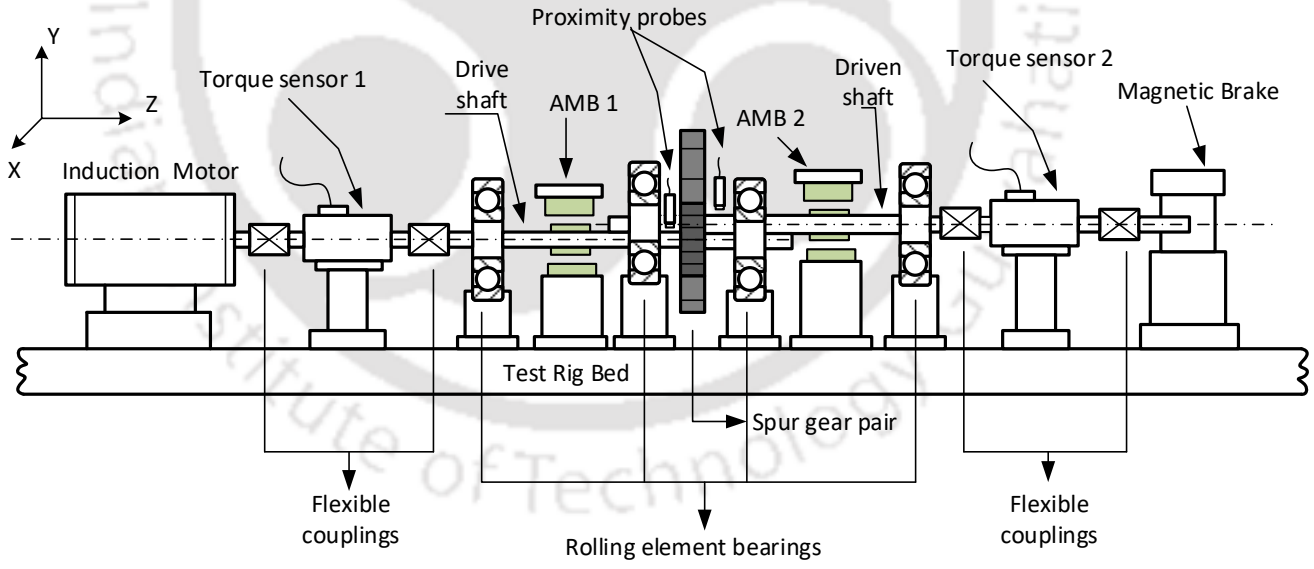

Figure 4.1 Proposed geared-rotor-AMB model

A mathematical model is developed to study the geared rotor system dynamics. The pinion and gear is modelled as wheels with angular velocity ω_p and ω_g, and polar mass moment of inertia I_{p_1} and I_{p_2}, respectively. The motor drives the input gear and the load provides the

brake torque to the driven gear. The input motor torque is named as T_P and the brake (load) torque as T_g with mass moment of inertia I_M and I_L, respectively. The input and output shafts are flexible with torsional stiffness k_{tp}, k_{tg} and lateral stiffness k_p, k_g, damping coefficients c_p, c_g, respectively. Along the contact pressure line, the mesh damping c_m is added to the model as an equivalent translational viscous damping coefficient, connected by spring with mesh stiffness k_m, which is tangent to the base circle radii r_p and r_g of the gear pair. Component of torsional damping is neglected since it is usually very small. The reason for this lies in the extremely low damping in the rotor torsional mode. In comparison to the damping in lateral modes, the torsional damping is about 10 times lower (Muszyńska 2005). Contributions to the lateral mode damping consists of material internal damping, structural damping (energy dissipated as between a rigid disk and elastic rotor), and finally, external damping. In the torsional mode, there exists only the single internal material damping mechanism (internal friction). The rotor while in running condition tends to have gear runout error due to the eccentricities e_p and e_g existing in the input and output gear giving rise to unbalance into the system.

For a simple analysis, the bearing stiffness and damping is ignored. x and y with subscripts p and g are the total translational DOFs of the pinion and geared shaft due to shaft flexibility and eccentricity in gears, respectively; while θ with subscripts MM, pp, gg, LL is the total rotational DOF about the z-axis of the motor, pinion, gear and brake load respectively. The input shaft has x_1, y_1 and output shaft has x_2, y_2 translational displacements and four torsional displacements due to gear meshing $\theta_M, \theta_p, \theta_g, \theta_L$ as shown in Fig. 4.2 in schematic diagram. Hence, the displacement equation with phase angles of pinion and gear runout defined by ϕ_p and ϕ_g can be written as

$$
\begin{aligned}
&x_p = x_1 + e_p \cos\left(\omega_p t + \phi_p\right) \; ; y_p = y_1 + e_p \sin\left(\omega_p t + \phi_p\right) \\
&x_g = x_2 + e_g \cos\left(-\omega_g t + \phi_g\right); y_g = y_2 + e_g \sin\left(-\omega_g t + \phi_g\right) \\
&\theta_{MM} = \theta_M + \omega_p t; \qquad \theta_{pp} = \theta_p + \omega_p t \\
&\theta_{gg} = \theta_g - \omega_g t; \qquad \theta_{LL} = \theta_L - \omega_g t
\end{aligned}
\tag{4.1}
$$

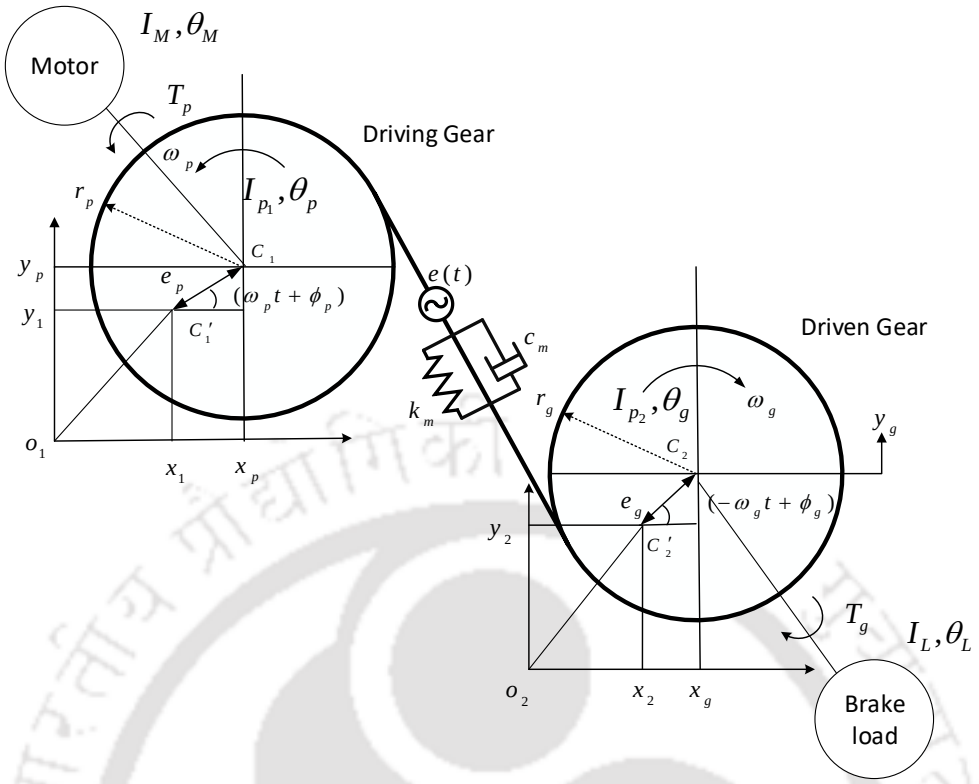

Figure 4.2 Gear mesh model with co-ordinate system

The static transmission error is modelled as an asymmetric STE as stated in Chapter 2, given by eqn. (2.2) and (2.3) with vibrational error excitation, $e(t)$, defined as small deviations in a smooth periodic signal during meshing of gears, while in operation. The deviations are like small undulations mathematically represented as the sum of mean transmission error e_m, which is constant, and varying transmission error, e_{fi}, changing with time, where $i = -n, \ldots -1, 0, 1, \ldots, n$, $n =$ number of harmonics, fluctuating about the mean.

If gears were rigid bodies, perfectly aligned and with perfectly conjugate tooth surfaces (e.g., involute profiles), the TE would be zero and the transmission of motion could be described analytically by the gear ratio. In reality, a variety of causes introduces deviations from ideal conditions and generates a variable TE that can be expressed as an angle or as a linear displacement. The angular definition is useful for torsional vibrations analysis, since it provides the relationship between the actual angular position of the driven shaft with respect to an input shaft rotation $r_p\theta_p - r_g\theta_g$. Given for each gear the rotation angle θ_p and θ_g the base radius r_p and r_g (refer Fig. 4.2).

The teeth deformation at the pitch point of the mating gears in the *x* and *y* directions are as a result of the vibrational displacement due to shaft deformation and gear runout. As indicated in Fig. 4.2, DTE along the mesh line of action with pressure angle ψ, due to the combined effect of shaft deformation, gear runouts and STE, in the *x* and *y* directions, can be expressed as

$$\begin{aligned}\delta_x &= x_1 - x_2 + e_p\cos\left(\omega_p t+\phi_p\right) - e_g\cos\left(-\omega_g t+\phi_g\right) + r_p\theta_p\cos\psi - r_g\theta_g\cos\psi - e_x\left(t\right)\\ \delta_y &= y_1 - y_2 + e_p\sin\left(\omega_p t+\phi_p\right) - e_g\sin\left(-\omega_g t+\phi_g\right) + r_p\theta_p\sin\psi - r_g\theta_g\sin\psi - e_y\left(t\right)\end{aligned} \tag{4.2}$$

4.3 Equation of Motion for Coupled Torsional-Lateral Vibration Analysis

The linear equation of motion for a pair of spur geared rotor integrated with radial active magnetic bearing considering gyroscopic effect is developed with a lumped parameter model having twelve degrees-of-freedom (DOFs) to carry out the coupled torsional-lateral vibration analysis. In inertial frame of reference, the energy equation of the geared-rotor AMB system with gyroscopic effect, i.e., the kinetic energy '*T*', potential energy '*U*', and Rayleigh's dissipation function '*D*' and the force vector '*P*' considering planer motion can be expressed as

$$T = \frac{1}{2}\begin{Bmatrix} m_1\left(\dot{x}_p^2+\dot{y}_p^2\right) + I_{d_1}(\dot{\varphi}_{x_1}^2+\dot{\varphi}_{y_1}^2) + I_{p_1}\omega_p(\dot{\varphi}_{x_1}\varphi_{y_1}-\varphi_{x_1}\dot{\varphi}_{y_1}) + I_{p_1}\omega_p^2 + I_M\dot{\theta}_{MM}^2 + I_{p_1}\dot{\theta}_{pp}^2 \\ m_2\left(\dot{x}_g^2+\dot{y}_g^2\right) + I_{d_2}(\dot{\varphi}_{x_2}^2+\dot{\varphi}_{y_2}^2) + I_{p_2}\omega_g(\dot{\varphi}_{x_2}\varphi_{y_2}-\varphi_{x_2}\dot{\varphi}_{y_2}) + I_{p_2}\omega_g^2 + I_{p_2}\dot{\theta}_{gg}^2 + I_L\dot{\theta}_{LL}^2 \end{Bmatrix} \tag{4.3}$$

On substituting eqn. (4.1) into (4.3), we get

$$T = \frac{1}{2}\begin{bmatrix} m_1\left\{\dot{x}_1 - e_p\omega_p\sin\left(\omega_p t+\phi_p\right)\right\}^2 + m_1\left\{\dot{y}_1 + e_p\omega_p\cos\left(\omega_p t+\phi_p\right)\right\}^2 + \\ +I_{d_1}\left(\dot{\varphi}_{x_1}^2+\dot{\varphi}_{y_1}^2\right) + I_{p_1}\omega_p\left(\dot{\varphi}_{x_1}\varphi_{y_1}-\varphi_{x_1}\dot{\varphi}_{y_1}\right) + I_{p_1}\omega_p^2 + I_M\left(\dot{\theta}_M+\omega_p\right)^2 + I_{p_1}\left(\dot{\theta}_p+\omega_p\right)^2 \\ m_2\left\{\dot{x}_2 + e_g\omega_g\sin\left(-\omega_g t+\phi_g\right)\right\}^2 + m_2\left\{\dot{y}_2 - e_g\omega_g\cos\left(-\omega_g t+\phi_g\right)\right\}^2 + \\ +I_{d_2}\left(\dot{\varphi}_{x_2}^2+\dot{\varphi}_{y_2}^2\right) + I_{p_2}\omega_g\left(\dot{\varphi}_{x_2}\varphi_{y_2}-\varphi_{x_2}\dot{\varphi}_{y_2}\right) + I_{p_2}\omega_g^2 + I_{p_2}\left(\dot{\theta}_g-\omega_g\right)^2 + I_L\left(\dot{\theta}_L-\omega_g\right)^2 \end{bmatrix} \tag{4.4}$$

Similarly, the term for potential energy can be written as

$$U=\frac{1}{2}\left\{\begin{array}{l} k_{pxx}x_p^2+k_{pyy}y_p^2+k_{px\varphi_y}x_p\varphi_{y_1}+k_{p\varphi_yx}\varphi_{y_1}x_p+k_{py\varphi_x}y_p\varphi_{x_1}+k_{p\varphi_xy}\varphi_{x_1}y_p+k_{p\varphi_x\varphi_x}\varphi_{x_1}\varphi_{x_1}+k_{p\varphi_y\varphi_y}\varphi_{y_1}\varphi_{y_1}+ \\ k_{gxx}{x_g}^2+k_{gyy}{y_g}^2+k_{gx\varphi_y}x_g\varphi_{y_2}+k_{g\varphi_yx}\varphi_{y_2}x_g+k_{gy\varphi_x}y_g\varphi_{x_2}+k_{g\varphi_xy}\varphi_{x_2}y_g+k_{g\varphi_x\varphi_x}\varphi_{x_2}\varphi_{x_2}+k_{g\varphi_y\varphi_y}\varphi_{y_2}\varphi_{y_2}+ \\ k_m\left({\delta_x}^2+{\delta_y}^2\right)+k_{tp}\left(\theta_{pp}-\theta_{MM}\right)^2+k_{tg}\left(\theta_{gg}-\theta_{LL}\right)^2 \end{array}\right\} \tag{4.5}$$

We know that for input shaft

$$k_{pxx}=k_{pyy}=k_p, k_{p\varphi_x\varphi_x}=k_{p\varphi_y\varphi_y},\ k_{px\varphi_y}=k_{py\varphi_x},\ k_{p\varphi_yx}=k_{p\varphi_xy} \tag{4.6}$$

Similarly, for output shaft

$$k_{gxx}=k_{gyy}=k_g,\ k_{g\varphi_x\varphi_x}=k_{g\varphi_y\varphi_y},\ k_{gx\varphi_y}=k_{gy\varphi_x},\ k_{g\varphi_yx}=k_{g\varphi_xy} \tag{4.7}$$

For the linear range, in the homogeneous and isotropic material,

$$k_{px\varphi_y}=k_{p\varphi_yx}\ ;\ k_{py\varphi_x}=k_{p\varphi_xy} \text{ and } k_{gx\varphi_y}=k_{g\varphi_yx}\ ;\ k_{gy\varphi_x}=k_{g\varphi_xy} \tag{4.8}$$

Rearranging and on substituting eqns. (4.6), (4.7), (4.8) in (4.5), we get

$$U=\frac{1}{2}\left[\begin{array}{l} k_p\left\{x_1+e_p\cos\left(\omega_pt+\phi_p\right)\right\}^2+k_p\left\{y_1+e_p\sin\left(\omega_pt+\phi_p\right)\right\}^2+2k_{p_{la}}\left\{x_1+e_p\cos\left(\omega_pt+\phi_p\right)\right\}\varphi_{y_1} \\ +2k_{p_{la}}\varphi_{x_1}\left\{y_1+e_p\sin\left(\omega_pt+\phi_p\right)\right\}+k_{p_a}\left(\varphi_{x_1}^2+\varphi_{y_1}^2\right)+k_{tp}\left(\theta_p-\theta_M\right)^2 \\ +k_g\left\{x_2+e_g\cos\left(-\omega_gt+\phi_g\right)\right\}^2+k_g\left\{y_2+e_g\sin\left(-\omega_gt+\phi_g\right)\right\}^2+2k_{g_{la}}\left\{x_2+e_g\cos\left(-\omega_gt+\phi_g\right)\right\}\varphi_{y_2} \\ +2k_{g_{la}}\varphi_{x_2}\left\{y_2+e_g\sin\left(-\omega_gt+\phi_g\right)\right\}+k_{g_a}\left(\varphi_{x_2}^2+\varphi_{y_2}^2\right)+k_{tg}\left(\theta_g-\theta_L\right)^2 \\ +k_m\left\{x_1-x_2+e_p\cos\left(\omega_pt+\phi_p\right)-e_g\cos\left(-\omega_gt+\phi_g\right)+r_p\theta_p\cos\psi-r_g\theta_g\cos\psi-e_x(t)\right\}^2 \\ +k_m\left\{y_1-y_2+e_p\sin\left(\omega_pt+\phi_p\right)-e_g\sin\left(-\omega_gt+\phi_g\right)+r_p\theta_p\sin\psi-r_g\theta_g\sin\psi-e_y(t)\right\}^2 \end{array}\right] \tag{4.9}$$

Likewise, the Rayleigh's dissipative function due to viscous damping can be written as

$$D=\frac{1}{2}\begin{Bmatrix} c_{pxx}\dot{x}_p^2+c_{pyy}\dot{y}_p^2+c_{px\varphi_y}\dot{x}_p\dot{\varphi}_{y_1}+c_{p\varphi_yx}\dot{\varphi}_{y_1}\dot{x}_p+c_{py\varphi_x}\dot{y}_p\dot{\varphi}_{x_1}+c_{p\varphi_xy}\dot{\varphi}_{x_1}\dot{y}_p+c_{p\varphi_x\varphi_x}\dot{\varphi}_{x_1}\dot{\varphi}_{x_1}+c_{p\varphi_y\varphi_y}\dot{\varphi}_{y_1}\dot{\varphi}_{y_1} \\ c_{gxx}\dot{x}_g{}^2+c_{gyy}\dot{y}_g{}^2+c_{gx\varphi_y}\dot{x}_g\dot{\varphi}_{y_2}+c_{g\varphi_yx}\dot{\varphi}_{y_2}\dot{x}_g+c_{gy\varphi_x}\dot{y}_g\dot{\varphi}_{x_2}+c_{g\varphi_xy}\dot{\varphi}_{x_2}\dot{y}_g+c_{g\varphi_x\varphi_x}\dot{\varphi}_{x_2}\dot{\varphi}_{x_2}+c_{g\varphi_y\varphi_y}\dot{\varphi}_{y_2}\dot{\varphi}_{y_2}+ \\ c_m\left(\dot{\delta}_x{}^2+\dot{\delta}_y{}^2\right) \end{Bmatrix} \tag{4.10}$$

Also, assuming that for input shaft

$$c_{pxx}=c_{pyy}=c_p\,;c_{p\varphi_x\varphi_x}=c_{p\varphi_y\varphi_y}\,;\;c_{px\varphi_y}=c_{py\varphi_x}\,;\;c_{p\varphi_yx}=c_{p\varphi_xy} \tag{4.11}$$

Similarly, for the output shaft

$$c_{gxx}=c_{gyy}=c_g\,;\;c_{g\varphi_x\varphi_x}=c_{g\varphi_y\varphi_y}\,;\;c_{gx\varphi_y}=c_{gy\varphi_x}\,;\;c_{g\varphi_yx}=c_{g\varphi_xy} \tag{4.12}$$

while, neglecting the coupled and rotational components of damping terms and taking linear range, in homogeneous and isotropic material, we get

$$c_{px\varphi_y}=c_{p\varphi_yx}=0\,;\;c_{gx\varphi_y}=c_{g\varphi_yx}=0\;;\;\;c_{p\varphi_x\varphi_x}=c_{g\varphi_x\varphi_x}=0 \tag{4.13}$$

So eqn. (4.10) becomes

$$D=\frac{1}{2}\begin{bmatrix} c_p\left\{\dot{x}_1-e_p\omega_p\sin\left(\omega_pt+\phi_p\right)\right\}^2+c_p\left\{\dot{y}_1+e_p\omega_p\cos\left(\omega_pt+\phi_p\right)\right\}^2+ \\ c_g\left\{\dot{x}_2+e_g\omega_g\sin\left(-\omega_gt+\phi_g\right)\right\}^2+c_g\left\{\dot{y}_2-e_g\omega_g\cos\left(-\omega_gt+\phi_g\right)\right\}^2+ \\ c_m\left\{\dot{x}_1-\dot{x}_2-e_p\omega_p\sin\left(\omega_pt+\phi_p\right)-e_g\omega_g\sin\left(-\omega_gt+\phi_g\right)-r_p\dot{\theta}_p\sin\psi+r_g\dot{\theta}_g\sin\psi-\dot{e}_x\left(t\right)\right\}^2+ \\ c_m\left\{\dot{y}_1-\dot{y}_2+e_p\omega_p\cos\left(\omega_pt+\phi_p\right)+e_g\omega_g\cos\left(-\omega_gt+\phi_g\right)+r_p\dot{\theta}_p\cos\psi-r_g\dot{\theta}_g\cos\psi-\dot{e}_y\left(t\right)\right\}^2 \end{bmatrix} \tag{4.14}$$

4.4 Equation of Motion in Matrix Form

The governing differential equation of the geared rotor system with the gyroscopic effect is derived using the extended Lagrange's equation and can be put into matrix form as

$$\mathbf{M}\ddot{\mathbf{q}}+\left(\mathbf{C}-\omega_L\mathbf{G}\right)\dot{\mathbf{q}}+\mathbf{K}\mathbf{q}=\mathbf{f}_{\text{unb}}+\mathbf{f}_{\text{r\_out}}+\mathbf{f}_{\text{mesh}}+\mathbf{f}_{\text{tor}}-\mathbf{f}_{\text{amb}} \tag{4.15}$$

The generalised coordinate **q** is given by

$$\mathbf{q}=\left\{q_1 \quad \cdots \quad q_{12}\right\}^T=\left\{x_1 \quad y_1 \quad \varphi_{y1} \quad \varphi_{x1} \quad \theta_M \quad \theta_p \quad x_2 \quad y_2 \quad \varphi_{y2} \quad \varphi_{x2} \quad \theta_g \quad \theta_L\right\}^T \tag{4.16}$$

where, **M** is the mass matrix, **C** is the damping matrix, **K** is the stiffness matrix, the gyroscopic effect is characterised by a skew-symmetric gyroscopic matrix **G**, $\mathbf{f}_{\text{unb}}(t)$ is the unbalance force vector, $\mathbf{f}_{\text{r\_out}}(t)$ is the force vector due to gear runout, $\mathbf{f}_{\text{amb}}(t)$ is the controlled magnetic force vector, $\mathbf{f}_{\text{mesh}}(t)$ is the dynamic mesh force vector acting on the system, $\mathbf{f}_{\text{tor}}(t)$ is the force due to external torque applied and **q**(t) is the generalised coordinate vector considering excitation at the pitch point of the gear mesh, while the details of the matrices are given below.

$$\mathbf{M}=\begin{bmatrix}
m_1 & 0 & 0 & 0 & 0 & 0 & 0 & 0 & 0 & 0 & 0 & 0 \\
0 & m_1 & 0 & 0 & 0 & 0 & 0 & 0 & 0 & 0 & 0 & 0 \\
0 & 0 & I_{d_1} & 0 & 0 & 0 & 0 & 0 & 0 & 0 & 0 & 0 \\
0 & 0 & 0 & I_{d_1} & 0 & 0 & 0 & 0 & 0 & 0 & 0 & 0 \\
0 & 0 & 0 & 0 & I_M & 0 & 0 & 0 & 0 & 0 & 0 & 0 \\
0 & 0 & 0 & 0 & 0 & I_{p_1} & 0 & 0 & 0 & 0 & 0 & 0 \\
0 & 0 & 0 & 0 & 0 & 0 & m_2 & 0 & 0 & 0 & 0 & 0 \\
0 & 0 & 0 & 0 & 0 & 0 & 0 & m_2 & 0 & 0 & 0 & 0 \\
0 & 0 & 0 & 0 & 0 & 0 & 0 & 0 & I_{d_2} & 0 & 0 & 0 \\
0 & 0 & 0 & 0 & 0 & 0 & 0 & 0 & 0 & I_{d_2} & 0 & 0 \\
0 & 0 & 0 & 0 & 0 & 0 & 0 & 0 & 0 & 0 & I_{p_2} & 0 \\
0 & 0 & 0 & 0 & 0 & 0 & 0 & 0 & 0 & 0 & 0 & I_L
\end{bmatrix} \quad \mathbf{q}=\begin{bmatrix}
x_1 \\ y_1 \\ \varphi_{y_1} \\ \varphi_{x_1} \\ \theta_M \\ \theta_p \\ x_2 \\ y_2 \\ \varphi_{y_2} \\ \varphi_{x_2} \\ \theta_g \\ \theta_L
\end{bmatrix}$$

$$(\mathbf{C}-\omega_L\mathbf{G})=\begin{bmatrix}
c_p+c_m & 0 & 0 & 0 & 0 & c_m r_p\cos\psi & -c_m & 0 & 0 & 0 & -c_m r_g\cos\psi & 0\\
0 & c_p+c_m & 0 & 0 & 0 & c_m r_p\sin\psi & 0 & -c_m & 0 & 0 & -c_m r_g\sin\psi & 0\\
0 & 0 & 0 & -\omega_p I_{p_1} & 0 & 0 & 0 & 0 & 0 & 0 & 0 & 0\\
0 & 0 & \omega_p I_{p_1} & 0 & 0 & 0 & 0 & 0 & 0 & 0 & 0 & 0\\
0 & 0 & 0 & 0 & 0 & 0 & 0 & 0 & 0 & 0 & 0 & 0\\
c_m r_p\cos\psi & c_m r_p\sin\psi & 0 & 0 & 0 & c_m {r_p}^2 & -c_m r_p\cos\psi & -c_m r_p\sin\psi & 0 & 0 & -c_m r_p r_g & 0\\
-c_m & 0 & 0 & 0 & 0 & -c_m r_p\cos\psi & c_g+c_m & 0 & 0 & 0 & c_m r_g\cos\psi & 0\\
0 & -c_m & 0 & 0 & 0 & -c_m r_p\sin\psi & 0 & c_g+c_m & 0 & 0 & c_m r_g\sin\psi & 0\\
0 & 0 & 0 & 0 & 0 & 0 & 0 & 0 & 0 & -\omega_g I_{p_2} & 0 & 0\\
0 & 0 & 0 & 0 & 0 & 0 & 0 & 0 & \omega_g I_{p_2} & 0 & 0 & 0\\
-c_m r_g\cos\psi & -c_m r_g\sin\psi & 0 & 0 & 0 & -c_m r_p r_g & c_m r_g\cos\psi & c_m r_g\sin\psi & 0 & 0 & c_m {r_g}^2 & 0\\
0 & 0 & 0 & 0 & 0 & 0 & 0 & 0 & 0 & 0 & 0 & 0
\end{bmatrix}$$

$$\mathbf{K}=\begin{bmatrix}
k_p+k_m & 0 & k_{px\varphi_y} & 0 & 0 & k_m r_p\cos\psi & -k_m & 0 & 0 & 0 & -k_m r_g\cos\psi & 0\\
0 & k_p+k_m & 0 & k_{px\varphi_y} & 0 & k_m r_p\sin\psi & 0 & -k_m & 0 & 0 & -k_m r_g\sin\psi & 0\\
k_{px\varphi_y} & 0 & k_{p\varphi_x\varphi_x} & 0 & 0 & 0 & 0 & 0 & 0 & 0 & 0 & 0\\
0 & k_{px\varphi_y} & 0 & k_{p\varphi_x\varphi_x} & 0 & 0 & 0 & 0 & 0 & 0 & 0 & 0\\
0 & 0 & 0 & 0 & k_{tp} & -k_{tp} & 0 & 0 & 0 & 0 & 0 & 0\\
k_m r_p\cos\psi & k_m r_p\sin\psi & 0 & 0 & -k_{tp} & k_{tp}+k_m {r_p}^2 & -k_m r_p\cos\psi & -k_m r_p\sin\psi & 0 & 0 & -k_m r_p r_g & 0\\
-k_m & 0 & 0 & 0 & 0 & -k_m r_p\cos\psi & k_g+k_m & 0 & k_{gx\varphi_y} & 0 & k_m r_g\cos\psi & 0\\
0 & -k_m & 0 & 0 & 0 & -k_m r_p\sin\psi & 0 & k_g+k_m & 0 & k_{gx\varphi_y} & k_m r_g\sin\psi & 0\\
0 & 0 & 0 & 0 & 0 & 0 & k_{gx\varphi_y} & 0 & k_{g\varphi_x\varphi_x} & 0 & 0 & 0\\
0 & 0 & 0 & 0 & 0 & 0 & 0 & k_{gx\varphi_y} & 0 & k_{g\varphi_x\varphi_x} & 0 & 0\\
-k_m r_g\cos\psi & -k_m r_g\sin\psi & 0 & 0 & 0 & -k_m r_p r_g & k_m r_g\cos\psi & k_m r_g\sin\psi & 0 & 0 & k_{tg}+k_m {r_g}^2 & -k_{tg}\\
0 & 0 & 0 & 0 & 0 & 0 & 0 & 0 & 0 & 0 & -k_{tg} & k_{tg}
\end{bmatrix}$$

The force vector equation in simplified form is written as: -

$$\mathbf{f}_{\text{unb}} = \begin{bmatrix} \left(m_1 e_p \omega_p^2\right)\cos\left(\omega_p t + \phi_p\right) \\ \left(m_1 e_p \omega_p^2\right)\sin\left(\omega_p t + \phi_p\right) \\ 0 \\ 0 \\ 0 \\ 0 \\ \left(m_2 e_g \omega_g^2\right)\cos\left(-\omega_g t + \phi_g\right) \\ \left(m_2 e_g \omega_g^2\right)\sin\left(-\omega_g t + \phi_g\right) \\ 0 \\ 0 \\ 0 \\ 0 \end{bmatrix} \quad \mathbf{f}_{\text{tor}} = \begin{bmatrix} 0 \\ 0 \\ 0 \\ 0 \\ T_p \\ 0 \\ 0 \\ 0 \\ 0 \\ 0 \\ 0 \\ -T_g \end{bmatrix} \quad \mathbf{f}_{\text{amb}} = \begin{bmatrix} -k_s x_1 + k_I i_{c_{x_1}} \\ -k_s y_1 + k_I i_{c_{y_1}} \\ 0 \\ 0 \\ 0 \\ 0 \\ -k_s x_2 + k_I i_{c_{x_2}} \\ -k_s y_2 + k_I i_{c_{y_2}} \\ 0 \\ 0 \\ 0 \\ 0 \end{bmatrix}$$

$$\mathbf{f}_{\text{r\_out}} = \begin{bmatrix} -k_p e_p \cos\left(\omega_p t + \phi_p\right) \\ -k_p e_p \sin\left(\omega_p t + \phi_p\right) \\ -k_{px\varphi_y} e_p \cos\left(\omega_p t + \phi_p\right) \\ -k_{px\varphi_y} e_p \sin\left(\omega_p t + \phi_p\right) \\ 0 \\ 0 \\ -k_g e_g \cos\left(-\omega_g t + \phi_g\right) \\ -k_g e_g \sin\left(-\omega_g t + \phi_g\right) \\ -k_{gx\varphi_y} e_g \cos\left(-\omega_g t + \phi_g\right) \\ -k_{gx\varphi_y} e_g \sin\left(-\omega_g t + \phi_g\right) \\ 0 \\ 0 \end{bmatrix} + \begin{bmatrix} c_p e_p \omega_p \sin\left(\omega_p t + \phi_p\right) \\ -c_p e_p \omega_p \cos\left(\omega_p t + \phi_p\right) \\ 0 \\ 0 \\ 0 \\ 0 \\ -c_g e_g \omega_g \sin\left(-\omega_g t + \phi_g\right) \\ c_g e_g \omega_g \cos\left(-\omega_g t + \phi_g\right) \\ 0 \\ 0 \\ 0 \\ 0 \end{bmatrix}$$

$$
\mathbf{f}_{\text{mesh}} = k_m \begin{bmatrix}
-e_p \cos\left(\omega_p t + \phi_p\right) + e_g \cos\left(-\omega_g t + \phi_g\right) + e_x(t) \\
-e_p \sin\left(\omega_p t + \phi_p\right) + e_g \sin\left(-\omega_g t + \phi_g\right) + e_y(t) \\
0 \\
0 \\
0 \\
-e_p r_p \begin{Bmatrix} \cos\left(\omega_p t + \phi_p\right) \\ +\sin\left(\omega_p t + \phi_p\right) \end{Bmatrix} + r_p \left\{ e_x(t) + e_y(t) \right\} + e_g r_p \begin{Bmatrix} \cos\left(-\omega_g t + \phi_g\right) \\ +\sin\left(-\omega_g t + \phi_g\right) \end{Bmatrix} \\
e_p \cos\left(\omega_p t + \phi_p\right) - e_g \cos\left(-\omega_g t + \phi_g\right) - e_x(t) \\
e_p \sin\left(\omega_p t + \phi_p\right) - e_g \sin\left(-\omega_g t + \phi_g\right) - e_y(t) \\
0 \\
0 \\
e_p r_g \begin{Bmatrix} \cos\left(\omega_p t + \phi_p\right) \\ +\sin\left(\omega_p t + \phi_p\right) \end{Bmatrix} - r_g \left\{ e_x(t) + e_y(t) \right\} - e_g r_g \begin{Bmatrix} \cos\left(-\omega_g t + \phi_g\right) \\ +\sin\left(-\omega_g t + \phi_g\right) \end{Bmatrix} \\
0
\end{bmatrix}
$$

$$
+ c_m \begin{bmatrix}
e_p \omega_p \sin\left(\omega_p t + \phi_p\right) + e_g \omega_g \sin\left(-\omega_g t + \phi_g\right) + \dot{e}_x(t) \\
-e_p \omega_p \cos\left(\omega_p t + \phi_p\right) - e_g \omega_g \cos\left(-\omega_g t + \phi_g\right) + \dot{e}_y(t) \\
0 \\
0 \\
0 \\
-r_p \left[-e_p \omega_p \begin{Bmatrix} \sin\left(\omega_p t + \phi_p\right) \\ -\cos\left(\omega_p t + \phi_p\right) \end{Bmatrix} - e_g \omega_g \begin{Bmatrix} \sin\left(-\omega_g t + \phi_g\right) \\ -\cos\left(-\omega_g t + \phi_g\right) \end{Bmatrix} - \begin{Bmatrix} \dot{e}_x(t) \\ +\dot{e}_y(t) \end{Bmatrix} \right] \\
-e_p \omega_p \sin\left(\omega_p t + \phi_p\right) - e_g \omega_g \sin\left(-\omega_g t + \phi_g\right) - \dot{e}_x(t) \\
e_p \omega_p \cos\left(\omega_p t + \phi_p\right) + e_g \omega_g \cos\left(-\omega_g t + \phi_g\right) - \dot{e}_y(t) \\
0 \\
0 \\
r_g \left[-e_p \omega_p \begin{Bmatrix} \sin\left(\omega_p t + \phi_p\right) \\ -\cos\left(\omega_p t + \phi_p\right) \end{Bmatrix} - e_g \omega_g \begin{Bmatrix} \sin\left(-\omega_g t + \phi_g\right) \\ -\cos\left(-\omega_g t + \phi_g\right) \end{Bmatrix} - \begin{Bmatrix} \dot{e}_x(t) \\ +\dot{e}_y(t) \end{Bmatrix} \right] \\
0
\end{bmatrix} \tag{4.17}
$$

Subsequently, numerical studies are performed with the equations expressed within a matrix-vector form, used to obtain the dynamic responses of the geared rotor AMB system.

4.5 Numerical Analysis of Geared Rotor AMB System with gyroscopic effect

The numerical simulation of the developed model for analysis of coupled vibrations in a geared rotor AMB system taking gyroscopic effect into account is performed using the system's EOM stated in eqn. (4.10). The input to the PID controller is the displacement at the sensor points itself. The time domain solution is obtained by using Simulink in MATLAB, which is shown in Fig.4.3. The time-step for the simulation is taken as 0.00006 s, and fourth-order Runge-Kutta (RK4) is taken as the solver, same as the previous case.

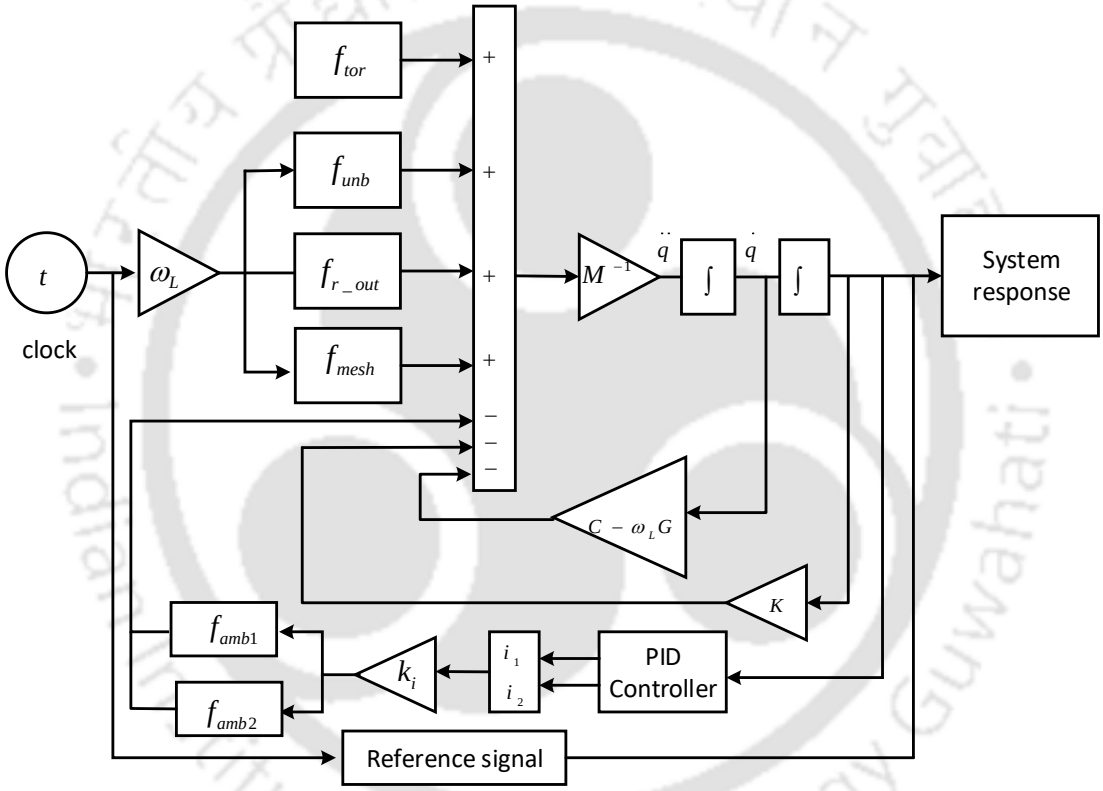

Figure. 4.3 Pictorial representation of the Simulink block

4.5.1 Numerical Simulation Results

The vibration response based on EOMs given in eqn. (4.15) are generated in both time and frequency domain. The dynamic response obtained for the selected parameters are given in Table 4.1.

Table 4.1

Assumed geared-rotor parameters

Parameters	**Assumed values**
Diameter of input and output shafts	0.012 m
Length of input and output shafts	0.4 m
Gear-pair module	1.5
Gear ratio	2
Gear-pair pressure angle (FDI)	20 deg.
Number of teeth (pinion)	25
Number of teeth (gear)	50
Shaft material density	7860 kg/m^3
Young's modulus	2.068×10^{11} Pa
m_1, m_2	2.88 kg, 3.38 kg
ω_p, ω_g	50:2:60 Hz, 25:30 Hz
e_p, e_g	0.0003 m, 0.0004 m
c_p, c_g	49.63 N-s/m, 69.5 N-s/m
c_m	150 N-s/m
k_m	12.0257×10^6 N/m
k_p, k_g	4.25×10^6 N/m, 6.62×10^6 N/m
$k_{px\varphi_y}, k_{gx\varphi_y}$	4.5×10^3 N/rad, 5.5×10^3 N/rad
$k_{p\varphi_x\varphi_x}, k_{g\varphi_x\varphi_x}$	1.7×10^3 Nm/rad, 1.5×10^3 Nm/rad
k_{tp}, k_{tg}	4.5×10^2 Nm/rad, 5.5×10^2 Nm/rad
ω_e	1250:50:1500 Hz
ϕ_p, ϕ_g	1.047 rad, 1.545 rad.
I_{p_1}, I_{p_2}	0.0048,0.0088 kg-m^2

I_{d_1}, I_{d_2}	0.0024,0.0044 kg-m^2
I_M, I_L	0.021, 0.0105 kg-m^2
T_p, T_g	5, 10 Nm
e_m	31 nm
ϕ_m	0.5236 rad.
e_{fi}	30 nm, 25 nm, 35 nm, 11 nm, 12 nm
ϕ_{fi}	0.9471 rad, 0.5640 rad, 0.3283 rad, 0.3654 rad, 0.3954 rad.

Table 4.2

PID Controller gains

	Gains	Values	Units
AMB 1	K_p	1800	A/m
	K_D	5	As/m
	K_I	1500	A/m-s
AMB 2	K_p	1800	A/m
	K_D	4	As/m
	K_I	1100	A/m-s

As explained in Chapter 2, the tuning of PID controller gains is selected by trial-and-error method and checked with Nyquist stability criteria. Table 4.2 shows the adjustable PID controller gain values, which gives the desired control current to the actuator poles, such that the vibration levels of the system are minimized.

4.5.2 Time domain solution

On solving the differential eqn. (4.15) by using fourth-order Runge-Kutta integration method, the performance of AMB can be obtained. The response for initial 5 sec. is discarded for a steady state response. The initial transient part is removed and the response recorded from 6-7 sec is shown in Fig. 4.4 since with a PID controller greater settling time is required. From the time domain numerical responses, it can be observed that the rotor transverse vibration is

suppressed efficiently by the radial forces generated by the AMB actuator. Since the geared rotor is subjected to have coupled torsional-lateral vibration so this tends to reduce the torsional vibration as well as shown in Fig. 4.4(c).

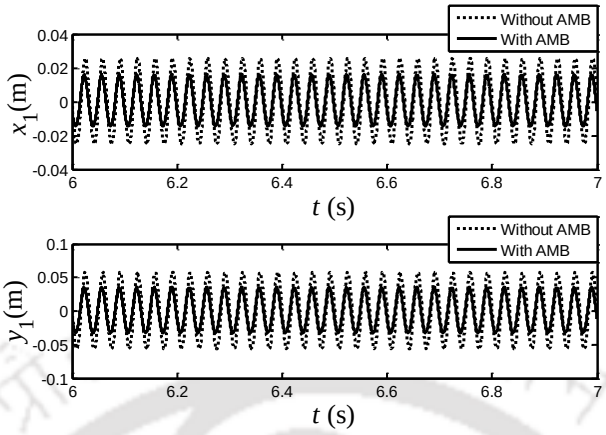

(a)

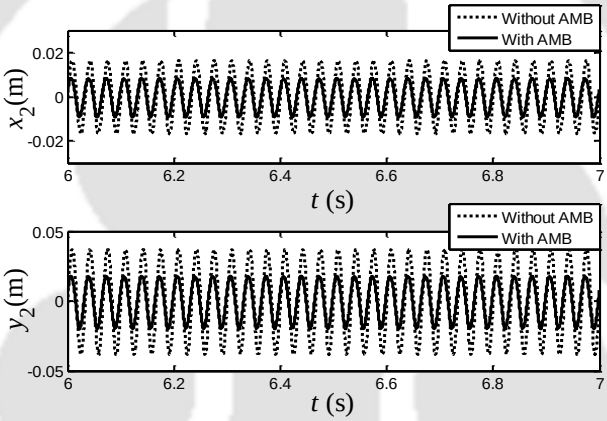

(b)

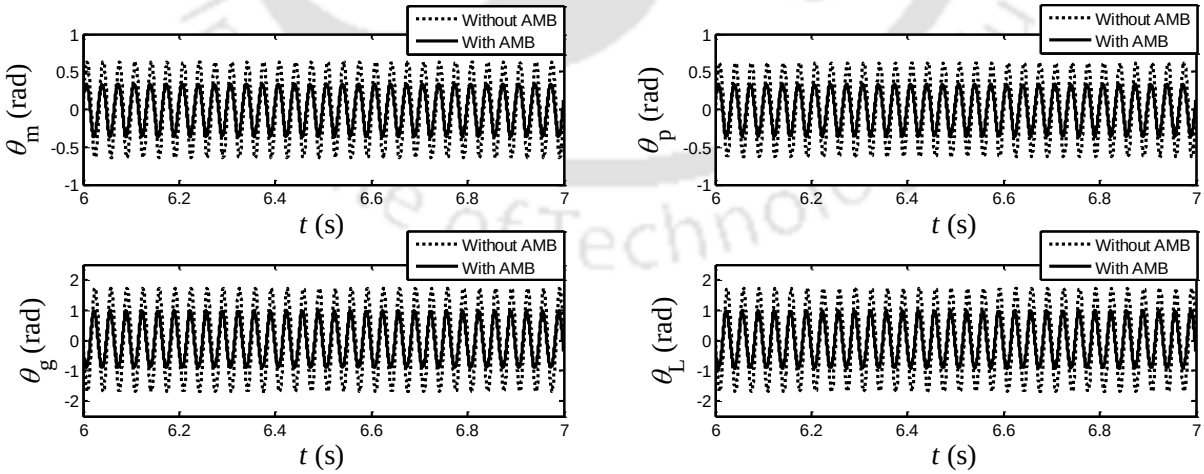

(c)

Figure 4.4. Time domain response at $\omega_p = 60\text{Hz}$, $\omega_g = 30\text{Hz}$, $\omega_e = 1500\text{Hz}$ (a) x, y displacement of input shaft (b) *x, y* displacement of output shaft (c) torsional displacement of motor, pinion, gear, load respectively.

4.5.3 Frequency domain solution

Full spectrum is constructed by taking complete cycles of time domain data. The amplitude and phase from full spectrum display the characteristics of vibration level at each frequency. The full spectrum displays multiple harmonics of excitation frequencies, solely due to the gear meshing error caused by the DTE. The relative amplitude between the forward and backward components indicates the ellipticity and the direction of precession. The spectrum shows number of peaks at mesh frequency (ω_e) of the gear pair and its harmonics. These can be observed from the spectrum diagram shown in Fig. 4.5. The geared rotor has both forward and backward whirl frequency components due to asymmetric DTE, where the harmonics of forward whirl excites the rotor in the same sense of rotation whereas the backward whirl excites the rotor in reverse sense of rotation, simultaneously, with the rotation of driving shaft. The amplitudes of full spectrum are shown on a logarithmic scale to emphasize the low amplitudes.

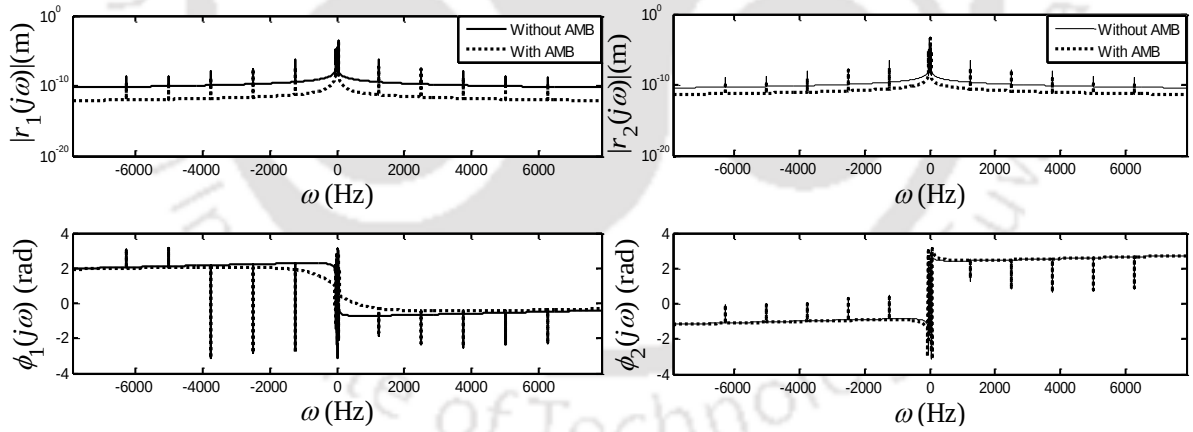

Figure 4.5. Full spectrum response generated at $\omega_p = 50\text{Hz}$, $\omega_g = 25\text{Hz}$, $\omega_e = 1250\text{Hz}$ (a) Amplitude and phase of complex translational displacement for input shaft (b) Amplitude and phase of complex translational displacement for output shaft

4.6 Representation of Equation of Motion in Complex Form

The vibration response based on EOM (4.15) can be generated into both time and frequency domain. For easy of computation translational displacements x_1, y_1; x_2, y_2 and $\varphi_{x1}, \varphi_{y1}$; $\varphi_{y2}, \varphi_{x2}$ of geared rotor and the AMB control currents i_{cx_1}, i_{cy_1}; i_{cx_2}, i_{cy_2} are combined as complex vectors r_1, r_2, $\varphi_1, \varphi_2, i_{c_1}$ and i_{c_2} respectively as shown in Chapter 3 from eqn. (3.18).

While combining above equations into complex form, the gyroscopic terms are combined as mentioned in Chapter 3, eqn. (3.19).

Thus, the EOMs of geared rotor in complex form taking gyroscopic effects in inertial co-ordinate frame is as follows

$$\bar{\mathbf{M}}\dot{\mathrm{v}} + \left(\bar{\mathbf{C}} - \mathrm{j}\omega_H \bar{\mathbf{G}}\right)\dot{\mathrm{v}} + \bar{\mathbf{K}}\mathrm{v} = \bar{\mathbf{f}}_{\mathrm{unb}} + \bar{\mathbf{f}}_{\mathrm{r\_out}} + \bar{\mathbf{f}}_{\mathrm{mesh}} + \bar{\mathbf{f}}_{\mathrm{tor}} - \bar{\mathbf{f}}_{\mathrm{amb}} \tag{4.18}$$

While the matrices of time domain EOMs of evaluated geared rotor AMB system in complex form are defined as follows:

$$\bar{\mathbf{M}} = \begin{bmatrix} m_1 & 0 & 0 & 0 & 0 & 0 & 0 & 0 \\ 0 & I_{d_1} & 0 & 0 & 0 & 0 & 0 & 0 \\ 0 & 0 & I_M & 0 & 0 & 0 & 0 & 0 \\ 0 & 0 & 0 & I_{p_1} & 0 & 0 & 0 & 0 \\ 0 & 0 & 0 & 0 & m_2 & 0 & 0 & 0 \\ 0 & 0 & 0 & 0 & 0 & I_{d_2} & 0 & 0 \\ 0 & 0 & 0 & 0 & 0 & 0 & I_{p_2} & 0 \\ 0 & 0 & 0 & 0 & 0 & 0 & 0 & I_L \end{bmatrix}; \mathrm{v} = \begin{Bmatrix} r_1 \\ \varphi_1 \\ \theta_M \\ \theta_p \\ r_2 \\ \varphi_2 \\ \theta_g \\ \theta_L \end{Bmatrix}$$

$$\left(\bar{\mathbf{C}} - \mathrm{j}\omega_H \bar{\mathbf{G}}\right) = \begin{bmatrix} c_p + c_m & 0 & 0 & c_m r_p e^{\mathrm{j}\psi} & -c_m & 0 & -c_m r_g e^{\mathrm{j}\psi} & 0 \\ 0 & -\mathrm{j}\omega_p I_{p_1} & 0 & 0 & 0 & 0 & 0 & 0 \\ 0 & 0 & 0 & 0 & 0 & 0 & 0 & 0 \\ c_m r_p e^{\mathrm{j}\psi} & 0 & 0 & c_m r_p^2 & -c_m r_p e^{\mathrm{j}\psi} & 0 & -c_m r_p r_g & 0 \\ -c_m & 0 & 0 & -c_m r_p e^{\mathrm{j}\psi} & c_g + c_m & 0 & c_m r_g e^{\mathrm{j}\psi} & 0 \\ 0 & 0 & 0 & 0 & 0 & -\mathrm{j}\omega_g I_{p_2} & 0 & 0 \\ -c_m r_g e^{\mathrm{j}\psi} & 0 & 0 & -c_m r_p r_g & c_m r_g e^{\mathrm{j}\psi} & 0 & c_m r_g^2 & 0 \\ 0 & 0 & 0 & 0 & 0 & 0 & 0 & 0 \end{bmatrix}$$

$$\bar{\mathbf{K}} = \begin{bmatrix} k_p + k_m & k_{px\varphi_y} & 0 & k_m r_p e^{j\psi} & -k_m & 0 & -k_m r_g e^{j\psi} & 0 \\ k_{px\varphi_y} & k_{p\varphi_x\varphi_x} & 0 & 0 & 0 & 0 & 0 & 0 \\ 0 & 0 & k_{tp} & -k_{tp} & 0 & 0 & 0 & 0 \\ k_m r_p e^{j\psi} & 0 & -k_{tp} & k_{tp} + k_m r_p^2 & -k_m r_p e^{j\psi} & 0 & -k_m r_p r_g & 0 \\ -k_m & 0 & 0 & -k_m r_p e^{j\psi} & k_g + k_m & k_{gx\varphi_y} & k_m r_g e^{j\psi} & 0 \\ 0 & 0 & 0 & 0 & k_{gx\varphi_y} & k_{g\varphi_x\varphi_x} & 0 & 0 \\ -k_m r_g e^{j\psi} & 0 & 0 & -k_m r_p r_g & k_m r_g e^{j\psi} & 0 & k_{tg} + k_m r_g^2 & -k_{tg} \\ 0 & 0 & 0 & 0 & 0 & 0 & -k_{tg} & k_{tg} \end{bmatrix}$$

$$\bar{\mathbf{f}}_{\text{unb}} = \begin{Bmatrix} m_1 e_p \omega_p^2 e^{j(\omega_p t + \phi_p)} \\ 0 \\ 0 \\ 0 \\ m_2 e_g \omega_g^2 e^{j(-\omega_g t + \phi_g)} \\ 0 \\ 0 \\ 0 \end{Bmatrix}; \bar{\mathbf{f}}_{\text{r\_out}} = \begin{Bmatrix} -k_p e_p e^{j(\omega_p t + \phi_p)} \\ -k_{px\varphi_y} e_p e^{j(\omega_p t + \phi_p)} \\ 0 \\ 0 \\ -k_g e_g e^{j(-\omega_g t + \phi_g)} \\ -k_{gx\varphi_y} e_g e^{j(-\omega_g t + \phi_g)} \\ 0 \\ 0 \end{Bmatrix} + \begin{Bmatrix} -j c_p e_p \omega_p e^{j(\omega_p t + \phi_p)} \\ 0 \\ 0 \\ 0 \\ j c_g e_g \omega_g e^{j(-\omega_g t + \phi_g)} \\ 0 \\ 0 \\ 0 \end{Bmatrix}$$

$$\bar{\mathbf{f}}_{\text{amb}} = -k_s \begin{Bmatrix} r_1 \\ 0 \\ 0 \\ 0 \\ r_2 \\ 0 \\ 0 \\ 0 \end{Bmatrix} + k_I \begin{Bmatrix} i_{c_1} \\ 0 \\ 0 \\ 0 \\ i_{c_2} \\ 0 \\ 0 \\ 0 \end{Bmatrix} \quad ; \quad \mathbf{f}_{\text{tor}} = \begin{bmatrix} 0 \\ 0 \\ 0 \\ T_p \\ 0 \\ 0 \\ -T_g \\ 0 \end{bmatrix}$$

$$\bar{\mathbf{f}}_{\text{mesh}} = k_m \begin{Bmatrix} -e_p e^{\mathrm{j}(\omega_p t+\phi_p)} + e_g e^{\mathrm{j}(-\omega_g t+\phi_g)} + \left(e_m e^{\mathrm{j}\phi_m} + \sum_{i=-n}^{n} e_{fi} e^{\mathrm{j}i(\omega_e t+\phi_{fi})} \right) \\ 0 \\ 0 \\ -e_p r_p \left\{ \begin{matrix} \dfrac{e^{\mathrm{j}(\omega_p t+\phi_p)} + e^{-\mathrm{j}(\omega_p t+\phi_p)}}{2} + \\ \dfrac{e^{\mathrm{j}(\omega_p t+\phi_p)} - e^{-\mathrm{j}(\omega_p t+\phi_p)}}{2\mathrm{j}} \end{matrix} \right\} + r_p \left\{ e_x(t) + e_y(t) \right\} + e_g r_p \left\{ \begin{matrix} \dfrac{e^{\mathrm{j}(-\omega_g t+\phi_g)} + e^{-\mathrm{j}(-\omega_g t+\phi_g)}}{2} + \\ \dfrac{e^{\mathrm{j}(-\omega_g t+\phi_g)} - e^{-\mathrm{j}(-\omega_g t+\phi_g)}}{2\mathrm{j}} \end{matrix} \right\} \\ e_p e^{\mathrm{j}(\omega_p t+\phi_p)} - e_g e^{\mathrm{j}(-\omega_g t+\phi_g)} - \left(e_m e^{\mathrm{j}\phi_m} + \sum_{i=-n}^{n} e_{fi} e^{\mathrm{j}i(\omega_e t+\phi_{fi})} \right) \\ 0 \\ e_p r_g \left\{ \begin{matrix} \dfrac{e^{\mathrm{j}(\omega_p t+\phi_p)} + e^{-\mathrm{j}(\omega_p t+\phi_p)}}{2} + \\ \dfrac{e^{\mathrm{j}(\omega_p t+\phi_p)} - e^{-\mathrm{j}(\omega_p t+\phi_p)}}{2\mathrm{j}} \end{matrix} \right\} - r_g \left\{ e_x(t) + e_y(t) \right\} - e_g r_g \left\{ \begin{matrix} \dfrac{e^{\mathrm{j}(-\omega_g t+\phi_g)} + e^{-\mathrm{j}(-\omega_g t+\phi_g)}}{2} + \\ \dfrac{e^{\mathrm{j}(-\omega_g t+\phi_g)} - e^{-\mathrm{j}(-\omega_g t+\phi_g)}}{2\mathrm{j}} \end{matrix} \right\} \\ 0 \end{Bmatrix}$$

$$+ c_m \begin{Bmatrix} -\mathrm{j}e_p\omega_p e^{\mathrm{j}(\omega_p t+\phi_p)} - \mathrm{j}e_g\omega_g e^{\mathrm{j}(-\omega_g t+\phi_g)} + \left(\mathrm{j}\omega_e \sum_{i=-n}^{n} i e_{fi} e^{\mathrm{j}i(\omega_e t+\phi_{fi})} \right) \\ 0 \\ 0 \\ -r_p \left[-e_p\omega_p \left\{ \begin{matrix} \dfrac{e^{\mathrm{j}(\omega_p t+\phi_p)} - e^{-\mathrm{j}(\omega_p t+\phi_p)}}{2\mathrm{j}} \\ -\dfrac{e^{\mathrm{j}(\omega_p t+\phi_p)} + e^{-\mathrm{j}(\omega_p t+\phi_p)}}{2} \end{matrix} \right\} - e_g\omega_g \left\{ \begin{matrix} \dfrac{e^{\mathrm{j}(-\omega_g t+\phi_g)} - e^{-\mathrm{j}(-\omega_g t+\phi_g)}}{2\mathrm{j}} \\ -\dfrac{e^{\mathrm{j}(-\omega_g t+\phi_g)} + e^{-\mathrm{j}(-\omega_g t+\phi_g)}}{2} \end{matrix} \right\} - \begin{Bmatrix} \dot{e}_x(t) \\ +\dot{e}_y(t) \end{Bmatrix} \right] \\ \mathrm{j}e_p\omega_p e^{\mathrm{j}(\omega_p t+\phi_p)} + \mathrm{j}e_g\omega_g e^{\mathrm{j}(-\omega_g t+\phi_g)} - \left(\mathrm{j}\omega_e \sum_{i=-n}^{n} i e_{fi} e^{\mathrm{j}i(\omega_e t+\phi_{fi})} \right) \\ 0 \\ r_g \left[-e_p\omega_p \left\{ \begin{matrix} \dfrac{e^{\mathrm{j}(\omega_p t+\phi_p)} - e^{-\mathrm{j}(\omega_p t+\phi_p)}}{2\mathrm{j}} \\ -\dfrac{e^{\mathrm{j}(\omega_p t+\phi_p)} + e^{-\mathrm{j}(\omega_p t+\phi_p)}}{2} \end{matrix} \right\} - e_g\omega_g \left\{ \begin{matrix} \dfrac{e^{\mathrm{j}(-\omega_g t+\phi_g)} - e^{-\mathrm{j}(-\omega_g t+\phi_g)}}{2\mathrm{j}} \\ -\dfrac{e^{\mathrm{j}(-\omega_g t+\phi_g)} + e^{-\mathrm{j}(-\omega_g t+\phi_g)}}{2} \end{matrix} \right\} - \begin{Bmatrix} \dot{e}_x(t) \\ +\dot{e}_y(t) \end{Bmatrix} \right] \\ 0 \end{Bmatrix}$$

(4.19)

4.6.1 Dynamic Condensation

The dynamic condensation method has been applied to eliminate the rotational DOFs for the convenience of parameter estimation from the identification algorithm as stated in Chapter 3 in section 3.5.2. The mass, stiffness, and damping matrices, and the displacement and force vectors are partitioned into sub-vectors and sub-matrices relating to master DOFs that are to be retained, and slave DOFs, which are to be eliminated. The frequency domain EOMs (4.18) can be partitioned like the subscript m and s representing the master and slave DOFs, respectively, and $\omega_H = \omega_p, \omega_g, \omega_e$ i.e., the three different excitation frequencies. The twelve DOFs of the system further reduces to eight DOFs as given below

$$\left\{x_1 \;\; y_1 \;\; \varphi_{y_1} \;\; \varphi_{x_1} \;\; \theta_M \;\; \theta_p \;\; x_2 \;\; y_2 \;\; \varphi_{y_2} \;\; \varphi_{x_2} \;\; \theta_g \;\; \theta_L\right\}^T = \left\{\mathbf{Q}_{1m} \;\; \mathbf{Q}_{1s} \;\; \theta_M \;\; \theta_p \;\; \mathbf{Q}_{2m} \;\; \mathbf{Q}_{2s} \;\; \theta_g \;\; \theta_L\right\}^T$$

with, $\mathbf{Q}_{1m} = \left\{x_1 \;\; y_1\right\}$, $\mathbf{Q}_{1s} = \left\{\varphi_{y1} \;\; \varphi_{x1}\right\}$, $\mathbf{Q}_{2m} = \left\{x_2 \;\; y_2\right\}$, $\mathbf{Q}_{2s} = \left\{\varphi_{y2} \;\; \varphi_{x2}\right\}$ (4.20)

Further the final EOMs after separating the master and slave DOFs takes the form

$$\left[\left(-(i^2\omega_H^2)\bar{\mathbf{M}}\right)+\mathrm{j}\left(i\omega_H\right)\left(\bar{\mathbf{C}}-\mathrm{j}\,\omega_H\bar{\mathbf{G}}\right)+\bar{\mathbf{K}}\right]\bar{\mathrm{v}}_i = \bar{\mathbf{f}}_{\mathrm{unb}}+\bar{\mathbf{f}}_{\mathrm{r\_out}}+\bar{\mathbf{f}}_{\mathrm{mesh}}+\bar{\mathbf{f}}_{\mathrm{tor}}-\bar{\mathbf{f}}_{\mathrm{amb}} \quad (4.21)$$

For which the matrices of EOMs i.e., eqn. (4.21) after separation of master and slave DOFs are written as: -

$$
\left(
-\left(i\omega_H\right)^2
\begin{bmatrix}
\mathbf{M}_{1mm} & \mathbf{0} & \mathbf{0} & \mathbf{0} & \mathbf{0} & \mathbf{0} & \mathbf{0} & \mathbf{0} \\
\mathbf{0} & \mathbf{M}_{1ss} & \mathbf{0} & \mathbf{0} & \mathbf{0} & \mathbf{0} & \mathbf{0} & \mathbf{0} \\
0 & 0 & I_M & 0 & 0 & 0 & 0 & 0 \\
0 & 0 & 0 & I_{p_1} & 0 & 0 & 0 & 0 \\
\mathbf{0} & \mathbf{0} & \mathbf{0} & \mathbf{0} & \mathbf{M}_{2mm} & \mathbf{0} & \mathbf{0} & \mathbf{0} \\
\mathbf{0} & \mathbf{0} & \mathbf{0} & \mathbf{0} & \mathbf{0} & \mathbf{M}_{2ss} & \mathbf{0} & \mathbf{0} \\
0 & 0 & 0 & 0 & 0 & 0 & I_{p_2} & 0 \\
0 & 0 & 0 & 0 & 0 & 0 & 0 & I_L
\end{bmatrix}
\right.
$$

$$
+\mathrm{j}\left(i\omega_H\right)
\left(
\begin{bmatrix}
\mathbf{C}_{1mm} & \mathbf{C}_{1ms} & \mathbf{0} & c_m r_p e^{\mathrm{j}\psi}\mathbf{I} & -c_m\mathbf{I} & \mathbf{0} & -c_m r_g e^{\mathrm{j}\psi}\mathbf{I} & \mathbf{0} \\
\mathbf{C}_{1ms} & \mathbf{C}_{1ss} & \mathbf{0} & \mathbf{0} & \mathbf{0} & \mathbf{0} & \mathbf{0} & \mathbf{0} \\
0 & 0 & 0 & 0 & 0 & 0 & 0 & 0 \\
c_m r_p e^{\mathrm{j}\psi} & 0 & 0 & c_m r_p^2 & -c_m r_p e^{\mathrm{j}\psi} & 0 & -c_m r_p r_g & 0 \\
-c_m\mathbf{I} & \mathbf{0} & \mathbf{0} & c_m r_p e^{\mathrm{j}\psi}\mathbf{I} & \mathbf{C}_{2mm} & \mathbf{C}_{2ms} & c_m r_g e^{\mathrm{j}\psi}\mathbf{I} & \mathbf{0} \\
\mathbf{0} & \mathbf{0} & \mathbf{0} & \mathbf{0} & \mathbf{C}_{2sm} & \mathbf{C}_{2ss} & \mathbf{0} & \mathbf{0} \\
-c_m r_g e^{\mathrm{j}\psi} & 0 & 0 & -c_m r_p r_g & c_m r_g e^{\mathrm{j}\psi} & 0 & c_m r_g^2 & 0 \\
0 & 0 & 0 & 0 & 0 & 0 & 0 & 0
\end{bmatrix}
\right.
$$

$$
-\mathrm{j}\,\omega_H
\begin{bmatrix}
\mathbf{0} & \mathbf{0} & \mathbf{0} & \mathbf{0} & \mathbf{0} & \mathbf{0} & \mathbf{0} & \mathbf{0} \\
\mathbf{0} & \mathbf{G}_{1ss} & \mathbf{0} & \mathbf{0} & \mathbf{0} & \mathbf{0} & \mathbf{0} & \mathbf{0} \\
0 & 0 & 0 & 0 & 0 & 0 & 0 & 0 \\
0 & 0 & 0 & 0 & 0 & 0 & 0 & 0 \\
0 & 0 & 0 & 0 & 0 & 0 & 0 & 0 \\
\mathbf{0} & \mathbf{0} & \mathbf{0} & \mathbf{0} & \mathbf{0} & \mathbf{G}_{2ss} & \mathbf{0} & \mathbf{0} \\
\mathbf{0} & \mathbf{0} & \mathbf{0} & \mathbf{0} & \mathbf{0} & \mathbf{0} & \mathbf{0} & \mathbf{0} \\
0 & 0 & 0 & 0 & 0 & 0 & 0 & 0
\end{bmatrix}
\right)
$$

$$
+
\begin{bmatrix}
\mathbf{K}_{1mm} & \mathbf{K}_{1ms} & \mathbf{0} & k_m r_p e^{\mathrm{j}\psi}\mathbf{I} & -k_m\mathbf{I} & \mathbf{0} & -k_m r_g e^{\mathrm{j}\psi}\mathbf{I} & \mathbf{0} \\
\mathbf{K}_{1sm} & \mathbf{K}_{1ss} & \mathbf{0} & \mathbf{0} & \mathbf{0} & \mathbf{0} & \mathbf{0} & \mathbf{0} \\
0 & 0 & k_{tp} & -k_{tp} & 0 & 0 & 0 & 0 \\
k_m r_p e^{\mathrm{j}\psi} & 0 & -k_{tp} & k_{tp} + k_m r_p^2 & -k_m r_p e^{\mathrm{j}\psi} & 0 & -k_m r_p r_g & 0 \\
-k_m\mathbf{I} & \mathbf{0} & \mathbf{0} & k_m r_p e^{\mathrm{j}\psi}\mathbf{I} & \mathbf{K}_{2mm} & \mathbf{K}_{2ms} & k_m r_g e^{\mathrm{j}\psi}\mathbf{I} & \mathbf{0} \\
\mathbf{0} & \mathbf{0} & \mathbf{0} & \mathbf{0} & \mathbf{K}_{2sm} & \mathbf{K}_{2ss} & \mathbf{0} & \mathbf{0} \\
-k_m r_g e^{\mathrm{j}\psi} & 0 & 0 & -k_m r_p r_g & k_m r_g e^{\mathrm{j}\psi} & 0 & k_{tg} + k_m r_g^2 & -k_{tg} \\
0 & 0 & 0 & 0 & 0 & 0 & -k_{tg} & k_{tg}
\end{bmatrix}
\right)
$$

$$
\begin{Bmatrix}
\mathbf{Q}_{1m} \\ \mathbf{Q}_{1s} \\ \theta_M \\ \theta_p \\ \mathbf{Q}_{2m} \\ \mathbf{Q}_{2s} \\ \theta_g \\ \theta_L
\end{Bmatrix}
=
\begin{Bmatrix}
\mathbf{f}_{1m} \\ \mathbf{f}_{1s} \\ \mathrm{f}_M \\ \mathrm{f}_p \\ \mathbf{f}_{2m} \\ \mathbf{f}_{2s} \\ \mathrm{f}_g \\ \mathrm{f}_L
\end{Bmatrix}
\tag{4.22}
$$

With,

$$\mathbf{M}_{1mm}=\begin{bmatrix} m_1 & 0 \\ 0 & m_1 \end{bmatrix};\quad \mathbf{M}_{2mm}=\begin{bmatrix} m_2 & 0 \\ 0 & m_2 \end{bmatrix};\quad \mathbf{M}_{1ss}=\begin{bmatrix} I_{d_1} & 0 \\ 0 & I_{d_1} \end{bmatrix};\quad \mathbf{M}_{2ss}=\begin{bmatrix} I_{d_2} & 0 \\ 0 & I_{d_2} \end{bmatrix};$$

$$\mathbf{G}_{1ss}=\begin{bmatrix} 0 & I_{p_1} \\ -I_{p_1} & 0 \end{bmatrix};\quad \mathbf{G}_{2ss}=\begin{bmatrix} 0 & I_{p_2} \\ -I_{p_2} & 0 \end{bmatrix};\quad \mathbf{C}_{1mm}=\begin{bmatrix} c_p+c_m & 0 \\ 0 & c_p+c_m \end{bmatrix};\quad \mathbf{C}_{1ms}=\mathbf{C}_{1sm}=\begin{bmatrix} 0 & 0 \\ 0 & 0 \end{bmatrix};$$

$$\mathbf{C}_{2mm}=\begin{bmatrix} c_g+c_m & 0 \\ 0 & c_g+c_m \end{bmatrix};\quad \mathbf{C}_{2ms}=\mathbf{C}_{2sm}=\begin{bmatrix} 0 & 0 \\ 0 & 0 \end{bmatrix};\quad \mathbf{C}_{1ss}=\mathbf{C}_{2ss}=\begin{bmatrix} 0 & 0 \\ 0 & 0 \end{bmatrix};$$

$$\mathbf{K}_{1mm}=\begin{bmatrix} k_p+k_m-k_s & 0 \\ 0 & k_p+k_m-k_s \end{bmatrix};\quad \mathbf{K}_{2mm}=\begin{bmatrix} k_g+k_m-k_s & 0 \\ 0 & k_g+k_m-k_s \end{bmatrix};$$

$$\mathbf{K}_{1ss}=\begin{bmatrix} k_{p\varphi_x\varphi_x} & 0 \\ 0 & k_{p\varphi_x\varphi_x} \end{bmatrix};\ \mathbf{K}_{2ss}=\begin{bmatrix} k_{g\varphi_x\varphi_x} & 0 \\ 0 & k_{g\varphi_x\varphi_x} \end{bmatrix};\ \mathbf{K}_{1ms}=\mathbf{K}_{1sm}=\begin{bmatrix} k_{px\varphi_y} & 0 \\ 0 & k_{px\varphi_y} \end{bmatrix};$$

$$\mathbf{K}_{2ms}=\mathbf{K}_{2sm}=\begin{bmatrix} k_{gx\varphi_y} & 0 \\ 0 & k_{gx\varphi_y} \end{bmatrix} \tag{4.23}$$

4.6.2 Development of Transformation Matrix

The general method for derivation of the transformation matrix, from the equation as per given in eqn. (4.21) is as follows

$$\begin{aligned} &\mathbf{K}_{1sm}\mathbf{Q}_{1m}+\mathbf{K}_{1ss}\mathbf{Q}_{1s}+i\omega_H^2\mathbf{G}_{1ss}\mathbf{Q}_{1s}-(i\omega_H)^2\mathbf{M}_{1ss}\mathbf{Q}_{1s}=\mathbf{0} \\ &\mathbf{K}_{2sm}\mathbf{Q}_{2m}+\mathbf{K}_{2ss}\mathbf{Q}_{2s}+i\omega_H^2\mathbf{G}_{2ss}\mathbf{Q}_{2s}-(i\omega_H)^2\mathbf{M}_{2ss}\mathbf{Q}_{2s}=\mathbf{0} \end{aligned} \tag{4.24}$$

and

$$\mathbf{Q}_{1m}=\mathbf{I}\mathbf{Q}_{1m},\ \mathbf{Q}_{2m}=\mathbf{I}\mathbf{Q}_{2m} \tag{4.25}$$

The transformation matrix is represented by '$\mathbf{T}^d$' and after dynamic condensation eliminating the four rotational coordinates $\varphi_{y_1},\varphi_{x_1}$ and $\varphi_{y_2},\varphi_{x_2}$ from eight generalised coordinates holds the following form

$$\begin{Bmatrix} \mathbf{Q}_{1m} \\ \mathbf{Q}_{1s} \\ \theta_M \\ \theta_p \\ \mathbf{Q}_{2m} \\ \mathbf{Q}_{2s} \\ \theta_g \\ \theta_L \end{Bmatrix} = \mathbf{T}^d \begin{Bmatrix} \mathbf{Q}_{1m} \\ \theta_M \\ \theta_p \\ \mathbf{Q}_{2m} \\ \theta_g \\ \theta_L \end{Bmatrix} \tag{4.26}$$

While,

$$\mathbf{T}^d = \begin{bmatrix} \mathbf{I} & \mathbf{0}\ \mathbf{0} & \mathbf{0} & \mathbf{0}\ \mathbf{0} \\ -\{\mathbf{K}_{1ss} + i\omega_H^2\mathbf{G}_{1ss} - (i\omega_H)^2\mathbf{M}_{1ss}\}^{-1}\mathbf{K}_{1sm} & \mathbf{0}\ \mathbf{0} & \mathbf{0} & \mathbf{0}\ \mathbf{0} \\ 0 & 0\ 0 & 0 & 0\ 0 \\ 0 & 0\ 0 & 0 & 0\ 0 \\ \mathbf{0} & \mathbf{0}\ \mathbf{0} & -\{\mathbf{K}_{1ss} + i\omega_H^2\mathbf{G}_{1ss} - (i\omega_H)^2\mathbf{M}_{1ss}\}^{-1}\mathbf{K}_{1sm} & \mathbf{0}\ \mathbf{0} \\ \mathbf{0} & \mathbf{0}\ \mathbf{0} & \mathbf{I} & \mathbf{0}\ \mathbf{0} \\ 0 & 0\ 0 & 0 & 0\ 0 \\ 0 & 0\ 0 & 0 & 0\ 0 \end{bmatrix} \tag{4.27}$$

Or, $\mathbf{T}^d = \begin{bmatrix} 1 & 0 & 0 & 0 & 0 & 0 & 0 & 0 \\ 0 & 1 & 0 & 0 & 0 & 0 & 0 & 0 \\ t^{d_1} & 0 & 0 & 0 & 0 & 0 & 0 & 0 \\ 0 & t^{d_1} & 0 & 0 & 0 & 0 & 0 & 0 \\ 0 & 0 & 0 & 0 & 0 & 0 & 0 & 0 \\ 0 & 0 & 0 & 0 & 0 & 0 & 0 & 0 \\ 0 & 0 & 0 & 1 & 0 & 0 & 0 & 0 \\ 0 & 0 & 0 & 0 & 1 & 0 & 0 & 0 \\ 0 & 0 & 0 & t^{d_2} & 0 & 0 & 0 & 0 \\ 0 & 0 & 0 & 0 & t^{d_2} & 0 & 0 & 0 \\ 0 & 0 & 0 & 0 & 0 & 0 & 0 & 0 \\ 0 & 0 & 0 & 0 & 0 & 0 & 0 & 0 \end{bmatrix}$

With, $t^{d_1} = \dfrac{-k_{px\varphi_y}}{-\left(i\omega_H\right)^2 I_{d_1} + i\omega_H^2 I_{p_1} + k_{p\varphi_x\varphi_x}}$; $t^{d_2} = \dfrac{-k_{gx\varphi_x}}{-\left(i\omega_H\right)^2 I_{d_2} + i\omega_H^2 I_{p_2} + k_{g\varphi_x\varphi_x}}$ (4.28)

On substituting the transformation matrix (eqn. 4.28) into EOMs (4.15), we get reduced order matrices with slave DOFs eliminated. The placement of reduced sub-matrices and vectors yields the final obtained equations of motion expressed in terms of master DOFs as

$$\left\{-\left(i\omega_H\right)^2\mathbf{M}^d+\mathrm{j}\left(i\omega_H\right)\left(\mathbf{C}^d-\mathrm{j}\,\omega_H\mathbf{G}^d\right)+\mathbf{K}^d\right\}\mathbf{Q}_m=\mathbf{f}^d \tag{4.29}$$

Where the matrices of dynamically condensed EOMs (4.29) are defined as follows: -

$$\mathbf{M}^d=\left(\mathbf{T}^d\right)^T\begin{bmatrix}\mathbf{M}_{1mm} & \mathbf{0} & \mathbf{0} & \mathbf{0} & \mathbf{0} & \mathbf{0} & \mathbf{0} & \mathbf{0}\\ \mathbf{0} & \mathbf{M}_{1ss} & \mathbf{0} & \mathbf{0} & \mathbf{0} & \mathbf{0} & \mathbf{0} & \mathbf{0}\\ 0 & 0 & I_M & 0 & 0 & 0 & 0 & 0\\ 0 & 0 & 0 & I_{p_1} & 0 & 0 & 0 & 0\\ \mathbf{0} & \mathbf{0} & \mathbf{0} & \mathbf{0} & \mathbf{M}_{2mm} & \mathbf{0} & \mathbf{0} & \mathbf{0}\\ \mathbf{0} & \mathbf{0} & \mathbf{0} & \mathbf{0} & \mathbf{0} & \mathbf{M}_{2ss} & \mathbf{0} & \mathbf{0}\\ 0 & 0 & 0 & 0 & 0 & 0 & I_{p_2} & 0\\ 0 & 0 & 0 & 0 & 0 & 0 & 0 & I_L\end{bmatrix}\mathbf{T}^d$$

$$=\begin{bmatrix}m_1+\left(t^{d_1}\right)^2 I_{d_1} & 0 & 0 & 0 & 0 & 0 & 0 & 0\\ 0 & m_1+\left(t^{d_1}\right)^2 I_{d_1} & 0 & 0 & 0 & 0 & 0 & 0\\ 0 & 0 & I_M & 0 & 0 & 0 & 0 & 0\\ 0 & 0 & 0 & I_{p_1} & 0 & 0 & 0 & 0\\ 0 & 0 & 0 & 0 & m_2+\left(t^{d_2}\right)^2 I_{d_2} & 0 & 0 & 0\\ 0 & 0 & 0 & 0 & 0 & m_2+\left(t^{d_2}\right)^2 I_{d_2} & 0 & 0\\ 0 & 0 & 0 & 0 & 0 & 0 & I_{p_2} & 0\\ 0 & 0 & 0 & 0 & 0 & 0 & 0 & I_L\end{bmatrix}$$

$$\mathbf{K}^d = \left(\mathbf{T}^d\right)^T \begin{bmatrix} \mathbf{K}_{1mm} & \mathbf{K}_{1ms} & \mathbf{0} & k_m r_p e^{j\psi}\mathbf{I} & -k_m\mathbf{I} & \mathbf{0} & -k_m r_g e^{j\psi}\mathbf{I} & \mathbf{0} \\ \mathbf{K}_{1sm} & \mathbf{K}_{1ss} & \mathbf{0} & \mathbf{0} & \mathbf{0} & \mathbf{0} & \mathbf{0} & \mathbf{0} \\ 0 & 0 & k_{tp} & -k_{tp} & 0 & 0 & 0 & 0 \\ k_m r_p e^{j\psi} & 0 & -k_{tp} & k_{tp}+k_m r_p^2 & -k_m r_p e^{j\psi} & 0 & -k_m r_p r_g & 0 \\ -k_m\mathbf{I} & \mathbf{0} & \mathbf{0} & k_m r_p e^{j\psi}\mathbf{I} & \mathbf{K}_{2mm} & \mathbf{K}_{2ms} & k_m r_g e^{j\psi}\mathbf{I} & \mathbf{0} \\ \mathbf{0} & \mathbf{0} & \mathbf{0} & \mathbf{0} & \mathbf{K}_{2sm} & \mathbf{K}_{2ss} & \mathbf{0} & \mathbf{0} \\ -k_m r_g e^{j\psi} & 0 & 0 & -k_m r_p r_g & k_m r_g e^{j\psi} & 0 & k_{tg}+k_m r_g^2 & -k_{tg} \\ 0 & 0 & 0 & 0 & 0 & 0 & -k_{tg} & k_{tg} \end{bmatrix} \mathbf{T}^d$$

$$= \begin{bmatrix} k_p^{'} & 0 & 0 & k_m r_p e^{j\psi} & -k_m & 0 & -k_m r_g e^{j\psi} & 0 \\ 0 & k_p^{'} & 0 & 0 & 0 & 0 & 0 & 0 \\ 0 & 0 & k_{tp} & -k_{tp} & 0 & 0 & 0 & 0 \\ k_m r_p e^{j\psi} & 0 & -k_{tp} & k_{tp}+k_m r_p^2 & -k_m r_p e^{j\psi} & 0 & -k_m r_p r_g & 0 \\ -k_m & 0 & 0 & k_m r_p e^{j\psi} & k_g^{'} & 0 & k_m r_g e^{j\psi} & 0 \\ 0 & 0 & 0 & 0 & 0 & k_g^{'} & 0 & 0 \\ -k_m r_g e^{j\psi} & 0 & 0 & -k_m r_p r_g & k_m r_g e^{j\psi} & 0 & k_{tg}+k_m r_g^2 & -k_{tg} \\ 0 & 0 & 0 & 0 & 0 & 0 & -k_{tg} & k_{tg} \end{bmatrix}$$

While $k_p^{'} = \left(k_p + k_m\right) - 2\left(t^{d_1}\right)k_{px\varphi_y} + \left(t^{d_1}\right)^2 k_{p\varphi_x\varphi_x}$; $k_g^{'} = \left(k_g + k_m\right) - 2\left(t^{d_2}\right)k_{gx\varphi_y} + \left(t^{d_2}\right)^2 k_{g\varphi_x\varphi_x}$

$$\mathbf{C}^d = \left(\mathbf{T}^d\right)^T \begin{bmatrix} \mathbf{C}_{1mm} & \mathbf{C}_{1ms} & \mathbf{0} & c_m r_p e^{j\psi}\mathbf{I} & -c_m\mathbf{I} & \mathbf{0} & -c_m r_g e^{j\psi}\mathbf{I} & \mathbf{0} \\ \mathbf{C}_{1ms} & \mathbf{C}_{1ss} & \mathbf{0} & \mathbf{0} & \mathbf{0} & \mathbf{0} & \mathbf{0} & \mathbf{0} \\ 0 & 0 & 0 & 0 & 0 & 0 & 0 & 0 \\ c_m r_p e^{j\psi} & 0 & 0 & c_m r_p^2 & -c_m r_p e^{j\psi} & 0 & -c_m r_p r_g & 0 \\ -c_m\mathbf{I} & \mathbf{0} & \mathbf{0} & c_m r_p e^{j\psi}\mathbf{I} & \mathbf{C}_{2mm} & \mathbf{C}_{2ms} & c_m r_g e^{j\psi}\mathbf{I} & \mathbf{0} \\ \mathbf{0} & \mathbf{0} & \mathbf{0} & \mathbf{0} & \mathbf{C}_{2sm} & \mathbf{C}_{2ss} & \mathbf{0} & \mathbf{0} \\ -c_m r_g e^{j\psi} & 0 & 0 & -c_m r_p r_g & c_m r_g e^{j\psi} & 0 & c_m r_g^2 & 0 \\ 0 & 0 & 0 & 0 & 0 & 0 & 0 & 0 \end{bmatrix} \mathbf{T}^d$$

$$= \begin{bmatrix} c_p^{'} & 0 & 0 & c_m r_p e^{j\psi} & -c_m & 0 & -c_m r_g e^{j\psi} & 0 \\ 0 & c_p^{'} & 0 & 0 & 0 & 0 & 0 & 0 \\ 0 & 0 & 0 & 0 & 0 & 0 & 0 & 0 \\ c_m r_p e^{j\psi} & 0 & 0 & c_m r_p^2 & -c_m r_p e^{j\psi} & 0 & -c_m r_p r_g & 0 \\ -c_m & 0 & 0 & c_m r_p e^{j\psi} & c_g^{'} & 0 & c_m r_g e^{j\psi} & 0 \\ 0 & 0 & 0 & 0 & 0 & c_g^{'} & 0 & 0 \\ -c_m r_g e^{j\psi} & 0 & 0 & -c_m r_p r_g & c_m r_g e^{j\psi} & 0 & c_m r_g^2 & 0 \\ 0 & 0 & 0 & 0 & 0 & 0 & 0 & 0 \end{bmatrix}$$

while $c_p^{'} = (c_p + c_m)$; $c_g^{'} = (c_g + c_m)$

$$\mathbf{G}^d = \left(\mathbf{T}^d\right)^T \omega_H \begin{bmatrix} \mathbf{0} & \mathbf{0} & \mathbf{0} & \mathbf{0} & \mathbf{0} & \mathbf{0} & \mathbf{0} & \mathbf{0} \\ \mathbf{0} & \mathbf{G}_{1ss} & \mathbf{0} & \mathbf{0} & \mathbf{0} & \mathbf{0} & \mathbf{0} & \mathbf{0} \\ 0 & 0 & 0 & 0 & 0 & 0 & 0 & 0 \\ 0 & 0 & 0 & 0 & 0 & 0 & 0 & 0 \\ 0 & 0 & 0 & 0 & 0 & 0 & 0 & 0 \\ \mathbf{0} & \mathbf{0} & \mathbf{0} & \mathbf{0} & \mathbf{0} & \mathbf{G}_{2ss} & \mathbf{0} & \mathbf{0} \\ \mathbf{0} & \mathbf{0} & \mathbf{0} & \mathbf{0} & \mathbf{0} & \mathbf{0} & \mathbf{0} & \mathbf{0} \\ 0 & 0 & 0 & 0 & 0 & 0 & 0 & 0 \end{bmatrix} \mathbf{T}^d$$

$$= \begin{bmatrix} 0 & -\left(t^{d_1}\right)^2 I_{p_1} \omega_p & 0 & 0 & 0 & 0 & 0 & 0 \\ \left(t^{d_1}\right)^2 I_{p_1} \omega_p & 0 & 0 & 0 & 0 & 0 & 0 & 0 \\ 0 & 0 & 0 & 0 & 0 & 0 & 0 & 0 \\ 0 & 0 & 0 & 0 & 0 & 0 & 0 & 0 \\ 0 & 0 & 0 & 0 & 0 & -\left(t^{d_2}\right)^2 I_{p_2} \omega_g & 0 & 0 \\ 0 & 0 & 0 & 0 & \left(t^{d_2}\right)^2 I_{p_2} \omega_g & 0 & 0 & 0 \\ 0 & 0 & 0 & 0 & 0 & 0 & 0 & 0 \\ 0 & 0 & 0 & 0 & 0 & 0 & 0 & 0 \end{bmatrix}$$

$$\mathbf{f}^d = \left(\mathbf{T}^d\right)^T \mathbf{f} = \begin{bmatrix} e_p \left(k_{px\varphi_y} t_{d_1} - k_p\right) e^{\mathrm{j}\left(\omega_p t + \phi_p\right)} \\ e_p \left(k_{px\varphi_y} t_{d_1} - k_p\right) e^{\mathrm{j}\left(\omega_p t + \phi_p\right)} \\ 0 \\ 0 \\ e_g \left(k_{gx\varphi_y} t_{d_2} - k_g\right) e^{\mathrm{j}\left(-\omega_g t + \phi_g\right)} \\ e_g \left(k_{gx\varphi_y} t_{d_2} - k_g\right) e^{\mathrm{j}\left(-\omega_g t + \phi_g\right)} \\ 0 \\ 0 \end{bmatrix}$$

(4.30)

4.7 Formulation of Identification Matrix

The identification algorithm can be derived and written in matrix form. As mentioned in Chapter 2, gears create vibrations at specific frequencies, related to number of teeth and the rotational speed of gears. Hence, the excitation forces due to gear meshing are multi-harmonic in nature. Herein, gear meshing forces are common to both shafts but opposite in direction so a forward excitation in pinion will give backward excitation in gear and since the systems EOM are linear, thereby applying principle of superposition, the assumed solution for eqns. (4.21) considering three different excitation frequencies, i.e., ω_p, ω_g and ω_e are combined. Now taking only the complex transverse vibrational displacements $r_1(t)$ and $r_2(t)$, the complex current $i_1(t)$ and $i_2(t)$, with dynamically condensed angular displacements $\varphi_1(t)$ and $\varphi_2(t)$ containing each harmonics from $i=-n,...,-1,0,1,2...n$ can be summed up as shown in Eqn. (2.27) and Eqn. (2.28) in Chapter 2. Since the harmonics of current signals should have the same frequency components as that of the rotor displacement signals. So, at any instant of time the output current signals from a PID controller can be expressed as given in eqn. (2.29) and eqn. (2.30) in Chapter 2. It is known that for identification of parameters from the geared rotor system, the complex regression equations have to be so arranged such that the known and unknowns are separated and kept on either side of equation. Both left and right sides of the equations contain multi-harmonic components ranging in $i=-n,...,-1,0,1,...,n$.

The dynamically condensed EOM (eqn. (4.29)) is changed into complex form with multi-harmonic frequencies. Taking the torsional-lateral coupled equation we get: -

(a) For input shaft: -

$$\begin{aligned}
&\left[\begin{pmatrix} -(i\omega_H)^2\left\{m_1+\left(t^{d_1}\right)^2 I_{d_1}\right\}+\mathrm{j}i\omega_H\left\{(c_p+c_m)+\mathrm{j}I_{p_1}\omega_H\left(t^{d_1}\right)^2\right\} \\ +\left(k_p+k_m\right)-2\left(t^{d_1}\right)k_{px\varphi_y}+\left(t^{d_1}\right)^2 k_{p\varphi_x\varphi_x}\end{pmatrix}\left(R_{ipH}\right)-\left(\mathrm{j}i\omega_H c_m+k_m\right)\left(R_{igH}\right)\right]\left(e^{\mathrm{j}i\omega_H t}\right) \\
&+\left\{k_m\left(r_p\theta_{ipH}-r_g\theta_{igH}\right)+\mathrm{j}i\omega_H c_m\left(r_p\theta_{ipH}-r_g\theta_{igH}\right)\right\}\left(e^{\mathrm{j}i\omega_H t}\right)e^{\mathrm{j}\psi} \\
&=\left\{\left(m_1 e_p\omega_p^2+k_{px\varphi_y}t_{d_1}e_p-k_p e_p-k_m e_p\right)-\mathrm{j}\left(c_p+c_m\right)e_p\omega_p\right\}e^{\mathrm{j}(\omega_p t+\phi_p)}+\left(k_m e_g-\mathrm{j}c_m e_g\omega_g\right)e^{\mathrm{j}(-\omega_g t+\phi_g)} \\
&+k_m\left[e_m e^{\mathrm{j}\phi_m}+\sum_{i=-n}^{n}\left\{\left(e_{fi}\right)e^{\mathrm{j}i(\omega_e t+\phi_{fi})}\right\}\right]+c_m\left\{\mathrm{j}\omega_e\sum_{i=-n}^{n}\left\{\left(ie_{fi}\right)e^{\mathrm{j}i(\omega_e t+\phi_{fi})}\right\}\right\}+k_s R_{ipH}e^{\mathrm{j}i\omega_H t}-k_I\sum_{i=-n}^{n}I_{ipH}e^{\mathrm{j}i\omega_H t}
\end{aligned} \tag{4.31}$$

$$\left[\left\{-\left(i\omega_H\right)^2\left(I_{p_1}\right)\right\}\left(\theta_{ipH}\right)+\left\{\mathrm{j}i\omega_H\left(c_m r_p e^{\mathrm{j}\psi}\right)+k_m r_p e^{\mathrm{j}\psi}\right\}\left(R_{ipH}\right)-\left\{\mathrm{j}i\omega_H\left(c_m r_p e^{\mathrm{j}\psi}\right)+k_m r_p e^{\mathrm{j}\psi}\right\}\left(R_{igH}\right)\right]\left(e^{\mathrm{j}i\omega_H t}\right)$$
$$-k_{tp}\left(\theta_{iMH}-\theta_{ipH}\right)+\left\{k_m r_p\left(r_p\theta_{ipH}-r_g\theta_{igH}\right)+\mathrm{j}i\omega_H c_m r_p\left(r_p\theta_{ipH}-r_g\theta_{igH}\right)\right\}\left(e^{\mathrm{j}i\omega_H t}\right)$$
$$=k_m\left[-e_p r_p\left\{\begin{matrix}\dfrac{e^{\mathrm{j}(\omega_p t+\phi_p)}+e^{-\mathrm{j}(\omega_p t+\phi_p)}}{2}+\\ \dfrac{e^{\mathrm{j}(\omega_p t+\phi_p)}-e^{-\mathrm{j}(\omega_p t+\phi_p)}}{2\mathrm{j}}\end{matrix}\right\}+r_p\left\{e_x(t)+e_y(t)\right\}+e_g r_p\left\{\begin{matrix}\dfrac{e^{\mathrm{j}(-\omega_g t+\phi_g)}+e^{-\mathrm{j}(-\omega_g t+\phi_g)}}{2}+\\ \dfrac{e^{\mathrm{j}(-\omega_g t+\phi_g)}-e^{-\mathrm{j}(-\omega_g t+\phi_g)}}{2\mathrm{j}}\end{matrix}\right\}\right]$$
$$-c_m r_p\left[-e_p\omega_p\left\{\begin{matrix}\dfrac{e^{\mathrm{j}(\omega_p t+\phi_p)}-e^{-\mathrm{j}(\omega_p t+\phi_p)}}{2\mathrm{j}}\\ -\dfrac{e^{\mathrm{j}(\omega_p t+\phi_p)}+e^{-\mathrm{j}(\omega_p t+\phi_p)}}{2}\end{matrix}\right\}-e_g\omega_g\left\{\begin{matrix}\dfrac{e^{\mathrm{j}(-\omega_g t+\phi_g)}-e^{-\mathrm{j}(-\omega_g t+\phi_g)}}{2\mathrm{j}}\\ -\dfrac{e^{\mathrm{j}(-\omega_g t+\phi_g)}+e^{-\mathrm{j}(-\omega_g t+\phi_g)}}{2}\end{matrix}\right\}-\left\{\dot{e}_x(t)+\dot{e}_y(t)\right\}\right]+T_p$$

(4.32)

(b) For output shaft: -

$$\left[\left(\begin{matrix}-(i\omega_H)^2\left\{m_2+\left(t^{d_2}\right)^2 I_{d_2}\right\}+\mathrm{j}i\omega_H\left\{(c_g+c_m)+\mathrm{j}I_{p_2}\omega_H\left(t^{d_2}\right)^2\right\}\\ +\left(k_g+k_m\right)-2\left(t^{d_2}\right)k_{gx\varphi_y}+\left(t^{d_2}\right)^2 k_{g\varphi_x\varphi_x}\end{matrix}\right)\left(R_{igH}\right)-\left(\mathrm{j}i\omega_H c_m+k_m\right)\left(R_{ipH}\right)\right]\left(e^{\mathrm{j}i\omega_H t}\right)$$
$$-\left\{k_m\left(r_p\theta_{ipH}-r_g\theta_{igH}\right)-\mathrm{j}i\omega_H c_m\left(r_p\theta_{ipH}-r_g\theta_{igH}\right)\right\}\left(e^{\mathrm{j}i\omega_H t}\right)e^{\mathrm{j}\psi}$$
$$=\left\{\left(m_2 e_g\omega_g^2+k_{gx\varphi_y}t_{d_2}e_g-k_g e_g-k_m e_g\right)+\mathrm{j}\left(c_g+c_m\right)e_g\omega_g\right\}e^{\mathrm{j}(-\omega_g t+\phi_g)}+\left(k_m e_p+\mathrm{j}c_m e_p\omega_p\right)e^{\mathrm{j}(\omega_p t+\phi_p)}$$
$$-k_m\left[e_m e^{\mathrm{j}\phi_m}+\sum_{i=-n}^{n}\left\{\left(e_{fi}\right)e^{\mathrm{j}i(\omega_e t+\phi_{fi})}\right\}\right]-c_m\left\{\mathrm{j}\omega_e\sum_{i=-n}^{n}\left\{\left(ie_{fi}\right)e^{\mathrm{j}i(\omega_e t+\phi_{fi})}\right\}\right\}+k_s R_{igH}e^{\mathrm{j}i\omega_H t}-k_I\sum_{i=-n}^{n}I_{igH}e^{\mathrm{j}i\omega_H t}$$

(4.33)

$$\left[\left\{-\left(i\omega_H\right)^2\left(I_{p_2}\right)\right\}\left(\theta_{igH}\right)+\left\{\mathrm{j}i\omega_H\left(c_m r_g e^{\mathrm{j}\psi}\right)+k_m r_g e^{\mathrm{j}\psi}\right\}\left(R_{igH}\right)-\left\{\mathrm{j}i\omega_H\left(c_m r_g e^{\mathrm{j}\psi}\right)+k_m r_g e^{\mathrm{j}\psi}\right\}\left(R_{ipH}\right)\right]\left(e^{\mathrm{j}i\omega_H t}\right)$$
$$+k_{tg}\left(\theta_{igH}-\theta_{iLH}\right)-\left\{k_m r_g\left(r_p\theta_{ipH}-r_g\theta_{igH}\right)-\mathrm{j}i\omega_H c_m r_g\left(r_p\theta_{ipH}-r_g\theta_{igH}\right)\right\}\left(e^{\mathrm{j}i\omega_H t}\right)$$
$$=k_m\left[e_p r_g\left\{\begin{matrix}\dfrac{e^{\mathrm{j}(\omega_p t+\phi_p)}+e^{-\mathrm{j}(\omega_p t+\phi_p)}}{2}+\\ \dfrac{e^{\mathrm{j}(\omega_p t+\phi_p)}-e^{-\mathrm{j}(\omega_p t+\phi_p)}}{2\mathrm{j}}\end{matrix}\right\}-r_g\left\{e_x(t)+e_y(t)\right\}-e_g r_g\left\{\begin{matrix}\dfrac{e^{\mathrm{j}(-\omega_g t+\phi_g)}+e^{-\mathrm{j}(-\omega_g t+\phi_g)}}{2}+\\ \dfrac{e^{\mathrm{j}(-\omega_g t+\phi_g)}-e^{-\mathrm{j}(-\omega_g t+\phi_g)}}{2\mathrm{j}}\end{matrix}\right\}\right]$$
$$+c_m r_g\left[-e_p\omega_p\left\{\begin{matrix}\dfrac{e^{\mathrm{j}(\omega_p t+\phi_p)}-e^{-\mathrm{j}(\omega_p t+\phi_p)}}{2\mathrm{j}}\\ -\dfrac{e^{\mathrm{j}(\omega_p t+\phi_p)}+e^{-\mathrm{j}(\omega_p t+\phi_p)}}{2}\end{matrix}\right\}-e_g\omega_g\left\{\begin{matrix}\dfrac{e^{\mathrm{j}(-\omega_g t+\phi_g)}-e^{-\mathrm{j}(-\omega_g t+\phi_g)}}{2\mathrm{j}}\\ -\dfrac{e^{\mathrm{j}(-\omega_g t+\phi_g)}+e^{-\mathrm{j}(-\omega_g t+\phi_g)}}{2}\end{matrix}\right\}-\left\{\dot{e}_x(t)+\dot{e}_y(t)\right\}\right]-T_g \tag{4.34}$$

For the formation of identification algorithm, the real regression equations can be obtained from the above equations (eqn. 4.31 to 4.34) by segregating the real and imaginary parts. Although there can be 78 real regression equations considering $n=5$. Herein, for the identification procedure, the coupled vibration equations in transverse direction 4.31 and 4.33 has been taken since the AMB force has been applied in those directions that leads to 52 number of equations (refer **Appendix A3**). The equations 4.32 and 4.34 depicting torsional component of coupled vibration does not contain AMB force vector and hence neglected. It was found that these 52 equations are able to estimate the 38 unknown parameters. As done in earlier chapters, these real regression equations are rearranged according to the rotor forward and backward whirl behaviour which is then expressed into the matrix form as

$$\mathbf{Ax = b} \tag{4.35}$$

where, $\mathbf{x}$ denotes the unknown column vector, $\mathbf{b}$ the known matrix and $\mathbf{A}$ the regressor, shown in **Appendix B3**. The unknown parameters, which needs to be estimated from the real regression equations are shown in **Appendix B3**. The identifiable parameters are then solved by using least-square regression method, which is given by the expression

$$\mathbf{x} = \left(\mathbf{A}^{\mathrm{T}}\mathbf{A}\right)^{-1}\mathbf{A}^{\mathrm{T}}\mathbf{b} \tag{4.36}$$

The values obtained from eqn. (4.36) are recombined suitably to determine the final looked-for 20 identifiable system parameters (i.e., the gear mesh stiffness, gear mesh damping,

eccentricity of input, output gear with respective unbalance phase, AMB displacement stiffness factor, AMB current stiffness factor, amplitude and phase of mean transmission error, amplitude and phase of variable transmission error (considering $n=5$) harmonics), given as

$$\lfloor k_m \;\; c_m \;\; e_p \;\; \phi_p \;\; e_g \;\; \phi_g \;\; k_s \;\; k_I \;\; e_m \;\; \phi_m \;\; e_{f1} \;\; e_{f2} \;\; e_{f3} \;\; e_{f4} \;\; e_{f5} \;\; \phi_{f1} \;\; \phi_{f2} \;\; \phi_{f3} \;\; \phi_{f4} \;\; \phi_{f5} \rfloor^T \tag{4.37}$$

The values obtained by identification of parameters from the developed algorithm is illustrated numerically in Section 4.7.1

4.7.1 Estimation of Parameters with Addition of Noise and Modelling Error

The parameter estimation is done by using multi-harmonic amplitude and phase information from the full spectrum in the identification problem. The identification algorithm obtained from the regression equation is given in **Appendix B3**. Here the assumed rotor-AMB physical parameters listed in Tables 4.1 and 4.2 are known values for the identification problem.

As done in earlier cases, to simulate the real measurement condition, Gaussian noise is added to time domain signals and random solution is obtained from numerical simulation to check the robustness of the identification algorithm. Also, the physical parameters like the mass, stiffness and damping taken for the numerical analysis may differ from the actual system properties. Hence, the sensitiveness of the identification algorithm is checked with the addition of bias errors in the density, length and Young's modulus of the system. Results of the estimation based on two speed ranges taken for the identification problem with clean and corrupted signals are summarised in Table 4.3 and 4.4. For the estimation a suitable range of multiple speeds, i.e. $\omega_p = 50-60$ Hz in step of 2 Hz, $\omega_g = 25-30$Hz in step of 1 Hz, and $\omega_e = 1250-1500$ Hz in step of 50 Hz has been taken for the simulation.

Table 4.3

Identification of parameters with addition of noise at multiple spin speeds

Parameters	Assumed values	Estimated values with different percentage of noise			
		0%	1%	2%	5%
c_m	150 Nsm^{-1}	158	146	186	166
k_m	12.03×10^6 Nm^{-1}	10.8×10^6	15.2×10^6	18.4×10^6	19.4×10^6
e_p	3×10^{-4} m	307×10^{-6}	301×10^{-6}	295×10^{-6}	320×10^{-6}
e_g	4×10^{-4} m	409×10^{-6}	405×10^{-6}	401×10^{-6}	415.5×10^{-6}
ϕ_p	1.047 rad	1.032	0.921	1.098	1.132
ϕ_g	1.545 rad	1.596	1.516	1.614	1.659
k_s	217573 Nm^{-1}	213986	213926	215743	209631
k_I	$43.5NA^{-1}$	44.57	44.57	45.6	43.8
e_m	31×10^{-8} m	244×10^{-6}	219×10^{-6}	232×10^{-6}	319×10^{-6}
ϕ_m	1.5236 rad	1.563	1.575	1.527	1.875
e_{f1}	30 nm	15	18	21	16
e_{f2}	25 nm	21	23	22	26
e_{f3}	35 nm	27	23	25	31
e_{f4}	11 nm	8.5	12	15	18
e_{f5}	12 nm	9.4	16	16	14
ϕ_{f1}	0.9471 rad	0.761	0.804	0.961	1.161
ϕ_{f2}	0.564 rad	0.658	0.443	0.536	0.689
ϕ_{f3}	0.3283 rad	0.360	0.407	0.393	0.413
ϕ_{f4}	0.3654 rad	0.440	0.405	0.375	0.431

ϕ_{f5}	0.3954 rad	0.485	0.385	0.326	0.429

Table 4.4

Identification of parameters with addition of modelling error

Parameters	**Assumed values**	**Estimated values with different percentage of noise**			
		0%	1%	2%	5%
c_m	150 Nsm^{-1}	158	160	172	189
k_m	12.03×10^6 Nm^{-1}	10.8×10^6	14.9×10^6	11.2×10^6	19.1×10^6
e_p	3×10^{-4} m	307×10^{-6}	298.3×10^{-6}	295.5×10^{-6}	273.3×10^{-6}
e_g	4×10^{-4} m	409×10^{-6}	396.4×10^{-6}	412×10^{-6}	422×10^{-6}
ϕ_p	1.047 rad	1.032	1.056	1.007	1.098
ϕ_g	1.545 rad	1.596	1.567	1.541	1.602
k_s	217573 Nm^{-1}	213986	211285	205543	220894
k_I	$43.5NA^{-1}$	44.57	45.3	48.8	48.3
e_m	31 nm	244×10^{-6}	234×10^{-6}	230×10^{-6}	229×10^{-6}
ϕ_m	1.5236 rad	1.563	1.554	1.574	1.564
e_{f1}	30 nm	15	32	26	29
e_{f2}	25 nm	21	22	25	27
e_{f3}	35 nm	27	35	33	39
e_{f4}	11 nm	8.5	11	10	15
e_{f5}	12 nm	9.4	16	12	16
ϕ_{f1}	0.9471 rad	0.761	0.883	1.034	1.102
ϕ_{f2}	0.564 rad	0.658	0.603	0.658	0.712

ϕ_{f3}	0.3283 rad	0.360	0.322	0.350	0.387
ϕ_{f4}	0.3654 rad	0.440	0.482	0.395	0.523
ϕ_{f5}	0.3954 rad	0.485	0.473	0.547	0.538

As it is known that for identification the range of speeds should be chosen judiciously so to get the best fit. It was observed that when the range of speed is taken i.e., $\omega_p = 50-52$ Hz in step of 2 Hz, $\omega_g = 25-26$ Hz in step of 1 Hz, and $\omega_e = 1250-1300$ Hz in step of 50 Hz, the estimated gear mesh stiffness and mesh damping, AMB displacement and current stiffness, amplitude of varying transmission error have good approximate values and pinion, gear eccentricity, phase angles have moderate variation from assumed values . However, when three speeds are taken gear eccentricity, runout phase angle, the phase angles of mean transmission error are improved. Although the value of gear mesh stiffness, amplitude and phase of varying transmission error are completely distorted.

4.8 Conclusions

An improved model has been developed for coupled torsional-lateral vibrations in a geared rotor AMB system along with gyroscopic effect considering gear run-out and asymmetric dynamic transmission error. An important source of torsional excitation is coupling with lateral mode of vibration. This coupling may occur due to rotor unbalance, unidirectional lateral constant forces acting on a rotor, through tangential forces (like those generated by rotor-surrounding fluid), and through gyroscopic effect. Uneven tooth mesh stiffness and tooth profile errors in gear-boxes, misaligned gears and/or couplings, or faulty rolling element bearings are other sources of torsional vibration excitations. Here, we have considered linear system with nominal torque in order to keep the gears in contact and no slip, no backlash. Therefore, not much effect due to torsional vibrations is observed. But in real systems there can be gyroscopic effect, coupled torsional-lateral effect, so the identification algorithm is further extended from mathematical model of coupled geared-rotor dynamics such that it can better estimate the faults. While developing the algorithm, since the transverse vibrations occur in radial directions i.e., x, y whereas the torsional displacements act about the z-axis i.e., rotor's central axis. Hence, the torsional displacements cannot be combined in complex form like that of transverse displacements. Also, the forward and backward whirl amplitudes of rotor

undergoing pure torsional vibrations are equal. Hence, plotting the full spectrum for rotor undergoing torsional-lateral (almost uncoupled) vibrations is of no significance and half spectrum of torsional vibrational displacements can be considered. The parameters have been estimated from the coupled vibration equations in transverse direction only since AMB force is applied in radial directions. The equations depicting torsional component of coupled vibration does not contain AMB force vector and hence neglected. From there the dynamic transmission error under loaded condition is predicted along with other rotor AMB system parameters and faults in similar manner as done in earlier chapters. The identification was done by taking the full spectrum information from various harmonics of frequencies present in the spectrum of transverse vibration and current responses. The estimated parameters were tested with different percentage of random noise and modelling errors to check the robustness of the developed algorithm. The experimental validation of the proposed method has been done by fabricating a laboratory test rig which is presented in the next Chapter 5.

CHAPTER 5 DESIGN AND EXPERIMENTAL INVESTIGATION OF ACTIVE CONTROL OF SPUR GEAR TRANSMISSIONS

5.1 Introduction

This chapter is focused on the investigation of experimental feasibility of active vibration control with Active Magnetic Bearings (AMBs), being applied to suppress the transverse vibrations in a geared rotor system against transmission error excitations at the gear mesh. An experiment test rig of the proposed spur geared rotor-AMB system has been set up in the Advanced Dynamics Laboratory at IIT Guwahati. The effectiveness of the dynamic model developed in the previous chapter is compared with and without the application of AMBs. The approach is based on an active control of the shaft transverse vibration with an electromagnetic actuator similar to the numerical simulation. The control forces are applied to the rotor shafts supported on conventional rolling element bearings by an eight-pole radial AMB, as an auxiliary component and a closed-loop linear output feedback control is employed for stable, reliable, and robust operation. A linear PD controller working on differential mode is used to generate the appropriate control signals and the experimental results are presented. It was found that there is considerable amount of reduction in the geared rotor vibration levels and correspondingly in overall measured gear noise levels. Further the responses so obtained from the experimental rig are computed suitably for parameter estimation from the developed rotor fault identification algorithm.

5.2 Design of Geared Rotor (AMB) System

A laboratory test rig has been designed and developed in IIT Guwahati and a real-time active control has been implemented considering a system of single staged spur gear mounted on shafts supported by conventional bearings at both ends as shown in Fig. 5.1. The distributed shaft inertia has not been considered in the present formulation due to relatively thin shaft. The rolling element bearings are assumed rigid in transverse direction and frictionless. Two AMBs are positioned at the input and output shafts next to the gear-pair in order to control the vibrations during the gear meshing. The shafts are flexible and of uniform cross-section, allowing both transverse and torsional displacements. The gear-pair deformation due to tooth

contact is neglected, except at the mesh line of action. The shaft centreline is defined along the *Z*-axis and *X*, *Y*-axis is positioned at the gear centres.

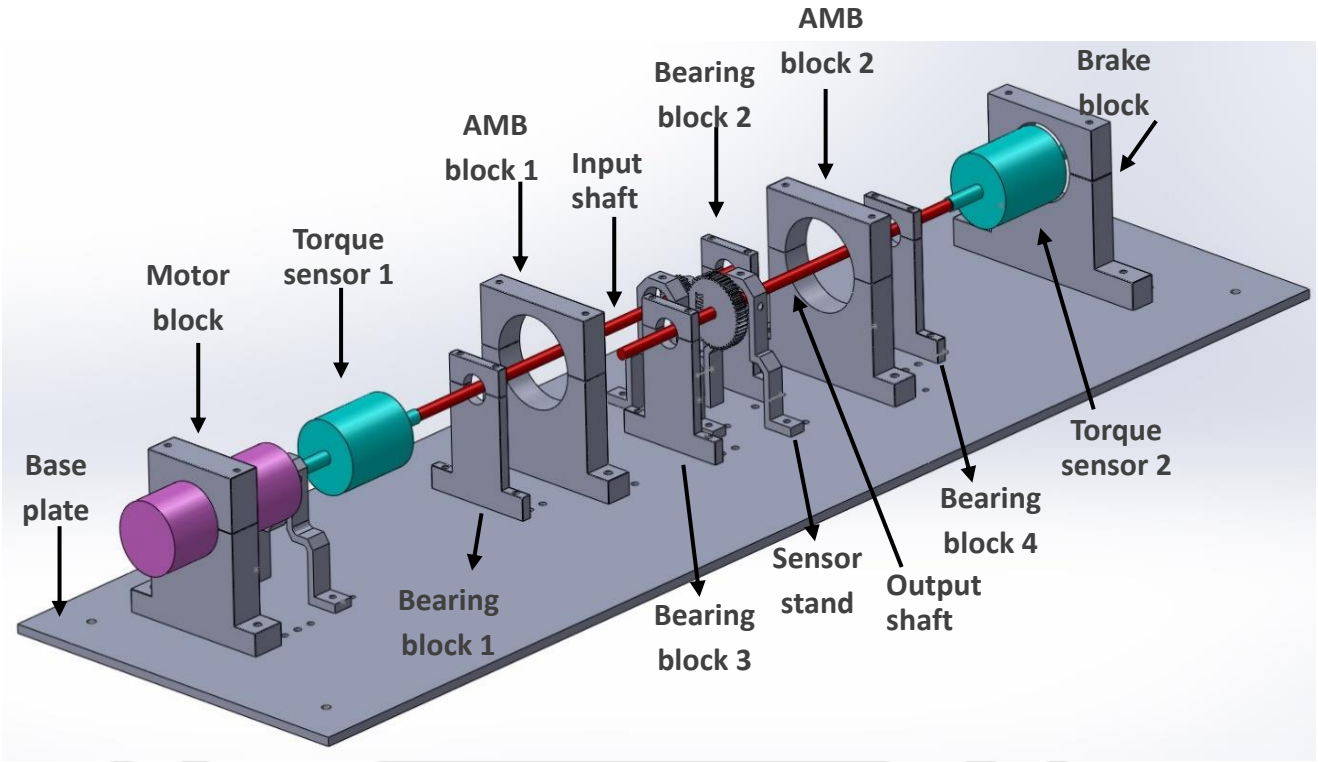

Figure 5.1 CAD model of test rig

The pinion is driven by a motor and the output gear is loaded with a brake load. Because of the flexible coupling, effect of transverse vibration is almost negligible at the motor and brake ends, and both of them are mounted on rigid pedestal/foundation. Hence, the motor and brake end are expected to undergo torsional vibrations. There might be a possibility of assembling error in the gear transmission systems. So, the dynamic transmission error due to eccentricities present in the geared rotor system has been discussed considering gear runouts (i.e., runouts lead to mass unbalances on shafts, and elastic, damping forces at the pitch point) along with AMBs.

5.3 Development of Laboratory Test Rig

The full configuration of AMB consists of a combination of mechanical, electrical, and electronic components, i.e., rotor, sensors, an electromagnetic actuator, power amplifiers, data acquisition system, and digital controller representing complex mechatronics system which is demonstrated in the subsequent sections.

5.3.1 Components of Test Rig

In the present section the different components i.e., actuator, motor, sensors, power amplifiers, controller which were used when designing the laboratory test rig is briefly described. For performing the laboratory test a schematic representation of the built geared rotor-AMB set up is shown in Fig.5.2. The rotor test rig consists of a pair of spur gear having centre distance of 56.25 mm. The pinion and gear have 25 and 50 number of teeth mounted on the input and output shafts of 450 mm length and 12 mm diameter supported by SKF rolling element bearings. The pinion and gear mass are 0.182 kg and 0.623 kg, respectively.

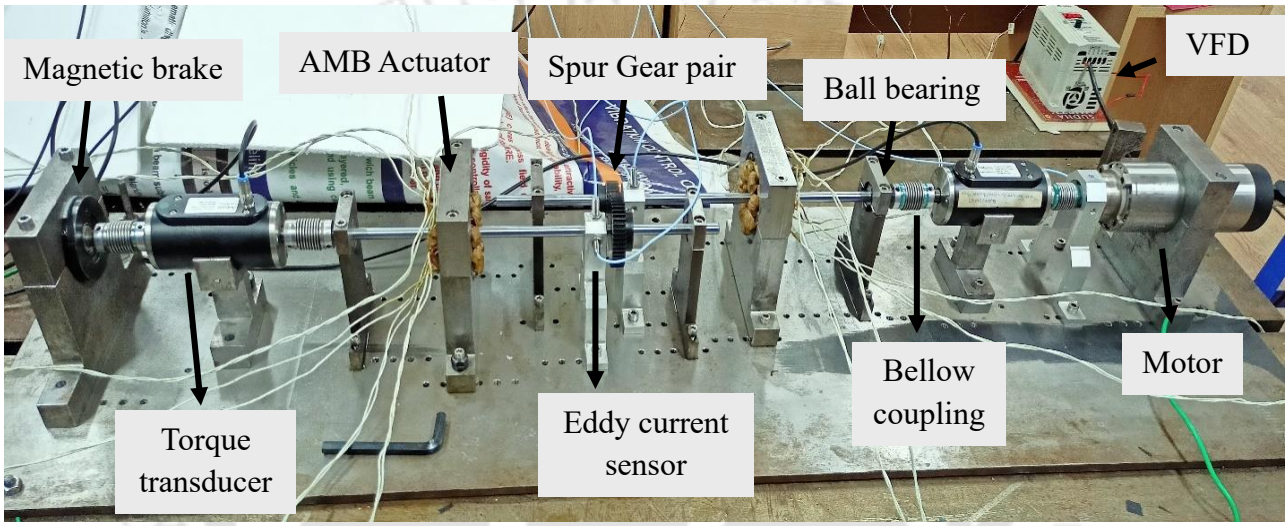

Figure 5.2 Schematic of assembled test rig overview

(1) Motor

A 1.5 kW CNC spindle servo motor of maximum speed limit 24000 rpm is used to drive the input shaft of the geared rotor with 400 Hz Variable frequency drive (VFD) for a precise motion control.

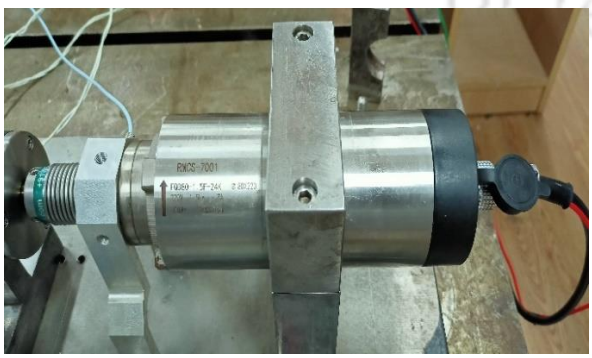

Figure 5.3 (a) Servo motor (b) Variable frequency drive

(2) Couplings

As it is known that bellow couplings have high torsional rigidity, good for angle preserving torque transmissions, can mitigate all forms of misalignment so they are used to connect the different rotor components, i.e., the input and output shafts to the motor spindle and the permanent magnetic brake (load capacity 0~1 Nm) and to the rotary type torque transducer.

(3) Active Magnetic Bearing Actuator

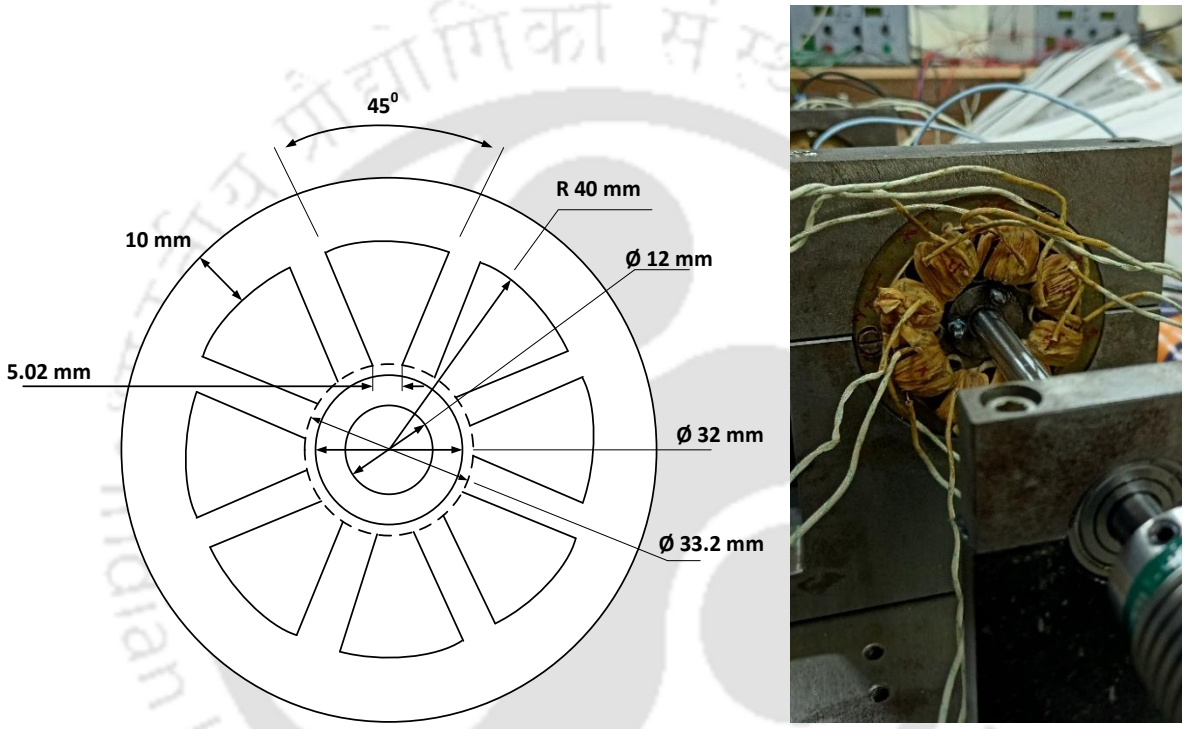

Figure 5.4 AMB actuator model

Two radial magnetic bearing actuators are placed on either side of the geared shafts next to the input and output gears and close to the ball bearings. The radial magnetic bearing actuator and the core is fabricated with laminated silicon steel sheets, i.e., the CRGO (Cold Rolled Grain Oriented) steel built as a stack of punched circular laminated sheets so as to keep the core losses and eddy-current losses low. The actuator consists of eight poles each uniformly spaced at an angle of 22.5 degrees from the pole pair centre line, and 8 mm length and 3 mm width. The core is fixed onto the geared rotor shafts via. interference fit and an air gap of 0.6 mm is maintained between the stator (actuator) and the rotor (core). Each pole pair has 100 number

of copper wire turns with specification 20 AWG (American wire gauge) and current density of 9.6154×10^{6} Am^{-2}. So, the maximum current carrying capacity of the coil per pole is 5 A.

(4) Magnetic Brake

Figure 5.5 (a) Permanent magnet brake (b) Front view

Here, Precision Tork permanent magnet brake has been used to provide constant torque independent of slip speed. Its advantage is that it offers overload and jam protection for all drivetrain components and also provide soft starts with zero slip when a pre-set torque is reached. Here the permanent magnet brake is of hollow bore configuration.

5.3.2 Instrumentation of Test Rig

(1) Torque Sensor

The Datum Electronics Series M425 non-contact rotary torque transducers has been used for the rotary torque measurement.

Figure 5.6 (a) M425 rotary torque transducer (b) Datum universal transducer interface

It is supplied as a complete transducer with bearings to support the stator unit on the rotating shaft. A separate sensor stand was made to mount the torque transducer that makes it fit in line with the drive train/test bed. It is then connected to the rotating shafts through bellow couplings using standard keyway shafts. A non-contact transmission system provides data directly proportional to torque. The transducer utilises a strain gauged shaft for torque measurement. The digital signals are transmitted to the stator providing the torque measurement. The datum universal transducer interface accept signals and display data from the rotary torque tranducer considering the effect of inertial load i.e. brake.

(2) Eddy Current Sensor

Proximity probes are noncontacting transducers that measure distance to a target. These sensors are used in rotating machinery to measure the vibration of a shaft. The vibrational displacement is measured by eddy current proximity sensor (as shown in Fig. 5.6 (a)). A proximitor assembly that contains five proximitor units are used as the proximitor voltage supplier cum proximitor output for the proximity sensor. The vibrational amplitude is measured by adjusting the gap of the sensor and the surface of the shaft in the linear range of −5.75±0.5 Vdc with proximity sensitivity (200 mV/mil ~ 7.874 V/mm) used to find the displacement from voltage. The eddy current sensors are placed in between the gear and AMBs and near to the gears since the vibrations occur due to gear meshing error, transferred to the flexible shaft and then to the entire system. Hence, the displacement vectors obtained from proximity probes are used to construct the AMB forces such that the geared shaft lateral vibrations can be minimized.

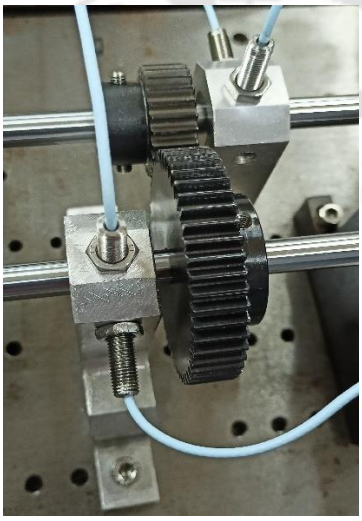

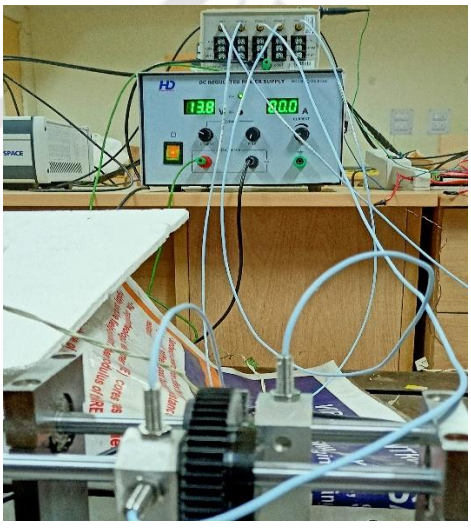

Figure 5.7 (a) Proximity probe near gear-pair (b) Proximitor assembly

(3) Current Probe

Figure 5.8 AC/DC current probe

The 1146B KEYSIGHT current probe is a 100A 100kHz instrument which has been used to measure the current flowing through the actuator coil. It can provide measurement of currents from 100mA to 100A rms, DC to 100kHz, without breaking the circuit and uses hall-effect sensor principles to measure AC and DC signals.

(4) Power Amplifiers

Figure 5.9 (a) Power amplifier (b) D.C voltage supplier

The power amplifier converts control signals to control currents. Here, the pulsewidth modulation (PWM) switching amplifier has been used to generate a high frequency signal, continuously switching in between a low voltage (-V) and a higher voltage (+V) with a variable duty cycle. By varying the duty cycle of the PWM, one gets a desired resultant voltage between –V and +V. A current controlled PD controller is used in the test rig. Advantages of current control is that simple PD or PID control is enough and for smaller systems, current control is

satisfactory. The amplifier in the current control is a voltage-to-current amplifier, which is suitable for the test setup.

(5) Digital Controller

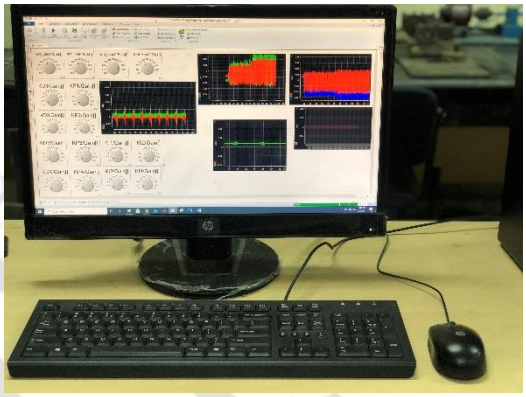

Figure 5.10 (a) dSPACE I/O board (b) dSPACE ControlDesk

Experiments were conducted on dSPACE DS1202 controller with 10 kHz sampling frequency. A dSPACE single-board hardware was used for building a real-time control system with the controller board. The hardware was programmed from Simulink via real-time interface. A set of Simulink blocks gives access to the dSPACE I/O boards. Dialog for altering simulation parameters, such as solver options and simulation time, and for generating C code, are directly accessible from the Simulink environment. ControlDesk provided a variety of virtual instruments for building and configuring virtual instrument panels according to the needs and a platform to perform a seamless experiment. The software provided a powerful layout for measurement and post-processing. All necessary tasks were performed in a single working environment from start to finish. The deviation in vibrational responses due to coupled effect is not much visible due to the low torque/load variation and is also influenced by the geometric parameters of the rotor. These results are experimentally verified in the subsequent sections.

5.4 Experimental Analysis

An experimental analysis has been done with practical demonstration of the proposed model. Since AMBs are open loop unstable system therefore feedback control is needed for a stable operation of the rotor, which is discussed in the following section.

5.4.1 Two-Axis Control with Radial Active Magnetic Bearings

The line diagram is shown in Fig. 5.11 and the whole active magnetic bearing control system is shown in Fig. 5.12

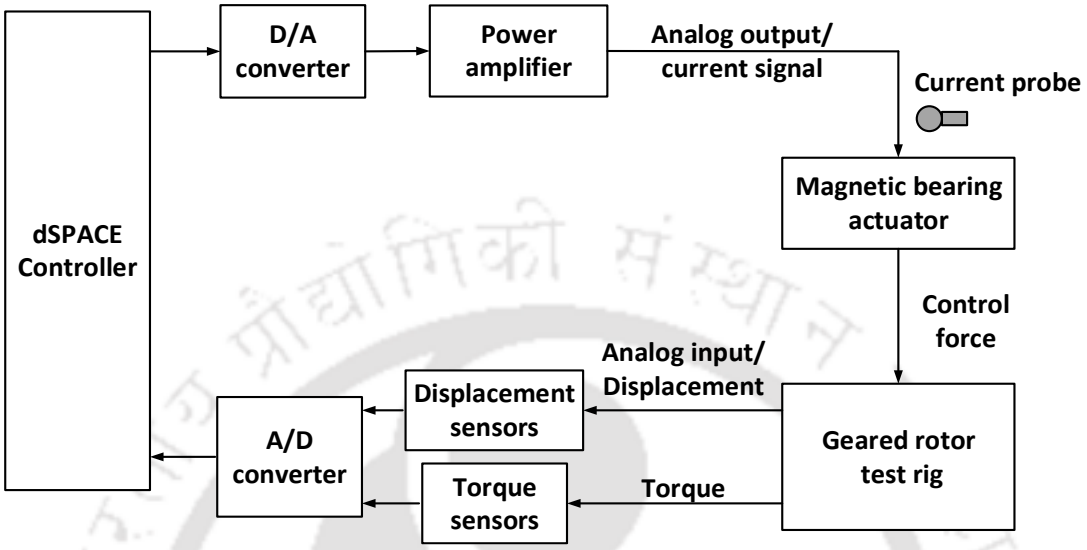

Figure 5.11 Line diagram showing signals in the developed test rig

The eddy current proximity probes are connected to a 5-channel proximitor assembly box, which is used as a voltage supplier and the output from the proximitor is connected to the ADC/DAC panel of controller board. The rotary torque transducer is connected to a datum universal interface (DUI), which functions as power supplier as well as interfacing with the PC, storing and displaying the data.

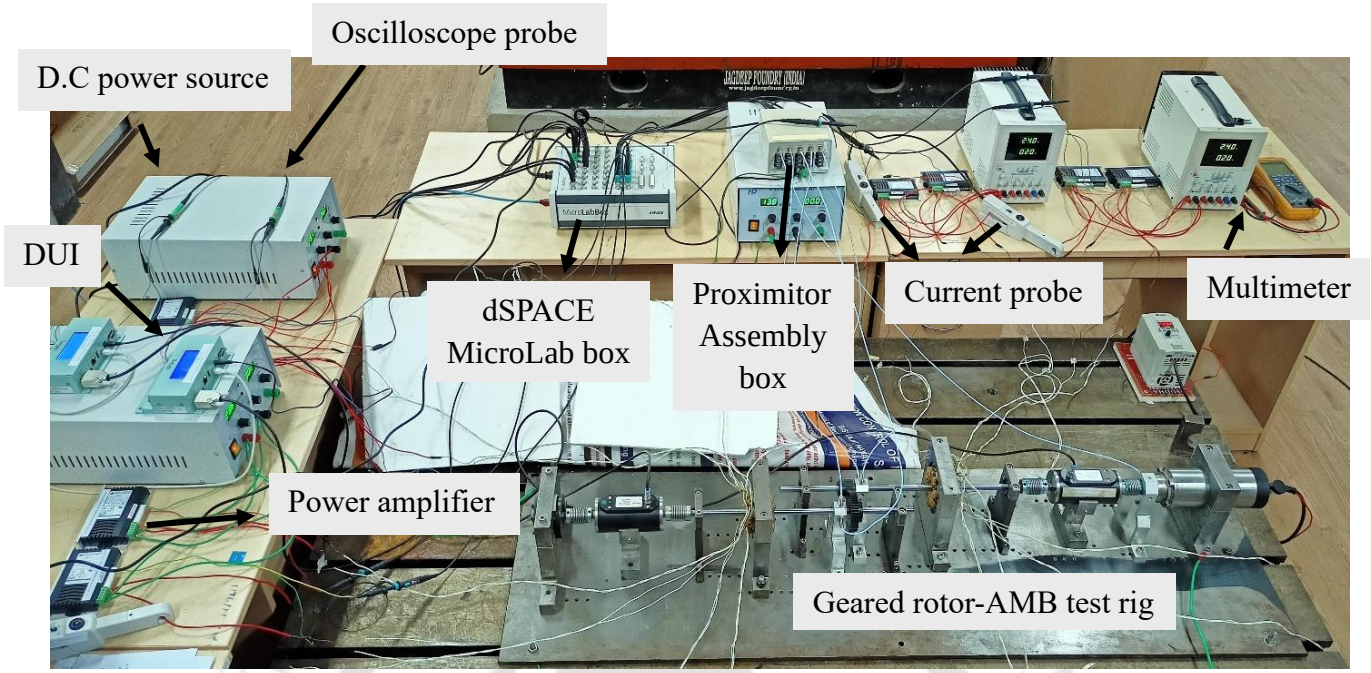

Figure 5.12 Control architecture of experimental rig

The two axes, i.e., the vertical and horizontal direction can be controlled independently. For that the differential driving mode is enabled for the linear control and real-time stabilization of the unstable AMB system. The signal acquired by eddy current sensors and torque sensors are sent to the dSPACE MicroLab box, which has I/O interfaces. dSPACE Control Desk version 6.3 is used for implementation of real-time feedback control algorithm, execution, and data acquisition. The two facing magnetic pole pairs make a bearing axis producing forces in the positive and negative axis directions. The AMB actuator is given same amount of bias current in both the transverse axis taking into account of the magnetic saturation and the desired suppression to be acquired.

The reference is set by bringing the displacement signal obtained from proximity probes to a mean (or reference) position. Simulink is used for building the model and controller values are set such that it is within the range of stable operation. Further, the stable region of operation of the rotor is acquired by applying external disturbances at different locations until the desired damping characteristics is obtained. The optimal gain values were obtained by the following procedure: Initially, the minimum gain values obtained from numerical simulations, i.e., K_P, K_D and K_I were set as an input keeping the rotor in stationary position. With an impact hammer test the rotor stability is checked and the maximum-minimum limit/range of gains were obtained experimentally keeping the rotor within the stable region. The procedure is

checked by increasing the K_P and K_D values within the range. This causes increase in the natural frequency of the rotor with AMB on account of the stiffening effect with proportional gain and the damping factor increases with increase in the derivative gain. The controller receives two position commands corresponding to the desired position of the rotor in the x, y directions and separately adjusts electrical currents in multiple electromagnets. Such a system is Multiple-Input-Multiple-Output (MIMO) control system. The linear PD control parameters are digitally tuned via. the hit and trial method. Often the transient response of the control system exhibits damped oscillations before reaching steady state.

The downside of the test rig was that the rotor could be operated up to 32 Hz since on increasing the speed the rotor vibrational displacement was also increasing and in turn touching the stator (AMB core), which can destabilize the system. Hence, the controller gains mentioned in this work can be used up to 29 Hz of operating speed. The rotor response is controlled using the digitally tuned K_P, K_D and K_I values (refer Table 5.1).

Table 5.1

Experimental PD controller gain values

Gains		Values	Units
AMB 1	K_P	2000	A/m
	K_D	2.5	As/m
	K_I	0	A/m-s
AMB 2	K_P	3500	A/m
	K_D	3.5	As/m
	K_I	0	A/m-s

Eight power amplifiers, i.e., servo A25100 PWM (pulse width modulation) amplifier, were used during the experimentation, which has 20 kHz switching frequency, (10~25 VDC, 15A). Two amplifiers are required for each transverse axis control, which is done via the current control mode. It is used to amplify the low power digital output voltage signal from the controller to a high-power analog voltage signal to be sent to the actuator coils with a gain setting of ~1 V/A. The magnified current signal energises the AMB actuator producing electromagnetic forces and controlling the disturbances coming from the geared rotor at

selected locations. Four 1146B KEYSIGHT AC/DC current probes (AC current accuracy 100 mV/A, and 10 mV/A with sensitivity 0.2 to 0.5 V/div) were used for measuring the control current in the coils of the actuator.

5.4.2 Study of Rotor Free Vibration Responses

In the experimental analysis, impact tests were performed on stationary shaft. The rotor is excited with an impulsive force with an impact hammer on geared shaft in still condition to obtain the corresponding natural frequency of the rotor system configuration described above with AMB. For time domain plot, the impact was given such that the first natural frequency is excited. However, noise at higher frequencies can be seen. But, amplitudes of these noises are very small to be visible in time domain data. The natural frequency of the rotor system is found to be approximately 109 Hz) as shown in Figure 5.13 (a, b). So, the first natural frequency of the system is 6600 rpm.

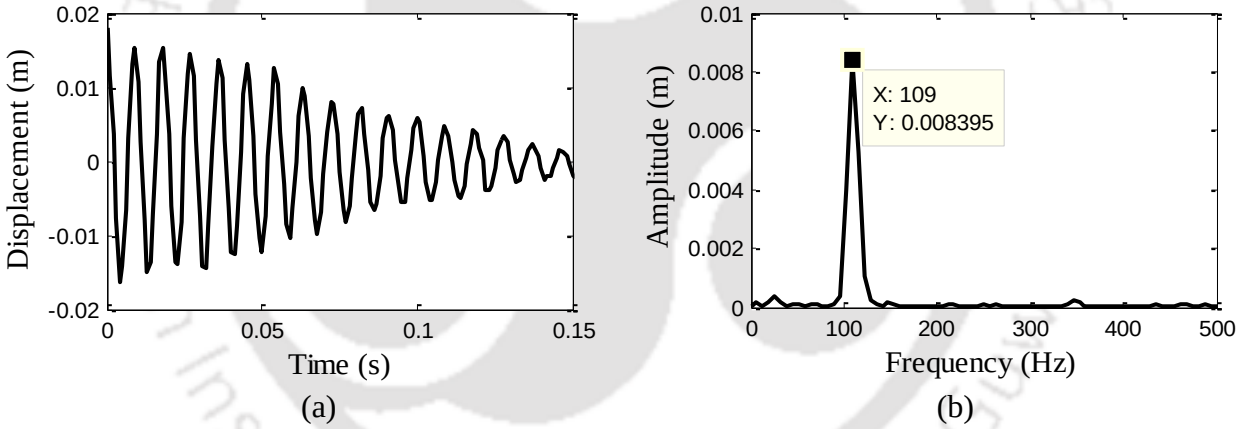

Figure 5.13 Natural frequency of shaft (a) time domain response (b) frequency domain response

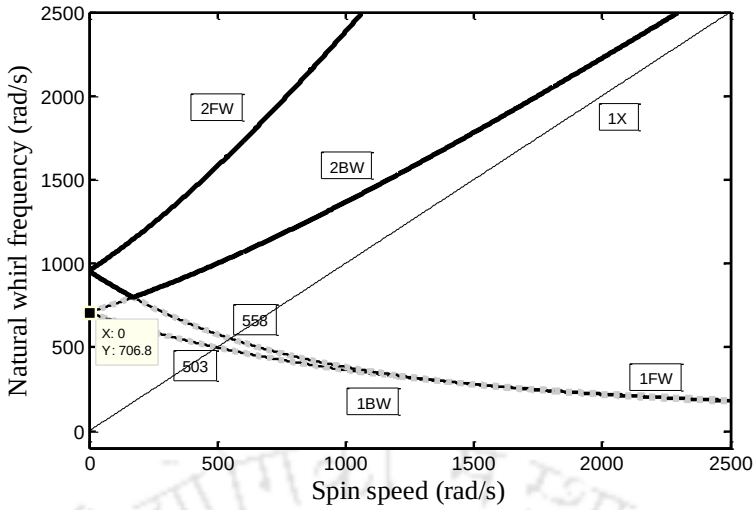

Figure 5.14 Campbell diagram with test rig configuration

The theoretical first natural frequency obtained by taking test rig configuration from Campbell diagram is 706.8 rad/s ~ = 112 Hz (Fig.5.14). The natural frequency obtained from the test rig, via. the impact hammer test is approximately 109 Hz (Fig. 2). So, model is very close to the actual system with some difference due to flexibility of bearing in test setup.

5.4.3 Study of Experimental Forced Vibration Responses

The response of the rotor vibration measured from the test rig are analysed in both time and frequency domain. The time domain vibration responses are recorded by first switching on the AMB and after running for 12 sec switching it off. After switching off the AMB, the amount of increase in vibrational amplitude can be observed which is shown in Fig. 5.15(a) and (c). This helped to view the difference in displacement amplitude with and without the effect of AMB. Equal bias current of 0.75A was given to both the axes of actuator coil of the input shaft and 0.85A was given to both the axes of the actuator coil of output shaft. The saturation limit of the current to be supplied to the actuator coil is set at 2A. It can be observed from Fig. 5.15(a) and (c) that as the gear is mounted in the vertical plane so, due to the inherent unbalance force, the I/O shaft displacement (x_1, x_2) i.e., experimentally taken as displacement in vertical direction is more than the corresponding I/O shaft displacement (y_1, y_2) i.e., experimentally taken as displacement in horizontal direction. The rotor experiences very less displacement in horizontal direction in the driving motor end because of not as much of the misalignment that might inadvertently have happened in the driven output end while assembling the test rig

components. This might be due to the bending of the flexible shaft due to dynamic forces exerted by the output gear onto the input pinon. Also, the sinusoidal vibration signals are having multiple harmonics due to transmission error. Consequently, the controller acts in such a way that it suppresses the vibration more in those direction which has experienced larger amplitude. Therefore, from Fig. 5.15(a) it can been observed that the vibration is reduced by almost 50 % in *x*-direction (vertical) of input shaft whereas very less reduction in amplitude has occurred in the *y*-direction (horizontal) of input shaft. Similar kind of behavior in responses of *x*-direction (vertical) and *y*-direction (horizontal) can be seen in output shaft (Fig. 5.15(c)) where AMB control has led to almost 40 % amplitude reduction. The control current recorded while suppressing the vibrational amplitude in both input and ouput shaft are shown in Fig. 5.15(b) and (d), respectively.

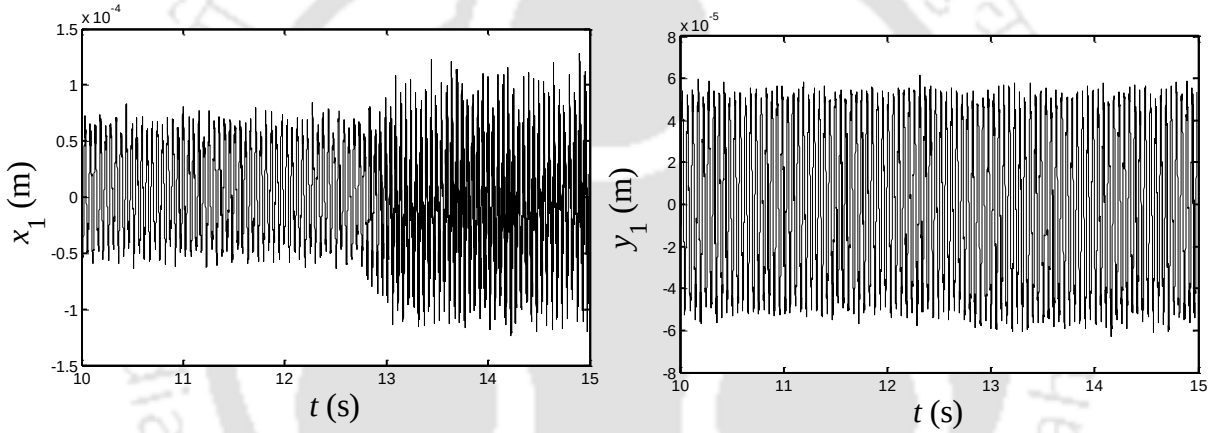

(a)

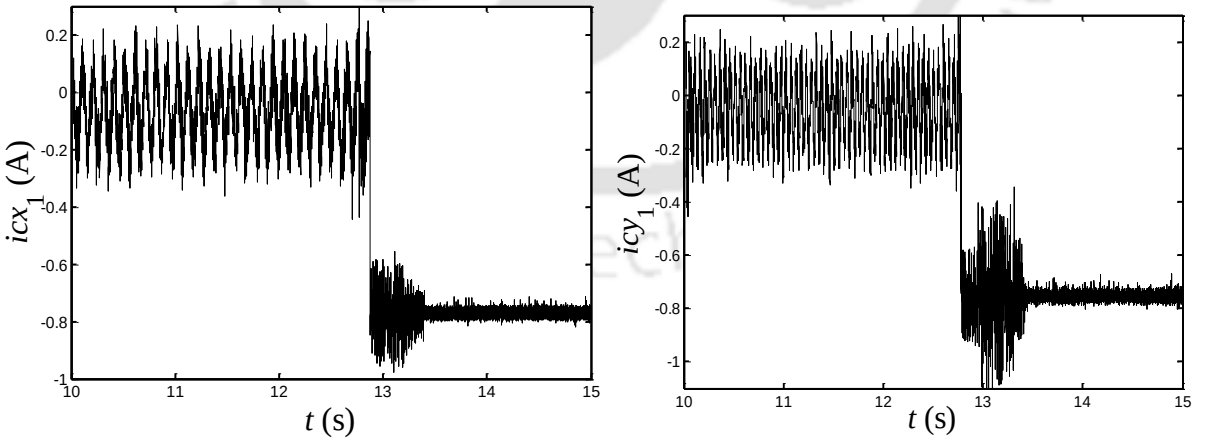

(b)

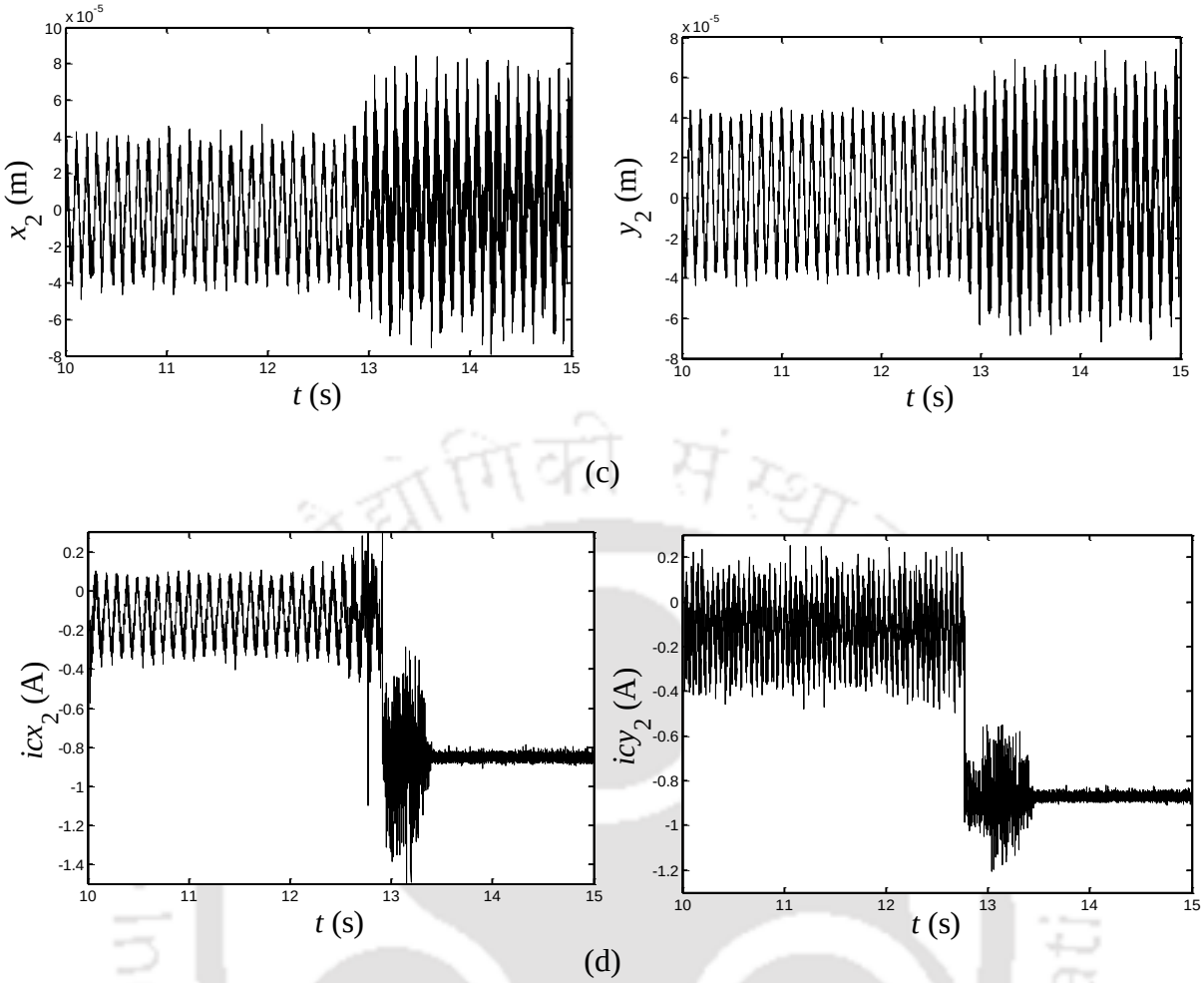

Figure 5.15 Comparison of responses obtained after AMB control (in x, y axes) (a) Vibrational displacement of pinion shaft (b) Control current in pinion shaft (c) Vibrational displacement of gear shaft (d) Control current in gear shaft

5.4.4 Experimental Orbit Plot

Orbit plot is drawn to give a visual representation of the motion of the rotating shaft. The comparison of the orbit plots (Fig. 5.16) illustrates the rotor whirling behavior during operation before and after the application of AMB. The response visibly shows the amount of reduction in the vibrational displacement of the rotor and the change in shaft position versus the angle of rotation.

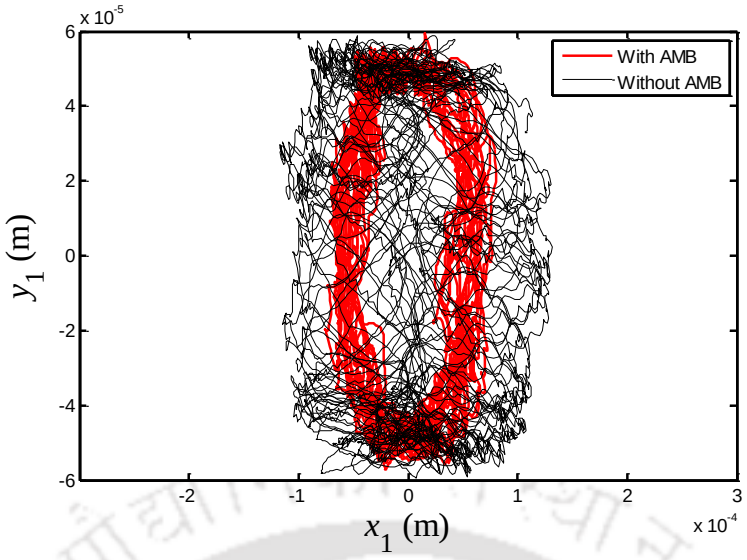

(a)

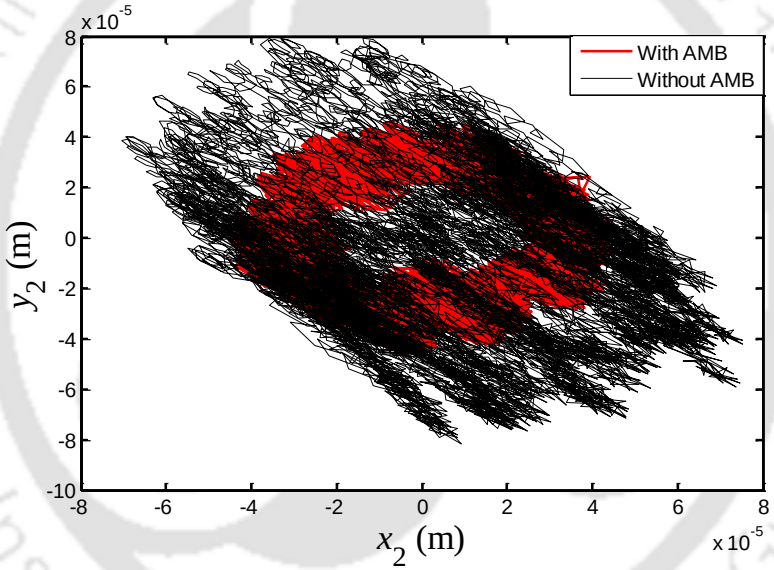

(b)

Figure 5.16 Comparison of orbit plot after AMB control (a) Input end (a) Output end

5.4.5 Experimental Full Spectrum Analysis

Full spectrum is the spectrum of an orbit. It is generated from the output of a pair of proximity sensors placed at right angles. Dynamic forces are generated due to unbalance and constant torque loading, which give rise to gear meshing error resulting in dynamic transmission error. The forward and backward whirl multiple peak frequencies can be seen in Fig. 5.17. With the implementation of AMB, the amplitude is reduced substantially in both the shafts. The

rotational speed of input end is 20 Hz and output end is 10 Hz while the gear mesh frequency is 500 Hz. A comparison in full spectrum plots up to 5X harmonics of the gear mesh frequencies are shown before and after AMB control. The 0 Hz frequency depicts the static deflection of the geared shaft. When considering the gear mesh frequencies, the full spectrum shows with AMB control in input shaft the reduction in vibrational amplitude is at 1X, 2X, -4X, 5X, -5X harmonics of ω_e whereas in output shaft the reduction can be seen at all 1X, -1X, 2X, 3X, -3X, 4X, -4X, 5X, -5X harmonics of ω_e. The difference in the reduction is due the fact that at present effect of AMBs on the overall vibration levels has been observed. Two AMBs are placed at input and output shaft which controls the vibration levels independently. We are considering rigid body mode of the rotor here. The AMBs are not positioned at antinodes targeting different mode shapes of the rotor. The different harmonics of ω_e may differ depending on shaft spin speed. The full spectrum plots are shown below in Fig. 5.17

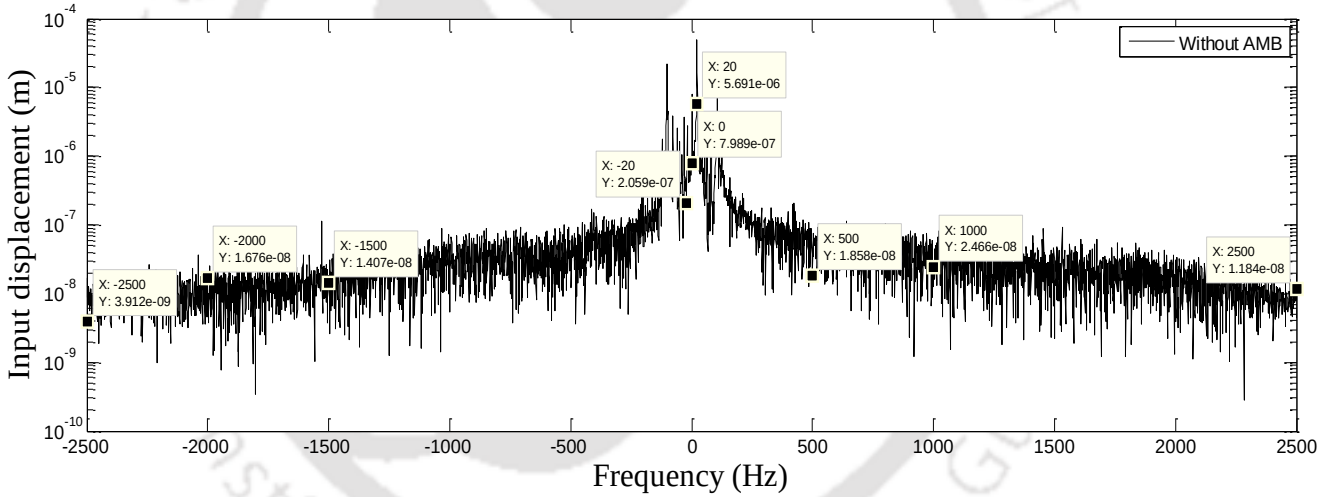

(a)

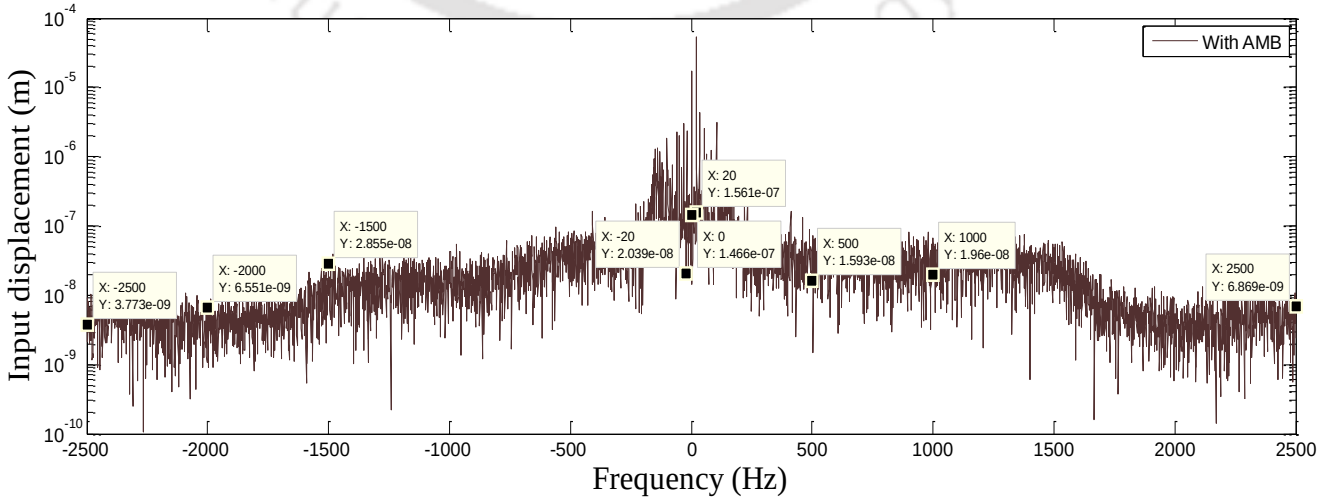

(b)

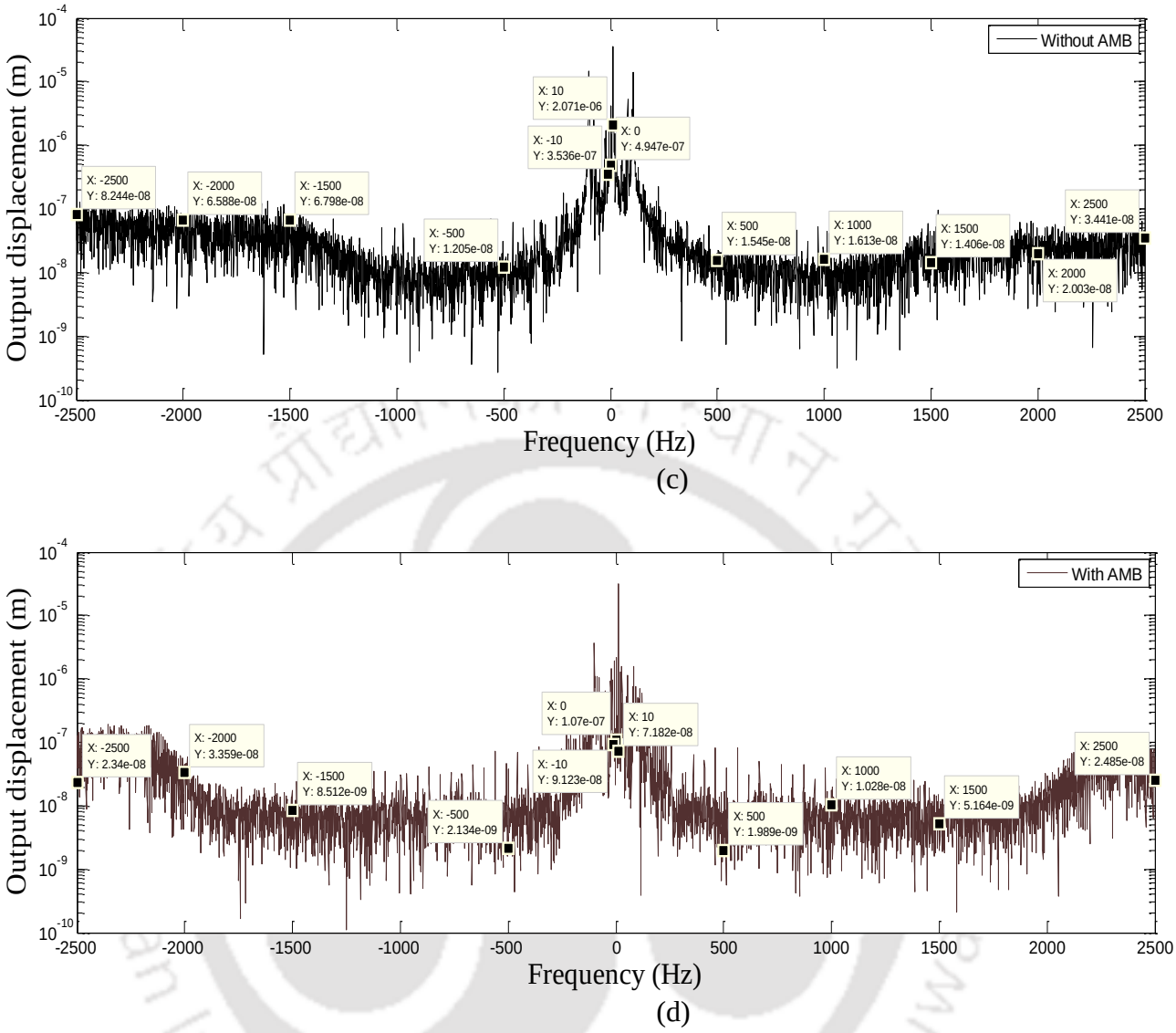

Figure 5.17 (a) Full spectrum plot before AMB control of input shaft (b) Full spectrum plot after AMB control in input shaft (c) Full spectrum plot before AMB control of output shaft (d) Full spectrum plot after AMB control of output shaft

From above Fig. 5.17 the different amplitude responses obtained by full spectrum of input shaft are tabulated in Table 5.2 and for output shaft in Table 5.3.

Table 5.2

Experimental displacement amplitude values from full spectrum of input shaft

No. of harmonics	Without AMB full spectrum response	With AMB full spectrum response

	Displacement amplitude (m)	Displacement amplitude (m)
0	7.989×10^{-7}	1.466×10^{-7}
1X ω_p (20 Hz)	5.691×10^{-6}	1.561×10^{-7}
−1X ω_p (-20 Hz)	2.059×10^{-7}	2.039×10^{-8}
1X ω_e (500 Hz)	1.858×10^{-8}	1.593×10^{-8}
2X ω_e (1000 Hz)	2.466×10^{-8}	1.96×10^{-8}
5X ω_e (2500 Hz)	1.184×10^{-8}	6.869×10^{-9}
−4X ω_e (-2000 Hz)	1.676×10^{-8}	6.551×10^{-9}
−5X ω_e (-2500 Hz)	3.912×10^{-9}	3.773×10^{-9}

Table 5.3

Experimental displacement amplitude values from full spectrum of output shaft

No. of harmonics	**Without AMB full spectrum response**	**With AMB full spectrum response**
	Displacement amplitude (m)	Displacement amplitude (m)
0	4.947×10^{-7}	1.07×10^{-7}
1X ω_g (10 Hz)	2.071×10^{-6}	7.182×10^{-8}
−1X ω_g (-10 Hz)	3.536×10^{-7}	9.123×10^{-8}
1X ω_e (500 Hz)	1.545×10^{-8}	1.989×10^{-9}
2X ω_e (1000 Hz)	1.613×10^{-8}	1.028×10^{-8}
3X ω_e (1500 Hz)	1.406×10^{-8}	5.164×10^{-9}
5X ω_e (2500 Hz)	3.441×10^{-8}	2.485×10^{-8}
−1X ω_e (-500 Hz)	1.205×10^{-8}	2.134×10^{-9}
−3X ω_e (-1500 Hz)	6.798×10^{-8}	8.512×10^{-9}
−4X ω_e (-2000 Hz)	6.588×10^{-8}	3.359×10^{-8}
−5X ω_e (-2500 Hz)	8.244×10^{-8}	2.34×10^{-8}

To analyze the torsional vibration characteristics of the geared rotor, the dynamic torque developed in the shaft and couplings of the system was measured. The load required to keep

the system running is kept same at all speeds. Even though the torque is uniformly varying, it fluctuates from the dynamics point of view. The variation in torque before and after the application of AMB is compared and has been shown in Fig. 5.18. The FFT plot shows small variations in dynamic torque with AMBs at all the gear mesh frequencies when plotted up to 5X harmonics of ω_e. This partially indicates less reduction in torsional vibration of the system. A radial AMB with linear controller will have minimal effect on torsional vibration unless effect of the coupled torsional-lateral vibrations is large.

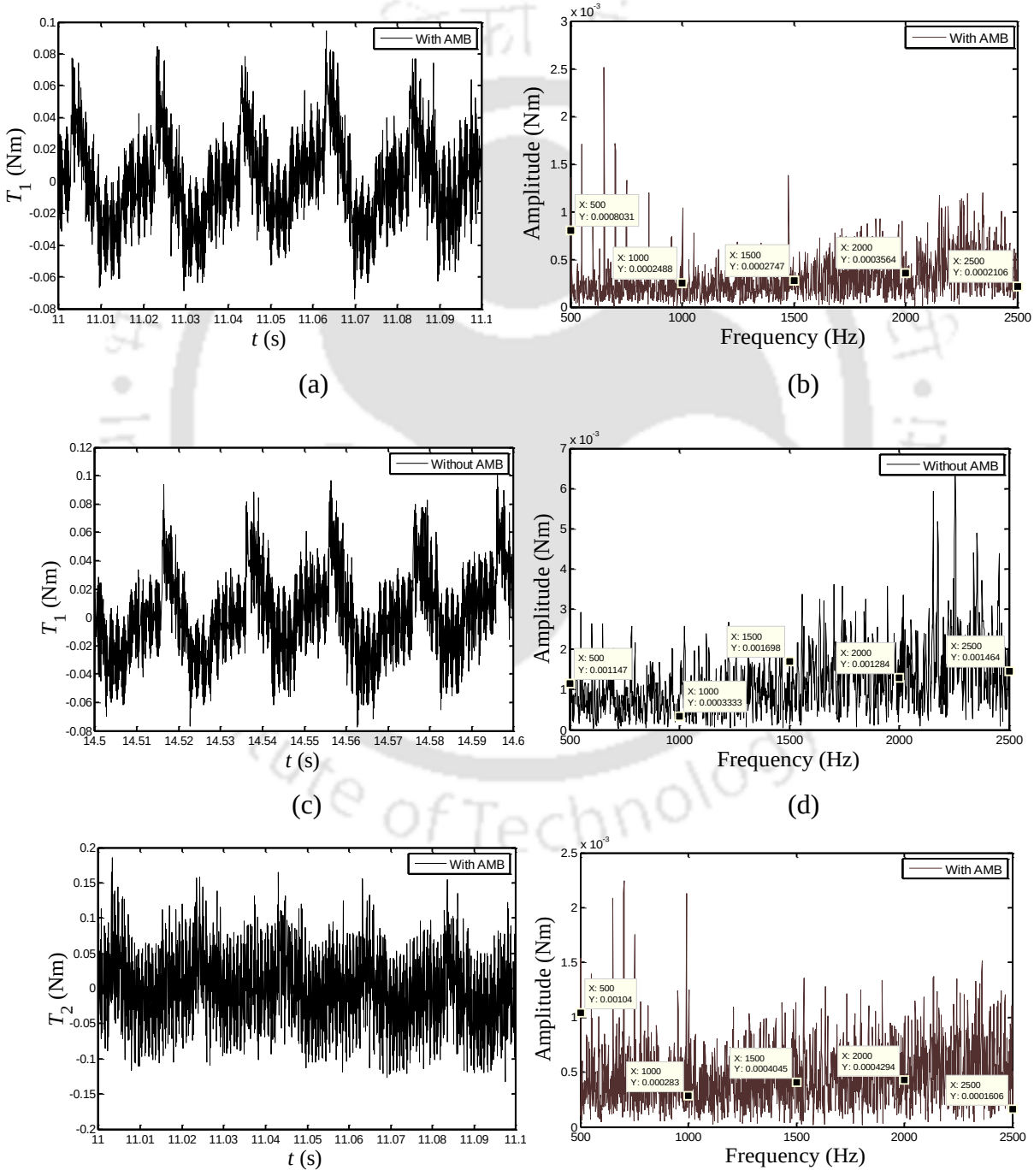

(e) (f)

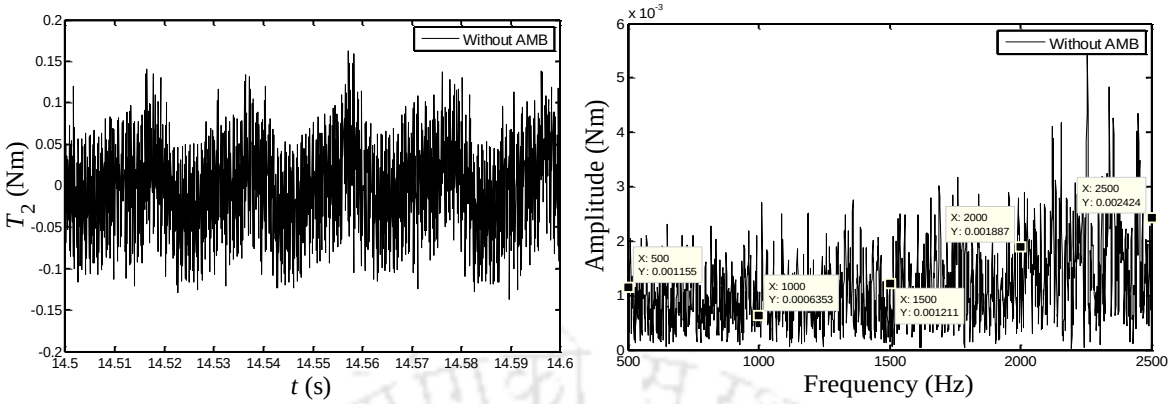

(g) (h)

Figure 5.18 (a) Comparison of variation in torque vs. time in input shaft with AMB (b) FFT plot of torque variation in input shaft after AMB control (c) Comparison of variation in torque vs time in input shaft without AMB (d) FFT plot of torque variation in input shaft without AMB (e) Comparison of variation in torque vs. time in output shaft with AMB (f) FFT plot of torque variation in output shaft after AMB control (g) Comparison of variation in torque vs. time in output shaft without AMB (h) FFT plot of torque variation in output shaft without AMB

From Fig. 5.18 the different amplitude responses obtained by the FFT plot of torque variation of input shaft are tabulated in Table 5.4 and for output shaft in Table 5.5.

Table 5.4. Experimental values of torque variation from FFT of input shaft

No. of harmonics	**With AMB FFT response**	**Without AMB FFT response**
	Torque variation (Nm)	Torque variation (Nm)
1X ω_e (500 Hz)	0.0008031	0.001147
2X ω_e (1000 Hz)	0.0002488	0.0003333
3X ω_e (1500 Hz)	0.0002747	0.001698
4X ω_e (2000 Hz)	0.0003564	0.001284
5X ω_e (2500 Hz)	0.0002106	0.001464

Table 5.5. Experimental values of torque variation from FFT of output shaft

No. of harmonics	**With AMB FFT response**	**Without AMB FFT response**
	Torque variation (Nm)	Torque variation (Nm)

1X ω_e (500 Hz)	0.00104	0.001155
2X ω_e (1000 Hz)	0.000283	0.0006353
3X ω_e (1500 Hz)	0.0004045	0.001211
4X ω_e (2000 Hz)	0.0004294	0.001887
5X ω_e (2500 Hz)	0.0001606	0.002424

To check the noise levels of the system, smartphone was used and is measured by iNVH application developed by Robert Bosch engineers. This app has a sound level meter that uses in built microphones and accelerometers to measure the different quantities. But the application can only log the data for dB values not for peak values or average values useful for the data interpretation. It has octave band calibration that allows user to do a sensitivity correction in each frequency band. The app has default time step of 0.09 s and saving every 11 samples per sec. then we are sampling every 0.99 s and then sampling frequency will be 1/ (0.09×11) ~ = 1 Hz. Hence, it seems to show some periodicity in the fluctuations of the noise level i.e., almost 1 Hz amplitude modulation. The recorded value showed ~4 dB reduction in overall noise levels during operation and is shown in Fig. 5.19.

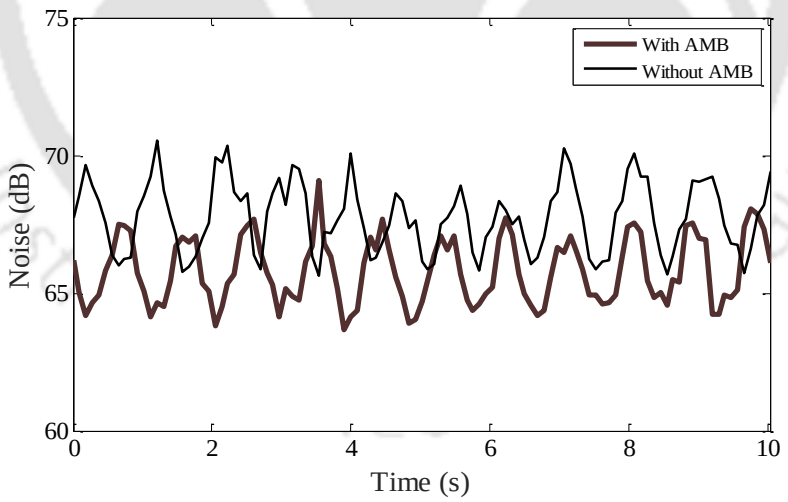

Figure 5.19 Comparison of overall reduction in radiated gear noise levels after AMB control.

5.5. Fault Identification from Experimental Responses

The identification of the geared rotor parameters from the measured signals of the laboratory test rig is explained for various speed ranges in the present section. The measured displacement responses are utilized as per the same methodology as described in the previous chapters of the

numerical experiment for estimation of multiple faults associated with the geared rotor integrated with AMB in the laboratory. The above estimation requires large data to be handled in time domain so the FFT based full spectrum has been applied. But it gives a phase shift that needs to be corrected and described in the next section.

5.5.1 Phase Compensation of Rotor Responses

The phase correction is required for consistency of phase angles of signals captured from rotor vibrations. To remove the uncertainty in phase difference, which is due to picking of time domain signals at different instant of time, phase compensation has been done, such that the measurements taken at random times can be synchronized with respect to a common reference signal. On the motor shaft, two different depth slots are available at 180^0 apart and the reference signal is measured corresponding to one of them. The measured reference signal compensates the phase lag or lead of the acquired vibration signals in the orthogonal direction for each spin speed. An eddy current sensor was placed close to the motor from which the reference signal was triggered once per revolution of the slot in the motor spindle like key phasor. The reference signal in vertical direction at spin speed $\omega_p = 28$ Hz is shown in Fig. 5.20

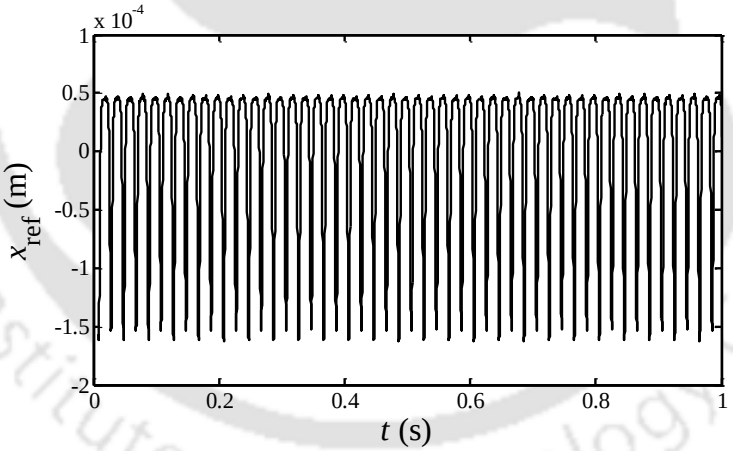

Figure 5.20 Reference signal of the system operating at approximately $\omega_p = 28$ Hz.

Due to the two slots present on spindle of the motor the reference signal is collected from the higher peaks corresponding to which transverse displacement and control current signals measured for different operating speeds are digitally processed further.

Since the responses from geared rotor-AMB system has multiple harmonics so a multi-harmonic phase reference signal is envisaged corresponding to a measured reference signal. Then the phase of displacement signals at each harmonic is subtracted with the phase of

corresponding harmonic of reference signal to get a corrected phase of displacement signal even when it has been captured at different times. The displacement signals were acquired considering multiple complete cycles of shaft rotation, $\omega t = 2\pi n$, where n is the number of complete cycles. This is to ensure minimum leakage errors during FFT. Here $\left|R_i(\omega)\right|$ is full-spectrum amplitude response at different frequencies and θ_i is the phase of i^{th} harmonic of the displacement response, where i is an integer (positive or negative). The time domain quadrature reference signal is converted to frequency domain using FFT process. ψ_i is phase of complex reference signal. Deducting ψ_i from the phase θ_i compensates for the phase shift in the full-spectrum displacement response obtained through FFT. Displacement phase after subtraction from the reference phase is known as the phase compensation, and are used for the identification of system fault parameters.

$$R_{ci}(\omega) = |R_i(\omega)| \angle(\theta_i - \psi_i) \tag{5.1}$$

where, $R_{ci}(\omega) = R_{ci,\text{Re}} + \text{j}R_{ci,\text{Im}}$ is the corrected full-spectrum complex displacement. Subscript c will not be used further to represent the phase corrected signal in the present analysis. The identification of system parameters is performed in the subsequent section.

5.5.2 Prediction of Multiple Geared Rotor Fault Parameters

The full spectrum amplitude and phase compensation responses are utilized in the developed identification algorithm for different speed ranges to identify the fault parameters associated with the test rig. In the present identification procedure, five harmonics of the vibration response and current signal are chosen for the analysis. To get more data sets and maintaining consistency with a high degree of accuracy, identification of parameters is done for combined speed cases, such as from 24 Hz to 26 Hz, 30 Hz to 32 Hz of the spin speed of rotor system with parameters summarized in Table 5.6. The above mentioned two speed cases measured data are fed to the regression matrix $\{\mathbf{A}\}_{52\times38}$ and the known matrix $\{\mathbf{b}\}_{52\times1}$ as stated in Chapter 2 in eqn. (3.49) for the quantitative estimation of multiple faults.

Table 5.6

Parameters of geared rotor test rig

Parameters	Assumed values
Diameter of input and output shafts	0.012 m
Length of input and output shafts	0.4 m
Gear-pair module	1.5
Gear ratio	2
Gear-pair pressure angle (FDI)	20 deg.
Pitch diameter (pinion)	37.5 mm
Pitch diameter (gear)	75 mm
Face width	15 mm
Gear thickness	25 mm
Number of teeth (pinion)	25
Number of teeth (gear)	50
Shaft material density	7860 kg/m^3
Young's modulus	2.068×10^{11} Pa
m_1, m_2	0.2944 kg, 0.8944 kg
ω_p, ω_g	20:28 Hz, 10:15 Hz
k_p, k_g	1.6032×10^5 N/m, 1.6032×10^5 N/m
c_p, c_g	49.63 Ns/m, 69.3 Ns/m
$k_{px\varphi_y}, k_{gx\varphi_y}$	3.8×10^3 N/rad, 3.8×10^3 N/rad
$k_{p\varphi_x\varphi_x}, k_{g\varphi_x\varphi_x}$	2.85×10^3 Nm/rad, 2.85×10^3 Nm/rad
ω_e	500:700 Hz
I_p, I_G	6.08×10^{-5},0.0011 kg-m^2
I_{d_1}, I_{d_2}	3.04×10^{-5}, 5.5×10^{-4} kg-m^2

Table 5.7

Experimentally estimated parameters with AMB for different speed ranges

Estimated parameters	ω_p **= 20 Hz, 21 Hz, 22 Hz**	ω_p **= 26 Hz, 27 Hz, 28 Hz**
c_m	276 Nsm^{-1}	188 Nsm^{-1}
k_m	5.89×10^6 Nm^{-1}	4.7×10^6 Nm^{-1}
e_p	2.33×10^{-6} m	1.9×10^{-6} m
e_g	3.4×10^{-6} m	3.16×10^{-6} m
ϕ_p	-1.992 rad	-2.389 rad
ϕ_g	-0.513 rad	1.903 rad
k_{s_1}	1.306×10^5 Nm^{-1}	1.623×10^5 Nm^{-1}
k_{i_1}	12.74 NA^{-1}	10.05 NA^{-1}
k_{s_2}	1.8×10^5 Nm^{-1}	1.23×10^5 Nm^{-1}
k_{i_2}	9.64 NA^{-1}	8.91 NA^{-1}
e_m	2.55×10^{-7} m	2.3×10^{-7} m
ϕ_m	1.734 rad	1.509 rad
e_{f1}	1.313×10^{-8} m	9.16×10^{-8} m
e_{f2}	2.663×10^{-8} m	2.396×10^{-8} m
e_{f3}	1.018×10^{-8} m	1.073×10^{-8} m
e_{f4}	2.35×10^{-7} m	5.138×10^{-7} m
e_{f5}	4.148×10^{-8} m	1.435×10^{-8} m
ϕ_{f1}	-1.638 rad	-2.366 rad
ϕ_{f2}	-2.549 rad	1.175 rad
ϕ_{f3}	-0.655 rad	-2.292 rad
ϕ_{f4}	-2.492 rad	0.609 rad

ϕ_{f5}	0.865 rad	-2.186 rad

Table 5.8

Experimental estimated parameters without AMB for different speed ranges

Estimated parameters	ω_p **=20 Hz, 21 Hz, 22 Hz**	ω_p **=26 Hz, 27 Hz, 28 Hz**
c_m	186 Nsm^{-1}	164.6 Nsm^{-1}
k_m	3.4×10^6 Nm^{-1}	2.8×10^6 Nm^{-1}
e_p	1.63×10^{-6} m	1.59×10^{-6} m
e_g	3.72×10^{-7} m	3.69×10^{-7} m
ϕ_p	2.225 rad	2.203 rad
ϕ_g	0.154 rad	-0.711 rad
e_m	4.13×10^{-7} m	4.5×10^{-7} m
ϕ_m	-0.055 rad	0.455 rad
e_{f1}	1.34×10^{-8} m	4.12×10^{-8} m
e_{f2}	6.22×10^{-8} m	3.31×10^{-8} m
e_{f3}	3.89×10^{-7} m	1.37×10^{-7} m
e_{f4}	1.08×10^{-6} m	6.84×10^{-6} m
e_{f5}	1.82×10^{-6} m	5.7×10^{-6} m
ϕ_{f1}	2.881 rad	2.927 rad
ϕ_{f2}	0.711 rad	-2.521 rad
ϕ_{f3}	2.661 rad	0.353 rad
ϕ_{f4}	2.192 rad	1.161 rad
ϕ_{f5}	-2.787 rad	-1.208 rad

The gear mesh stiffness, gear mesh damping, runout of input gear and phase, runout of output gear and phase, AMB displacement stiffness constant, AMB current stiffness constant, mean transmission error and phase, variable transmission error corresponding to different harmonics and respective phase angles has been identified experimentally with and without the application of AMB and is shown in Table 5.7 and Table 5.8. It can be observed from the estimated parameters that the mesh damping taking all the speed ranges is found to be between 150 to 300 Nsm^{-1}. The gear mesh stiffness parameter is found to be in the range of 10^6 Nm^{-1} to 10^7 Nm^{-1}. The eccentricity in both the input and output gear is found to be quite small i.e., in microns which shows that there is not much alignment error. The force-displacement factor and force-current factor of AMB is in the range of the analytically calculated values given in the numerical simulation section (refer Chapter 2, eqn. (2.9)) which is around 1.9×10^5 Nm^{-1} and 12 NA^{-1}, respectively. With the suppression of vibration, the transmission error is also found to be lessened by the application of AMB. This can be assessed from the magnitude of the mean and varying transmission error. Thus, preventive measures can be taken with the identification of faults while maintaining the health of the machinery. The estimated parameters are also validated indirectly using the numerical simulation, which is shown in the next section.

5.5.3 Validation of the Numerical Model with Experimentally Estimated Parameters

The experimental results are verified with the numerical model as there might be uncertainties present in the laboratory test rig and the data acquisition system, which might be falsifying the estimated parameters. To check the cogency of the numerical model, instead of assuming the gear-rotor parameters, the parameters so obtained by running the identification algorithm with test rig signals are used into the numerical model and the responses are obtained and the simulated response operating at a spin speed of $\omega_p = 20$ Hz, $\omega_g = 10$ Hz is shown in Fig. 5.20. The amplitude of multiple harmonics in full spectrum response obtained experimentally from the test rig at the same spin speed of $\omega_p = 20$ Hz, $\omega_g = 10$ Hz given by Fig. 5.16 is then compared with this response in Fig. 5.20 which shows similar response pattern.

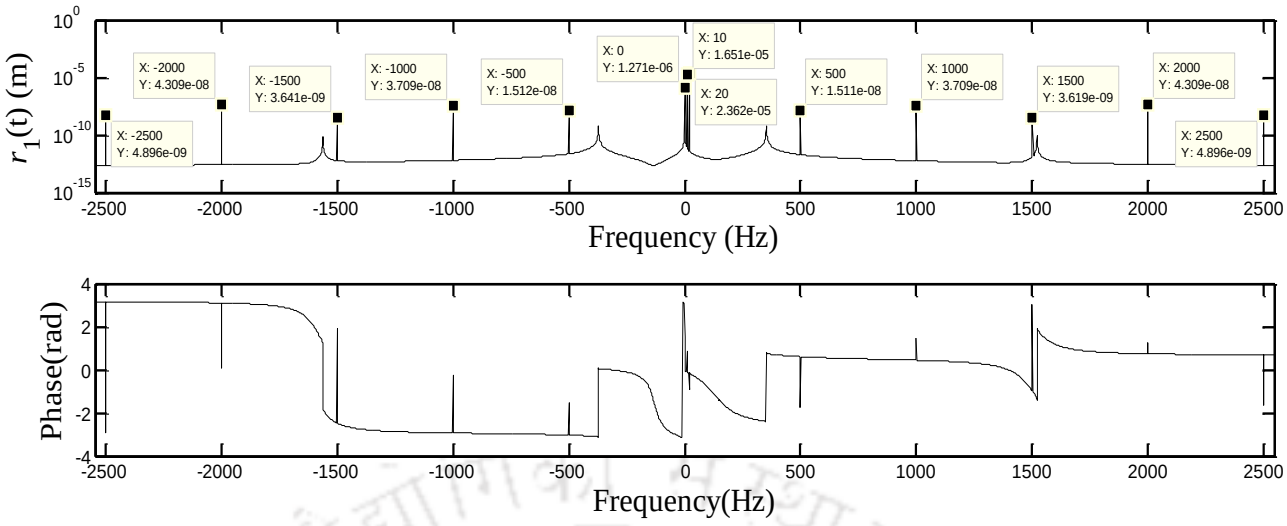

(a)

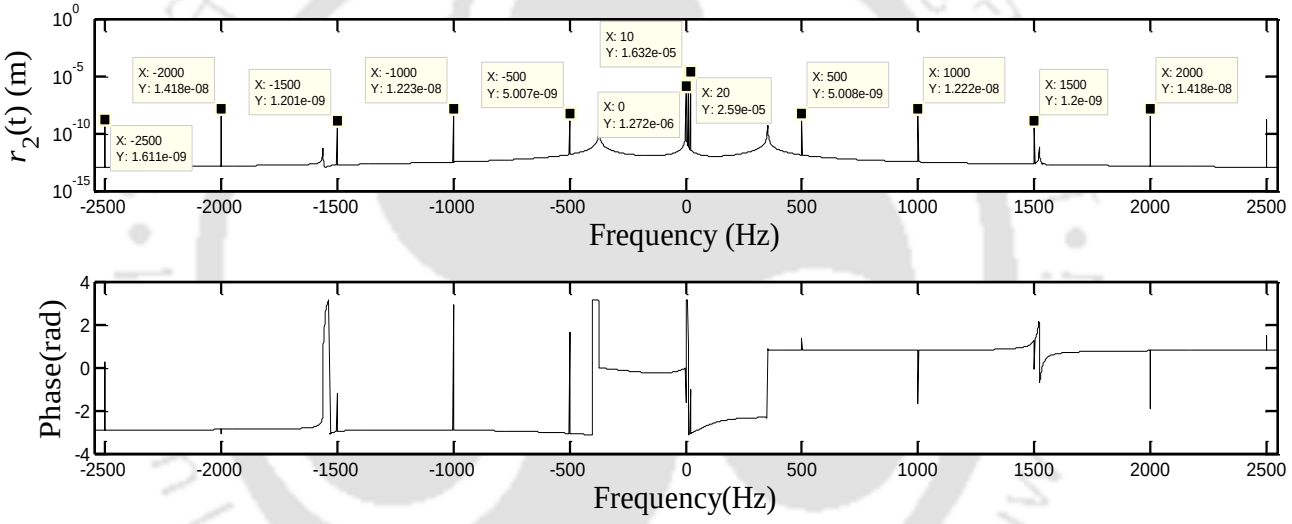

(b)

Figure 5.20 Simulated full spectrum amplitude and phase response (a) input shaft (b) output shaft operating at spin speed $\omega_p = 20$ Hz, $\omega_g = 10$ Hz

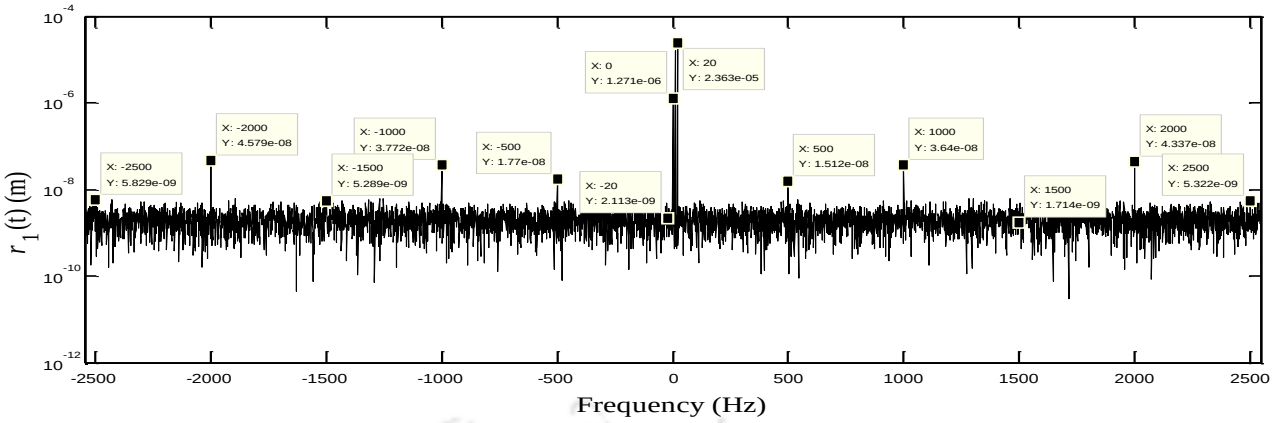

(a)

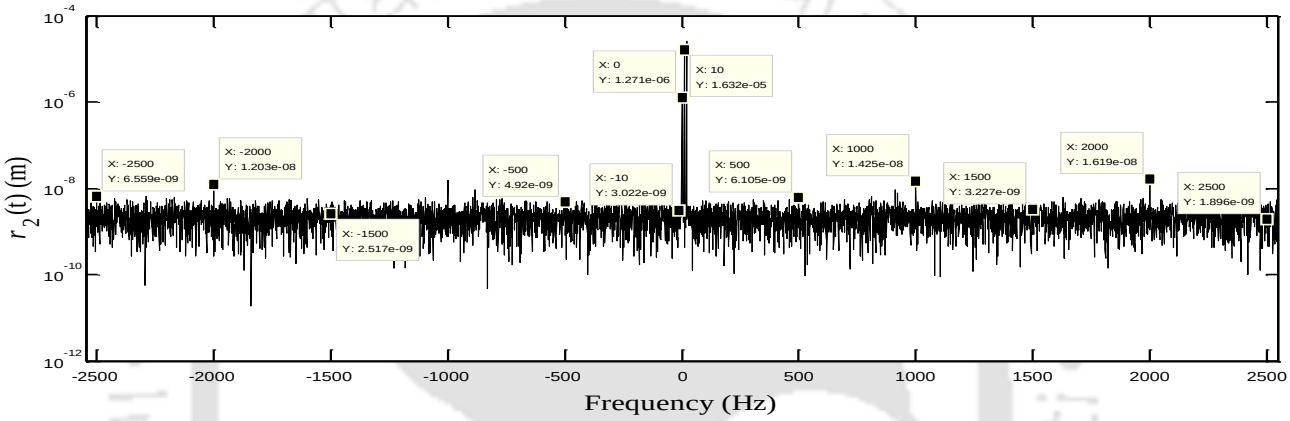

(b)

Figure 5.21 Simulated full spectrum amplitude with 5% random noise addition (a) input shaft (b) output shaft operating at spin speed $\omega_p = 20$ Hz, $\omega_g = 10$ Hz

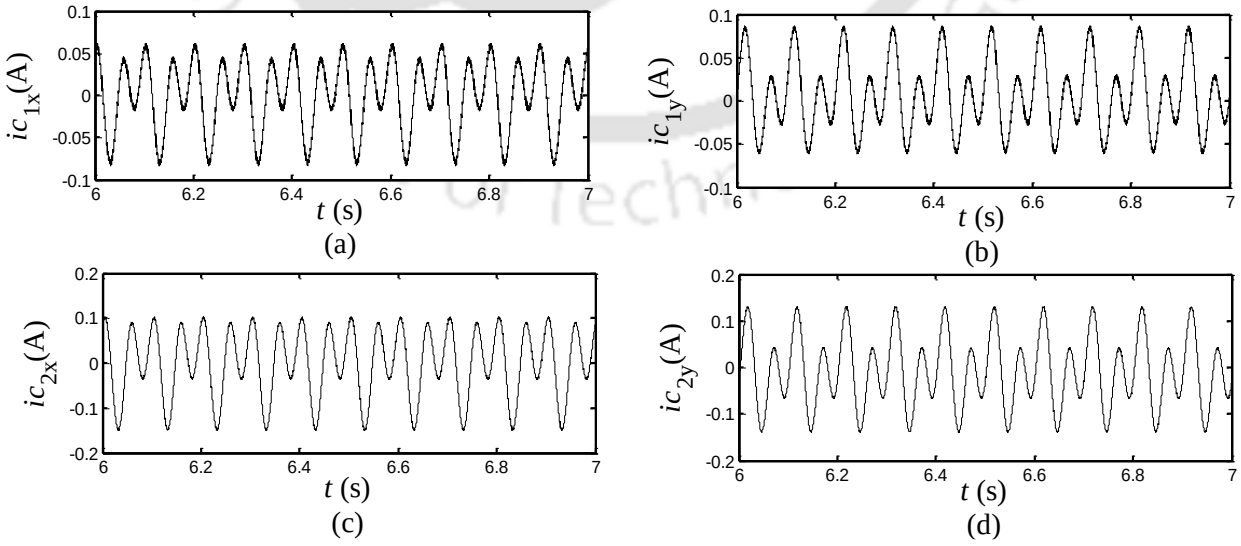

Figure 5.22 Simulated control current signal (a) input shaft (b) output shaft operating at $\omega_p = 20$ Hz, $\omega_g = 10$ Hz of spin speed

Following the full spectrum responses 5% random noise has been added into the numerical model with exact input parameters obtained from test rig and shown in Fig. 5.21. Consequently, the variation of control current with time is also obtained and shown in Fig. 5.22. By comparing first Fig. 5.16 (b), (d) with Fig. 5.20, 5.21 and second Fig. 5.14 (b), (d) with 5.22 it can be observed that the measured responses and the simulated responses are close enough and the pattern of the responses in the two cases are very similar, which verifies the identification methodology.

5.6 Conclusions

In this work a method for suppressing the vibrations caused by variations during gear meshing and rotor faults has been presented. A mathematical model has been developed for the numerical simulation of the proposed geared rotor AMB system and experimentally verified by a laboratory test rig. A classical PD controller employing linear control theory is used to achieve the desired control of the geared rotor by magnetic actuators working in differential driving mode. With feedback of the displaced rotor position, the controller values were adjusted suitably to achieve the desired stiffness and damping characteristics of the AMBs. The maximum attenuation that could be attained was nearly 50% after fine tuning of the controller gains. Although founding a consistency between the simulated and experimental responses shows the proposed method's operational feasibility, the manual tuning process used in this work is cumbersome since separate adjustments have to be done for different operating speed ranges. Here the experiments were conducted under constant loading condition. An improvement can be made by deploying a more automated active control scheme involving an adaptive controller, which can be more effective for reducing the coupled vibrations irrespective of the speed and load variation. It can be seen from the full spectrum that the amplitude of vibration at the various gear tooth meshing frequencies between 500 Hz to 2500 Hz was reduced quite efficiently. The experimental results have yielded about overall ~4 dB reduction in noise owing to vibrations by gear meshing. Hence, this study can significantly contribute to the prevent of damage of gearbox mountings with the help of AMBs.

Further, the experimental signals of rotor vibrational displacement and AMB control current signals, are utilized to validate the numerical model of the developed identification algorithm to estimate the fault parameters, such as the mesh damping, eccentricity with phase, mesh stiffness, mean and variable transmission error with phase and AMB parameters associated with the test rig. With real-time active control of vibrational amplitude achieved by the radial magnetic bearing mounted onto the geared shafts, the correlation of the estimated parameters between the numerically tested results with the experimental ones provides a clear perspective of the influence of different faults onto the others during operation of the machine. It would be a good practice to identify the sources of multiple harmonics due to various faults associated with the rotating machinery and the same methodology can be implemented to diagnose the health of a machine as a preventive measure for condition monitoring. From the present analysis, it can be concluded that the developed identification algorithm can approximate the system dynamics and quantify the different multiple faults in a geared rotor system.

CHAPTER 6 CONCLUSIONS AND FUTURE SCOPE

6.1 Summary of the Present Work

The aim of this research work is to reduce the gear mesh vibrations by applying actively controlled electromagnetic forces with AMBs placed on the geared rotor shafts. It is known that geared rotors are assumed to vibrate torsionally however due to bearings and shaft deflections, any gear dynamic analysis must include the lateral vibrations as well (i.e., movement perpendicular to the gear axis). With this perspective, it has been envisioned that if the gearbox internal shaft transverse vibration can be controlled effectively with the help of active magnetic bearings, then the gears and the surrounding support structures can be prevented from failure due to vibrations. Gear mesh vibrations can propagate through the shafts to the rolling element bearings and the gearbox casing to become a source of radiated noise. This gets characterized by high-amplitude tones emerging from broadband noise whose frequencies lie in the range of maximum human ear sensitivity. In the context of continuous improvement in the acoustic comfort of passengers, it is therefore necessary to analyse and optimize gearbox vibrations in order to reduce casing noise radiations. In addition, it is difficult to obtain the magnitude and phase information of varying transmission error, which is a major concern for the gear noise. Hence, an identification algorithm based on least-squares regression technique has been developed to quantify the transmission error values and other rotor fault parameters.

With this frame a transmission error-based gear dynamic model was developed. The common assembly errors comprise of position errors of the centres of the pinion and gear or deviations between the axes of rotation and the principal polar axes of inertia of the pinion and the gear. These errors generate eccentricities and runout characterised by strong once-per-revolution excitations.

Initially a 4 DOF model for the transverse vibration analysis of a geared rotor system with gear run-out and dynamic transmission error is carried out with help of lumped parameter model. This 4 DOF model served the purpose of benchmarking various procedures, which was used later in the next models addressing greater complexities. A time varying mesh stiffness was considered in the form of transmission error for a single pair of teeth engagement. With the help of active magnetic bearings, the novel concept of active vibration control of transverse vibrations in a spur geared rotor was done effectively. The transmission error is modeled as an

asymmetric dynamic transmission error so full spectrum was chosen for spectral analysis. A novel identification algorithm was developed using regression equations from the mathematical model which estimated the system fault parameters, i.e., the gear mesh stiffness, gear mesh damping, runout of input gear and phase, runout of output gear and phase, AMB displacement stiffness constant, AMB current stiffness constant, mean transmission error and phase, variable transmission error corresponding to different harmonics and respective phase angles. This identification was done using full spectrum responses as the rotor has multiple harmonics due to gear meshing error. The estimated parameters were tested with different random noise and modelling errors to check the robustness of the developed algorithm.

Next, gyroscopic effect on transverse vibration of geared rotor AMB system is analysed if the gears may be offset from mid-span of the rotor. So, the model is updated to 8 DOF by adding rotational DOF i.e., angular displacement of gear wheel about the diametral axes, arising from gyroscopic effect due to offset gears. Since angular displacements pose practical difficulty of accurate measurement, a dynamic reduction scheme was implemented to eliminate the rotational displacements in identification equations and the regression equations were obtained to develop the identification algorithm. So, it will better estimate the transmission error and other parameters. The same procedure follows and full spectrum of AMB current signals in conjunction with vibration displacements was used for the estimation of parameters, tested with different percentage of random noise and modelling errors.

A real system will have all the effect including the torsional one. Hence, the mathematical model is improved to 12 DOF system so that it can approximate the real system behaviour.
In actual scenario there can be gyroscopic effect, coupled torsional-lateral effect, hence the algorithm is updated such that it can estimate the parameters more efficiently in real systems. Relative to the torsional vibration, the lateral vibration of the gear pair is more easily affected by the gyroscopic effect. A nominal torque is applied in order to keep the gears in contact hence, there was not much torsional effect in the system. The simulations showed that in case of coupled torsional-lateral vibrations, controlling the transverse vibration with linear PID will have small effect on torsional vibration reduction unless a better control system is designed. The parameters were estimated from half spectrum of torsional component and full spectrum of transverse vibration component of coupled system. The algorithm development becomes

complex with addition of torsional vibrations and subsequently estimation. Hence, the identification method works better in case of transverse vibration.

The numerical model of the proposed geared rotor AMB system is experimentally verified by a laboratory test rig. The experiments successfully suppressed the vibrations by 40-50% with a classical PD controller working in differential driving mode. The limitation was rotor could be operated up to 32 Hz since on increasing the speed, the rotor vibrational displacement was also increasing and in turn touching the stator (AMB core) which can destabilize the system. Hence, the controller gains mentioned in this work can be used up to 29 Hz of operating speed. At present the experimental measurement of torsional displacements was not done because of some issue in laser vibrometer. However, we tried to show the effect of AMBs on torque variations which showed little difference in torque variations due to low brake load applied. Further, no significant work has been done on the controller design to suppress higher harmonics of ω_e. Hence, there is difference in the reduction in vibrational amplitude of different harmonics of ω_e in input/output shaft. From the present outcome, further studies can be conducted for the design of an adaptive controller aiming at suppressing the amplitude of gear mesh frequencies. The experimental signals of rotor vibrational displacement and AMB current signals, were utilized to validate the identification algorithm. The experimental data helped in understanding the system dynamics and test the efficiency of the developed algorithm.

6.2 Main Contributions of the Research Work

1. Different Mathematical models of spur geared rotor system comprising of effects of gyroscopic moments, gear mesh deformation, runout error, dynamic transmission error integrated with active magnetic bearings was developed. Based on the proposed model, linear equations of motion have been derived using Lagrange's principle and the vibration analysis were conducted.

2. Transmission error was modeled as an asymmetric TE, which is the sum of mean and fluctuating value as a Fourier series function. This was useful to obtain the full spectrum responses containing both multiple forward and backward whirl frequency components and phase information.

3. With the help of active magnetic bearings significant amount of geared rotor transverse vibrational displacement are suppressed considering effects of unbalance, gear runout error and variable transmission error. The active control was done quite effectively with a closed loop PID controller numerically and later demonstrated experimentally.

4. The transverse vibrational amplitude (m) versus gear mesh frequencies (Hz) plot using full spectrum was checked up to 5X gear mesh frequencies and from numerical simulation it was found to get attenuated at all the gear mesh frequencies.

5. Identification algorithm was developed using the regression method taking different types of forced vibration cases i.e., transverse, gyroscopic effect and coupled torsional-lateral dynamics in geared-rotor-AMB system and quantification of faults was done, such as the mesh damping, eccentricity with phase, mesh stiffness, mean and variable transmission error with phase and AMB parameters associated with the test rig. Measurement noise and modelling errors were added to check the robustness of the algorithm which gave favorable results.

6. A test rig was fabricated based on the proposed model to check the feasibility and practical implementation of the proposed model that can control the gear vibration and noise. The numerical results of the proposed model of geared rotor AMB system was compared with that of the responses obtained from the experimental test rig. The practical design guidelines of the active control system of a magnetic bearing in terms of sensors, actuators, power amplifiers and real-time controller implementation has been presented and its effectiveness in suppressing the gear induced housing vibrations and noise was explicitly described.

7. With a simple linear PD controller the maximum attenuation that could be attained was nearly 50% after fine tuning of the controller gains. Experimental full spectrum responses showed that the amplitude of vibration at the various gear tooth meshing frequencies were reduced quite efficiently except for few harmonics. The experimental results have also yielded about ~4 dB reduction in overall noise owing to vibrations by gear meshing.

8. Experimental data collected from the geared rotor AMB test rig was used to validate the developed identification algorithm. It was seen that with the suppression of amplitude of

vibration at various gear mesh frequencies the transmission error got lessened. Thus, it can be concluded that AMBs can effectively prevent the damage of the gearbox components with active vibration control.

6.3 Limitations of the Thesis Work

1. Since a radial magnetic bearing acts in radial direction so there was not much effect seen on torsional vibration of the system numerically. Although good consistency was found between the simulated and experimental responses showing the operational feasibility of the proposed method. The manual tuning process used in this work is cumbersome since separate adjustments has to be performed for different operating speed, and also operation was done under constant loading condition. An improvement can be made by deploying a more robust active control scheme involving an adaptive controller, which can be more effective for reducing the coupled vibrations irrespective of the speed and load variation.

2. The identification algorithms are model-based and developed using a linear mathematical model with constant mesh stiffness and damping. The non-linear factors like friction in meshing and backlash error were neglected. The rolling element bearings were considered rigid. The modelling parameters required in the identification needs to be considered accurately.

3. Due to inadequate sensors, the torsional vibrations could not be measured and the effect of AMBs on gear torsional vibration could not be comprehended experimentally. Due to which the numerical results obtained from the identification algorithm developed in case of coupled torsional-lateral vibration could not be validated experimentally.

4. All the identification algorithms require measurements in two orthogonal directions. In reality, the measurement locations on the shaft may not be accessible because of other mountings over the shaft.

6.4 Recommendations for Future Work

Some recommendations to extend the modelling approach and design of the experimental set up follow from the presented research:

1. In the current study simple modelling approaches were used for initial estimations. More advanced modelling of the geared rotor AMB system would be significant in simulating rotordynamic behaviour. It is recommended to include nonlinearity like friction in meshing, backlash and examine time varying mesh stiffness, dynamic forces and so on.

2. Besides, an adaptation to operating conditions can be made by an adaptive active control scheme with AMBs in a multi gear transmission system under transient operating conditions with varying load and varying speeds.

3. In order to prepare a model to simulate the experimental setup the support structure should be included. In the present research, equivalent support models consist of springs and dampers depicting shafts, gears but bearing forces were excluded. It is suggested to investigate the whole system with a detailed finite element modelling and identification of support parameters to improve the accuracy of the model.

4. In the present research an experimental setup has been designed. As an improvement to the current experimental setup, the drive system and bearings that operate at higher speeds can be investigated. In this way gyroscopic effect on the stability of proposed geared rotor-AMB system at higher speeds can be examined experimentally.

5. In helicopters noise measurements have shown that main gearboxes highly contribute to the overall cabin noise. Helicopters are known to be particularly noisy with cabin noise levels above 90 dB hardly endurable without appropriate ear protections. Helicopter noise reduction is therefore a serious concern for designers. On-board noise measurements highlight that the prominent contributions of main gearboxes which generate high-amplitude peaks in cabin noise spectra, exceeding broadband noise by up to 30 dB are located in the frequency range of maximum human ear sensitivity (between 1000 Hz and 5000 Hz). With active control of gear mesh vibrations, the results can be further used for active noise control which can have a great significance in reducing the helicopter cabin noise.

6. Under impact load conditions, an adaptive control method for dynamic load suppression based on torque compensation can be proposed. The key design parameters that influence the system dynamic performance such as stiffness of axles, inertia, etc., can be identified for further enhancement in vibration suppression and shock resistance.

7. Assembly or mounting errors like if the shafts are not perfectly parallel, misalignments arise and the contact zones between the mating teeth can be significantly altered. This can lead to substantial amount of gear meshing error. Thus, the present analysis can be extended by considering the effect of different types of coupling misalignment on gear transmission error.

8. Other research topics may include determining gear teeth crack initiation points, crack propagation path, and evaluation of various fault growth indicators using laboratory vibration signals and comparing them with field vibration signals.

Appendix A Equations for Developing the Identification Algorithm

Appendix A1: Conversion of complex regression equations into real regression equations for 4 DOF geared rotor-AMB system

Segregation of real and imaginary terms from complex regression eqn. (2.36) to (2.43)

(a) For the input shaft:

Case I. For $i=0$, regression equations after separating the real and imaginary parts are

$$\left(k_p+k_m-k_s\right)\left(R_{0p,Re}e^{0\mathrm{j}\omega_p t}\right)-k_m\left(R_{0g,Re}e^{0\mathrm{j}\omega_p t}\right)=-k_I\left(I_{0p,Re}e^{0\mathrm{j}\omega_p t}\right) \tag{A1.1}$$

$$\left(k_p+k_m-k_s\right)\left(R_{0p,Im}e^{0\mathrm{j}\omega_p t}\right)-k_m\left(R_{0g,Im}e^{0\mathrm{j}\omega_p t}\right)=-k_I\left(I_{0p,Im}e^{0\mathrm{j}\omega_p t}\right) \tag{A1.2}$$

Case II. For $i=1$, i.e. excitation frequency is $\omega_L=\omega_p$ then equations after separating the real and imaginary parts are

$$\begin{aligned}&m_1\left(-\omega_p^2R_{1pp,Re}e^{\mathrm{j}\omega_p t}\right)-\left(c_p+c_m\right)\left(\omega_pR_{1pp,Im}e^{\mathrm{j}\omega_p t}\right)+c_m\left(\omega_pR_{1gp,Im}e^{\mathrm{j}\omega_p t}\right)+\left(k_p+k_m-k_s\right)\left(R_{1pp,Re}e^{\mathrm{j}\omega_p t}\right)\\&-k_m\left(R_{1gp,Re}e^{\mathrm{j}\omega_p t}\right)=\left(m_1\omega_p^2-k_p-k_m\right)e^{\mathrm{j}\omega_p t}(e_p\cos\phi_p)+\left(c_p+c_m\right)\omega_pe^{\mathrm{j}\omega_p t}(e_p\sin\phi_p)-k_I\left(I_{1pp,Re}e^{\mathrm{j}(\omega_p t)}\right)\end{aligned} \tag{A1.3}$$

$$\begin{aligned}&m_1\left(-\omega_p^2R_{1pp,Im}e^{\mathrm{j}\omega_p t}\right)+\left(c_p+c_m\right)\left(\omega_pR_{1pp,Re}e^{\mathrm{j}\omega_p t}\right)-c_m\left(\omega_pR_{1gp,Re}e^{\mathrm{j}\omega_p t}\right)+\left(k_p+k_m-k_s\right)\left(R_{1pp,Im}e^{\mathrm{j}\omega_p t}\right)\\&-k_m\left(R_{1gp,Im}e^{\mathrm{j}\omega_p t}\right)=\left(m_1\omega_p^2-k_p-k_m\right)e^{\mathrm{j}\omega_p t}(e_p\sin\phi_p)-\left(c_p+c_m\right)\omega_pe^{\mathrm{j}\omega_p t}(e_p\cos\phi_p)-k_I\left(I_{1pp,Im}e^{\mathrm{j}(\omega_p t)}\right)\end{aligned} \tag{A1.4}$$

Case III. When $i=-1$, i.e. excitation frequency is $\omega_L=\omega_g$ then equations after separating the real and imaginary parts are

$$\begin{aligned}&m_1\left(-\omega_g^2R_{-1pg,Re}e^{-\mathrm{j}\omega_g t}\right)+\left(c_p+c_m\right)\left(\omega_gR_{-1pg,Im}e^{-\mathrm{j}\omega_g t}\right)-c_m\left(\omega_gR_{-1gg,Im}e^{-\mathrm{j}\omega_g t}\right)-k_m\left(R_{-1gg,Re}e^{-\mathrm{j}\omega_g t}\right)\\&+\left(k_p+k_m-k_s\right)\left(R_{-1pg,Re}e^{-\mathrm{j}\omega_g t}\right)=\left(k_m\right)e^{-\mathrm{j}\omega_g t}(e_g\cos\phi_g)+\left(c_m\omega_g\right)e^{-\mathrm{j}\omega_g t}(e_g\sin\phi_g)-k_I\left(I_{-1pg,Re}e^{-\mathrm{j}(\omega_g t)}\right)\end{aligned}$$

(A1.5)

$$m_1\left(-\omega_g^2 R_{-1pg,Im}e^{-j\omega_g t}\right)-\left(c_p+c_m\right)\left(\omega_g R_{-1pg,Re}e^{-j\omega_g t}\right)+c_m\left(\omega_g R_{-1gg,Re}e^{-j\omega_g t}\right)-k_m\left(R_{-1gg,Im}e^{-j\omega_g t}\right)$$
$$+\left(k_p+k_m-k_s\right)\left(R_{-1pg,Im}e^{-j\omega_g t}\right)=\left(k_m\right)e^{-j\omega_g t}(e_g\sin\phi_g)-\left(c_m\omega_g\right)e^{-j\omega_g t}(e_g\cos\phi_g)-k_I\left(I_{-1pg,Im}e^{-j(\omega_g t)}\right)$$

(A1.6)

Case IV. When $i=-n,...,-1,0,1,...,n$, i.e. excitation frequency is $\omega_L=\omega_e$ then equations after separating the real and imaginary parts are

$$m_1\left(-i^2\omega_e^2 R_{ipe,Re}e^{ji\omega_e t}\right)-\left(c_p+c_m\right)\left(i\omega_e\sum_{i=-n}^{n}R_{ipe,Im}e^{ji\omega_e t}\right)+c_m\left(i\omega_e R_{ige,Im}e^{ji\omega_e t}\right)$$
$$+\left(k_p+k_m-k_s\right)\left(R_{ipe,Re}e^{ji\omega_e t}\right)-k_m\left(R_{ige,Re}e^{ji\omega_e t}\right)=k_m\left[e_m e^{j\phi_m}+\sum_{i=-n}^{n}\left(e_{fi}e^{ji(\omega_e t+\phi_{fi})}\right)\right]-k_I\left(I_{ipe,Re}e^{ji\omega_e t}\right) \quad \text{(A1.7)}$$

$$m_1\left(-i^2\omega_e^2 R_{ipe,Im}e^{ji\omega_e t}\right)+\left(c_p+c_m\right)\left(i\omega_e\sum_{i=-n}^{n}R_{ipe,Re}e^{ji\omega_e t}\right)-c_m\left(i\omega_e R_{ige,Re}e^{ji\omega_e t}\right)$$
$$+\left(k_p+k_m-k_s\right)\left(R_{ipe,Im}e^{ji\omega_e t}\right)-k_m\left(R_{ige,Im}e^{ji\omega_e t}\right)=c_m\left\{i\omega_e\sum_{i=-n}^{n}\left(e_{fi}e^{ji(\omega_e t+\phi_{fi})}\right)\right\}-k_I\left(I_{ipe,Im}e^{ji\omega_e t}\right) \quad \text{(A1.8)}$$

(b) Similarly considering the output shaft:

Case I. For $i=0$, regression equations after separating the real and imaginary parts are

$$\left(k_g+k_m-k_s\right)\left(R_{0g,Re}e^{0j\omega_g t}\right)-k_m\left(R_{0p,Re}e^{0j\omega_g t}\right)=-k_I\left(I_{0g,Re}e^{0j\omega_g t}\right) \quad \text{(A1.9)}$$

$$\left(k_g+k_m-k_s\right)\left(R_{0g,Im}e^{0j\omega_g t}\right)-k_m\left(R_{0p,Im}e^{0j\omega_g t}\right)=-k_I\left(I_{0g,Im}e^{0j\omega_g t}\right) \quad \text{(A1.10)}$$

Case II. When $i=1$, i.e. the excitation frequency is $\omega_L=\omega_p$ then equations after separating the real and imaginary parts are

$$m_2\left(-\omega_p^2 R_{1gp,Re}e^{j\omega_p t}\right)-\left(c_g+c_m\right)\left(\omega_p R_{1gp,Im}e^{j\omega_p t}\right)+c_m\left(\omega_p R_{1pp,Im}e^{j\omega_p t}\right)-k_m\left(R_{1pp,Re}e^{j\omega_p t}\right)$$
$$\left(k_g+k_m-k_s\right)\left(R_{1gp,Re}e^{j\omega_p t}\right)=\left(k_m\right)e^{j\omega_p t}(e_p\cos\phi_p)-\left(c_m\omega_p\right)e^{j\omega_p t}(e_p\sin\phi_p)-k_I\left(I_{1gp,Re}e^{j\omega_p t}\right) \quad \text{(A1.11)}$$

$$m_2\left(-\omega_p^2 R_{1gp,Im}e^{j\omega_p t}\right)+\left(c_g+c_m\right)\left(\omega_p R_{1gp,Re}e^{j\omega_p t}\right)-c_m\left(\omega_p R_{1pp,Re}e^{j\omega_p t}\right)-k_m\left(R_{1pp,Im}e^{j\omega_p t}\right)$$
$$\left(k_g+k_m-k_s\right)\left(R_{1gp,Im}e^{j\omega_p t}\right)=\left(k_m\right)e^{j\omega_p t}(e_p\sin\phi_p)+\left(c_m\omega_p\right)e^{j\omega_p t}(e_p\cos\phi_p)-k_I\left(I_{1gp,Im}e^{j\omega_p t}\right) \quad \text{(A1.12)}$$

Case III. When $i=-1$, i.e. excitation frequency is $\omega_L=\omega_g$ then equations after separating the real and imaginary parts are

$$m_2\left(-\omega_g^2 R_{-1gg,Re}e^{-j\omega_g t}\right)+\left(c_g+c_m\right)\left(\omega_g R_{-1gg,Im}e^{-j\omega_g t}\right)-c_m\left(\omega_g R_{-1pg,Im}e^{-j\omega_g t}\right)+\left(k_g+k_m-k_s\right)\left(R_{-1gg,Re}e^{-j\omega_g t}\right)$$
$$-k_m\left(R_{-1pg,Re}e^{-j\omega_g t}\right)=\left(m_2\omega_g^2-k_g-k_m\right)e^{-j\omega_g t}(e_g\cos\phi_g)-\left(c_g\omega_g+c_m\omega_g\right)e^{-j\omega_g t}(e_g\sin\phi_g)-k_I\left(I_{-1gg,Re}e^{-j\omega_g t}\right) \quad \text{(A1.13)}$$

$$m_2\left(-\omega_g^2 R_{-1gg,Im}e^{-j\omega_g t}\right)-\left(c_g+c_m\right)\left(\omega_g R_{-1gg,Re}e^{-j\omega_g t}\right)+c_m\left(\omega_g R_{-1pg,Re}e^{-j\omega_g t}\right)+\left(k_g+k_m-k_s\right)\left(R_{-1gg,Im}e^{-j\omega_g t}\right)$$
$$-k_m\left(R_{-1pg,Im}e^{-j\omega_g t}\right)=\left(m_2\omega_g^2-k_g-k_m\right)e^{-j\omega_g t}(e_g\sin\phi_g)+\left(c_g\omega_g+c_m\omega_g\right)e^{-j\omega_g t}(e_g\cos\phi_g)-k_I\left(I_{-1gg,Im}e^{-j\omega_g t}\right) \quad \text{(A1.14)}$$

Case IV. When $i=-5,...,-1,0,1,...5$, i.e. the excitation frequency is $\omega_L=\omega_e$ then equations after separating the real and imaginary parts are

$$m_2\left(-i^2\omega_e^2 R_{ige,Re}e^{ji\omega_e t}\right)-\left(c_g+c_m\right)\left(i\omega_e R_{ige,Im}e^{ji\omega_e t}\right)+c_m\left(i\omega_e R_{ipe,Im}e^{ji\omega_e t}\right)+\left(k_g+k_m-k_s\right)\left(R_{ige,Re}e^{ji\omega_e t}\right)$$
$$-k_m\left(R_{ipe,Re}e^{ji\omega_e t}\right)=-k_m\left[e_m e^{j\phi_m}+\sum_{i=-n}^{n}\left(e_{fi}e^{ji(\omega_e t+\phi_{fi})}\right)\right]-k_I\left(I_{ige,Re}e^{ji\omega_e t}\right) \quad \text{(A1.15)}$$

$$m_2\left(-i^2\omega_e^2 R_{ige,Im}e^{ji\omega_e t}\right)+\left(c_g+c_m\right)\left(i\omega_e R_{ige,Re}e^{ji\omega_e t}\right)-c_m\left(i\omega_e R_{ipe,Re}e^{ji\omega_e t}\right)+\left(k_g+k_m-k_s\right)\left(R_{ige,Im}e^{ji\omega_e t}\right)$$
$$-k_m\left(R_{ipe,Im}e^{ji\omega_e t}\right)=-c_m\left\{i\omega_e\sum_{i=-n}^{n}\left(e_{fi}e^{ji(\omega_e t+\phi_{fi})}\right)\right\}-k_I\left(I_{ige,Im}e^{ji\omega_e t}\right) \quad \text{(A1.16)}$$

Appendix A2: Conversion of complex regression equations into real regression equations for 8 DOF geared rotor-AMB system

The real regression form by separating real and imaginary quantities, from complex regression equations (3.20) to (3.21) for i^{th} harmonic is:

$$m_1' = m_1 + \left(t^{d_1}\right)^2 I_{d_1};\ m_2' = m_2 + \left(t^{d_2}\right)^2 I_{d_2};\ c_p' = c_p + c_m;\ c_g' = c_g + c_m;$$

$$k_p' = k_p - 2\left(t^{d_1}\right)k_{pla} + \left(t^{d_1}\right)^2 k_{pa};\ k_g' = k_g - 2\left(t^{d_2}\right)k_{gla} + \left(t^{d_2}\right)^2 k_{ga}$$

(a) For the input shaft:

Case I. For $i = 0$, regression equations after separating the real and imaginary parts are

$$\left(k_p' + k_m\right)\left(R_{0p,Re}e^{0\mathrm{j}\omega_p t}\right) - k_m\left(R_{0g,Re}e^{0\mathrm{j}\omega_p t}\right) = k_s\left(R_{0p,Re}e^{0\mathrm{j}\omega_p t}\right) - k_I\left(I_{0p,Re}e^{0\mathrm{j}\omega_p t}\right) \tag{A2.1}$$

$$\left(k_p' + k_m\right)\left(R_{0p,Im}e^{0\mathrm{j}\omega_p t}\right) - k_m\left(R_{0g,Im}e^{0\mathrm{j}\omega_p t}\right) = k_s\left(R_{0p,Im}e^{0\mathrm{j}\omega_p t}\right) - k_I\left(I_{0p,Im}e^{0\mathrm{j}\omega_p t}\right) \tag{A2.2}$$

Case II. when excitation frequency is $\omega_L = \omega_p$ then equations after separating the real and imaginary parts are

$$\left[\left\{-\left(i\omega_p\right)^2 m_1' - i\omega_p{}^2 I_{p_1}\left(t^{d_1}\right)^2 + k_p'\right\}\left(R_{ipp,\mathrm{re}}\right) - i\omega_p c_p'\left(R_{ipp,\mathrm{im}}\right) + \left(i\omega_p c_m\right)\left(R_{igp,\mathrm{im}}\right) - k_m\left(R_{igp,\mathrm{re}}\right)\right]\left(e^{\mathrm{j}i\omega_p t}\right)$$
$$= \left(m_1\omega_p^2 + k_{pla}t_{d_1} - k_{pll} - k_m\right)e^{\mathrm{j}\omega_p t}(e_p\cos\phi_p) + c_p'\omega_p e^{\mathrm{j}\omega_p t}(e_p\sin\phi_p) + k_s R_{ipp,\mathrm{re}}e^{\mathrm{j}i\omega_p t} - k_I I_{ipp,\mathrm{re}}e^{\mathrm{j}i\omega_p t}$$

(A2.3)

$$\left[\left\{-\left(i\omega_p\right)^2 m_1' - i\omega_p{}^2 I_{p_1}\left(t^{d_1}\right)^2 + k_p'\right\}\left(R_{ipp,\mathrm{im}}\right) + i\omega_p c_p'\left(R_{ipp,\mathrm{re}}\right) - \left(i\omega_p c_m\right)\left(R_{igp,\mathrm{re}}\right) - k_m\left(R_{igp,\mathrm{im}}\right)\right]\left(e^{\mathrm{j}i\omega_p t}\right)$$
$$= \left(m_1\omega_p^2 + k_{pla}t_{d_1} - k_p - k_m\right)e^{\mathrm{j}\omega_p t}(e_p\sin\phi_p) - c_p'\omega_p e^{\mathrm{j}\omega_p t}(e_p\cos\phi_p) + k_s R_{ipp,\mathrm{im}}e^{\mathrm{j}i\omega_p t} - k_I I_{ipp,\mathrm{im}}e^{\mathrm{j}i\omega_p t}$$

(A2.4)

Case III. When excitation frequency is $\omega_L = \omega_g$ then equations after separating the real and imaginary parts are

$$\left[\left(-(i\omega_g)^2 m_1' - i\omega_g{}^2 I_{p_1}\left(t^{d_1}\right)^2 + k_p'\right)\left(R_{ipg,\mathrm{re}}\right) - i\omega_g c_p'\left(R_{ipg,\mathrm{im}}\right) + i\omega_g c_m\left(R_{igg,\mathrm{im}}\right) - k_m\left(R_{igg,\mathrm{re}}\right)\right]\left(e^{\mathrm{j}i\omega_g t}\right)$$
$$= \left(k_m\right)e^{-\mathrm{j}\omega_g t}(e_g\cos\phi_g) + \left(c_m\omega_g\right)e^{-\mathrm{j}\omega_g t}(e_g\sin\phi_g) + k_s R_{ipg,\mathrm{re}}e^{\mathrm{j}i\omega_g t} - k_I I_{ipg,\mathrm{re}}e^{\mathrm{j}i\omega_g t}$$

(A2.5)

$$\left[\left(-(i\omega_g)^2 m_1' - i\omega_g{}^2 I_{p_1}\left(t^{d_1}\right)^2 + k_p'\right)\left(R_{ipg,\mathrm{im}}\right) + i\omega_g c_p'\left(R_{ipg,\mathrm{re}}\right) - i\omega_g c_m\left(R_{igg,\mathrm{re}}\right) - k_m\left(R_{igg,\mathrm{im}}\right)\right]\left(e^{\mathrm{j}i\omega_g t}\right)$$
$$= \left(k_m\right)e^{-\mathrm{j}\omega_g t}(e_g\sin\phi_g) - \left(c_m\omega_g\right)e^{-\mathrm{j}\omega_g t}(e_g\cos\phi_g) + k_s R_{ipg,\mathrm{im}}e^{\mathrm{j}i\omega_g t} - k_I I_{ipg,\mathrm{im}}e^{\mathrm{j}i\omega_g t}$$

(A2.6)

Case IV. When excitation frequency is $\omega_L = \omega_e$ then equations after separating the real and imaginary parts are

$$\left[\left(-(i\omega_e)^2 m_1' - i\omega_e{}^2 I_{p_1}\left(t^{d_1}\right)^2 + k_p'\right)\left(R_{ipe,\mathrm{re}}\right) - i\omega_e c_p'\left(R_{ipe,\mathrm{im}}\right) + i\omega_e c_m\left(R_{ige,\mathrm{im}}\right) - k_m\left(R_{ige,\mathrm{re}}\right)\right]\left(e^{\mathrm{j}i\omega_e t}\right)$$
$$= k_m\left[e_m e^{\mathrm{j}\phi_m} + \sum_{i=-n}^{n}\left(e_{fi}e^{\mathrm{j}i(\omega_e t+\phi_{fi})}\right)\right] + k_s R_{ipe,\mathrm{re}}e^{\mathrm{j}i\omega_e t} - k_I I_{ipe,\mathrm{re}}e^{\mathrm{j}i\omega_e t}$$

(A2.7)

$$\left[\left(-(i\omega_e)^2 m_1' - i\omega_e{}^2 I_{p_1}\left(t^{d_1}\right)^2 + k_p'\right)\left(R_{ipe,\mathrm{im}}\right) + i\omega_e c_p'\left(R_{ipe,\mathrm{re}}\right) - i\omega_e c_m\left(R_{ige,\mathrm{re}}\right) - k_m\left(R_{ige,\mathrm{im}}\right)\right]\left(e^{\mathrm{j}i\omega_e t}\right)$$
$$= c_m\left\{i\omega_e\sum_{i=-n}^{n}\left(e_{fi}e^{\mathrm{j}i(\omega_e t+\phi_{fi})}\right)\right\} + k_s R_{ipe,\mathrm{im}}e^{\mathrm{j}i\omega_e t} - k_I I_{ipe,\mathrm{im}}e^{\mathrm{j}i\omega_e t}$$

(A2.8)

(b) Similarly considering the output shaft:

Case I. For $i = 0$, regression equations after separating the real and imaginary parts are

$$\left(k_g'\right)\left(R_{0g,\mathrm{re}}e^{0\,\mathrm{j}\omega_g t}\right) - k_m\left(R_{0p,\mathrm{re}}e^{0\,\mathrm{j}\omega_g t}\right) = k_s\left(R_{0g,\mathrm{re}}e^{0\,\mathrm{j}\omega_g t}\right) - k_I\left(I_{0g,\mathrm{re}}e^{0\,\mathrm{j}\omega_g t}\right) \quad \text{(A2.9)}$$

$$\left(k_g'\right)\left(R_{0g,\mathrm{im}}e^{0\,\mathrm{j}\omega_g t}\right) - k_m\left(R_{0p,\mathrm{im}}e^{0\,\mathrm{j}\omega_g t}\right) = k_s\left(R_{0g,\mathrm{im}}e^{0\,\mathrm{j}\omega_g t}\right) - k_I\left(I_{0g,\mathrm{im}}e^{0\,\mathrm{j}\omega_g t}\right) \quad \text{(A2.10)}$$

Case II. When the excitation frequency is $\omega_L = \omega_p$ then equations after separating the real and imaginary parts are

$$\left[\left(-(i\omega_p)^2 m_2' - i\omega_p{}^2 I_{p_2}\left(t^{d_2}\right)^2 + k_g'\right)\left(R_{igp,\mathrm{re}}\right) - i\omega_p c_g'\left(R_{igp,\mathrm{im}}\right) + i\omega_p c_m\left(R_{ipp,\mathrm{im}}\right) - k_m\left(R_{ipp,\mathrm{re}}\right)\right]\left(e^{\mathrm{j}i\omega_p t}\right)$$
$$= \left(k_m\right)e^{\mathrm{j}\omega_p t}(e_p\cos\phi_p) - \left(c_m\omega_p\right)e^{\mathrm{j}\omega_p t}(e_p\sin\phi_p) + k_s R_{igp,\mathrm{re}}e^{\mathrm{j}i\omega_p t} - k_I\sum_{i=-n}^{n} I_{igp,\mathrm{re}}e^{\mathrm{j}i\omega_p t}$$

(A2.11)

$$\left[\left(-(i\omega_p)^2 m_2' - i\omega_p{}^2 I_{p_2}\left(t^{d_2}\right)^2 + k_g'\right)\left(R_{igp,\mathrm{im}}\right) + i\omega_p c_g'\left(R_{igp,\mathrm{re}}\right) - i\omega_p c_m\left(R_{ipp,\mathrm{re}}\right) - k_m\left(R_{ipp,\mathrm{im}}\right)\right]\left(e^{\mathrm{j}i\omega_p t}\right)$$
$$= \left(k_m\right)e^{\mathrm{j}\omega_p t}(e_p\sin\phi_p) + \left(c_m\omega_p\right)e^{\mathrm{j}\omega_p t}(e_p\cos\phi_p) + k_s R_{igp,\mathrm{im}}e^{\mathrm{j}i\omega_p t} - k_I I_{igp,\mathrm{im}}e^{\mathrm{j}i\omega_p t}$$

(A2.12)

Case III. When excitation frequency is $\omega_L = \omega_g$ then equations after separating the real and imaginary parts are

$$\left[\left(-(i\omega_g)^2 m_2' - i\omega_g{}^2 I_{p_2}\left(t^{d_2}\right)^2 + k_g'\right)\left(R_{igg,\mathrm{re}}\right) - i\omega_g c_g'\left(R_{igg,\mathrm{im}}\right) + i\omega_g c_m\left(R_{ipg,\mathrm{im}}\right) - k_m\left(R_{ipg,\mathrm{re}}\right)\right]\left(e^{\mathrm{j}i\omega_g t}\right)$$
$$= \left(m_2\omega_g^2 + k_{gx\varphi_y}t_{d_2} - k_g - k_m\right)e^{-\mathrm{j}\omega_g t}(e_g\cos\phi_g) - c_g'\omega_g e^{-\mathrm{j}\omega_g t}(e_g\sin\phi_g) + k_s R_{igg,\mathrm{re}}e^{\mathrm{j}i\omega_g t} - k_I I_{igg,\mathrm{re}}e^{\mathrm{j}i\omega_g t}$$

(A2.13)

$$\left[\left(-(i\omega_g)^2 m_2' - i\omega_g{}^2 I_{p_2}\left(t^{d_2}\right)^2 + k_g'\right)\left(R_{igg,\mathrm{im}}\right) + i\omega_g c_g'\left(R_{igg,\mathrm{re}}\right) - i\omega_g c_m\left(R_{ipg,\mathrm{re}}\right) - k_m\left(R_{ipg,\mathrm{im}}\right)\right]\left(e^{\mathrm{j}i\omega_g t}\right)$$
$$= \left(m_2\omega_g^2 + k_{gx\varphi_y}t_{d_2} - k_g - k_m\right)e^{-\mathrm{j}\omega_g t}(e_g\sin\phi_g) + c_g'\omega_g e^{-\mathrm{j}\omega_g t}(e_g\cos\phi_g) + k_s R_{igg,\mathrm{im}}e^{\mathrm{j}i\omega_g t} - k_I I_{igg,\mathrm{im}}e^{\mathrm{j}i\omega_g t}$$

(A2.14)

Case IV. When the excitation frequency is $\omega_L = \omega_e$ then equations after separating the real and imaginary parts are

$$\left[\left(-(i\omega_e)^2 m_2' - i\omega_e{}^2 I_{p_2}\left(t^{d_2}\right)^2 + k_g'\right)\left(R_{ige,\mathrm{re}}\right) - i\omega_e c_g'\left(R_{ige,\mathrm{im}}\right) + i\omega_e c_m\left(R_{ipe,\mathrm{im}}\right) - k_m\left(R_{ipe,\mathrm{re}}\right)\right]\left(e^{\mathrm{j}i\omega_e t}\right)$$
$$= -k_m\left[e_m e^{\mathrm{j}\phi_m} + \sum_{i=-n}^{n}\left(e_{fi} e^{\mathrm{j}i(\omega_e t+\phi_{fi})}\right)\right] + k_s R_{ige,\mathrm{re}} e^{\mathrm{j}i\omega_e t} - k_I I_{ige,\mathrm{re}} e^{\mathrm{j}i\omega_e t}$$

(A2.15)

$$\left[\left(-(i\omega_e)^2 m_2' - i\omega_e{}^2 I_{p_2}\left(t^{d_2}\right)^2 + k_g'\right)\left(R_{ige,\mathrm{im}}\right) + i\omega_e c_g'\left(R_{ige,\mathrm{re}}\right) - i\omega_e c_m\left(R_{ipe,\mathrm{re}}\right) - k_m\left(R_{ipe,\mathrm{im}}\right)\right]\left(e^{\mathrm{j}i\omega_e t}\right)$$
$$= -c_m\left\{i\omega_e \sum_{i=-n}^{n}\left(e_{fi} e^{\mathrm{j}i(\omega_e t+\phi_{fi})}\right)\right\} + k_s R_{ige,\mathrm{im}} e^{\mathrm{j}i\omega_e t} - k_I I_{ige,\mathrm{im}} e^{\mathrm{j}i\omega_e t}$$

(A2.16)

Appendix A3: Conversion of complex regression equations into real regression equations for 12 DOF geared rotor-AMB system

The real regression form by separating real and imaginary quantities, from complex regression equations (4.31) to (4.33) for i^{th} harmonic is:

$$m_1' = m_1 + \left(t^{d_1}\right)^2 I_{d_1};\ m_2' = m_2 + \left(t^{d_2}\right)^2 I_{d_2};$$

$$c_p' = c_p + c_m;\ c_g' = c_g + c_m;$$

$$k_p' = k_p - 2\left(t^{d_1}\right)k_{px\varphi_y} + \left(t^{d_1}\right)^2 k_{p\varphi_x\varphi_x};\ k_g' = k_g - 2\left(t^{d_2}\right)k_{gx\varphi_y} + \left(t^{d_2}\right)^2 k_{g\varphi_x\varphi_x}$$

(a) For the input shaft:

Case I. For $i = 0$, regression equations after separating the real and imaginary parts are

$$\begin{aligned}&\left(k_p' + k_m\right)\left(R_{0p,Re}e^{0\mathrm{j}\omega_p t}\right) - k_m\left(R_{0g,Re}e^{0\mathrm{j}\omega_p t}\right) + \left\{k_m\left(r_p\theta_{0p,Re} - r_g\theta_{0g,Re}\right)\right\}\left(e^{0\mathrm{j}\omega_p t}\right)\cos\psi \\ &= k_m e_m\cos\phi_m + k_s\left(R_{0p,Re}e^{0\mathrm{j}\omega_p t}\right) - k_I\left(I_{0p,Re}e^{0\mathrm{j}\omega_p t}\right)\end{aligned} \tag{A3.1}$$

$$\begin{aligned}&\left(k_p' + k_m\right)\left(R_{0p,Im}e^{0\mathrm{j}\omega_p t}\right) - k_m\left(R_{0g,Im}e^{0\mathrm{j}\omega_p t}\right) + \left\{k_m\left(r_p\theta_{0p,Im} - r_g\theta_{0g,Im}\right)\right\}\left(e^{0\mathrm{j}\omega_p t}\right)\sin\psi \\ &= k_m e_m\sin\phi_m + k_s\left(R_{0p,Im}e^{0\mathrm{j}\omega_p t}\right) - k_I\left(I_{0p,Im}e^{0\mathrm{j}\omega_p t}\right)\end{aligned} \tag{A3.2}$$

Case II. when excitation frequency is $\omega_H = \omega_p$ then equations after separating the real and imaginary parts are

$$\begin{aligned}&\left[\left\{-\left(i\omega_p\right)^2 m_1' - i\omega_p{}^2 I_{p_1}\left(t^{d_1}\right)^2 + k_p' + k_m\right\}\left(R_{ipp,Re}\right) - i\omega_p\left(c_p + c_m\right)\left(R_{ipp,Im}\right) + \left(i\omega_p c_m\right)\left(R_{igp,Im}\right) - k_m\left(R_{igp,Re}\right)\right]\left(e^{\mathrm{j}i\omega_p t}\right) \\ &+\left[k_m\left\{r_p\cos\psi\left(\theta_{ipp,Re}\right) - r_g\left(\theta_{igp,Re}\right)\right\} - i\omega_p c_m\left\{r_p\sin\psi\left(\theta_{ipp,Im}\right) - r_g\left(\theta_{igp,Im}\right)\right\}\right]\left(e^{\mathrm{j}i\omega_p t}\right) \\ &= \left(m_1\omega_p^2 + k_{px\varphi_y}t_{d_1} - k_p - k_m\right)e^{\mathrm{j}\omega_p t}\left(e_p\cos\phi_p\right) + \left(c_p + c_m\right)\omega_p e^{\mathrm{j}\omega_p t}\left(e_p\sin\phi_p\right) + k_s R_{ipp,Re}e^{\mathrm{j}\omega_p t} - k_I I_{ipp,Re}e^{\mathrm{j}\omega_p t}\end{aligned} \tag{A3.3}$$

$$\left[\left\{-\left(i\omega_p\right)^2 m_1' - i\omega_p{}^2 I_{p_1}\left(t^{d_1}\right)^2 + k_p' + k_m\right\}\left(R_{ipp,Im}\right) + i\omega_p\left(c_p + c_m\right)\left(R_{ipp,Re}\right) - \left(i\omega_p c_m\right)\left(R_{igp,Re}\right) - k_m\left(R_{igp,Im}\right)\right]\left(e^{\mathrm{j}i\omega_p t}\right)$$
$$+\left[-k_m\left\{r_p \sin\psi\left(\theta_{ipp,Im}\right) - r_g\left(\theta_{igp,Im}\right)\right\} + i\omega_p c_m\left\{r_p \cos\psi\left(\theta_{ipp,Re}\right) - r_g\left(\theta_{igp,Re}\right)\right\}\right]\left(e^{\mathrm{j}i\omega_p t}\right)$$
$$= \left(m_1\omega_p^2 + k_{px\varphi_y} t_{d_1} - k_p - k_m\right)e^{\mathrm{j}\omega_p t}\left(e_p \sin\phi_p\right) - \left(c_p + c_m\right)\omega_p e^{\mathrm{j}\omega_p t}\left(e_p \cos\phi_p\right) + k_s R_{ipp,Im} e^{\mathrm{j}\omega_p t} - k_I I_{ipp,Im} e^{\mathrm{j}\omega_p t}$$

(A3.4)

Case III. When excitation frequency is $\omega_H = \omega_g$ then equations after separating the real and imaginary parts are

$$\left[\left(-(i\omega_g)^2 m_1' - i\omega_g{}^2 I_{p_1}\left(t^{d_1}\right)^2 + k_p' + k_m\right)\left(R_{ipg,Re}\right) - i\omega_g\left(c_p + c_m\right)\left(R_{ipg,Im}\right) + i\omega_g c_m\left(R_{igg,Im}\right) - k_m\left(R_{igg,Re}\right)\right]\left(e^{\mathrm{j}i\omega_g t}\right)$$
$$+\left[k_m\left\{r_p \cos\psi\left(\theta_{ipg,Re}\right) - r_g\left(\theta_{igg,Re}\right)\right\} - i\omega_g c_m\left\{r_p \sin\psi\left(\theta_{ipg,Im}\right) - r_g\left(\theta_{igp,Im}\right)\right\}\right]\left(e^{\mathrm{j}i\omega_g t}\right)$$
$$= \left(k_m\right)e^{-\mathrm{j}\omega_g t}\left(e_g \cos\phi_g\right) + \left(c_m\omega_g\right)e^{-\mathrm{j}\omega_g t}\left(e_g \sin\phi_g\right) + k_s R_{ipg,Re} e^{-\mathrm{j}\omega_g t} - k_I I_{ipg,Re} e^{-\mathrm{j}\omega_g t}$$

(A3.5)

$$\left[\left(-(i\omega_g)^2 m_1' - i\omega_g{}^2 I_{p_1}\left(t^{d_1}\right)^2 + k_p' + k_m\right)\left(R_{ipg,Im}\right) + i\omega_g\left(c_p + c_m\right)\left(R_{ipg,Re}\right) - i\omega_g c_m\left(R_{igg,Re}\right) - k_m\left(R_{igg,Im}\right)\right]\left(e^{\mathrm{j}i\omega_g t}\right)$$
$$+\left[-k_m\left\{r_p \sin\psi\left(\theta_{ipg,Im}\right) - r_g\left(\theta_{igg,Im}\right)\right\} + i\omega_g c_m\left\{r_p \cos\psi\left(\theta_{ipg,Re}\right) - r_g\left(\theta_{igg,Re}\right)\right\}\right]\left(e^{\mathrm{j}i\omega_g t}\right)$$
$$= \left(k_m\right)e^{-\mathrm{j}\omega_g t}(e_g \sin\phi_g) - \left(c_m\omega_g\right)e^{-\mathrm{j}\omega_g t}(e_g \cos\phi_g) + k_s R_{ipg,Im} e^{-\mathrm{j}\omega_g t} - k_I I_{ipg,Im} e^{-\mathrm{j}\omega_g t}$$

(A3.6)

Case IV. When excitation frequency is $\omega_H = \omega_e$ then equations after separating the real and imaginary parts are

$$\left[\left(-(i\omega_e)^2 m_1' - i\omega_e{}^2 I_{p_1}\left(t^{d_1}\right)^2 + k_p' + k_m\right)\left(R_{ipe,Re}\right) - i\omega_e\left(c_p + c_m\right)\left(R_{ipe,Im}\right) + i\omega_e c_m\left(R_{ige,Im}\right) - k_m\left(R_{ige,Re}\right)\right]\left(e^{\mathrm{j}i\omega_e t}\right)$$
$$+\left[k_m\left\{r_p \cos\psi\left(\theta_{ipe,Re}\right) - r_g\left(\theta_{ige,Re}\right)\right\} - i\omega_e c_m\left\{r_p \sin\psi\left(\theta_{ipe,Im}\right) - r_g\left(\theta_{ige,Im}\right)\right\}\right] = k_m\left\{\sum_{i=-n}^{n}\left(e_{fi}\cos\phi_{fi}\right)e^{\mathrm{j}i\omega_e t}\right\}$$
$$+k_s R_{ipe,Re} e^{\mathrm{j}i\omega_e t} - k_I I_{ipe,Re} e^{\mathrm{j}i\omega_e t}$$

(A3.7)

$$\left[\left(-(i\omega_e)^2 m_1' - i\omega_e{}^2 I_{p_1}\left(t^{d_1}\right)^2 + k_p' + k_m\right)\left(R_{ipe,Im}\right) + i\omega_e\left(c_p + c_m\right)\left(R_{ipe,Re}\right) - i\omega_e c_m\left(R_{ige,Re}\right) - k_m\left(R_{ige,Im}\right)\right]\left(e^{\mathrm{j}i\omega_e t}\right)$$
$$+\left[k_m \sin\psi\left\{r_p\left(\theta_{ipe,Im}\right) - r_g\left(\theta_{ige,Im}\right)\right\} + i\omega_e c_m \cos\psi\left\{r_p\left(\theta_{ipe,Re}\right) - r_g\left(\theta_{ige,Re}\right)\right\}\right]\left(e^{\mathrm{j}i\omega_e t}\right)$$
$$= c_m\left\{i\omega_e \sum_{i=-n}^{n}\left(e_{fi}\sin\phi_{fi}\right)\right\}e^{\mathrm{j}i\omega_e t} + k_s R_{ipe,Im} e^{\mathrm{j}i\omega_e t} - k_I I_{ipe,Im} e^{\mathrm{j}i\omega_e t}$$

(A3.8)

(b) Similarly considering the output shaft:

Case I. For $i = 0$, regression equations after separating the real and imaginary parts are

$$\left(k_g' + k_m\right)\left(R_{0g,\mathrm{re}} e^{0\,\mathrm{j}\omega_g t}\right) - k_m\left(R_{0p,\mathrm{re}} e^{0\,\mathrm{j}\omega_g t}\right) - \left\{k_m\left(r_p\theta_{0p,Re} - r_g\theta_{0g,Re}\right)\right\}\left(e^{0\,\mathrm{j}\omega_g t}\right)\cos\psi$$
$$= -k_m e_m \cos\phi_m + k_s\left(R_{0g,\mathrm{re}} e^{0\,\mathrm{j}\omega_g t}\right) - k_I\left(I_{0g,\mathrm{re}} e^{0\,\mathrm{j}\omega_g t}\right) \qquad \text{(A3.9)}$$

$$\left(k_g' + k_m\right)\left(R_{0g,Im} e^{0\,\mathrm{j}\omega_g t}\right) - k_m\left(R_{0p,Im} e^{0\,\mathrm{j}\omega_g t}\right) + \left\{k_m\left(r_p\theta_{0p,Re} - r_g\theta_{0g,Re}\right)\right\}\left(e^{0\,\mathrm{j}\omega_g t}\right)\sin\psi$$
$$= k_m e_m \sin\phi_m + k_s\left(R_{0g,Im} e^{0\,\mathrm{j}\omega_g t}\right) - k_I\left(I_{0g,Im} e^{0\,\mathrm{j}\omega_g t}\right) \qquad \text{(A3.10)}$$

Case II. When the excitation frequency is $\omega_H = \omega_p$ then equations after separating the real and imaginary parts are

$$\left[\left(-(i\omega_p)^2 m_2' - i\omega_p{}^2 I_{p_2}\left(t^{d_2}\right)^2 + k_g'\right)\left(R_{igp,Re}\right) - i\omega_p c_g'\left(R_{igp,Im}\right) + i\omega_p c_m\left(R_{ipp,Im}\right) - k_m\left(R_{ipp,Re}\right)\right]\left(e^{\mathrm{j}i\omega_p t}\right)$$
$$-\left[k_m\cos\psi\left\{r_p\left(\theta_{ipp,Re}\right) - r_g\left(\theta_{igp,Re}\right)\right\} + i\omega_p c_m \sin\psi\left\{r_p\left(\theta_{ipp,Im}\right) - r_g\left(\theta_{igp,Im}\right)\right\}\right]\left(e^{\mathrm{j}i\omega_p t}\right)$$
$$= \left(k_m\right)e^{\mathrm{j}\omega_p t}\left(e_p\cos\phi_p\right) - \left(c_m\omega_p\right)e^{\mathrm{j}\omega_p t}\left(e_p\sin\phi_p\right) + k_s R_{igp,Re} e^{\mathrm{j}\omega_p t} - k_I I_{igp,Re} e^{\mathrm{j}\omega_p t}$$

(A3.11)

$$\left[\left(-(i\omega_p)^2 m_2' - i\omega_p{}^2 I_{p_2}\left(t^{d_2}\right)^2 + k_g'\right)\left(R_{igp,Im}\right) + i\omega_p c_g'\left(R_{igp,Re}\right) - i\omega_p c_m\left(R_{ipp,Re}\right) - k_m\left(R_{ipp,Im}\right)\right]\left(e^{\mathrm{j}i\omega_p t}\right)$$
$$-\left[k_m\sin\psi\left\{r_p\left(\theta_{ipp,Im}\right) - r_g\left(\theta_{igp,Im}\right)\right\} - i\omega_p c_m\cos\psi\left\{r_p\left(\theta_{ipp,Re}\right) - r_g\left(\theta_{igp,Re}\right)\right\}\right]\left(e^{\mathrm{j}i\omega_p t}\right)$$
$$= \left(k_m\right)e^{\mathrm{j}\omega_p t}\left(e_p\sin\phi_p\right) + \left(c_m\omega_p\right)e^{\mathrm{j}\omega_p t}\left(e_p\cos\phi_p\right) + k_s R_{igp,Im} e^{\mathrm{j}\omega_p t} - k_I I_{igp,Im} e^{\mathrm{j}\omega_p t}$$

(A3.12)

Case III. When excitation frequency is $\omega_H = \omega_g$ then equations after separating the real and imaginary parts are

$$\left[\left(-(i\omega_g)^2 m_2' - i\omega_g{}^2 I_{p_2}\left(t^{d_2}\right)^2 + k_g'\right)\left(R_{igg,Re}\right) - i\omega_g c_g'\left(R_{igg,Im}\right) + i\omega_g c_m\left(R_{ipg,Im}\right) - k_m\left(R_{ipg,Re}\right)\right]\left(e^{\mathrm{j}i\omega_g t}\right)$$
$$-\left[k_m\cos\psi\left\{r_p\left(\theta_{ipg,Re}\right) - r_g\left(\theta_{igg,Re}\right)\right\} + i\omega_g c_m\sin\psi\left\{r_p\left(\theta_{ipg,Im}\right) - r_g\left(\theta_{igp,Im}\right)\right\}\right]\left(e^{\mathrm{j}i\omega_g t}\right)$$
$$= \left(m_2\omega_g^2 + k_{gx\varphi_y} t_{d_2} - k_g - k_m\right)e^{-\mathrm{j}\omega_g t}\left(e_g\cos\phi_g\right) - \left(c_g + c_m\right)\omega_g e^{-\mathrm{j}\omega_g t}\left(e_g\sin\phi_g\right) + k_s R_{igg,Re}e^{-\mathrm{j}\omega_g t} - k_I I_{igg,Re}e^{-\mathrm{j}\omega_g t}$$

(A3.13)

$$\left[\left(-(i\omega_g)^2 m_2' - i\omega_g{}^2 I_{p_2}\left(t^{d_2}\right)^2 + k_g'\right)\left(R_{igg,Im}\right) + i\omega_g c_g'\left(R_{igg,Re}\right) - i\omega_g c_m\left(R_{ipg,Re}\right) - k_m\left(R_{ipg,Im}\right)\right]\left(e^{\mathrm{j}i\omega_g t}\right)$$
$$-\left[k_m\sin\psi\left\{r_p\left(\theta_{ipg,Im}\right) - r_g\left(\theta_{igg,Im}\right)\right\} - i\omega_g c_m\cos\psi\left\{r_p\left(\theta_{ipg,Re}\right) - r_g\left(\theta_{igg,Re}\right)\right\}\right]\left(e^{\mathrm{j}i\omega_g t}\right)$$
$$= \left(m_2\omega_g^2 + k_{gx\varphi_y} t_{d_2} - k_g - k_m\right)e^{-\mathrm{j}\omega_g t}\left(e_g\sin\phi_g\right) + \left(c_g + c_m\right)\omega_g e^{-\mathrm{j}\omega_g t}\left(e_g\cos\phi_g\right) + k_s R_{igg,Im}e^{-\mathrm{j}\omega_g t} - k_I I_{igg,Im}e^{-\mathrm{j}\omega_g t}$$

(A3.14)

Case IV. When the excitation frequency is $\omega_H = \omega_e$ then equations after separating the real and imaginary parts are

$$\left[\left(-(i\omega_e)^2 m_2' - i\omega_e{}^2 I_{p_2}\left(t^{d_2}\right)^2 + k_g'\right)\left(R_{ige,Re}\right) - i\omega_e c_g'\left(R_{ige,Im}\right) + i\omega_e c_m\left(R_{ipe,Im}\right) - k_m\left(R_{ipe,Re}\right)\right]\left(e^{\mathrm{j}i\omega_e t}\right)$$
$$-\left[k_m\cos\psi\left\{r_p\left(\theta_{ipe,Re}\right) - r_g\left(\theta_{ige,Re}\right)\right\} + i\omega_e c_m\sin\psi\left\{r_p\left(\theta_{ipe,Im}\right) - r_g\left(\theta_{ige,Im}\right)\right\}\right]\left(e^{\mathrm{j}i\omega_e t}\right)$$
$$= -k_m\left\{\sum_{i=-n}^{n}\left(e_{fi}\cos\phi_{fi}\right)\right\} + k_s R_{ige,Re}e^{\mathrm{j}i\omega_e t} - k_I I_{ige,Re}e^{\mathrm{j}i\omega_e t}$$

(A3.15)

$$\left[\left(-(i\omega_e)^2 m_2' - i\omega_e{}^2 I_{p_2}\left(t^{d_2}\right)^2 + k_g'\right)\left(R_{ige,Im}\right) + i\omega_e\left(c_g + c_m\right)\left(R_{ige,Re}\right) - i\omega_e c_m\left(R_{ipe,Re}\right) - k_m\left(R_{ipe,Im}\right)\right]\left(e^{\mathrm{j}i\omega_e t}\right)$$
$$-\left[k_m\sin\psi\left\{r_p\left(\theta_{ipe,Im}\right) - r_g\left(\theta_{ige,Im}\right)\right\} - i\omega_e c_m\cos\psi\left\{r_p\left(\theta_{ipe,Re}\right) - r_g\left(\theta_{ige,Re}\right)\right\}\right]\left(e^{\mathrm{j}i\omega_e t}\right)$$
$$= -c_m\left\{i\omega_e\sum_{i=-n}^{n}\left(e_{fi}\sin\phi_{fi}\right)\right\} + k_s R_{ige,Im}e^{\mathrm{j}i\omega_e t} - k_I I_{ige,Im}e^{\mathrm{j}i\omega_e t}$$

(A3.16)

Appendix B Matrices of Identification Algorithm

Appendix B1: Identification Algorithm for 4 DOF geared rotor-AMB system

Considering the equations given in Appendix (A1.1) to (A1.16), column matrix with known quantities $\{\mathbf{b}\}_{52\times1}$ and vector of identifiable parameters $\{\mathbf{x}\}_{38\times1}$ used in the estimation of various system fault parameters are as follows

$$\{\mathbf{x}\}_{38\times1}=\begin{Bmatrix} k_m \\ c_m \\ k_m e_{\mathrm{pRe}} \\ k_m e_{\mathrm{pIm}} \\ k_m e_{g\,\mathrm{Re}} \\ k_m e_{g\,\mathrm{Im}} \\ c_m e_{\mathrm{pRe}} \\ c_m e_{\mathrm{pIm}} \\ c_m e_{g\,\mathrm{Re}} \\ c_m e_{g\,\mathrm{Im}} \\ e_{\mathrm{pRe}} \\ e_{\mathrm{pIm}} \\ e_{g\,\mathrm{Re}} \\ e_{g\,\mathrm{Im}} \\ k_s \\ k_I \\ k_m e_{mx} \\ k_m e_{my} \\ k_m e_{fx1} \\ \vdots \\ k_m e_{fx5} \\ k_m e_{fy1} \\ \vdots \\ k_m e_{fy5} \\ c_m e_{fx1} \\ \vdots \\ c_m e_{fx5} \\ c_m e_{fy1} \\ \vdots \\ c_m e_{fy5} \end{Bmatrix};\qquad \{\mathbf{b}\}_{52\times1}=\begin{Bmatrix} m_1\omega_p^2 R_{1pp,Re}-k_p R_{1pp,Re}+\omega_p c_p R_{1pp,Im} \\ m_2\omega_p^2 R_{1gp,Re}-k_g R_{1gp,Re}+\omega_p c_g R_{1gp,Im} \\ i^2 m_1\omega_e^2 R_{ipe,Re}-k_p R_{ipe,Re}+i\omega_e c_p R_{ipe,Im} \\ i^2 m_2\omega_e^2 R_{ige,Re}-k_g R_{ige,Re}+i\omega_e c_g R_{ige,Im} \\ -k_p R_{0p,Re} \\ -k_g R_{0g,Re} \\ m_1\omega_g^2 R_{-1pg,Re}-k_p R_{-1pg,Re}-\omega_g c_p R_{-1pg,Im} \\ m_2\omega_g^2 R_{-1gg,Re}-k_g R_{-1gg,Re}-\omega_g c_g R_{-1gg,Im} \\ i^2 m_1\omega_e^2 R_{-ipe,Re}-k_p R_{-ipe,Re}-i\omega_e c_p R_{-ipe,Im} \\ i^2 m_2\omega_e^2 R_{-ige,Re}-k_g R_{-ige,Re}-i\omega_e c_g R_{-ige,Im} \\ m_1\omega_p^2 R_{1pp,Im}-k_p R_{1pp,Im}-\omega_p c_p R_{1pp,Re} \\ m_2\omega_p^2 R_{1gp,Im}-k_g R_{1gp,Im}-\omega_p c_g R_{1gp,Re} \\ i^2 m_1\omega_e^2 R_{ipe,Im}-k_p R_{ipe,Im}-i\omega_e c_p R_{ipe,Re} \\ i^2 m_2\omega_e^2 R_{ige,Im}-k_g R_{ige,Im}-i\omega_e c_g R_{ige,Re} \\ -k_p R_{0p,Im} \\ -k_g R_{0g,Im} \\ m_1\omega_g^2 R_{-1pg,Im}-k_p R_{-1pg,Im}+\omega_g c_p R_{-1pg,Re} \\ m_2\omega_g^2 R_{-1gg,Im}-k_g R_{-1gg,Im}+\omega_g c_g R_{-1gg,Re} \\ i^2 m_1\omega_e^2 R_{-ipe,Im}-k_p R_{-ipe,Im}+i\omega_e c_p R_{-ipe,Re} \\ i^2 m_2\omega_e^2 R_{-ige,Im}-k_g R_{-ige,Im}+i\omega_e c_g R_{-ige,Re} \end{Bmatrix} \tag{B1.1}$$

Writing the regressor $\{\mathbf{A}\}_{52\times 38}$, the columns 1 through 12 and the regressor $\{\mathbf{A}\}_{52\times 38}$, the columns 12 through 38, while, $\{\mathbf{A}\}_{52\times 38} = \left[\{\mathbf{A1}\}_{52\times 12} \;\; \{\mathbf{A2}\}_{52\times 26}\right]_{52\times 38}$ are given as

$$\{\mathbf{A1}\}_{52\times 12} = \begin{bmatrix}
R_{1pp,\mathrm{Re}} - R_{1gp,\mathrm{Re}} & \omega_p\left(R_{1gp,Im} - R_{1pp,Im}\right) & 1 & 0 & 0 & 0 & 0 & -\omega_p & 0 & 0 & k_p - m_1\omega_p^2 & -c_p\omega_p \\
R_{1gp,\mathrm{Re}} - R_{1pp,\mathrm{Re}} & \omega_p\left(R_{1pp,Im} - R_{1gp,Im}\right) & -1 & 0 & 0 & 0 & 0 & \omega_p & 0 & 0 & 0 & 0 \\
R_{npe,\mathrm{Re}} - R_{nge,\mathrm{Re}} & i\omega_e\left(R_{nge,Im} - R_{npe,Im}\right) & 0 & 0 & 0 & 0 & 0 & 0 & 0 & 0 & 0 & 0 \\
\vdots & \vdots & \vdots & \vdots & \vdots & \vdots & \vdots & \vdots & \vdots & \vdots & \vdots & \vdots \\
R_{nge,\mathrm{Re}} - R_{npe,\mathrm{Re}} & i\omega_e\left(R_{npe,Im} - R_{nge,Im}\right) & 0 & 0 & 0 & 0 & 0 & 0 & 0 & 0 & 0 & 0 \\
\vdots & \vdots & \vdots & \vdots & \vdots & \vdots & \vdots & \vdots & \vdots & \vdots & \vdots & \vdots \\
R_{0p,\mathrm{Re}} - R_{0g,\mathrm{Re}} & 0 & 0 & 0 & 0 & 0 & 0 & 0 & 0 & 0 & 0 & 0 \\
R_{0g,\mathrm{Re}} - R_{0p,\mathrm{Re}} & 0 & 0 & 0 & 0 & 0 & 0 & 0 & 0 & 0 & 0 & 0 \\
R_{-1pg,\mathrm{Re}} - R_{-1gg,\mathrm{Re}} & \omega_g\left(R_{-1pg,Im} - R_{-1gg,Im}\right) & 0 & 0 & -1 & 0 & 0 & 0 & 0 & -\omega_g & 0 & 0 \\
R_{-1gg,\mathrm{Re}} - R_{-1pg,\mathrm{Re}} & \omega_g\left(R_{-1gg,Im} - R_{-1pg,Im}\right) & 0 & 0 & 1 & 0 & 0 & 0 & 0 & \omega_g & 0 & 0 \\
R_{-npe,\mathrm{Re}} - R_{-nge,\mathrm{Re}} & i\omega_e\left(R_{-npe,Im} - R_{-nge,Im}\right) & 0 & 0 & 0 & 0 & 0 & 0 & 0 & 0 & 0 & 0 \\
\vdots & \vdots & \vdots & \vdots & \vdots & \vdots & \vdots & \vdots & \vdots & \vdots & \vdots & \vdots \\
R_{-nge,\mathrm{Re}} - R_{-npe,\mathrm{Re}} & i\omega_e\left(R_{-nge,Im} - R_{-npe,Im}\right) & 0 & 0 & 0 & 0 & 0 & 0 & 0 & 0 & 0 & 0 \\
\vdots & \vdots & \vdots & \vdots & \vdots & \vdots & \vdots & \vdots & \vdots & \vdots & \vdots & \vdots \\
R_{1pp,Im} - R_{1gp,Im} & \omega_p\left(R_{1pp,\mathrm{Re}} - R_{1gp,\mathrm{Re}}\right) & 0 & 1 & 0 & 0 & \omega_p & 0 & 0 & 0 & c_p\omega_p & k_p - m_1\omega_p^2 \\
R_{1gp,Im} - R_{1pp,Im} & \omega_p\left(R_{1gp,\mathrm{Re}} - R_{1pp,\mathrm{Re}}\right) & 0 & -1 & 0 & 0 & -\omega_p & 0 & 0 & 0 & 0 & 0 \\
R_{npe,Im} - R_{nge,Im} & i\omega_e\left(R_{npe,\mathrm{Re}} - R_{nge,\mathrm{Re}}\right) & 0 & 0 & 0 & 0 & 0 & 0 & 0 & 0 & 0 & 0 \\
\vdots & \vdots & \vdots & \vdots & \vdots & \vdots & \vdots & \vdots & \vdots & \vdots & \vdots & \vdots \\
R_{nge,Im} - R_{npe,Im} & i\omega_e\left(R_{nge,\mathrm{Re}} - R_{npe,\mathrm{Re}}\right) & 0 & 0 & 0 & 0 & 0 & 0 & 0 & 0 & 0 & 0 \\
\vdots & \vdots & \vdots & \vdots & \vdots & \vdots & \vdots & \vdots & \vdots & \vdots & \vdots & \vdots \\
R_{0p,Im} - R_{0g,Im} & 0 & 0 & 0 & 0 & 0 & 0 & 0 & 0 & 0 & 0 & 0 \\
R_{0g,Im} - R_{0p,Im} & 0 & 0 & 0 & 0 & 0 & 0 & 0 & 0 & 0 & 0 & 0 \\
R_{-1pg,Im} - R_{-1gg,Im} & \omega_g\left(R_{-1gg,\mathrm{Re}} - R_{-1pg,\mathrm{Re}}\right) & 0 & 0 & 0 & -1 & 0 & 0 & \omega_g & 0 & 0 & 0 \\
R_{-1gg,Im} - R_{-1pg,Im} & \omega_g\left(R_{-1pg,\mathrm{Re}} - R_{-1gg,\mathrm{Re}}\right) & 0 & 0 & 0 & 1 & 0 & 0 & -\omega_g & 0 & 0 & 0 \\
R_{-npe,Im} - R_{-nge,Im} & i\omega_e\left(R_{-nge,\mathrm{Re}} - R_{-npe,\mathrm{Re}}\right) & 0 & 0 & 0 & 0 & 0 & 0 & 0 & 0 & 0 & 0 \\
\vdots & \vdots & \vdots & \vdots & \vdots & \vdots & \vdots & \vdots & \vdots & \vdots & \vdots & \vdots \\
R_{-nge,Im} - R_{-npe,Im} & i\omega_e\left(R_{-npe,\mathrm{Re}} - R_{-nge,\mathrm{Re}}\right) & 0 & 0 & 0 & 0 & 0 & 0 & 0 & 0 & 0 & 0 \\
\vdots & \vdots & \vdots & \vdots & \vdots & \vdots & \vdots & \vdots & \vdots & \vdots & \vdots & \vdots
\end{bmatrix} \tag{B1.2}$$

$$\{\mathbf{A2}\}_{52\times 26}=\begin{bmatrix}
0 & 0 & -R_{1pp,Re} & I_{1pp,Re} & 0 & 0 & 0 & \cdots & 0 & \cdots & 0 & \cdots & 0 & \cdots \\
0 & 0 & -R_{1gp,Re} & I_{1gp,Re} & 0 & 0 & 0 & \cdots & 0 & \cdots & 0 & \cdots & 0 & \cdots \\
0 & 0 & -R_{npe,Re} & I_{npe,Re} & 0 & 0 & -1 & \cdots & 0 & \cdots & 0 & \cdots & n\omega_e & \cdots \\
\vdots & \vdots & \vdots & \vdots & \vdots & \vdots & \vdots & \ddots & \vdots & \ddots & \vdots & \ddots & \vdots & \ddots \\
0 & 0 & -R_{nge,Re} & I_{nge,Re} & 0 & 0 & 1 & \cdots & 0 & \cdots & 0 & \cdots & -n\omega_e & \cdots \\
\vdots & \vdots & \vdots & \vdots & \vdots & \vdots & \vdots & \ddots & \vdots & \ddots & \vdots & \ddots & \vdots & \ddots \\
0 & 0 & -R_{0p,Re} & I_{0p,Re} & -1 & 0 & 0 & \cdots & 0 & \cdots & 0 & \cdots & 0 & \cdots \\
0 & 0 & -R_{0g,Re} & I_{0g,Re} & 1 & 0 & 0 & \cdots & 0 & \cdots & 0 & \cdots & 0 & \cdots \\
0 & 0 & -R_{-1pg,Re} & I_{-1pg,Re} & 0 & 0 & 0 & \cdots & 0 & \cdots & 0 & \cdots & 0 & \cdots \\
k_g-m_2\omega_g^2 & c_g\omega_g & -R_{-1gg,Re} & I_{-1gg,Re} & 0 & 0 & 0 & \cdots & 0 & \cdots & 0 & \cdots & 0 & \cdots \\
0 & 0 & -R_{-npe,Re} & I_{-npe,Re} & 0 & 0 & -1 & \cdots & 0 & \cdots & 0 & \cdots & -n\omega_e & \cdots \\
\vdots & \vdots & \vdots & \vdots & \vdots & \vdots & \vdots & \ddots & \vdots & \ddots & \vdots & \ddots & \vdots & \ddots \\
0 & 0 & -R_{-nge,Re} & I_{-nge,Re} & 0 & 0 & 1 & \cdots & 0 & \cdots & 0 & \cdots & n\omega_e & \cdots \\
\vdots & \vdots & \vdots & \vdots & \vdots & \vdots & \vdots & \ddots & \vdots & \ddots & \vdots & \ddots & \vdots & \ddots \\
0 & 0 & -R_{1pp,Im} & I_{1pp,Im} & 0 & 0 & 0 & \cdots & 0 & \cdots & 0 & \cdots & 0 & \cdots \\
0 & 0 & -R_{1gp,Im} & I_{1gp,Im} & 0 & 0 & 0 & \cdots & 0 & \cdots & 0 & \cdots & 0 & \cdots \\
0 & 0 & -R_{npe,Im} & I_{npe,Im} & 0 & 0 & 0 & \cdots & -1 & \cdots & -n\omega_e & \cdots & 0 & \cdots \\
\vdots & \vdots & \vdots & \vdots & \vdots & \vdots & \vdots & \ddots & \vdots & \ddots & \vdots & \ddots & \vdots & \ddots \\
0 & 0 & -R_{nge,Im} & I_{nge,Im} & 0 & 0 & 0 & \cdots & 1 & \cdots & n\omega_e & \cdots & 0 & \cdots \\
\vdots & \vdots & \vdots & \vdots & \vdots & \vdots & \vdots & \ddots & \vdots & \ddots & \vdots & \ddots & \vdots & \ddots \\
0 & 0 & -R_{0p,Im} & I_{0p,Im} & 0 & -1 & 0 & \cdots & 0 & \cdots & 0 & \cdots & 0 & \cdots \\
0 & 0 & -R_{0g,Im} & I_{0g,Im} & 0 & 1 & 0 & \cdots & 0 & \cdots & 0 & \cdots & 0 & \cdots \\
0 & 0 & -R_{-1pg,Im} & I_{-1pg,Im} & 0 & 0 & 0 & \cdots & 0 & \cdots & 0 & \cdots & 0 & \cdots \\
-c_g\omega_g & k_g-m_2\omega_g^2 & -R_{-1gg,Im} & I_{-1gg,Im} & 0 & 0 & 0 & \cdots & 0 & \cdots & 0 & \cdots & 0 & \cdots \\
0 & 0 & -R_{-npe,Im} & I_{-npe,Im} & 0 & 0 & 0 & \cdots & -1 & \cdots & n\omega_e & \cdots & 0 & \cdots \\
\vdots & \vdots & \vdots & \vdots & \vdots & \vdots & \vdots & \ddots & \vdots & \ddots & \vdots & \ddots & \vdots & \ddots \\
0 & 0 & -R_{-nge,Im} & I_{-nge,Im} & 0 & 0 & 0 & \cdots & 1 & \cdots & -n\omega_e & \cdots & 0 & \cdots \\
\vdots & \vdots & \vdots & \vdots & \vdots & \vdots & \vdots & \ddots & \vdots & \ddots & \vdots & \ddots & \vdots & \ddots
\end{bmatrix} \tag{B1.3}$$

Appendix B2: Identification Algorithm for 8 DOF geared rotor-AMB system

Considering the equations given in Appendix (A2.1) to (A2.16), the regression matrix $\{\mathbf{A}\}_{52\times38}$, column matrix with known quantities $\{\mathbf{b}\}_{52\times1}$ and vector of identifiable parameters $\{\mathbf{x}\}_{38\times1}$ used in the estimation of various system fault parameters are as follows

$$\{\mathbf{x}\}_{38\times1}=\begin{Bmatrix} k_m \\ c_m \\ k_m e_{\mathrm{pRe}} \\ k_m e_{\mathrm{pIm}} \\ k_m e_{g\,\mathrm{Re}} \\ k_m e_{g\,\mathrm{Im}} \\ c_m e_{\mathrm{pRe}} \\ c_m e_{\mathrm{pIm}} \\ c_m e_{g\,\mathrm{Re}} \\ c_m e_{g\,\mathrm{Im}} \\ e_{\mathrm{pRe}} \\ e_{\mathrm{pIm}} \\ e_{g\,\mathrm{Re}} \\ e_{g\,\mathrm{Im}} \\ k_s \\ k_I \\ k_m e_{mx} \\ k_m e_{my} \\ k_m e_{fx1} \\ \vdots \\ k_m e_{fx5} \\ k_m e_{fy1} \\ \vdots \\ k_m e_{fy5} \\ c_m e_{fx1} \\ \vdots \\ c_m e_{fx5} \\ c_m e_{fy1} \\ \vdots \\ c_m e_{fy5} \end{Bmatrix}; \qquad \{\mathbf{B}\}_{52\times1}=\begin{bmatrix} (\omega_p^2 m_1' - k_p' + \omega_p^2 \left(t^{d_1}\right)^2 I_{p_1}) R_{1pp,\mathrm{Re}} + \omega_p c_p' R_{1pp,Im} \\ (\omega_p^2 m_2' - k_g' + \omega_p^2 \left(t^{d_2}\right)^2 I_{p_2}) R_{-1gp,\mathrm{Re}} - \omega_p c_g' R_{1gp,Im} \\ (i^2\omega_e^2 m_1' - k_p' + i\omega_e^2 \left(t^{d_1}\right)^2 I_{p_1}) R_{ipe,\mathrm{Re}} + i\omega_e c_p' R_{ipe,Im} \\ (i^2\omega_e^2 m_2' - k_g' + i\omega_e^2 \left(t^{d_2}\right)^2 I_{p_2}) R_{ige,\mathrm{Re}} + i\omega_e c_g' R_{ige,Im} \\ -k_p' R_{p0,\mathrm{Re}} \\ -k_g' R_{g0,\mathrm{Re}} \\ (\omega_g^2 m_1' - k_p' - \omega_g^2 \left(t^{d_1}\right)^2 I_{p_1}) R_{1pg,\mathrm{Re}} - \omega_g c_p' R_{1pg,Im} \\ (\omega_g^2 m_2' - k_g' - \omega_g^2 \left(t^{d_2}\right)^2 I_{p_2}) R_{-1gg,\mathrm{Re}} - \omega_g c_g' R_{-1gg,Im} \\ (i^2\omega_e^2 m_1' - k_p' - i\omega_e^2 \left(t^{d_1}\right)^2 I_{p_1}) R_{-ipe,\mathrm{Re}} - i\omega_e c_p' R_{-ipe,Im} \\ (i^2\omega_e^2 m_2' - k_g' - i\omega_e^2 \left(t^{d_2}\right)^2 I_{p_2}) R_{-ige,\mathrm{Re}} - i\omega_e c_g' R_{-ige,Im} \\ (\omega_p^2 m_1' - k_p' + \omega_p^2 \left(t^{d_1}\right)^2 I_{p_1}) R_{1pp,Im} - \omega_p c_p' R_{1pp,\mathrm{Re}} \\ (\omega_p^2 m_2' - k_g' + \omega_p^2 \left(t^{d_2}\right)^2 I_{p_2}) R_{1gp,Im} - \omega_p c_g' R_{1gp,\mathrm{Re}} \\ (i^2\omega_e^2 m_1' - k_p' + i\omega_e^2 \left(t^{d_1}\right)^2 I_{p_1}) R_{ipe,Im} - i\omega_e c_p' R_{ipe,\mathrm{Re}} \\ (i^2\omega_e^2 m_2' - k_g' + i\omega_e^2 \left(t^{d_2}\right)^2 I_{p_2}) R_{ige,Im} - i\omega_e c_g' R_{ige,\mathrm{Re}} \\ -k_p' R_{p0,Im} \\ -k_g' R_{g0,Im} \\ (\omega_g^2 m_1' - k_p' - \omega_g^2 \left(t^{d_1}\right)^2 I_{p_1}) R_{-1pg,Im} + \omega_g c_p' R_{-1pg,\mathrm{Re}} \\ (\omega_g^2 m_2' - k_g' - \omega_g^2 \left(t^{d_2}\right)^2 I_{p_2}) R_{-1gg,Im} + \omega_g c_g' R_{-1gg,\mathrm{Re}} \\ (i^2\omega_e^2 m_1' - k_p' - i\omega_e^2 \left(t^{d_1}\right)^2 I_{p_1}) R_{-ipe,Im} + i\omega_e c_p' R_{-ipe,\mathrm{Re}} \\ (i^2\omega_e^2 m_2' - k_g' - i\omega_e^2 \left(t^{d_2}\right)^2 I_{p_2}) R_{-ige,Im} + i\omega_e c_g' R_{-ige,\mathrm{Re}} \end{bmatrix}$$

(B2.1)

Writing the regressor $\{\mathbf{A}\}_{52\times 38}$, the columns 1 through 12 are given as

$$\{\mathbf{A1}\}_{52\times 12} = \begin{bmatrix}
R_{1pp,Re}-R_{1gp,Re} & \omega_p\left(R_{1gp,Im}-R_{1pp,Im}\right) & 1 & 0 & 0 & 0 & 0 & -\omega_p & 0 & 0 & k_p+k_{pla}t_{d_1}-m_1\omega_p^2 & -c_p\omega_p \\
R_{1gp,Re}-R_{1pp,Re} & \omega_p\left(R_{1pp,Im}-R_{1gp,Im}\right) & -1 & 0 & 0 & 0 & 0 & \omega_p & 0 & 0 & 0 & 0 \\
R_{npe,Re}-R_{nge,Re} & i\omega_e\left(R_{nge,Im}-R_{npe,Im}\right) & 0 & 0 & 0 & 0 & 0 & 0 & 0 & 0 & 0 & 0 \\
\vdots & \vdots & \vdots & \vdots & \vdots & \vdots & \vdots & \vdots & \vdots & \vdots & \vdots & \vdots \\
R_{nge,Re}-R_{npe,Re} & i\omega_e\left(R_{npe,Im}-R_{nge,Im}\right) & 0 & 0 & 0 & 0 & 0 & 0 & 0 & 0 & 0 & 0 \\
\vdots & \vdots & \vdots & \vdots & \vdots & \vdots & \vdots & \vdots & \vdots & \vdots & \vdots & \vdots \\
R_{0p,Re}-R_{0g,Re} & 0 & 0 & 0 & 0 & 0 & 0 & 0 & 0 & 0 & 0 & 0 \\
R_{0g,Re}-R_{0p,Re} & 0 & 0 & 0 & 0 & 0 & 0 & 0 & 0 & 0 & 0 & 0 \\
R_{-1pg,Re}-R_{-1gg,Re} & \omega_g\left(R_{-1pg,Im}-R_{-1gg,Im}\right) & 0 & 0 & -1 & 0 & 0 & 0 & 0 & -\omega_g & 0 & 0 \\
R_{-1gg,Re}-R_{-1pg,Re} & \omega_g\left(R_{-1gg,Im}-R_{-1pg,Im}\right) & 0 & 0 & 1 & 0 & 0 & 0 & 0 & \omega_g & 0 & 0 \\
R_{-npe,Re}-R_{-nge,Re} & i\omega_e\left(R_{-npe,Im}-R_{-nge,Im}\right) & 0 & 0 & 0 & 0 & 0 & 0 & 0 & 0 & 0 & 0 \\
\vdots & \vdots & \vdots & \vdots & \vdots & \vdots & \vdots & \vdots & \vdots & \vdots & \vdots & \vdots \\
R_{-nge,Re}-R_{-npe,Re} & i\omega_e\left(R_{-nge,Im}-R_{-npe,Im}\right) & 0 & 0 & 0 & 0 & 0 & 0 & 0 & 0 & 0 & 0 \\
\vdots & \vdots & \vdots & \vdots & \vdots & \vdots & \vdots & \vdots & \vdots & \vdots & \vdots & \vdots \\
R_{1pp,Im}-R_{1gp,Im} & \omega_p\left(R_{1pp,Re}-R_{1gp,Re}\right) & 0 & 1 & 0 & 0 & \omega_p & 0 & 0 & 0 & c_p\omega_p & k_p+k_{pla}t_{d_1}-m_1\omega_p^2 \\
R_{1gp,Im}-R_{1pp,Im} & \omega_p\left(R_{1gp,Re}-R_{1pp,Re}\right) & 0 & -1 & 0 & 0 & -\omega_p & 0 & 0 & 0 & 0 & 0 \\
R_{npe,Im}-R_{nge,Im} & i\omega_e\left(R_{npe,Re}-R_{nge,Re}\right) & 0 & 0 & 0 & 0 & 0 & 0 & 0 & 0 & 0 & 0 \\
\vdots & \vdots & \vdots & \vdots & \vdots & \vdots & \vdots & \vdots & \vdots & \vdots & \vdots & \vdots \\
R_{nge,Im}-R_{npe,Im} & i\omega_e\left(R_{nge,Re}-R_{npe,Re}\right) & 0 & 0 & 0 & 0 & 0 & 0 & 0 & 0 & 0 & 0 \\
\vdots & \vdots & \vdots & \vdots & \vdots & \vdots & \vdots & \vdots & \vdots & \vdots & \vdots & \vdots \\
R_{0p,Im}-R_{0g,Im} & 0 & 0 & 0 & 0 & 0 & 0 & 0 & 0 & 0 & 0 & 0 \\
R_{0g,Im}-R_{0p,Im} & 0 & 0 & 0 & 0 & 0 & 0 & 0 & 0 & 0 & 0 & 0 \\
R_{-1pg,Im}-R_{-1gg,Im} & \omega_g\left(R_{-1gg,Re}-R_{-1pg,Re}\right) & 0 & 0 & 0 & -1 & 0 & 0 & \omega_g & 0 & 0 & 0 \\
R_{-1gg,Im}-R_{-1pg,Im} & \omega_g\left(R_{-1pg,Re}-R_{-1gg,Re}\right) & 0 & 0 & 0 & 1 & 0 & 0 & -\omega_g & 0 & 0 & 0 \\
R_{-npe,Im}-R_{-nge,Im} & i\omega_e\left(R_{-nge,Re}-R_{-npe,Re}\right) & 0 & 0 & 0 & 0 & 0 & 0 & 0 & 0 & 0 & 0 \\
\vdots & \vdots & \vdots & \vdots & \vdots & \vdots & \vdots & \vdots & \vdots & \vdots & \vdots & \vdots \\
R_{-nge,Im}-R_{-npe,Im} & i\omega_e\left(R_{-npe,Re}-R_{-nge,Re}\right) & 0 & 0 & 0 & 0 & 0 & 0 & 0 & 0 & 0 & 0 \\
\vdots & \vdots & \vdots & \vdots & \vdots & \vdots & \vdots & \vdots & \vdots & \vdots & \vdots & \vdots
\end{bmatrix} \tag{B2.2}$$

Continuing with writing the regressor $\{\mathbf{A}\}_{52\times38}$, the columns 12 through 38 are given as

$$\{\mathbf{A2}\}_{52\times26} = \begin{bmatrix}
0 & 0 & -R_{1pp,Re} & I_{1pp,Re} & 0 & 0 & 0 & \cdots & 0 & \cdots & 0 & \cdots & 0 & \cdots \\
0 & 0 & -R_{1gp,Re} & I_{1gp,Re} & 0 & 0 & 0 & \cdots & 0 & \cdots & 0 & \cdots & 0 & \cdots \\
0 & 0 & -R_{npe,Re} & I_{npe,Re} & 0 & 0 & -1 & \cdots & 0 & \cdots & 0 & \cdots & n\omega_e & \cdots \\
\vdots & \vdots & \vdots & \vdots & \vdots & \vdots & \vdots & \ddots & \vdots & \ddots & \vdots & \ddots & \vdots & \ddots \\
0 & 0 & -R_{nge,Re} & I_{nge,Re} & 0 & 0 & 1 & \cdots & 0 & \cdots & 0 & \cdots & -n\omega_e & \cdots \\
\vdots & \vdots & \vdots & \vdots & \vdots & \vdots & \vdots & \ddots & \vdots & \ddots & \vdots & \ddots & \vdots & \ddots \\
0 & 0 & -R_{0p,Re} & I_{0p,Re} & -1 & 0 & 0 & \cdots & 0 & \cdots & 0 & \cdots & 0 & \cdots \\
0 & 0 & -R_{0g,Re} & I_{0g,Re} & 1 & 0 & 0 & \cdots & 0 & \cdots & 0 & \cdots & 0 & \cdots \\
0 & 0 & -R_{-1pg,Re} & I_{-1pg,Re} & 0 & 0 & 0 & \cdots & 0 & \cdots & 0 & \cdots & 0 & \cdots \\
k_g + k_{gla}t_{d_2} - m_2\omega_g^2 & c_g\omega_g & -R_{-1gg,Re} & I_{-1gg,Re} & 0 & 0 & 0 & \cdots & 0 & \cdots & 0 & \cdots & 0 & \cdots \\
0 & 0 & -R_{-npe,Re} & I_{-npe,Re} & 0 & 0 & -1 & \cdots & 0 & \cdots & 0 & \cdots & -n\omega_e & \cdots \\
\vdots & \vdots & \vdots & \vdots & \vdots & \vdots & \vdots & \ddots & \vdots & \ddots & \vdots & \ddots & \vdots & \ddots \\
0 & 0 & -R_{-nge,Re} & I_{-nge,Re} & 0 & 0 & 1 & \cdots & 0 & \cdots & 0 & \cdots & n\omega_e & \cdots \\
\vdots & \vdots & \vdots & \vdots & \vdots & \vdots & \vdots & \ddots & \vdots & \ddots & \vdots & \ddots & \vdots & \ddots \\
0 & 0 & -R_{1pp,Im} & I_{1pp,Im} & 0 & 0 & 0 & \cdots & 0 & \cdots & 0 & \cdots & 0 & \cdots \\
0 & 0 & -R_{1gp,Im} & I_{1gp,Im} & 0 & 0 & 0 & \cdots & 0 & \cdots & 0 & \cdots & 0 & \cdots \\
0 & 0 & -R_{npe,Im} & I_{npe,Im} & 0 & 0 & 0 & \cdots & -1 & \cdots & -n\omega_e & \cdots & 0 & \cdots \\
\vdots & \vdots & \vdots & \vdots & \vdots & \vdots & \vdots & \ddots & \vdots & \ddots & \vdots & \ddots & \vdots & \ddots \\
0 & 0 & -R_{nge,Im} & I_{nge,Im} & 0 & 0 & 0 & \cdots & 1 & \cdots & n\omega_e & \cdots & 0 & \cdots \\
\vdots & \vdots & \vdots & \vdots & \vdots & \vdots & \vdots & \ddots & \vdots & \ddots & \vdots & \ddots & \vdots & \ddots \\
0 & 0 & -R_{0p,Im} & I_{0p,Im} & 0 & -1 & 0 & \cdots & 0 & \cdots & 0 & \cdots & 0 & \cdots \\
0 & 0 & -R_{0g,Im} & I_{0g,Im} & 0 & 1 & 0 & \cdots & 0 & \cdots & 0 & \cdots & 0 & \cdots \\
0 & 0 & -R_{-1pg,Im} & I_{-1pg,Im} & 0 & 0 & 0 & \cdots & 0 & \cdots & 0 & \cdots & 0 & \cdots \\
-c_g\omega_g & k_g + k_{gla}t_{d_2} - m_2\omega_g^2 & -R_{-1gg,Im} & I_{-1gg,Im} & 0 & 0 & 0 & \cdots & 0 & \cdots & 0 & \cdots & 0 & \cdots \\
0 & 0 & -R_{-npe,Im} & I_{-npe,Im} & 0 & 0 & 0 & \cdots & -1 & \cdots & n\omega_e & \cdots & 0 & \cdots \\
\vdots & \vdots & \vdots & \vdots & \vdots & \vdots & \vdots & \ddots & \vdots & \ddots & \vdots & \ddots & \vdots & \ddots \\
0 & 0 & -R_{-nge,Im} & I_{-nge,Im} & 0 & 0 & 0 & \cdots & 1 & \cdots & -n\omega_e & \cdots & 0 & \cdots \\
\vdots & \vdots & \vdots & \vdots & \vdots & \vdots & \vdots & \ddots & \vdots & \ddots & \vdots & \ddots & \vdots & \ddots
\end{bmatrix} \tag{B2.3}$$

While, $\{\mathbf{A}\}_{52\times38} = \left[\{\mathbf{A1}\}_{52\times12} \quad \{\mathbf{A2}\}_{52\times26}\right]_{52\times38}$ (B2.4)

Appendix B3: Identification Algorithm for 12 DOF geared rotor-AMB system

Considering the equations given in Appendix (A3.1) to (A3.16), the regression matrix $\{\mathbf{A}\}_{52\times38}$, column matrix with known quantities $\{\mathbf{b}\}_{52\times1}$ and vector of identifiable parameters $\{\mathbf{x}\}_{38\times1}$ used in the estimation of various system fault parameters are as follows

$$\{\mathbf{x}\}_{38\times1}=\begin{Bmatrix} k_m \\ c_m \\ k_m e_{\mathrm{pRe}} \\ k_m e_{\mathrm{pIm}} \\ k_m e_{g\,\mathrm{Re}} \\ k_m e_{g\,\mathrm{Im}} \\ c_m e_{\mathrm{pRe}} \\ c_m e_{\mathrm{pIm}} \\ c_m e_{g\,\mathrm{Re}} \\ c_m e_{g\,\mathrm{Im}} \\ e_{\mathrm{pRe}} \\ e_{\mathrm{pIm}} \\ e_{g\,\mathrm{Re}} \\ e_{g\,\mathrm{Im}} \\ k_s \\ k_I \\ k_m e_{mx} \\ k_m e_{my} \\ k_m e_{fx1} \\ \vdots \\ k_m e_{fx5} \\ k_m e_{fy1} \\ \vdots \\ k_m e_{fy5} \\ c_m e_{fx1} \\ \vdots \\ c_m e_{fx5} \\ c_m e_{fy1} \\ \vdots \\ c_m e_{fy5} \end{Bmatrix};\quad \{\mathbf{B}\}_{78\times1}=\begin{bmatrix} \left(\omega_p^2 m_1' - k_p' + \omega_p^2 \left(t^{d_1}\right)^2 I_{p_1}\right) R_{1pp,\mathrm{Re}} + \omega_p c_p' R_{1pp,Im} \\ \left(\omega_p^2 m_2' - k_g' + \omega_p^2 \left(t^{d_2}\right)^2 I_{p_2}\right) R_{-1gp,\mathrm{Re}} - \omega_p c_g' R_{-1gp,Im} \\ \left(i^2\omega_e^2 m_1' - k_p' + i\omega_e^2 \left(t^{d_1}\right)^2 I_{p_1}\right) R_{ipe,\mathrm{Re}} + i\omega_e c_p' R_{ipe,Im} \\ \left(i^2\omega_e^2 m_2' - k_g' + i\omega_e^2 \left(t^{d_2}\right)^2 I_{p_2}\right) R_{ige,\mathrm{Re}} + i\omega_e c_g' R_{ige,Im} \\ -k_p' R_{p0,\mathrm{Re}} \\ -k_g' R_{g0,\mathrm{Re}} \\ (\omega_g^2 m_1' - k_p' - \omega_g^2 \left(t^{d_1}\right)^2 I_{p_1}) R_{1pg,\mathrm{Re}} - \omega_g c_p' R_{1pg,Im} \\ (\omega_g^2 m_2' - k_g' - \omega_g^2 \left(t^{d_2}\right)^2 I_{p_2}) R_{-1gg,\mathrm{Re}} - \omega_g c_g' R_{-1gg,Im} \\ (i^2\omega_e^2 m_1' - k_p' - i\omega_e^2 \left(t^{d_1}\right)^2 I_{p_1}) R_{-ipe,\mathrm{Re}} - i\omega_e c_p' R_{-ipe,Im} \\ (i^2\omega_e^2 m_2' - k_g' - i\omega_e^2 \left(t^{d_2}\right)^2 I_{p_2}) R_{-ige,\mathrm{Re}} - i\omega_e c_g' R_{-ige,Im} \\ (\omega_p^2 m_1' - k_p' + \omega_p^2 \left(t^{d_1}\right)^2 I_{p_1}) R_{1pp,Im} - \omega_p c_p' R_{1pp,\mathrm{Re}} \\ (\omega_p^2 m_2' - k_g' + \omega_p^2 \left(t^{d_2}\right)^2 I_{p_2}) R_{-1gp,Im} - \omega_p c_g' R_{-1gp,\mathrm{Re}} \\ (i^2\omega_e^2 m_1' - k_p' + i\omega_e^2 \left(t^{d_1}\right)^2 I_{p_1}) R_{ipe,Im} - i\omega_e c_p' R_{ipe,\mathrm{Re}} \\ (i^2\omega_e^2 m_2' - k_g' + i\omega_e^2 \left(t^{d_2}\right)^2 I_{p_2}) R_{ige,Im} - i\omega_e c_g' R_{ige,\mathrm{Re}} \\ -k_p' R_{p0,Im} \\ -k_g' R_{g0,Im} \\ (\omega_g^2 m_1' - k_p' - \omega_g^2 \left(t^{d_1}\right)^2 I_{p_1}) R_{-1pg,Im} + \omega_g c_p' R_{-1pg,\mathrm{Re}} \\ (\omega_g^2 m_2' - k_g' - \omega_g^2 \left(t^{d_2}\right)^2 I_{p_2}) R_{-1gg,Im} + \omega_g c_g' R_{-1gg,\mathrm{Re}} \\ (i^2\omega_e^2 m_1' - k_p' - i\omega_e^2 \left(t^{d_1}\right)^2 I_{p_1}) R_{-ipe,Im} + i\omega_e c_p' R_{-ipe,\mathrm{Re}} \\ (i^2\omega_e^2 m_2' - k_g' - i\omega_e^2 \left(t^{d_2}\right)^2 I_{p_2}) R_{-ige,Im} + i\omega_e c_g' R_{-ige,\mathrm{Re}} \end{bmatrix} \tag{B3.1}$$

Considering the following terms as

$$\left\{r_p\left(\theta_{ipp,Re}\right)-r_g\left(\theta_{igp,Re}\right)\right\}=t_{p,Re} \qquad -i\omega_p\left\{r_p\left(\theta_{ipp,Im}\right)-r_g\left(\theta_{igp,Im}\right)\right\}=tt_{p,Re}$$

$$\left\{r_p\left(\theta_{ipp,Im}\right)-r_g\left(\theta_{igp,Im}\right)\right\}=t_{p,Im} \qquad +i\omega_p\left\{r_p\left(\theta_{ipp,Re}\right)-r_g\left(\theta_{igp,Re}\right)\right\}=tt_{p,Im}$$

$$\left\{r_p\left(\theta_{ipg,Re}\right)-r_g\left(\theta_{igg,Re}\right)\right\}=t_{g,Re} \qquad -i\omega_g c_m\left\{r_p\left(\theta_{ipg,Im}\right)-r_g\left(\theta_{igp,Im}\right)\right\}=tt_{g,Re}$$

$$\left\{r_p\left(\theta_{ipg,Im}\right)-r_g\left(\theta_{igg,Im}\right)\right\}=t_{g,Im} \qquad +i\omega_g c_m\left\{r_p\left(\theta_{ipg,Re}\right)-r_g\left(\theta_{igg,Re}\right)\right\}=tt_{g,Im}$$

$$\left\{r_p\left(\theta_{ipe,Re}\right)-r_g\left(\theta_{ige,Re}\right)\right\}=t_{e,Re} \qquad -i\omega_e c_m\left\{r_p\left(\theta_{ipe,Im}\right)-r_g\left(\theta_{ige,Im}\right)\right\}=tt_{e,Re}$$

$$\left\{r_p\left(\theta_{ipe,Im}\right)-r_g\left(\theta_{ige,Im}\right)\right\}=t_{e,Im} \qquad +i\omega_e c_m\left\{r_p\left(\theta_{ipe,Re}\right)-r_g\left(\theta_{ige,Re}\right)\right\}=tt_{e,Im}$$

And writing the regressor $\{\mathbf{A}\}_{52\times 38}$, the columns 1 through 12 are given as $\{\mathbf{A1}\}_{52\times 12}$ =

$$\begin{bmatrix}
R_{1pp,Re}-R_{1gp,Re}+t_{p,Re}\cos\psi & \omega_p\left(R_{1gp,Im}-R_{1pp,Im}\right)-tt_{p,Re}\sin\psi & 1 & 0 & 0 & 0 & 0 & -\omega_p & 0 & 0 & k_p+k_{px\varphi_y}t_{d_1}-m_1\omega_p^2 & -c_p\omega_p \\
R_{1gp,Re}-R_{1pp,Re}-t_{p,Re}\cos\psi & \omega_p\left(R_{1pp,Im}-R_{1gp,Im}\right)+tt_{p,Re}\sin\psi & -1 & 0 & 0 & 0 & 0 & \omega_p & 0 & 0 & 0 & 0 \\
R_{npe,Re}-R_{nge,Re}+t_{ne,Re}\cos\psi & i\omega_e\left(R_{nge,Im}-R_{npe,Im}\right)-tt_{ne,Re}\sin\psi & 0 & 0 & 0 & 0 & 0 & 0 & 0 & 0 & 0 & 0 \\
\vdots & \vdots & \vdots & \vdots & \vdots & \vdots & \vdots & \vdots & \vdots & \vdots & \vdots & \vdots \\
R_{nge,Re}-R_{npe,Re}-t_{ne,Re}\cos\psi & i\omega_e\left(R_{npe,Im}-R_{nge,Im}\right)+tt_{ne,Re}\sin\psi & 0 & 0 & 0 & 0 & 0 & 0 & 0 & 0 & 0 & 0 \\
\vdots & \vdots & \vdots & \vdots & \vdots & \vdots & \vdots & \vdots & \vdots & \vdots & \vdots & \vdots \\
R_{0p,Re}-R_{0g,Re} & 0 & 0 & 0 & 0 & 0 & 0 & 0 & 0 & 0 & 0 & 0 \\
R_{0g,Re}-R_{0p,Re} & 0 & 0 & 0 & 0 & 0 & 0 & 0 & 0 & 0 & 0 & 0 \\
R_{-1pg,Re}-R_{-1gg,Re}+t_{g,Re}\cos\psi & \omega_g\left(R_{-1pg,Im}-R_{-1gg,Im}\right)-tt_{g,Re}\sin\psi & 0 & 0 & -1 & 0 & 0 & 0 & 0 & -\omega_g & 0 & 0 \\
R_{-1gg,Re}-R_{-1pg,Re}-t_{g,Re}\cos\psi & \omega_g\left(R_{-1gg,Im}-R_{-1pg,Im}\right)+tt_{g,Re}\sin\psi & 0 & 0 & 1 & 0 & 0 & 0 & 0 & \omega_g & 0 & 0 \\
R_{-npe,Re}-R_{-nge,Re}-t_{ne,Re}\cos\psi & i\omega_e\left(R_{-npe,Im}-R_{-nge,Im}\right)-tt_{ne,Re}\sin\psi & 0 & 0 & 0 & 0 & 0 & 0 & 0 & 0 & 0 & 0 \\
\vdots & \vdots & \vdots & \vdots & \vdots & \vdots & \vdots & \vdots & \vdots & \vdots & \vdots & \vdots \\
R_{-nge,Re}-R_{-npe,Re}+t_{ne,Re}\cos\psi & i\omega_e\left(R_{-nge,Im}-R_{-npe,Im}\right)+tt_{ne,Re}\sin\psi & 0 & 0 & 0 & 0 & 0 & 0 & 0 & 0 & 0 & 0 \\
\vdots & \vdots & \vdots & \vdots & \vdots & \vdots & \vdots & \vdots & \vdots & \vdots & \vdots & \vdots \\
R_{1pp,Im}-R_{1gp,Im}-t_{p,Im}\sin\psi & \omega_p\left(R_{1pp,Re}-R_{1gp,Re}\right)+tt_{p,Im}\cos\psi & 0 & 1 & 0 & 0 & \omega_p & 0 & 0 & 0 & c_p\omega_p & k_p+k_{px\varphi_y}t_{d_1}-m_1\omega_p^2 \\
R_{1gp,Im}-R_{1pp,Im}+t_{p,Im}\sin\psi & \omega_p\left(R_{1gp,Re}-R_{1pp,Re}\right)-tt_{p,Im}\cos\psi & 0 & -1 & 0 & 0 & -\omega_p & 0 & 0 & 0 & 0 & 0 \\
R_{npe,Im}-R_{nge,Im}-t_{ne,Im}\sin\psi & i\omega_e\left(R_{npe,Re}-R_{nge,Re}\right)+tt_{ne,Im}\cos\psi & 0 & 0 & 0 & 0 & 0 & 0 & 0 & 0 & 0 & 0 \\
\vdots & \vdots & \vdots & \vdots & \vdots & \vdots & \vdots & \vdots & \vdots & \vdots & \vdots & \vdots \\
R_{nge,Im}-R_{npe,Im}+t_{ne,Im}\sin\psi & i\omega_e\left(R_{nge,Re}-R_{npe,Re}\right)-tt_{ne,Im}\cos\psi & 0 & 0 & 0 & 0 & 0 & 0 & 0 & 0 & 0 & 0 \\
\vdots & \vdots & \vdots & \vdots & \vdots & \vdots & \vdots & \vdots & \vdots & \vdots & \vdots & \vdots \\
R_{0p,Im}-R_{0g,Im} & 0 & 0 & 0 & 0 & 0 & 0 & 0 & 0 & 0 & 0 & 0 \\
R_{0g,Im}-R_{0p,Im} & 0 & 0 & 0 & 0 & 0 & 0 & 0 & 0 & 0 & 0 & 0 \\
R_{-1pg,Im}-R_{-1gg,Im}-t_{g,Im}\sin\psi & \omega_g\left(R_{-1gg,Re}-R_{-1pg,Re}\right)+tt_{g,Im}\cos\psi & 0 & 0 & 0 & -1 & 0 & 0 & \omega_g & 0 & 0 & 0 \\
R_{-1gg,Im}-R_{-1pg,Im}+t_{g,Im}\sin\psi & \omega_g\left(R_{-1pg,Re}-R_{-1gg,Re}\right)-tt_{g,Im}\cos\psi & 0 & 0 & 0 & 1 & 0 & 0 & -\omega_g & 0 & 0 & 0 \\
R_{-npe,Im}-R_{-nge,Im}-t_{ne,Im}\sin\psi & i\omega_e\left(R_{-nge,Re}-R_{-npe,Re}\right)+tt_{ne,Im}\cos\psi & 0 & 0 & 0 & 0 & 0 & 0 & 0 & 0 & 0 & 0 \\
\vdots & \vdots & \vdots & \vdots & \vdots & \vdots & \vdots & \vdots & \vdots & \vdots & \vdots & \vdots \\
R_{-nge,Im}-R_{-npe,Im}+t_{ne,Im}\sin\psi & i\omega_e\left(R_{-npe,Re}-R_{-nge,Re}\right)-tt_{ne,Im}\cos\psi & 0 & 0 & 0 & 0 & 0 & 0 & 0 & 0 & 0 & 0 \\
\vdots & \vdots & \vdots & \vdots & \vdots & \vdots & \vdots & \vdots & \vdots & \vdots & \vdots & \vdots
\end{bmatrix}$$

(B3.2)

Continuing with writing the regressor $\{\mathbf{A}\}_{52\times 38}$, the columns 12 through 38 are given as

$$\{\mathbf{A2}\}_{52\times 26} = \begin{bmatrix}
0 & 0 & -R_{1pp,Re} & I_{1pp,Re} & 0 & 0 & 0 & \cdots & 0 & \cdots & 0 & \cdots & 0 & \cdots \\
0 & 0 & -R_{1gp,Re} & I_{1gp,Re} & 0 & 0 & 0 & \cdots & 0 & \cdots & 0 & \cdots & 0 & \cdots \\
0 & 0 & -R_{npe,Re} & I_{npe,Re} & 0 & 0 & -1 & \cdots & 0 & \cdots & 0 & \cdots & n\omega_e & \cdots \\
\vdots & \vdots & \vdots & \vdots & \vdots & \vdots & \vdots & \ddots & \vdots & \ddots & \vdots & \ddots & \vdots & \ddots \\
0 & 0 & -R_{nge,Re} & I_{nge,Re} & 0 & 0 & 1 & \cdots & 0 & \cdots & 0 & \cdots & -n\omega_e & \cdots \\
\vdots & \vdots & \vdots & \vdots & \vdots & \vdots & \vdots & \ddots & \vdots & \ddots & \vdots & \ddots & \vdots & \ddots \\
0 & 0 & -R_{0p,Re} & I_{0p,Re} & -1 & 0 & 0 & \cdots & 0 & \cdots & 0 & \cdots & 0 & \cdots \\
0 & 0 & -R_{0g,Re} & I_{0g,Re} & 1 & 0 & 0 & \cdots & 0 & \cdots & 0 & \cdots & 0 & \cdots \\
0 & 0 & -R_{-1pg,Re} & I_{-1pg,Re} & 0 & 0 & 0 & \cdots & 0 & \cdots & 0 & \cdots & 0 & \cdots \\
k_g + k_{gx\varphi_y} t_{d_2} - m_2\omega_g^2 & c_g\omega_g & -R_{-1gg,Re} & I_{-1gg,Re} & 0 & 0 & 0 & \cdots & 0 & \cdots & 0 & \cdots & 0 & \cdots \\
0 & 0 & -R_{-npe,Re} & I_{-npe,Re} & 0 & 0 & -1 & \cdots & 0 & \cdots & 0 & \cdots & -n\omega_e & \cdots \\
\vdots & \vdots & \vdots & \vdots & \vdots & \vdots & \vdots & \ddots & \vdots & \ddots & \vdots & \ddots & \vdots & \ddots \\
0 & 0 & -R_{-nge,Re} & I_{-nge,Re} & 0 & 0 & 1 & \cdots & 0 & \cdots & 0 & \cdots & n\omega_e & \cdots \\
\vdots & \vdots & \vdots & \vdots & \vdots & \vdots & \vdots & \ddots & \vdots & \ddots & \vdots & \ddots & \vdots & \ddots \\
0 & 0 & -R_{1pp,Im} & I_{1pp,Im} & 0 & 0 & 0 & \cdots & 0 & \cdots & 0 & \cdots & 0 & \cdots \\
0 & 0 & -R_{1gp,Im} & I_{1gp,Im} & 0 & 0 & 0 & \cdots & 0 & \cdots & 0 & \cdots & 0 & \cdots \\
0 & 0 & -R_{npe,Im} & I_{npe,Im} & 0 & 0 & 0 & \cdots & -1 & \cdots & -n\omega_e & \cdots & 0 & \cdots \\
\vdots & \vdots & \vdots & \vdots & \vdots & \vdots & \vdots & \ddots & \vdots & \ddots & \vdots & \ddots & \vdots & \ddots \\
0 & 0 & -R_{nge,Im} & I_{nge,Im} & 0 & 0 & 0 & \cdots & 1 & \cdots & n\omega_e & \cdots & 0 & \cdots \\
\vdots & \vdots & \vdots & \vdots & \vdots & \vdots & \vdots & \ddots & \vdots & \ddots & \vdots & \ddots & \vdots & \ddots \\
0 & 0 & -R_{0p,Im} & I_{0p,Im} & 0 & -1 & 0 & \cdots & 0 & \cdots & 0 & \cdots & 0 & \cdots \\
0 & 0 & -R_{0g,Im} & I_{0g,Im} & 0 & 1 & 0 & \cdots & 0 & \cdots & 0 & \cdots & 0 & \cdots \\
0 & 0 & -R_{-1pg,Im} & I_{-1pg,Im} & 0 & 0 & 0 & \cdots & 0 & \cdots & 0 & \cdots & 0 & \cdots \\
-c_g\omega_g & k_g + k_{gx\varphi_y} t_{d_2} - m_2\omega_g^2 & -R_{-1gg,Im} & I_{-1gg,Im} & 0 & 0 & 0 & \cdots & 0 & \cdots & 0 & \cdots & 0 & \cdots \\
0 & 0 & -R_{-npe,Im} & I_{-npe,Im} & 0 & 0 & 0 & \cdots & -1 & \cdots & n\omega_e & \cdots & 0 & \cdots \\
\vdots & \vdots & \vdots & \vdots & \vdots & \vdots & \vdots & \ddots & \vdots & \ddots & \vdots & \ddots & \vdots & \ddots \\
0 & 0 & -R_{-nge,Im} & I_{-nge,Im} & 0 & 0 & 0 & \cdots & 1 & \cdots & -n\omega_e & \cdots & 0 & \cdots \\
\vdots & \vdots & \vdots & \vdots & \vdots & \vdots & \vdots & \ddots & \vdots & \ddots & \vdots & \ddots & \vdots & \ddots
\end{bmatrix} \tag{B3.3}$$

While, $\{\mathbf{A}\}_{52\times 38} = \left[\{\mathbf{A1}\}_{52\times 12} \quad \{\mathbf{A2}\}_{52\times 26}\right]_{52\times 38}$ (B3.4)

Appendix C: Nyquist Stability Criteria

Let G_C be the transfer function of the controller, G_B be the transfer function of actuator (magnetic bearing), G_A be the transfer function of amplifier gain k_A, G_{sn} be the transfer function of the overall sensor correction gain k_{sn}. We have the following transfer functions for a system with PID controller (Tiwari, 2017):

$$G_C = \left(\frac{K_p s + K_I + K_D s^2}{s} \right) \tag{C.1}$$

$$G_B = \frac{-k_i}{ms^2 + \left(c_p + c_m\right)s + \left(k_p + k_m - k_s\right)}, G_A = k_A, G_{sn} = k_{sn} \tag{C.2}$$

The closed loop transfer function of the proposed geared rotor-AMB model, as shown as in block diagram in Fig. 5. is given by

$$G(s) = \frac{G_{CBA}(s)}{1 + G_{CBA}(s)G_{sn}(s)} \tag{C.3}$$

The open loop transfer function of the proposed geared rotor-AMB model is, $G_{CBA}(s)G_{sn}(s)$

where, $G_{CBA}(s) = G_C G_B G_A = \left(\frac{K_p s + K_I + K_D s^2}{s} \right) \left(\frac{k_I}{ms^2 + \left(c_p + c_m\right)s + \left(k_p + k_m + k_s\right)} \right) k_A$ (C.4)

Therefore, for the negative feedback of the proposed geared rotor-AMB system, the overall closed loop transfer function is given by

$$G(s) = \frac{\left(K_p s + K_I + K_D s^2\right) k_I k_A}{ms^3 + \left(c_p + c_m + K_D k_I k_A k_{sn}\right)s^2 + \left(k_p + k_m + k_s + K_p k_I k_A k_{sn}\right)s + K_I k_I k_A k_{sn}} \tag{C.5}$$

Appendix D: Flow chart of identification algorithm

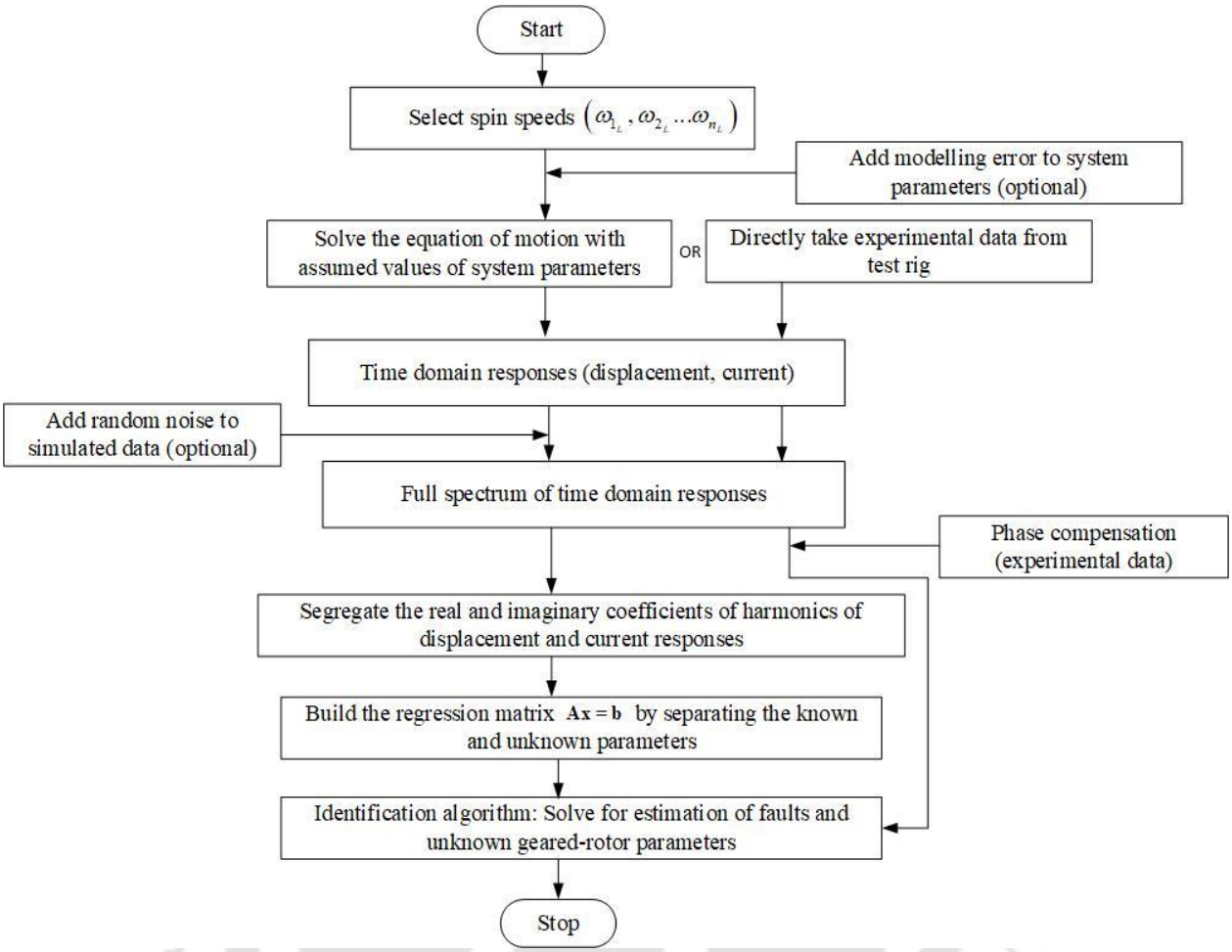

REFERENCES

Andrews J D, "A finite element analysis of bending stresses induced in external and internal involute spur gears. " The Journal of Strain Analysis for Engineering Design, Volume 26, pp. 152 – 163, 1991.

Athavale S. M., Krishnaswami R. and Kuo E. Y., "Estimation of Statistical Distribution of Composite Manufactured Transmission Error. " A Precursor to Gear Whine, for a Helical Planetary Gear System, SAE 2001-01-1507, 2001.

Blankenship G. W., and Singh R., "A Comparative Study of Selected Gear Mesh Interface Dynamic Models. " DE-Vol. 43-1, International Power Transmission and Gearing Conference, Vol 1, ASME, 1992.

Bartelmus W., Zimroz R., "A new feature for monitoring the condition of gearboxes in non-stationary operating conditions. " Mech. Syst. Signal Process. 23: 1528–1534, 2009.

Barrett T. S., Palazzolo A. B., Kascak A. F., "Active vibration control of rotating machinery using piezoelectric actuators incorporating flexible casing effects. " Trans. ASME—Journal of Engineering for Gas Turbines and Power, 117, pp.176–87, 1995.

Barbaraci G., Mariotti G V, Piscopo A., " Active magnetic bearing design study. " J Vib. Control, 19(16), pp. 2491–2505, 2013.

Bartelmus Walter, “Mathematical modelling and computer simulations as an aid to gearbox diagnostics. " Mechanical Systems and Signal Processing, Volume 15, Issue 5, September 2001, Pages 855-871, 2001.

Chung C. H., Steyer G., Abe T., Clapper M. and Shah C., "Gear Noise Reduction Through Transmission Error Control and Gear Blank Dynamic Tuning. " presented at the SAE Sound & Vibration Conference, Traverse City, SAE paper no. 1999-01-1766, May 1999.

Dudley D. W. and Townsend Dennis P., " Dudley's Gear Handbook. " 2nd Edition, McGraw Hill, New York, 1991.

Dudley D. W., "Handbook of Practical Gear Design. " McGraw-Hill Inc., 1984.

Dogruer, C. and Pirsoltan, A. K., "Active vibration control of a single-stage spur gearbox. " Mechanical Systems and Signal Processing 85: 429-444, 2017.

Eritenel Tugan and Parker R.G., "An investigation of tooth mesh nonlinearity and partial contact loss in gear pairs using a lumped-parameter model. " Mech. Mach. Theory 56, 28–51, 2012.

Fan L., Wang S., Wang X., Han F., Lyu H., "Nonlinear dynamic modeling of a helicopter planetary gear train for carrier plate crack fault diagnosis. " Chinese Journal of Aeronautics, Vol. 29, pp. 675-687, 2016.

Frolov K. V. and Kosarev O. I., "Control of gear vibrations at their source. " International Applied Mechanics, Vol. 39, No. 1, 2003.

Feng Z., Zuo M.J., "Vibration signal models for fault diagnosis of planetary gearboxes. " J. Sound Vib. 331: 4919–4939, 2012.

Feng Z., Zuo M.J., "Fault diagnosis of planetary gearboxes via torsional vibration signal analysis. " Mech. Syst. Signal Process. 36: 401–421, 2013.

Friswell MI and Mottershead JE, "Finite Element Model Updating in Structural Dynamics. " Kluwer Academic Publishers, Dordrecht, the Netherlands, 1995.

Guangjian W., Lin C., Li Y., Shuaidong Z., "Research on the dynamic transmission error of a spur gear pair with eccentricities by finite element method. " Mechanism and Machine Theory 109, 1-13, 2017.

Gregory R.W., Harris S.L., Munro R.G., "Dynamic behaviour of spur gears. " Proceedings of the Institution of Mechanical Engineers, 1963.

Glover R. C. and Rauen D. G., "Gear Transmission Error Metric for Use with Gear Inspection Machine. " presented at the SAE Sound & Vibration Conference, Traverse City, SAE 2003-01-1663, May 2003.

Gregory R.W., Harris S. L., and Munro R.G., "A Method of Measuring Transmission Error in Spur Gears of 1:1 Ratio." Journal of Scientific Instruments, vol. 40, pp.5-9, 1963.

Gelman L., Zimroz R., Birkel J., Leigh-Firbank H., Simms D., Waterland B., Whitehurst G., "Adaptive vibration condition monitoring technology for local tooth damage in gearboxes. " Insight Non-Destr. Test. Cond. Monit. 47: 461–464, 2005.

Gembler W., Schweitzer H., Maier R., Pucher M., "Helicopter interior noise reduction by active gearbox struts. " Proceedings of the 54th annual forum of the American Helicopter Society, Washington DC, USA, pp.216–229. Fairfax, VA: American Helicopter Society, Inc., 20–22 May 1998.

Goodman R K and Millott T A., "Design, development, and flight testing of the active vibration control system for the Sikorsky S-92. " In: Proceedings of the 51st annual forum of the American Helicopter Society, Virginia Beach, VA, USA, pp.764–771. Fairfax, VA: American Helicopter Society, Inc., 2–4 May 2000

Guan Y. H., Shepard W. S. Jr., Lim T. C., " Direct hybrid adaptive control of gear pair vibration." ASME Journal of Dynamic Systems, Measurement and Control, 125, pp.585–594, 2003.

Guan Y. H., Li M., Lim T. C., Shepard W. S., " Comparative analysis of actuator concept for active gear pair vibration control. " Journal of Sound and Vibration, 269, pp. 273–294, 2004.

Gahler C., Mohler M. and Herzog R., "Multivariable identification of active magnetic bearing systems. " JSME International Journal Series C Mechanical Systems, Machine Elements and Manufacturing 40(4), pp. 584–592, 1997.

Hoffmann F., Maier R., Janker P., "Helicopter interior noise reduction by using active gearbox struts. " In: 12th AIAA/CEAS aeroacoustics conference, Cambridge, MA, USA, pp.2625–2634. MA: AIAA, 8–10 May 2006.

Heverly D., "Optimal actuator placement and active structure design for control of helicopter airframe vibrations. " PhD Thesis, Pennsylvania State University, USA, 2002.

Hadjiloucas S., Walker G. C., Bowen J. W. and Karatzas L. S., "Performance limitations of piezoelectric and force feedback electrostatic transducers in different applications." J. Phys.: Conf. Ser.178 012036, 2009.

Hiroaki Endo and Nader Sawalhi, "Gearbox Simulation Models with Gear and Bearing Faults." Mechanical Engineering, Dr. Murat Gokcek (Ed.), ISBN: 978-953-51-0505-3, 2012.

Harris C. M., "Handbook of Acoustical Measurements and Noise Control. " 3rd edition, McGraw-Hill Inc, 1991.

Houser D. R., Oswald F. B., Valco M. J., Drago R. J., and Lenski J. W., "Comparison of transmission error predictions with noise measurements for several spur and helical gears. " In Proceedings of 30th AIAA, SAE, and ASEE Propulsion Conference, Indianapolis, AIAA-94-3366, pp. 1–16, 1994.

Houser Donald R. and Blankenship G. W, "Methods for Measuring Gear Transmission Error Under Load and at Operating Speeds. " JOURNAL OF PASSENGER CARS, SAE Transactions Vol. 98, Section 6, pp. 1367-1374, 1989.

Houser D., Harianto J., Sorenson J., Lim T., Myers C., Gordon B. and Berry S., "Case History: Engine Timing Gear Noise Reduction. " Proceedings of the 1999 Noise and Vibration Conference, SAE Technical Paper 1999-01-1716.

Imlach J., Blair B. J., Allaire P. E., "Measured and predicted force and stiffness characteristics of industrial magnetic bearings. " ASME Journal of Tribology, 113(4): 784-788, 1991.

Kim W., Lee J.Y., Chung J., "Dynamic analysis for a planetary gear with time-varying pressure angles and contact ratios. " Journal of Sound and Vibration, 331, pp. 883-901, 2012.

Kawai R., Ari S., and Iwatsubo T., "Coupled Lateral Torsional Vibration of a Geared Rotor System. " International Conference on Vibrations in Rotating Machinery, 3rd, Mechanical Engineering Publications, London, pp. 59-66, 1984.

Kayama F., "The Dynamics of Parallel Axis Gears in an Automotive Transmission. " PhD Thesis, University of Leeds, 2005.

Kimman M.H., Langen H.H., R.H. Munnig Schmidt, "A miniature milling spindle with active magnetic bearings. " Mechatronics, 20: pp. 224–235, 2010.

Knospe Carl R., "Active magnetic bearings for machining applications. " Control Engineering Practice 15: 307 – 313, 2007.

Kahrmann A. and Singh R., "Non-Linear Dynamics of a Spur Gear Pair. " Journal of sound and vibration, 142(1), pp. 49-75, 1990.

Li G., Lin Z., Allaire P.E., Luo J., " Modeling of a high speed rotor test rig with active magnetic bearings. " Transactions of the ASME, Journal of Vibration and Acoustics, 128(3), pp. 269–281, 2006.

Lees A., Sinha J. k., Friswell M. I., "The identification of the unbalance of a flexible rotating machine from a single rundown." ASME J. Eng. Gas Turbines Power 126(2): 416-421, 2004.

Loutridis S.J., "Instantaneous energy density as a feature for gear fault detection. " Mechanical Systems and Signal Processing 20 (5), 1239–1253, 2006.

Lin H. H. and Liou C. H., "A Parametric Study of Spur Gear Dynamics. " NSAS/CR— 1998-206598, January, 1998.

Li S. and Kahraman A., "A Transient Mixed Elastohydrodynamic Lubrication Model for Spur Gear Pairs. " Journal of Tribology, Vol. 132, 2010.

Lin T., Ou H., Li R., "A finite element method for 3D static and dynamic contact/impact analysis of gear drives. " Comput. Methods Appl. Mech. Eng. 196, 1716–1728, 2007.

Liang Xihui, Ming J.Zuo, Zhipeng Feng, "Dynamic modeling of gearbox faults: A review. " Mechanical Systems and Signal Processing, Volume 98, pp. 852-876, 2018.

Liang X., Zhang H., Liu L., Zuo M.J., "The influence of tooth pitting on the mesh stiffness of a pair of external spur gears. " Mech. Mach. Theory 106, 1–15, 2016.

Liang X., Zuo M.J., Pandey M., "Analytically evaluating the influence of crack on the mesh stiffness of a planetary gear set. " Mech. Mach. Theory 76, 20–38, 2014.

Lei Y., Zuo M.J., "Gear crack level identification based on weighted k nearest neighbor classification algorithm. " Mech. Syst. Signal Process. 23:1535–1547, 2009.

Liang X., Zuo M.J., Chen W., "Dynamics based vibration signal modeling for tooth fault diagnosis of planetary gearboxes. " in: M. Demetgul, M. Ünal (Eds.), Fault Diagnosis and Detection, InTech, 2017.

Maliha R., Dogruer U.C. and Ozguven H.N., "Nonlinear dynamic modeling of gear-shaft-disk-bearing systems using finite elements and describing functions. " Journal of Mechanical Design 126, pp. 534–541, 2004.

Munro R. G., "Optimum profile relief and transmission error in spur gears. " Proceedings of the First Institution of Mechanical Engineers International Conference on Gearbox Noise and Vibration, Cambridge, 1990.

Mark W.D., "Analysis of the vibratory excitation of gear systems: basic theory. " Journal of the Acoustical Society of America, 1978.

Munro R. G., "A review of the theory and measurement of gear transmission error. " Proceedings of the First IMechE Conference on Gearbox Noise and Vibration, paper C404/032, pp. 3–10, 1990.

Munro R. G. and Houser D. R., "Transmission Error Concepts. " The Gear Noise Short Course, Oct 2003.

Muszyńska, A., "Rotordynamics" (1st ed.). CRC Press, Taylor and Francis Group, Boca Raton, May 2005.

Mitchell L. D., and Daws J.W., "A Basic Approach to Gearbox Noise Prediction. " SAE Technical Paper 821065, International Off Highway Meeting & Exposition, Milwaukee, Sep 13-16, 1982.

Maier R., Hoffmann F and Tewes S., "Active vibration isolation system for helicopter interior noise reduction. " In: 8th AIAA/CEAS aeroacoustics conference, Breckenridge, CO, USA, 17–19 June 2002. CO: AIAA.

Maslen E. H., "Magnetic Bearing." University of Virginia. Department of Mechanical, Aerospace, and Nuclear Engineering, Charlottesville, Virginia, 2000.

Mahmood R S and Heverly D E., "In-flight demonstration of active vibration control technologies on the Bell 429 helicopter. " In: Proceedings of the 68th annual forum of the American Helicopter Society, Fort Worth, TX, USA, pp.1173–1182. Fairfax, VA: American Helicopter Society, Inc., 1–3 May 2012

Montague G. T., Kascak A. F., Palazzolo A., Manchala D., Thomas E., "Feedforward control of gear mesh vibration using piezoelectric actuators. " Shock and Vibration 1(5): 473-484, 1994.

Mushi S E, Lin Z, Allaire P E, " Design, construction, and modeling of a flexible rotor active magnetic bearing test rig. " IEEE/ASME Trans Mechatron, 17(6), pp. 1170–1182, 2011.

Özgüven H. N. and Houser D. R., "Mathematical Models used in Gear Dynamics – A Review. " Journal of sound and vibration, 121(3), pp. 383-411, 1988.

Özgüven H. N. and Houser D. R., "Dynamic Analysis of High Speed Gears by Using Loaded Static Transmission Error. " Journal of Sound and Vibration, Vol. 125, No. 1, pp. 71-83, 1988b.

Parker R.G., Vijayakar S.M., Imajo T., "Non-linear dynamic response of a spur gear pair: modelling and experimental comparisons. " J. Sound Vib. 237: 435–455, 2000.

Parker R.G., Agashe V., Vijayakar S.M., "Dynamic response of a planetary gear system using a finite element/contact mechanics model. " J. Mech. Des. 122: 304–310, 1999.

Polajžer B, Ritonja J, Štumberger G, Dolinar D, J-P Lecointe, " Decentralized PI/PD position control for active magnetic bearings. " Electr Eng, 89(1), pp. 53–59, 2006.

Rincon A. Fernandez del, Viadero F., Iglesias M., García P., de-Juan A., Sancibrian R., "A model for the study of meshing stiffness in spur gear transmissions. " Mech. Mach. Theory 61: 30–58, 2013.

Rebbechi B., Howard C., Hansen C., "Active control of gearbox vibration. " INTER-NOISE and NOISE-CON Congress and Conference Proceedings, Institute of Noise Control Engineering, Dec 02-04, Fort Lauderdale, Florida, USA, 1999.

Rajan G. and Tiwari R., " On-line High-Speed Balancing of Flexible Rotor-Bearing System Using Virtual Trial Unbalances at Slow Run. " International Journal of Mechanical Sciences, 183, 105786, pp. 1-18, 2020.

Rao B. R. and Tiwari R., "Detection of asymmetric transmission error in geared rotor system through transverse vibration analysis using full spectrum." Propulsion and Power research, Vol. 9, Issue 3, 255-280, 2020.

Sutton T. J., Elliott S. J., Brennan M. J., Heron K. H., "Active isolation of multiple structural waves on a helicopter gearbox support strut. " D.A.C. Jessop, Journal of Sound and Vibration, 205(1), 81-101, 1997.

Schweitzer G. and Maslen E. H., " Magnetic Bearings: Theory, Design, and Application to Rotating Machinery. " Springer-Verlag Berlin Heidelberg, 2009.

Srinivas R.Siva, Tiwari R., Kannababu Ch., "Application of active magnetic bearings in flexible rotordynamic systems – A state-of-the-art review. " Mechanical Systems and Signal Processing, Volume 106, Pages 537-572, 2018.

Singh S. and Tiwari R, "Model-based Switching Crack Identification in a Jeffcott Rotor with an Offset Disc Integrated with an Active Magnetic Bearing. " ASME Journal of Dynamic Systems, Measurement and Control. DOI: 10.1115/1.4032292, 2015.

Smith J. D., "Gear Noise and Vibration. " Marcel Dekker Inc., New York, 1999.

Smith J. D., "Gear Noise and Vibration. " 2nd Edition, Marcel Dekker Inc., New York, 2003.

Tiwari R., "Rotor Systems: Analysis and Identification. " CRC Press, Taylor and Francis Group, Boca Raton, FL, USA, 2017.

Tiwari R., "Conditioning of regression matrices for simultaneous estimation of the residual unbalance and bearing dynamic parameters. " Mechanical Systems and Signal Processing 19(5): 1082-1095, 2005.

Tiwari R., and Chakravarthy V., "Simultaneous estimation of the residual unbalance and bearing dynamic parameters from the experimental data in a rotor-bearing system." Mechanism and Machine Theory 44(4): 792-812, 2009.

Velex P., Chapron M., Fakhfakh H., Bruyere J., Becquerelle S., "On transmission errors and profile modifications minimising dynamic tooth loads in multi-mesh gears. " Journal of Sound and Vibration, 379: 28-52, 2016.

Vázquez J. A., Maslen E. H., Ahn H.-J. and Han D.-C., "Model identification of a rotor with magnetic bearings. " ASME Turbo Expo 2001: Power for Land, Sea, and Air. American Society of Mechanical Engineers, V004T03A059–V004T03A059, 2001.

Wang H., Zhang F., Li H., Sun W., and Luo S., "Experimental Analysis of an Active Vibration Frequency Control in Gearbox. " Hindawi, Shock and Vibration, Article ID 1402697, 9 pages, Volume 2018.

Wu S., Zuo M J., Parey A., "Simulation of spur gear dynamics and estimation of fault growth. " Journal of Sound and Vibration 317(3-5): 608-624, 2008.

Zhong W. and Palazzolo A., " Magnetic Bearing Rotordynamic System Optimization Using Multi-Objective Genetic Algorithms. " ASME J. of Dynamic Systems, Measurement and Control, 137(2), 021012, 2014.

Publications from the Present Research

Journal Publications

1. Majumder, G., Tiwari, R., " Transverse Vibration of Geared-Rotor Integrated with Active Magnetic Bearings in Identification of Multiple Faults. " **ASME Journal of Dynamic Systems, Measurement, and Control,** September 2021; 143(9): 091003.

2. Majumder, G., Tiwari, R., " Application of Active Magnetic Bearings in Control and Estimation of Geared-Rotor Faults in High Speed Offset Spur Gear Transmission System. " **Mechanical Systems and Signal Processing**, Vol. 176, 15 August 2022, 109113. ISSN 0888-3270,

3. Majumder, G., Tiwari, R., " Experimental Study on Vibration Control of Spur Geared Rotor System Using Active Magnetic Bearings. " **Journal of Sound and Vibration**, Vol. 532, 18 August 2022, 117005, ISSN: 0022-460X.

Conference Publication

1. Majumder, G. and Tiwari, R., 2019, "Vibration Control of Spur Geared Rotor Systems with Transmission Errors by Active Magnetic Bearings". **ASME Power Transmission and Gearing Conference, IDETC2019** - 97176, V010T11A017; 9 pages, Anaheim, CA, USA, Aug 18-21, 2019. Conference Paper Presented, 08/2019.